



Advances in Tunable Diode Laser Spectroscopy  
using Residual Amplitude Modulation Techniques

Keith Ruxton

Department of Electronic and Electrical Engineering

Centre for Microsystems and Photonics

A thesis submitted to the Department of Electronic and Electrical Engineering of the

University of Strathclyde for the degree of Doctor of Philosophy

August 2010

This thesis is the result of the authors original research. It has been composed by the author and has not been previously submitted for examination which has lead to the award of a degree.

The copyright of this thesis belongs to the author under the terms of the United Kingdom Copyright Acts as qualified by University of Strathclyde Regulation 3.50. Due acknowledgment must always be made of the use of any material contained in, or derived from, this thesis.

Signed: Keith Ruxton

Date: 25/09/2010

# Acknowledgements

A massive thanks to Walter and George for being top supervisors! What can I say, Walter with the big ideas and George sorting out the details the best tag team you could have for doing a PhD. The last three years has been for the most part an enjoyable experience, thanks to Walter for his excellent guidance and support and to George for his willingness to discuss any issues at a drop of a hat. Thanks also to Kevin who helped me get up to speed when I started and for letting me take over his experiment. If it wasn't for his research and help I would still be down in the lab.

Thanks to Arup, my partner in crime, Mick and Ian for your input and assistance throughout the PhD and to Jamie for our morning chats while you were waiting for the kettle to boil and introducing me to the kettlebell. To everyone else in CMP thanks for the banter and good luck to those who still have the fun task of writing their thesis.

A big thanks to my family for their support over the years, especially to my mum and dad. Most importantly, thank you Elizabeth for your solid support throughout my PhD, you kept me on the path, I don't know where I would be without you!

Finally, thanks to the Engineering and Physical Science Research Council and the Atomic Weapons Establishment for funding my PhD.

This thesis is brought to you by L<sup>A</sup>T<sub>E</sub>X, cheers Mick!

# Abstract

The recovery and analysis of the 1<sup>st</sup> harmonic signals in tunable diode laser spectroscopy (TDLS) with wavelength modulation (WM) are limited by the presence of background residual amplitude modulation (RAM), upon which the small gas signals are superimposed. The implementation of a novel optical approach to suppress the background RAM, a large unwanted background signal, is presented. The research presented includes advancements made in this context on two recent analysis techniques, the phasor decomposition (PD) method and the RAM technique. Both are calibration free and can extract the absolute gas absorption line shape from the recovered harmonic signals. The optical approach developed uses a fibre delay branch placed in parallel with a gas cell that when both branch outputs are combined the background RAM signal is suppressed, resulting in improved equipment sensitivity, due to increased signal amplification.

Also presented, are developments made in the mathematical modelling necessary to successfully extract the absolute gas absorption line shapes from the directly recovered RAM signals under a wide range of experimental conditions. This new model includes the distortion effects caused by WM/intensity modulation (IM) signals at high modulation indices, such that, correction factors can be applied to the recorded signals to recover the absolute gas absorption line shape. A wide range of experimental results for a methane absorption line at 1650.96nm are presented and compared with theoretical line shapes provided from the HITRAN 2004 database. The agreement between experimental and theory validates the new model and developed procedures to successfully recover the absolute gas absorption line shape.

The research then focuses on a procedure to scale and compare the amplitudes in terms of laser power of the recovered 1<sup>st</sup> harmonic WM/IM, 2<sup>nd</sup> harmonic WM/IM and RAM absorption signals with theory. The presented results validate recently developed expressions that can be used to calculate theoretical signal amplitudes. The latter part of the investigation determines the optimum operating conditions for when the extracted RAM absorption amplitude is greater than the recovered

1<sup>st</sup> harmonic WM/IM and 2<sup>nd</sup> harmonic WM/IM signals. The experimental results for this investigation, again focused on the 1650.96nm line, validate the developed processes and procedures. These advancements are beneficial towards robust stand alone calibration free instrumentation that can be used by industry for gas measurement/detection applications.

# Contents

<b>1</b>	<b>Introduction and Review</b>	<b>1</b>
1.1	Overview . . . . .	1
1.2	TDLS with Direct Detection . . . . .	3
1.3	TDLS with Wavelength Modulation . . . . .	5
1.4	Summary . . . . .	12
1.5	Thesis Aims and Objectives . . . . .	13
1.6	Thesis Outline . . . . .	14
<b>2</b>	<b>Fundamentals of Molecular Spectroscopy</b>	<b>16</b>
2.1	Overview . . . . .	16
2.2	Formation of Line Spectra . . . . .	17
2.3	Width of Line Spectra . . . . .	18
2.3.1	Overview . . . . .	18
2.3.2	Natural Broadening . . . . .	18
2.3.3	Doppler Broadening . . . . .	19
2.3.4	Collision Broadening . . . . .	20
2.4	Intensity of Line Spectra . . . . .	20
2.4.1	Overview . . . . .	20
2.4.2	Transition Probability . . . . .	20
2.4.3	Population of States . . . . .	21
2.4.4	The Beer-Lambert Law . . . . .	21
2.5	Infra Red Spectroscopy . . . . .	22
2.6	Vibrational/Rotational Spectroscopy of the Methane molecule . . . . .	25
2.7	Extracting Gas Concentration and Pressure . . . . .	29

2.7.1	Overview . . . . .	29
2.7.2	Gas Concentration . . . . .	29
2.7.3	Gas Pressure . . . . .	30
2.8	Modelling Line Spectra . . . . .	32
2.9	Summary . . . . .	34
<b>3</b>	<b>Analytical Methodology - Conventional Techniques</b>	<b>35</b>
3.1	Overview . . . . .	35
3.2	RAM Technique . . . . .	36
3.3	Phasor Decomposition Method . . . . .	40
3.4	Amplitude Investigation . . . . .	44
3.4.1	Overview . . . . .	44
3.4.2	Power of 1 <sup>st</sup> Derivative Signal - Conventional TDLS with WM isolated from RAM . . . . .	45
3.4.3	Power of 2 <sup>nd</sup> Derivative Signal - Conventional TDLS with WM . . . . .	46
3.4.4	Intensity of Absolute Gas Absorption Line Shape . . . . .	48
3.5	Correction Factor Implementation . . . . .	51
3.6	Summary . . . . .	54
<b>4</b>	<b>Experimental Methodology</b>	<b>56</b>
4.1	Overview . . . . .	56
4.2	Laser and Drive Electronics . . . . .	58
4.3	Delay Fibre and Gas Cell . . . . .	61
4.3.1	Overview . . . . .	61
4.3.2	Delay Line Branch . . . . .	61
4.3.3	Gas Cell Branch . . . . .	62
4.4	Receiver Electronics . . . . .	66
4.5	System Characterisation . . . . .	67
4.5.1	Overview . . . . .	67
4.5.2	Wavelength Referencing . . . . .	68
4.5.3	Laser Tuning and Modulation Coefficients . . . . .	73

4.5.4	IM and WM Phase Separation . . . . .	78
4.6	Summary . . . . .	81
<b>5</b>	<b>Validation of RAM Nulling for 1<sup>st</sup> Harmonic TDLS with RAM</b>	<b>82</b>
5.1	Overview . . . . .	82
5.2	RAM Technique with RAM Nulling . . . . .	84
5.2.1	Overview . . . . .	84
5.2.2	Revised Analytical Methodology . . . . .	85
5.2.3	Experimental Methodology . . . . .	88
5.2.4	10.13%CH <sub>4</sub> :N <sub>2</sub> Results . . . . .	92
5.2.5	Measurement of Concentration and Pressure . . . . .	96
5.2.6	1.02%CH <sub>4</sub> :N <sub>2</sub> Results . . . . .	97
5.2.7	Measurement of Concentration and Pressure . . . . .	100
5.2.8	Summary of Results . . . . .	101
5.3	PD Method with RAM Nulling . . . . .	102
5.3.1	Revised Analytical Methodology . . . . .	102
5.3.2	Experimental Methodology . . . . .	103
5.3.3	10.13%CH <sub>4</sub> :N <sub>2</sub> Results . . . . .	106
5.3.4	Measurement of Concentration and Pressure . . . . .	110
5.3.5	1.02%CH <sub>4</sub> :N <sub>2</sub> Results . . . . .	110
5.3.6	Measurement of Concentration and Pressure . . . . .	114
5.3.7	Summary of Results . . . . .	115
5.4	Overall Summary and Conclusions . . . . .	115
<b>6</b>	<b>Optimisation of 1<sup>st</sup> Harmonic TDLS with RAM</b>	<b>117</b>
6.1	Overview . . . . .	117
6.2	Scaling Factor Calculations . . . . .	119
6.3	Signal Amplitude Investigation: Low Modulation Frequency Range	121
6.3.1	Overview . . . . .	121
6.3.2	10.13%CH <sub>4</sub> :N <sub>2</sub> Results . . . . .	122
6.3.3	1.02%CH <sub>4</sub> :N <sub>2</sub> Results . . . . .	133
6.3.4	Discussion of Results . . . . .	144

*Contents*

6.4	Signal Amplitude Investigation: High Modulation Frequency Range	144
6.4.1	Overview . . . . .	144
6.4.2	10.13%CH <sub>4</sub> :N <sub>2</sub> Results . . . . .	145
6.4.3	1.02%CH <sub>4</sub> :N <sub>2</sub> Results . . . . .	150
6.4.4	Discussion of Results . . . . .	153
6.5	Overall Summary and Conclusions . . . . .	153
<b>7</b>	<b>Conclusions and Further Work</b>	<b>155</b>
7.1	Conclusions . . . . .	155
7.2	Further Work . . . . .	158
	<b>References</b>	<b>160</b>
<b>A</b>	<b>Publications</b>	<b>167</b>
<b>B</b>	<b>2<sup>nd</sup> order Taylor series expansion of Lorentzian line shape</b>	<b>170</b>
<b>C</b>	<b>MATLAB code - RAM technique with RAM Nulling</b>	<b>172</b>
<b>D</b>	<b>MATLAB code - PD method with RAM Nulling</b>	<b>188</b>
<b>E</b>	<b>MATLAB code - Amplitude Investigation Part I</b>	<b>205</b>
<b>F</b>	<b>MATLAB code - Amplitude Investigation Part II</b>	<b>208</b>

# List of Abbreviations and Symbols

$A$	$\alpha_o Cl$
AC	Alternating Current
ADC	Analogue to Digital Converter
$Af_m(\lambda)$	Recorded line shape
$\alpha$	Molar absorption coefficient
$\alpha_o$	Molar absorption coefficient at line centre
$a_n$	Fourier coefficient
$C$	Concentration expressed as the fractional number of molecules
$c$	Speed of light in a vacuum ( $3 \times 10^8 \text{ms}^{-1}$ )
$C_f(\lambda)$	Correction function
$\text{CH}_4$	Methane
DAC	Digital to Analogue Converter
DC	Direct Current
$\Delta$	$(\lambda - \lambda_c)/\gamma$
$\Delta E$	Energy difference
$\Delta I$	Amplitude of IM
$\Delta V$	Voltage deviation ( $pk - pk$ )
$\delta\lambda$	Wavelength deviation
$\delta\nu$	Frequency deviation
$\delta I$	Intensity deviation
$\delta i$	Current deviation
DFB	Distributed Feedback
DR	Dynamic Reserve
$E$	Energy
$f$	Modulation frequency
$f(\lambda)$	True line shape
FSR	Free Spectral Range
FWHM	Full Width Half Maximum

$\gamma$	High width half maximum line width (expressed in Hz or nm)
$\Gamma_D$	Full width half maximum of Doppler line shape
$\Gamma_L$	Full width half maximum of Lorentzian line shape
$h$	Planck's constant ( $6.63 \times 10^{-34}$ Js)
$\hbar$	$h/2\pi$
HITRAN	High Resolution Transmission molecular absorption database
HWHM	Half Width Half Maximum
$I(\nu)$	Voigt profile
$I_{in}$	Input intensity
IM	Intensity Modulation
InGaAs	Indium Gallium Arsenide
$I_o(\lambda)$	Incident intensity of laser
$I_{out}$	Output intensity
$I_t(\lambda)$	Transmitted intensity of laser
$J$	Rotational quantum number
$k$	Boltzmann constant ( $1.38 \times 10^{-23}$ JK <sup>-1</sup> )
$\kappa$	Modulation coefficient
$l$	Absorbing path length
$L$	Optical path length of resonator
$L(\nu)$	Lorentzian profile
$\lambda$	Laser wavelength
$\lambda_c$	Centre Wavelength
LIA	Lock In Amplifier
$m$	Modulation index (expressed as $\delta\nu/\gamma$ or $\delta\lambda/\gamma$ )
$M$	Molecular weight
MIR	Mid Infra Red
$N$	Number of molecules per unit volume
$n$	Number of moles
N <sub>2</sub>	Nitrogen
$n_e$	Effective refractive index

NIR	Near Infra Red
$N_o$	Number of molecules at STP
$\nu$	Laser frequency
$\nu_o$	Frequency at line centre
OFN	Oxygen free nitrogen
$\omega$	Angular frequency ( $2\pi f$ )
$OP_x$	X measurement axis of LIA
$OP_y$	Y measurement axis of LIA
$P$	Pressure
PC	Polarisation Controller
PD	Phasor Decomposition
$\psi$	FM/IM phase separation
$\psi'$	WM/IM phase separation
QCL	Quantum Cascade Laser
$r$	Internuclear distance
$R$	Universal gas constant ( $82.0575\text{atm}\cdot\text{cm}^3/\text{mol}\cdot^\circ\text{K}$ )
RAM	Residual Amplitude Modulation
$S$	Line Strength
SNR	Signal to Noise Ratio
STP	Standard Temperature and Pressure
$T$	Temperature
TDLS	Tunable Diode Laser Spectroscopy
$v$	Vibrational quantum number
VOA	Variable Optical Attenuator
WM	Wavelength Modulation
WMS	Wavelength Modulation Spectroscopy
$\chi_e$	Anharmonicity constant
$\xi(\omega)$	Current tuning coefficient
$\chi_n$	Mole fraction of species $n$

# Chapter 1

## Introduction and Review

---

### 1.1 Overview

Gas detection/composition measurements have become vital in today's society for a number of applications, ranging from methane monitoring on landfill sites to industrial process control in gas based systems (e.g. fuel cells). Over the years industry has adopted tunable diode laser spectroscopy (TDLS) as its preferred choice for gas composition measurements. Early TDLS techniques addressed the strong fundamental rotation-vibration absorption lines in the mid infra red (MIR) [1–6] using lead-salt lasers made from IV-VI semiconductor materials; however, the need to actively cool the lasers and detectors and the high component cost restricted the wide spread use of such systems. Furthermore, at wavelengths above  $2\mu\text{m}$ , silica becomes opaque, hence standard optical fibre can't be used, thus, forcing the electrical components of the detection system to be in the vicinity of the potentially hazardous/dangerous environment, which could be intrinsically unsafe. Materials such as chalcogenide and fluoride can be used in the fabrication of fibre compatible for MIR applications. Progress in the MIR range has been made with the implementation of quantum cascade (QC) lasers [7–9]. These lasers are an improvement from their lead-salt based counterparts, as they can be thermoelectrically cooled, plus they can achieve stable single mode operation

and better output powers. However, the main disadvantage of QC lasers is their high cost.

Near infra red (NIR) components and systems, originally developed for the optical fibre telecommunications industry, including distributed feedback (DFB) lasers and indium gallium arsenide (InGaAs) photodiodes, can be used to address the weaker 1<sup>st</sup> overtone absorption lines of the target gases [10–13]. Even though the absorption strengths of the gas lines in the NIR are weaker by at least an order of magnitude [14], the readily available, low cost and reliable components made it advantageous for industry to adopt NIR TDLS [15–17] for many gas measurement applications. Furthermore, the available NIR detectors were an order of magnitude better than the MIR detectors in terms of sensitivity, therefore giving similar measurement sensitivities compared to MIR TDLS. Finally, as the components and the wavelength of operation were compatible with standard telecommunications single mode optical fibre, the measurement sites could be remote and multi-point [14, 18], allowing a optical network of sensors to be implemented. By implementing a network the primary electronic measurement unit, including the laser source and receiver, can be removed from the potentially hazardous environment.

The three main conventional variants of TDLS are: TDLS with direct detection [3, 6], TDLS with wavelength modulation (WM) [1, 2, 4–6, 12, 13, 16] and TDLS with frequency modulation (FM) [1, 10, 12, 13, 19]. TDLS with direct detection allows for the absolute gas absorption line shape to be easily recovered from the recorded gas measurement. This simplistic approach recovers the absorption line shape through normalisation to a no gas signal or a baseline fit to the off-line points on the gas signal, therefore knowledge of system/laser parameters is not required. TDLS with WM is more complex and requires the use of a lock-in amplifier (LIA) to recover the harmonic signals of the absolute gas absorption line shape. The main difference between TDLS with FM and TDLS with WM lies in the applied modulation frequency relative to the line width ( $\gamma$ ) of the absorption feature [1]. In conventional TDLS with WM the modulation frequency

is in the range of 10kHz to 100kHz compared to  $\gamma=2.5\text{GHz}$ , whereas in TDLS with FM the modulation frequency is of similar order to the line width of the absorption feature. Therefore, TDLS with WM is preferred over TDLS with FM as the receiver electronics don't require a high bandwidth. In this work the focus is on TDLS with WM. In conventional WM spectroscopy (WMS), knowledge of system/laser parameters are required to extract the gas concentration and pressure from the recovered harmonic signals. There is a trade off between the complexity of the signal analysis and the increase in measurement sensitivity, which is usually required for industrial applications.

Advancements have been made in the field of TDLS with WM in the form of the phasor decomposition (PD) method and the residual amplitude modulation (RAM) technique [20, 21]. In the conventional approach, analysis techniques are used to extract gas parameters from signals that are proportional to the derivatives of the gas absorption line shape. The advantage of these new techniques is that they are capable of directly extracting the absolute gas absorption line shape from the recovered 1<sup>st</sup> harmonic signal from the LIA. Theoretical line shapes are then curve fitted to the extracted signal to obtain values for gas concentration and pressure.

The following sections will introduce the principals of the conventional TDLS approaches along with a review of the recent advancements. The objectives and aims of this research will then be given, highlighting the intended contribution to the field of NIR TDLS for gas detection/composition measurements.

## **1.2 TDLS with Direct Detection**

TDLS with direct detection uses a diode laser, which has an output wavelength that is close to an absorption line of the target gas. The principles of molecular spectroscopy are given in chapter 2. The laser wavelength is thermally tuned to be close to the absorption line. The output of the laser typically addresses a vessel containing the target gas, such that the target gas interacts with the

laser radiation over a fixed length open path. Modulation is applied using a low frequency ramp (5-1000Hz depending on the application) scanning the laser centre wavelength repetitively through the absorption feature. The transmitted laser power level is monitored by a photodiode detector and the absolute gas absorption line shape is extracted from the recorded signal on the detector. Figure 1.1 shows a simplified schematic of a NIR TDLS with direct detection system and Figure 1.2 shows a graphical representation of TDLS with direct detection.

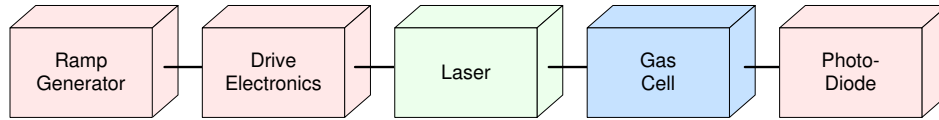


Figure 1.1: Schematic of NIR TDLS with direct detection system

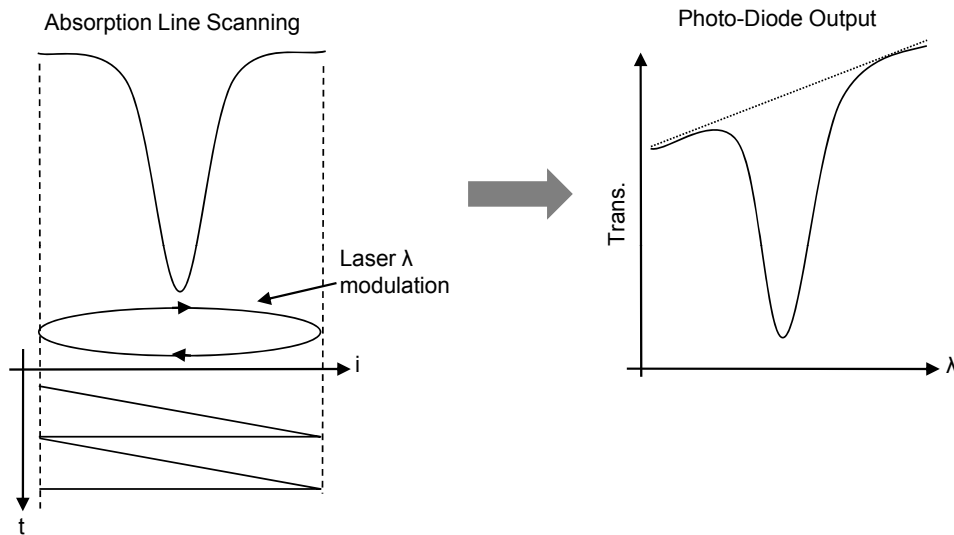


Figure 1.2: An illustration of NIR TDLS with direct detection

As mentioned, the laser output intensity is modulated by the ramp current. Any variation in transmitted laser power due to the presence of the target gas will result in an absorption signal being superimposed on the ramp of the received laser transmission signal. To recover the absolute gas absorption line shape the recorded absorption signal from the detector is normalised to a no gas signal or baseline fit to the off-line points of the recorded absorption signal. The normalised signal, similar to Figure 1.5(a), can then be used to extract the gas concentration and pressure. Concentration is directly proportional to the normalised absorption

depth when the gas sample is optically thin (absorption depth  $\ll 1$ ). The level of absorption is given by the Beer-Lambert Law, described in section 2.4.4. Gas pressure is related to the width of the normalised absorption line shape, discussed in more detail in section 2.7. To successfully extract concentration and pressure using the measured absorption depth and width, accurate measurements of the transmitted and incident laser intensity must be made. A more practical solution to extract concentration and pressure is to use a curve fitting process. This is accomplished by varying the concentration and pressure of the theoretical line shape until a match to the normalised absorption line shape is found, through a least squares approach. The resulting values for concentration and pressure are then taken as the experimentally measured gas parameters.

The main benefit of using TDLS with direct detection is the ability to recover the absolute gas absorption line shape through a simple normalisation procedure. This procedure doesn't require knowledge of system parameters and therefore is calibration free. However, there are limitations of using direct detection, the most significant being  $1/f$  laser noise, which is greatest at DC. Furthermore, as the absorption signal is superimposed on a large background ramp, low concentration ( $<1\%$ ) absorption signals can be lost within the ramp. The above limitations can be resolved by TDLS with WM, where the signals are generated and recovered at a sufficiently high frequency to eliminate  $1/f$  noise, giving greater measurement sensitivity and allowing for lower gas concentrations to be detectable.

### **1.3 TDLS with Wavelength Modulation**

TDLS with WM allows for greater measurement sensitivity as the signals are no longer recorded at DC, but at a selected higher frequency, therefore eliminating  $1/f$  noise and improving the signal to noise ratio (SNR). To implement TDLS with WM a number of additional elements are added to the direct detection system. Firstly, there is dual modulation applied to the laser: as well as the low frequency ramp there is also a high frequency sinusoid ( $>10\text{kHz}$ ) applied. As

before, the ramp current scans the laser centre wavelength through the absorption feature and the high frequency, sinusoidal WM, interrogates the gas line. As well as the sinusoid modulating the laser's wavelength it also modulates the laser's intensity. This intensity modulation (IM) produces a background signal known as the background residual amplitude modulation (RAM). The interaction of the WM with the gas line results in modulation of the transmitted laser power through the gas, producing IM signals at the fundamental modulation frequency and its higher harmonics (referred to as the WM/IM signal) at the photodiode detector output. The other addition to the experimental system for TDLS with WM is a LIA, connected to the output of the photodiode detector. The revised schematic for TDLS with WM is shown by Figure 1.3.

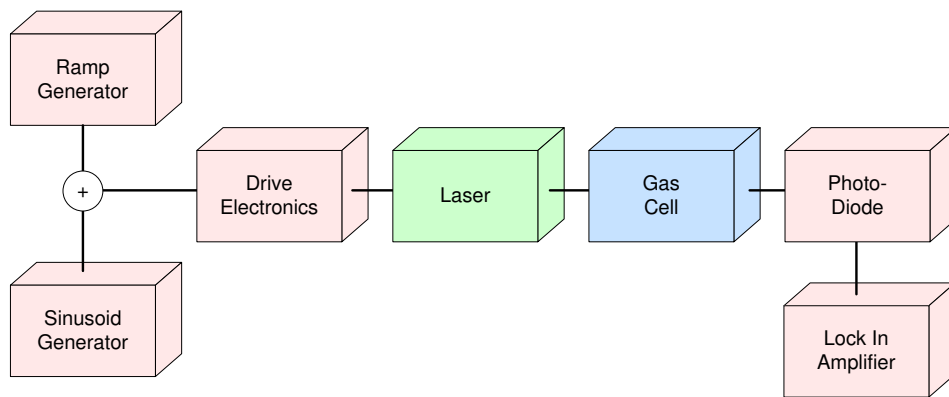


Figure 1.3: Schematic of NIR TDLS with WM system

A LIA can be configured to select and measure the variation in amplitude of an input signal at a given reference frequency. If the LIA was set to observe the 1<sup>st</sup> harmonic signal then the reference would be set to the fundamental WM frequency, whereas if the 2<sup>nd</sup> harmonic was selected the reference would be set to double the fundamental frequency [22, 23]. Figure 1.4 illustrates the interaction of the modulated laser output with the gas line. Neglecting the background IM signal, the laser WM interacts with the gas line, to produce an IM signal whose amplitude is proportional to the gradient of the gas line. The IM signal is then processed by a LIA, which measures the variation in the amplitude of the input signal and produces a signal that is proportional to a derivative of the gas line. If the 1<sup>st</sup> harmonic is selected on the LIA the output will be proportional to

the 1<sup>st</sup> derivative of gas line, if the 2<sup>nd</sup> harmonic is selected the output will be proportional to the 2<sup>nd</sup> derivative and so on for higher harmonics. In the case of the 1<sup>st</sup> harmonic signal, the background IM signal will also be present on the LIA output.

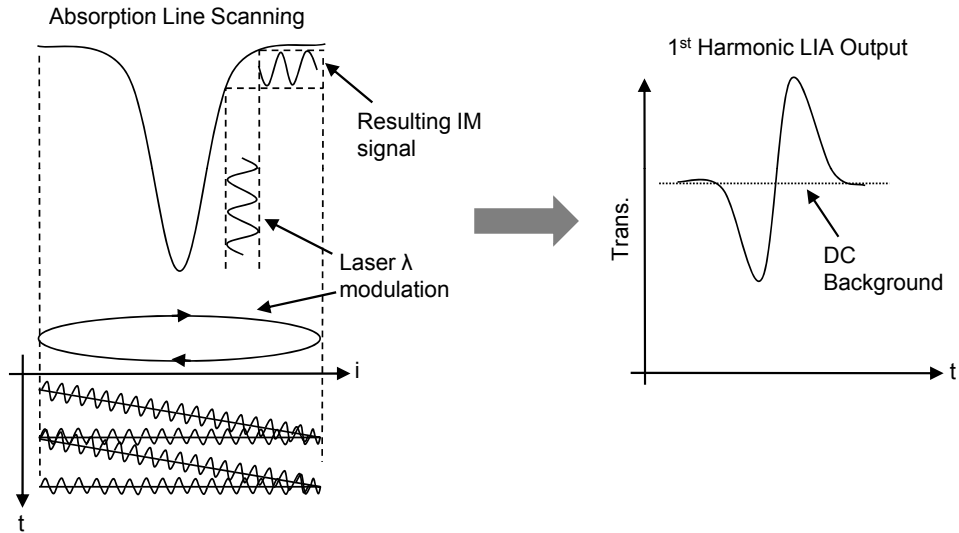
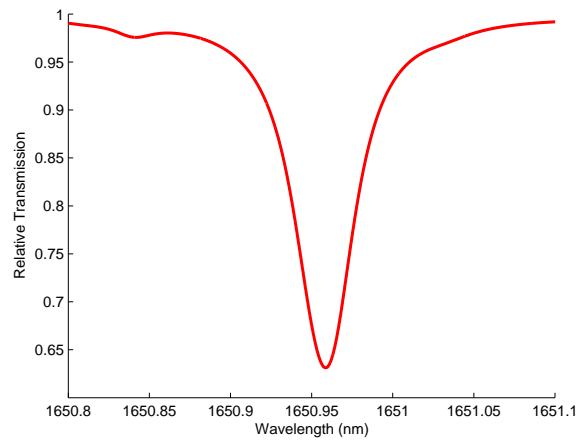
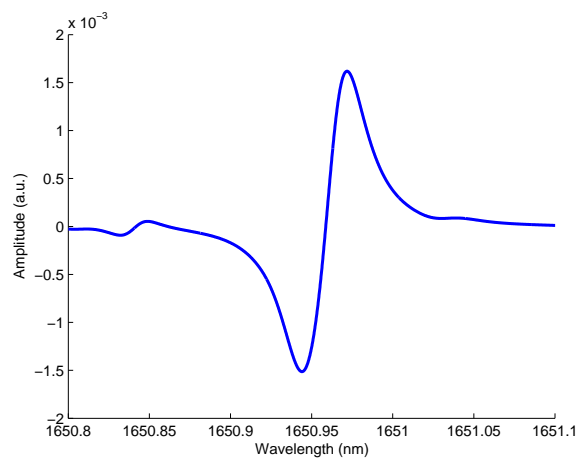


Figure 1.4: An illustration of NIR TDLS with WM

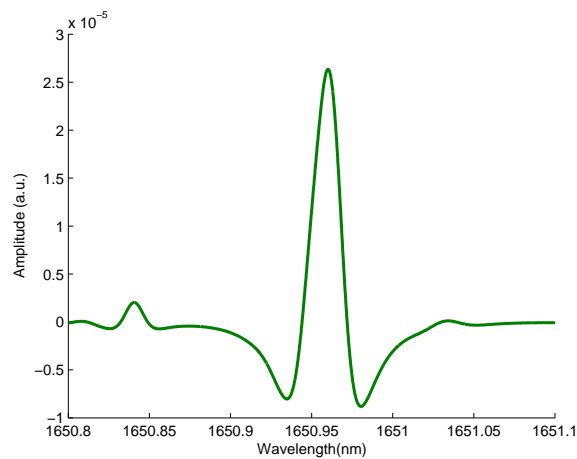
A key parameter in determining the nature and amplitude of the recorded signals is the modulation index,  $m$ , defined as the ratio of the amplitude of the wavelength deviation around the centre wavelength ( $\delta\lambda$ ) to the half width half maximum (HWHM) of the gas absorption line ( $\gamma$ ) i.e.  $m = \delta\lambda/\gamma$ . For small modulation indices,  $m$  ( $<0.2$ ), the  $n^{\text{th}}$  harmonic signal amplitude is proportional to the  $n^{\text{th}}$  derivative of the absolute gas absorption line shape. Figure 1.5 shows a theoretical absolute gas absorption line shape along with its corresponding 1<sup>st</sup> and 2<sup>nd</sup> derivative line shapes as measured via a LIA. When  $m$  is increased, the recorded signals become distorted as there are contributions from higher order Fourier terms of the line shape function. Thus, to enable the recovery of the true line shape, correction factors need to be applied, discussed in more detail in chapter 3.



(a) Absolute gas absorption line shape



(b) 1<sup>st</sup> derivative line shape



(c) 2<sup>nd</sup> derivative line shape

Figure 1.5: Typical signal line shapes recorded using TDLS with WM based on the absolute line shape, 10.13%CH<sub>4</sub>:N<sub>2</sub> at 1Bar and 20°C.

Knowing the value of  $m$  is crucial when analysing the recorded gas signal, as it dictates the level of correction applied to the signal. If pressure is varying, this will lead to variations in line width of the absorption feature which affects  $\gamma$  and will result in variations in  $m$ . Conventional analysis techniques rely heavily on accurate knowledge of system parameters to extract gas parameters. This is a major limiting factor of these techniques. However, the PD method and RAM technique don't suffer from this issue as the absolute transmission line shapes are recovered and gas parameters are extracted by curve fitting theoretical line shapes to them [20,21].

A major limiting factor of using 1<sup>st</sup> harmonic detection in TDLS with WM techniques is the presence of a large unwanted background signal, arising from the direct power modulation of the laser by the high frequency sinusoid. This signal, referred to as the background RAM, produces, in first harmonic detection, a high background signal at the output of the LIA, upon which the small signals resulting from the gas absorption are superimposed. Instrument amplification and sensitivity must be chosen to accommodate this high background signal and prevent saturation. The dynamic range of the instrument then determines (limits) the low end resolution and compromises the sensitivity of the signal recovery. In addition, the RAM signal, attenuated by the gas absorption, further distorts the recovered 1<sup>st</sup> harmonic WM/IM signal. The origin of RAM in WM spectroscopy and its distorting effects on the various harmonic signals have been well studied [13,20–23].

The high background 1<sup>st</sup> harmonic RAM signal is not present on the higher harmonics. Hence, to eliminate the problems associated with it, 2<sup>nd</sup> harmonic detection is widely used [24–26], resulting in improved signal resolution and sensitivity. However, 2<sup>nd</sup> harmonic detection has its own set of problems. A small background signal arising from the RAM is present on the recovered signal and it can cause distortion problems [27]. Of greater significance, though, is that the 2<sup>nd</sup> harmonic signal is not related to the absolute transmission function of the gas line but to its second derivative, similar to the 1<sup>st</sup> harmonic signal

being related to the 1<sup>st</sup> derivative of the absolute transmission function. These derivative signals are strongly dependent on the modulation index,  $m$ . This means that regeneration of the absolute line shape function is difficult and would require accurate knowledge of  $m$ , plus knowledge of the phase and amplitude of the distorting signals arising from the RAM. There are also issues of instrument scaling factors and normalisation to contend with. For these reasons calibration is needed to extract accurate concentration measurements from 2<sup>nd</sup> harmonic signals or indeed any of the WM/IM signals, including the 1<sup>st</sup> harmonic. Such calibration approaches can be successful if  $m$  remains constant or is known. Difficulties then arise in situations where the pressure is varying and unknown, leading to  $m$  variations through  $\gamma$  or when variations in  $\delta\lambda$  arise due to changes in the laser with time or temperature. For these reasons, use of 2<sup>nd</sup> harmonic signal presents difficulties in the design of stand alone instruments for maintenance free use in the field for long periods of time. However, a recent development [28] has demonstrated a calibration free 2<sup>nd</sup> harmonic detection technique, that normalises the 2<sup>nd</sup> harmonic signal with the 1<sup>st</sup> harmonic signal to extract the concentration and pressure of the target gas, without the need for calibration.

Recently, two new approaches to TDLS with WM, namely the RAM technique and the phasor decomposition (PD) method [20, 21], have been demonstrated to directly yield absolute gas absorption line shapes from the 1<sup>st</sup> harmonic signal. These techniques offer significant advantages for use in stand alone instrumentation in industrial process control applications: calibration is not required and, as such, the elimination of errors arising from the calibration process and drift therein results in more accurate measurement of the gas absorption line shape, concentration and pressure. However, as with any 1<sup>st</sup> harmonic analysis technique, the achievable signal resolution and measurement sensitivity are limited by the high background RAM signal.

In previous work, the problem of the high background on first harmonic signals has been addressed by electronic cancellation of RAM after detection [29–32]. Double-beam-double-detector schemes have been developed where the separately

detected signals arising from a reference arm and a measurement arm (including the gas measurement region / cell) are combined (subtracted) to cancel the common-mode noise and the baseline arising from the RAM [29, 32]. In the most recent attempt to remove the unwanted distortion of the 2<sup>nd</sup> harmonic signal arising from the RAM, a digitally generated  $2f$  component with appropriately adjusted amplitude and phase, was added to the laser current modulation [25].

The research reported here takes a novel optical approach due to its ease of implementation and low cost to suppress the background RAM before the receiver stage. This is accomplished by splitting the modulated laser output power into two paths, one directed through a gas cell and the other through a fibre delay line, and recombining just before the photodiode detector. The sinusoidal modulation frequency / delay are chosen to ensure a  $\pi$  phase separation between the IM of the two components at the re-combination point. The amplitudes of the anti-phase IM signals are balanced using a variable optical attenuator (VOA) in the delay line arm, so that, in the absence of gas or off-line, they cancel at the combiner output. The resulting DC signal is rejected by the LIA making the output zero and thus eliminating the high background RAM signal. In the presence of gas the imbalance at the combination stage output directly reflects the concentration-dependent absorption of the gas.

By using the above techniques the absolute gas absorption line shape (using TDLS with PD) and its 1<sup>st</sup> and 2<sup>nd</sup> derivative line shapes (using TDLS with PD and conventional 2<sup>nd</sup> harmonic detection respectively) can be recovered. Ideally, it is most desirable to recover the absolute line shape where gas concentration and pressure can be directly extracted, through curve fitting methods. However, at conventional modulation frequencies, 10kHz-100kHz [17], used for TDLS with PD, the amplitude of the absolute line shape is small compared to the recorded harmonic signals, namely the 1<sup>st</sup> derivative line shape. It will be shown that as the sinusoidal modulation frequency is increased the recorded amplitude of the signal containing the absolute line shape increases with frequency and the amplitude of the 1<sup>st</sup> derivative remains constant. This leads onto the second

part of this research, an amplitude investigation showing the optimum operating point for absolute line shape recovery using TDLS with PD through varying the sinusoidal modulation frequency.

## **1.4 Summary**

This chapter has given an introduction to the motivations for using TDLS for gas detection/composition measurements and how industry has adopted NIR TDLS. The basic principals of TDLS with direct detection and TDLS with WM were given highlighting their strengths and weaknesses, followed by a review of recent advancements. Concluding in the introduction of the research aims: a novel optical technique to suppress the background RAM and an amplitude investigation to determine the optimum operating conditions for TDLS with PD.

## 1.5 Thesis Aims and Objectives

The overall aim of this research is to develop existing TDLS with WM analysis techniques to improve measurement integrity and measurement resolution giving better methods for calibration free, robust and field deployable techniques that can be used in industrial applications. The intention is to achieve an improvement of measurement sensitivity, which is currently limited by the presence of the background RAM. The optimisation of system parameters to achieve absolute gas absorption signals that have comparable or greater amplitude than the corresponding 1<sup>st</sup> and 2<sup>nd</sup> derivative signals will also improve system performance. Therefore, the following objectives for this thesis have been identified:

1. The development of a novel optical approach to remove the unwanted background RAM from the measured 1<sup>st</sup> harmonic signal, and thus remove any limitation that this imposes on the signal resolution and sensitivity. The approach will split the modulated laser signal into two branches, where one goes through the gas cell and the second goes through a fibre delay line, introducing a  $\pi$  phase change in the modulated laser signal. The two paths are then re-combined before the photodiode receiver and the resulting effect is the suppression of the background RAM.
2. The execution of an amplitude investigation to determine the optimum sinusoidal modulation frequency for best recovery of the absolute gas absorption line shape contained within the 1<sup>st</sup> harmonic signal. This will be achieved by varying the modulation frequency and the modulation index,  $m$ . In the process the signal amplitudes of the absolute line shape and its 1<sup>st</sup> and 2<sup>nd</sup> derivatives in terms of variation of transmitted laser power arising from the interaction of the incident power with a gas absorption line will be compared to theory.

## **1.6 Thesis Outline**

Chapter 1 has given an overview of two common TDLS techniques, TDLS with direct detection and TDLS with WM, introducing the benefits and issues associated with each technique. The biggest limitation of TDLS with WM was highlighted: the presence of a large unwanted background signal on the recorded signals and how a novel optical technique will be implemented to suppress this background signal. Also described, is the intention to investigate the amplitudes, in terms of measured power, of the recorded harmonic signals and the recovered absolute gas absorption line shape.

Chapter 2 gives an overview into the fundamentals of molecular spectroscopy. The factors that influence the shape, depth and width of a gas absorption line shape are discussed. This is followed by the modelling of theoretical line shapes using a Voigt profile for comparison with experimentally recovered absolute gas absorption line shapes.

Chapter 3 introduces analytical models used to evaluate conventional TDLS with WM analysis techniques used in this research. Also the processes used to generate the theoretical amplitudes of the various gas line shapes used to compare to experimental amplitudes are discussed.

Chapter 4 gives a detailed description of the experimental system used in this research. Including detailed methods on how to characterise important system parameters, allowing for the accurate recovery of the absolute gas absorption line shape and aid in the amplitude investigation into evaluating the optimum sinusoidal modulation frequency for TDLS with WM.

Chapter 5 presents revised analytical models used to illustrate the process for recovering the absolute gas absorption line shape when implementing RAM nulling, the process used to suppress the background RAM. The presented results use the experimental system given in chapter 4. Through this the presented method to suppress the background RAM signal will be validated along with the accurate recovery of the absolute gas absorption line shape.

Chapter 6 gives analysis of theoretical and experimental amplitudes of gas absorption line shapes, used in the amplitude investigation described in chapter 3. This investigation uses a simplified version of the experimental system given in chapter 4 to find the optimum sinusoidal modulation frequency, providing the best conditions for recovery of the absolute gas absorption line shape from the 1<sup>st</sup> harmonic signal.

Chapter 7 will present the conclusions gained from this body of research along with possible future developments.

# Chapter 2

## Fundamentals of Molecular Spectroscopy

---

### 2.1 Overview

This chapter only intends to give a sufficient introduction to the basics of molecular spectroscopy to enable the reader to understand the analytical and measurement processes used. For a more detailed explanation there are a number of excellent texts that can be consulted: [33–38]. Molecular spectroscopy is the study of the interaction between electromagnetic radiation and the molecular dipole and can give an insight into the composition of a target specimen. It is based on the principle of quantisation of energy, where a molecule's energy exists at discrete allowed levels. The energy of the molecule can be stored in a variety of forms e.g. rotational energy, vibrational energy and electronic energy. A molecule moves from one level to another when a finite amount of energy, in the form of a photon, is applied or released. Therefore the energy of the photon required to make a transition is the difference between two energy levels. When a molecule moves to a higher energy state this is known as absorption and if the molecule drops to a lower energy state it is emission. The absorption or emission spectra are used to determine the composition of the target specimen.

## 2.2 Formation of Line Spectra

A simple example of absorption is when an electron in an atom is excited by electromagnetic radiation and is elevated to a higher energy level. The transition to the higher energy level is illustrated by Figure 2.1.

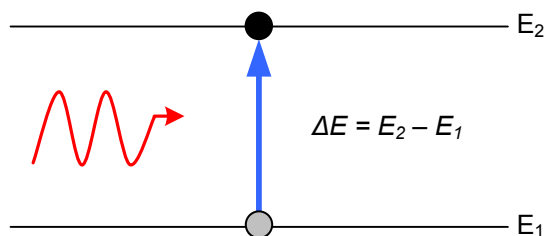


Figure 2.1: Absorption from electromagnetic radiation

The required energy of a photon to make the transition between energy levels is described by Planck's equation:

$$\Delta E = h\nu = \frac{hc}{\lambda} \quad (2.1)$$

where  $h$  is Planck's constant, ( $6.63 \times 10^{-34}$  Js),  $\nu$  and  $\lambda$  are the frequency and wavelength of the emitted radiation respectively. As absorption is a function of frequency, a laser can be scanned through a known absorption feature. If the target gas is present a decrease in transmitted laser power is observed, producing a unique absorption spectrum. This absorption spectrum can then be examined to ascertain the concentration, pressure and even temperature of the gas. An analytical process for the extraction of concentration and pressure is discussed in section 2.7.

The electromagnetic spectrum is arbitrarily divided into regions, the limits of which are not well defined. However the energy transition processes are quite different between regions, as illustrated by Figure 2.2 and summarised below:

- $\gamma$ -ray - Rearrangement of nuclear particles produces changes in energy
- X-ray - Involves the excitement of inner electrons of the atom
- Visible and Ultra Violet - Involves the excitement of the valence electrons of the atom

- Infra Red - Transitions associated with the vibrational levels, this is discussed in section 2.5
- Microwave - Transitions associated with the rotational levels
- Radio Frequency - Transitions associated with the reversal spin of a nucleus or electron

	Change of Nuclear configuration	Electronic Transitions		Vibrational Transition	Rotational Transitions	Nuclear Orientation
	γ-ray	X-ray	Visible & Ultra Violet	Infra Red	Microwave	Radio Frequency
$\lambda$ (m)	$10^{-12}$	$10^{-10}$	$10^{-8}$	$10^{-6}$	$10^{-4}$	$10^{-2}$
$f$ (Hz)	$3 \times 10^{20}$		$3 \times 10^{16}$		$3 \times 10^{12}$	$3 \times 10^6$
$E$ (Jmole <sup>-1</sup> )	$10^{11}$		$10^7$		$10^3$	$10^{-3}$

Figure 2.2: Electromagnetic Spectrum and transition processes

## 2.3 Width of Line Spectra

### 2.3.1 Overview

Spectral absorption lines are not infinitely sharp; there are a number of factors that contribute to their width, including natural broadening, Doppler broadening and collision broadening. The following sections give a brief description of these factors.

### 2.3.2 Natural Broadening

Natural broadening is due to Heisenberg's uncertainty principle, which states that if a molecule occupies a state for a limited time,  $\Delta t$  seconds, then the energy of that state is uncertain to an extent  $\Delta E$ , given by:

$$\Delta E \Delta t \approx \frac{h}{2\pi} \approx 10^{-34} \text{ Js} \quad (2.2)$$

where  $h$  is Planck's constant. From this it can be seen that if the molecule was left it would reside in the lowest energy state and remain there for an infinite time, giving  $\Delta E = 0$  as  $\Delta t = \infty$ . The lifetime of an excited electronic state is approximately  $10^{-8}$ s giving a  $\Delta E$  of  $10^{-26}$ J, associated with this energy is a radiation frequency,  $\nu$  with an uncertainty given by:

$$\Delta\nu \approx \frac{\Delta E}{h} \approx \frac{h}{2\pi h \Delta t} \approx \frac{1}{2\pi \Delta t} \quad (2.3)$$

Using the value for  $\Delta t$  from above, in equation (2.3), a value of  $10^8$ Hz for  $\nu$  would be achieved, this value for uncertainty is small compared to the usual radiation frequency,  $10^{14}$ Hz -  $10^{16}$ Hz, for such transitions. Therefore the natural line width is said to be small. Natural broadening is best modelled by a Lorentzian profile.

### 2.3.3 Doppler Broadening

Doppler broadening is a consequence of Doppler shift in the molecule's absorption wavelength. This shift is present due to the random motion of the molecule, resulting in the up and down shifting of the absorption wavelength. Up shifted (in frequency) is when the molecule moves in the opposite direction to the electromagnetic radiation and the position of absorption peak appears lower in wavelength. Down shifted (in frequency) is when the molecule moves in the same direction as the electromagnetic radiation and the position of absorption peak appears higher in wavelength. Therefore there is a spread of absorption wavelengths. This type of broadening is best modelled by a Gaussian profile, as the motion of the molecules has a Gaussian distribution. Doppler broadening can be described by the following equation:

$$\Gamma_D = 7.1623 \times 10^{-7} \nu_o \left( \frac{T}{M} \right)^{0.5} \quad (2.4)$$

where  $\Gamma_D$  is the full width half maximum (FWHM) of the line shape,  $\nu_o$  is the line centre frequency,  $T$  is temperature and  $M$  is the molecular weight of the absorbing species. As Doppler broadening affects the line width differently depending on the absorbing molecule, it is therefore classed as an inhomogeneous broadening process.

### 2.3.4 Collision Broadening

Collision broadening, also known as pressure broadening, arises due to the fact that gas molecules are always in constant motion and therefore collide with each other. The collision broadening coefficient is dependent on pressure, temperature and the species of the colliding gas, given by:

$$\Gamma_L = P \sum_n \chi_n \Gamma_L^n(T_o) \left( \frac{T_o}{T} \right)^{m_n} \quad (2.5)$$

where  $\chi_n$  is the mole fraction of species  $n$ ,  $\Gamma_L^n(T_o)$  is the broadening parameter for each species at a reference temperature,  $T_o$ , and  $m_n$  is a temperature dependent coefficient. The collisions cause a blurring of the energy levels giving rise to spectra lines that are broad rather than sharp. This type of broadening is best modelled by a Lorentzian profile. The effects of collision broadening on the line width are independent of the absorbing atom; therefore it is classed as a homogeneous broadening process.

## 2.4 Intensity of Line Spectra

### 2.4.1 Overview

There are three main factors that influence the intensity of the line: transition probability, population of states and path length. These factors are briefly discussed in the following sections.

### 2.4.2 Transition Probability

A detailed analysis of absolute transition probabilities is beyond the scope of this work as it involves detailed knowledge of the quantum mechanical wave functions of the transitional states. However, a qualitative approach can be taken to determine whether a transition has a probability of zero or non-zero. To decide which transitions give rise to spectral lines selection rules are determined.

Later in this chapter the selection rule for rotational and rotational/vibrational transitions for the methane molecule is shown as  $\Delta J = 0, \pm 1$ , where  $J$  is the rotational quantum number. Transitions outside the given selection rule range have no observable spectra.

### 2.4.3 Population of States

At higher energy levels the molecule population density decreases. This is due to the larger energies required to make these transitions. The ratio of population between an upper energy state and a lower energy state is known as the Boltzmann Distribution and is given by:

$$\frac{N_{Upper}}{N_{Lower}} = e^{\left(\frac{-\Delta E}{kT}\right)} \quad (2.6)$$

where  $\Delta E$  is the energy difference between the two levels,  $k$  is the Boltzmann constant ( $1.38 \times 10^{-23} \text{JK}^{-1}$ ) and  $T$  is the temperature in Kelvin.

### 2.4.4 The Beer-Lambert Law

The Beer-Lambert Law is a logarithmic relationship that describes the output intensity,  $I_{out}$ , of an absorbing medium for a given input intensity,  $I_{in}$ , and is given by:

$$I_{out} = I_{in}e^{(-\alpha Cl)} \approx I_{in}(1 - \alpha Cl) \quad (2.7)$$

where  $\alpha$  is the molar absorption coefficient of the target gas,  $C$  is the gas concentration defined as the fractional number of molecules with reference to the number of molecules at Standard Temperature and Pressure (STP) and  $l$  is the length of absorbing path. The approximation of  $(1 - \alpha Cl)$  is only valid when  $\alpha Cl \ll 1$ . This relationship is used as the foundation in chapter 3 to analyse the absorption of a target gas.

## 2.5 Infra Red Spectroscopy

In section 2.2 it was mentioned that IR spectroscopy is a result of molecular vibrations. In such vibrations, the distance between the atoms fluctuates. Molecular vibrations are said to be IR active if the vibration changes the dipole moment of the molecule. The best way to analyse these vibrations is to treat the movement of the bond in a diatomic molecule as a spring. In the following example the hydrogen chloride (HCl) molecule is used. Figure 2.3 shows the compression or stretching of the HCl molecule.

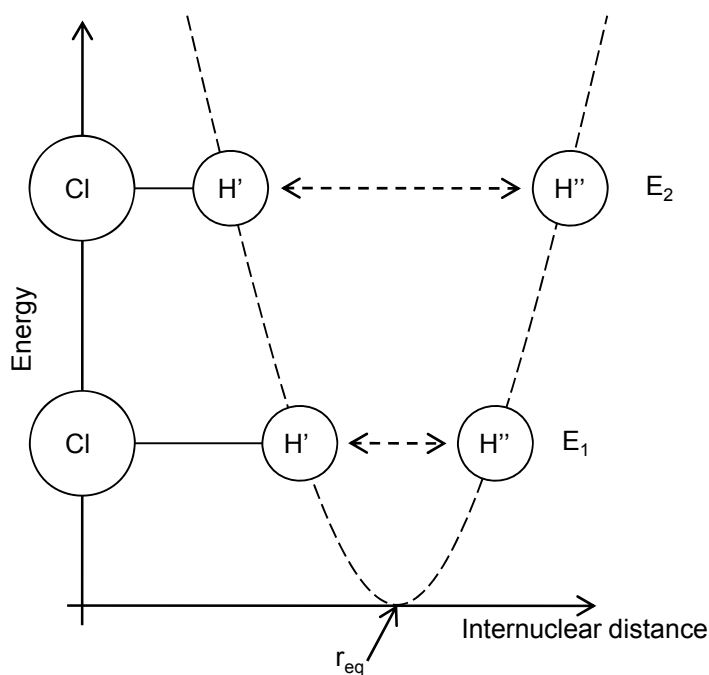


Figure 2.3: Energy against internuclear distance of the HCl molecule

It can be assumed that the bond, like a spring, obeys Hooke's Law therefore the relationship between the molecule's energy and the bond length is given by:

$$E = \frac{1}{2} k(r - r_{eq})^2 \quad (2.8)$$

where  $E$  is the molecule's energy,  $k$  is the force constant,  $r$  is the internuclear distance and  $r_{eq}$  is the equilibrium internuclear distance. In Figure 2.3 it is shown that the heavy chlorine atom is essentially fixed and it is the lighter hydrogen atom that moves, this is an acceptable assumption to make as it is the bond length that is important.

Like all energy levels they are quantised, for vibrational energies they can be defined by using equation (2.8) in the Schrödinger equation [33–35] resulting in:

$$E_v = \left(v + \frac{1}{2}\right) \hbar\omega \quad (v = 0, 1, 2, \dots) \quad (2.9)$$

where  $v$  is the vibrational quantum number,  $\hbar$  is  $h/2\pi$  and  $\omega$  is the oscillation frequency. By examining equation (2.9) two observations can be made, the first is that at  $v = 0$  the energy is non-zero and the second is the spacing between energy levels is  $\hbar\omega$ . Figure (2.4) illustrates these points.

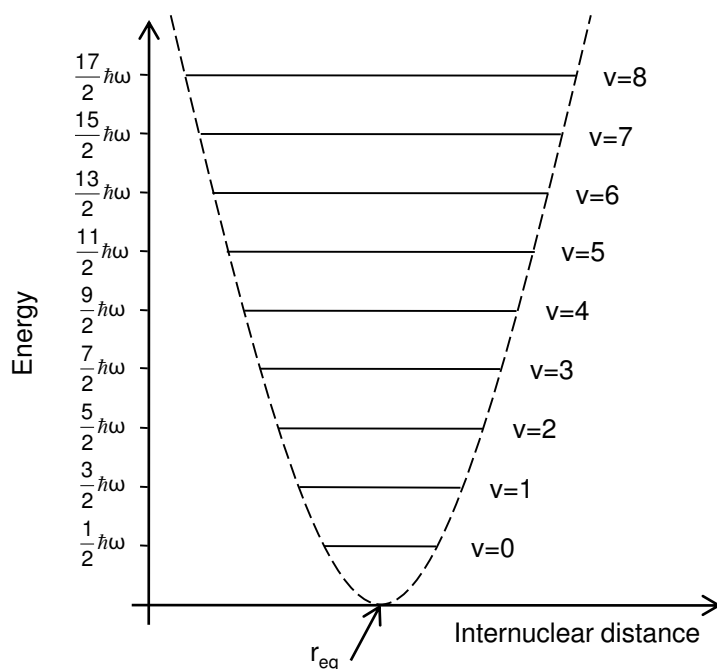


Figure 2.4: Vibrational levels for diatomic molecule undergoing simple harmonic motion

As molecules do not behave under the laws of simple harmonic motion, a more detailed model is required. The main reason for this is as the bond is continually stretched it reaches a point where it breaks and the molecule dissociates into atoms. Also, the energy level separation is no longer a constant and is defined by the Schrödinger equation using the anharmonic model [33] and is given by:

$$E_v = \hbar\omega_e \left\{ 1 - \chi_e \left(v + \frac{1}{2}\right) \right\} \left(v + \frac{1}{2}\right) \quad (2.10)$$

where  $\omega_e$  is the new oscillation frequency and  $\chi_e$  is the anharmonicity constant.

Figure 2.5 illustrates the new model for a typical molecule; it shows the oscillation's anharmonic nature.

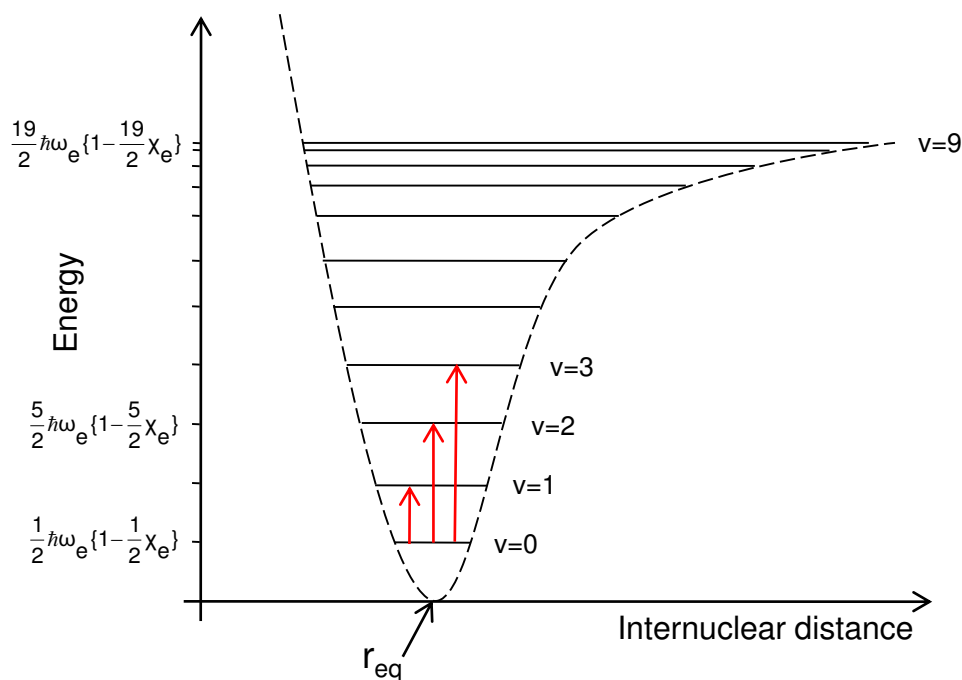


Figure 2.5: Vibrational levels for diatomic molecule undergoing anharmonic motion

The selection rule for simple harmonic oscillation was  $\Delta v = \pm 1$ , but for anharmonic oscillation, transitions are possible between two energy levels giving rise to  $\Delta v = \pm 1, \pm 2, \pm 3$ , etc. The three strongest transitions are shown on Figure 2.5 by the red arrows. The transition from  $v = 0$  to  $v = 1$  ( $\Delta v = +1$ ) is called the fundamental transition. The transition from  $v = 0$  to  $v = 2$  ( $\Delta v = +2$ ) is the 1<sup>st</sup> overtone transition, this is observed at twice the fundamental frequency and is weaker compared to the fundamental transition. Finally, the transition from  $v = 0$  to  $v = 3$  ( $\Delta v = +3$ ) is the 2<sup>nd</sup> overtone transition, this is observed at three times the fundamental frequency and is weaker than both the fundamental and 1<sup>st</sup> overtone transition. The outlined allowed transitions govern the emission or absorption of a photon for a given molecule.

## 2.6 Vibrational/Rotational Spectroscopy of the Methane molecule

For this research, methane was exclusively used as the target gas as a variety of certified concentrations were readily available. In addition, the demand for the detection/measurement of methane in industrial applications is on the increase. As methane is a polyatomic molecule, it is essential to study the vibrations and symmetry of such molecules. The number of fundamental vibrations of a molecule is governed by the number of atoms and whether it is linear or non-linear. For a molecule that consists of  $N$  atoms the number of fundamental vibrations possible is  $3N-5$  if the molecule is linear and  $3N-6$  fundamental vibrations if the molecule is non-linear. Both have  $N-1$  bonds therefore  $N-1$  of the vibrations are bond-stretching motions. The remaining vibrations,  $2N-4$  (linear) and  $2N-5$  (non-linear), are bending motions [34].

Methane,  $\text{CH}_4$ , is classed as a tetrahedral spherical-top molecule and is non-linear, thus it has nine ( $3*5-6$ ) theoretical fundamental vibrations. However a number of these modes occur at the same oscillation frequency, therefore they contribute to the same absorption spectra and are said to be degenerate. Methane has four fundamental modes; one is double degenerate and two are triple degenerate, thus accounting for the 9 modes, these are shown by Figure 2.6 [34]. Only two of the four modes ( $\nu_3$  and  $\nu_4$ ) are infra red active, due to a change in the dipole moment because of the vibrations.

The analysis of molecules to this point has assumed that absorption spectra produced was from energy transitions due to vibrations in the bonds only. To complete the analysis, rotational energy transitions of the molecule have to be considered also. Treatment of this is simplified by the Born-Oppenheimer approximation which allows the total energy to be treated as the summation of the vibrational and rotational energies [33]:

$$E_{Total} = E_{Rot.} + E_{Vib.} \quad (2.11)$$

The full expression is given as:

$$E_{Total} = \frac{h^2}{8\pi^2I} J(J+1) + \hbar\omega_e \left\{ 1 - \chi_e \left( v + \frac{1}{2} \right) \right\} \left( v + \frac{1}{2} \right) \quad (2.12)$$

where  $I$  is the moment of inertia and  $J$  is the rotational quantum number. The selection rule for the rotational transitions is  $\Delta J = 0, \pm 1$ . When  $\Delta J=0$  this is termed the Q branch of the absorption spectra,  $\Delta J=-1$  is the P branch and  $\Delta J=+1$  is the R branch. Figure 2.7 illustrates the possible energy transitions in the P, Q and R branches.

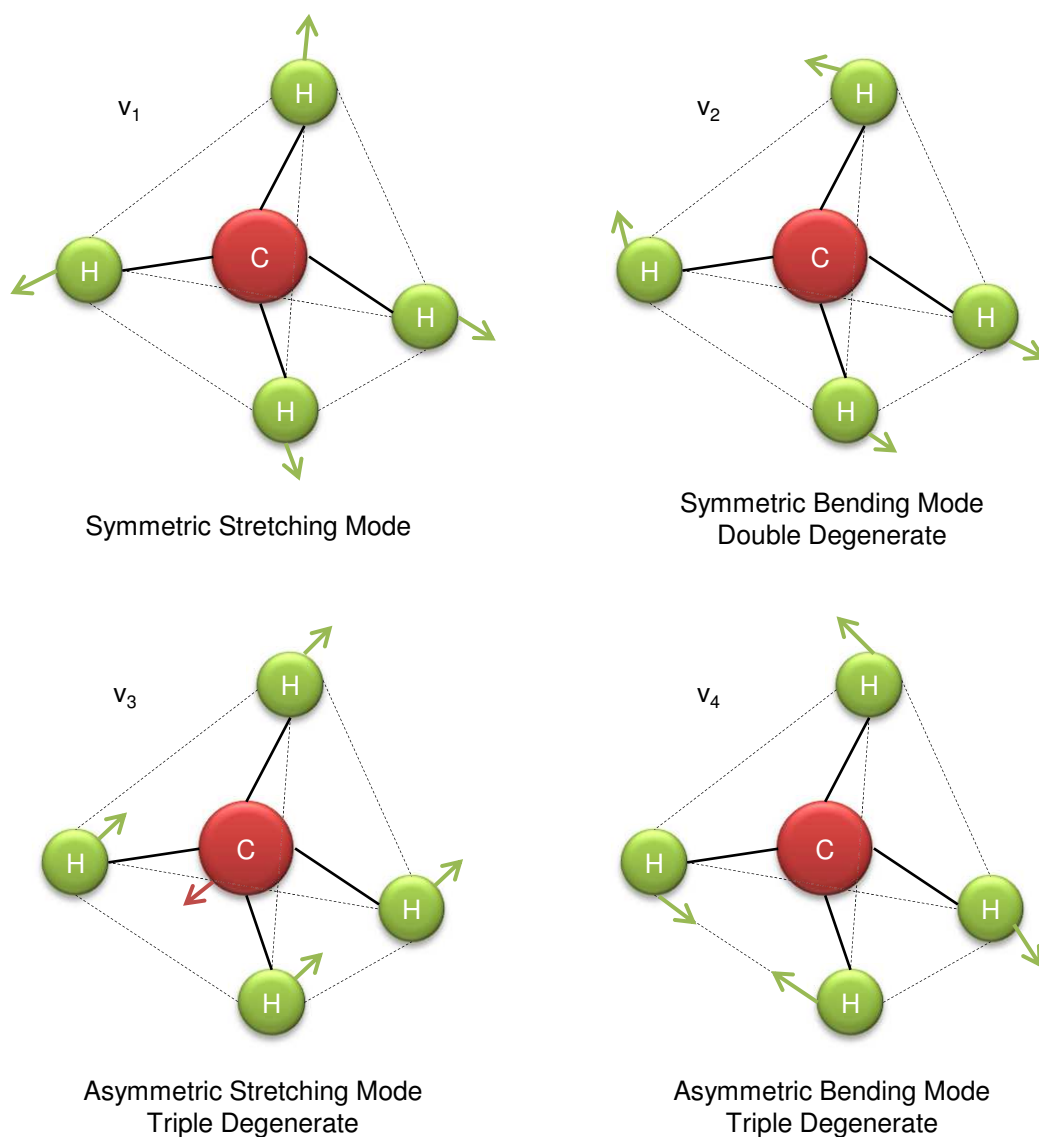


Figure 2.6: The infra red active vibrational modes of  $\text{CH}_4$

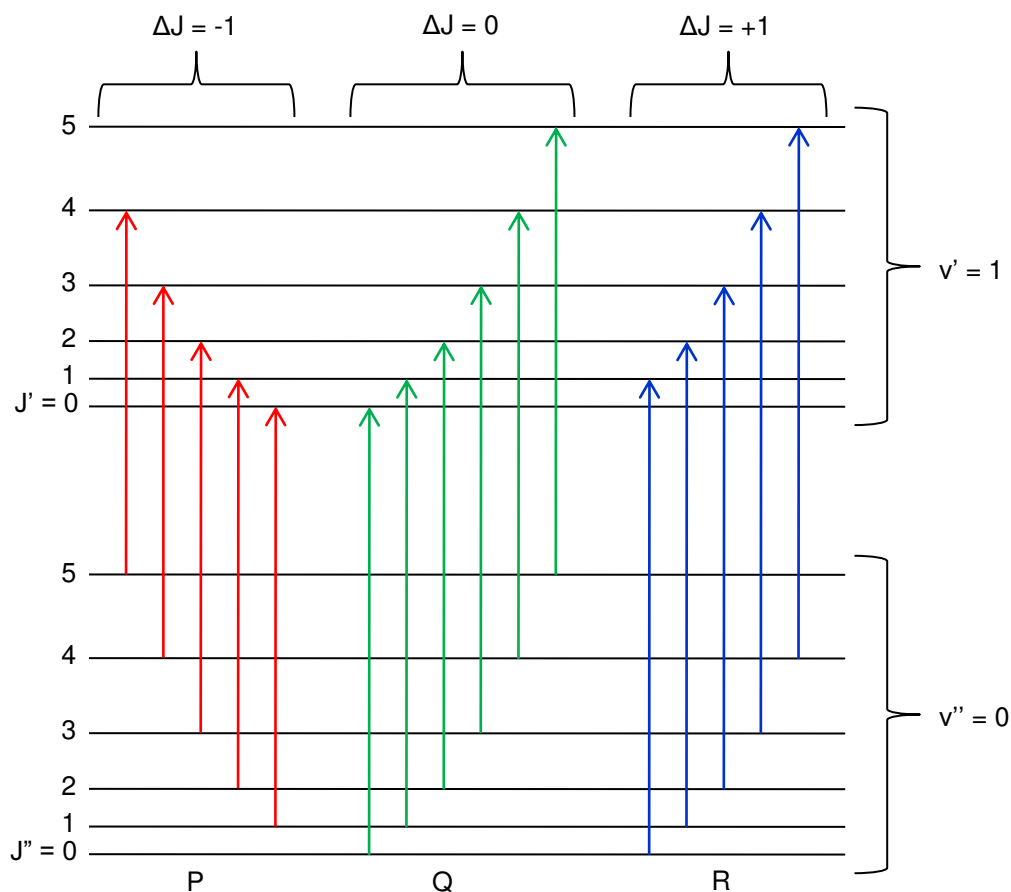


Figure 2.7: Rotational energy transitions between two vibrational states

As previously stated, a full analysis of molecular vibration is complex and beyond the scope of this work. However a number of important points have to be discussed. Vibrations can not be classed as simple harmonic motion therefore overtone transitions are possible at multiples of the fundamental frequency. These transitions are weaker than the fundamental, but, due to accidental degeneracy, where different vibrations close in frequency, combine, strong absorption spectra can result. Furthermore, combined vibration/rotation transitions (see Figure 2.7) are allowed giving rise to the P, Q and R branches of IR spectra. Therefore absorption spectra for gas molecules are unique and complex. The fundamental absorption spectrum at MIR and the 1<sup>st</sup> overtone absorption spectrum at the NIR for 1.02%CH<sub>4</sub>:N<sub>2</sub> at STP with a path length of 5.9cm are shown in Figures 2.8 and 2.9.

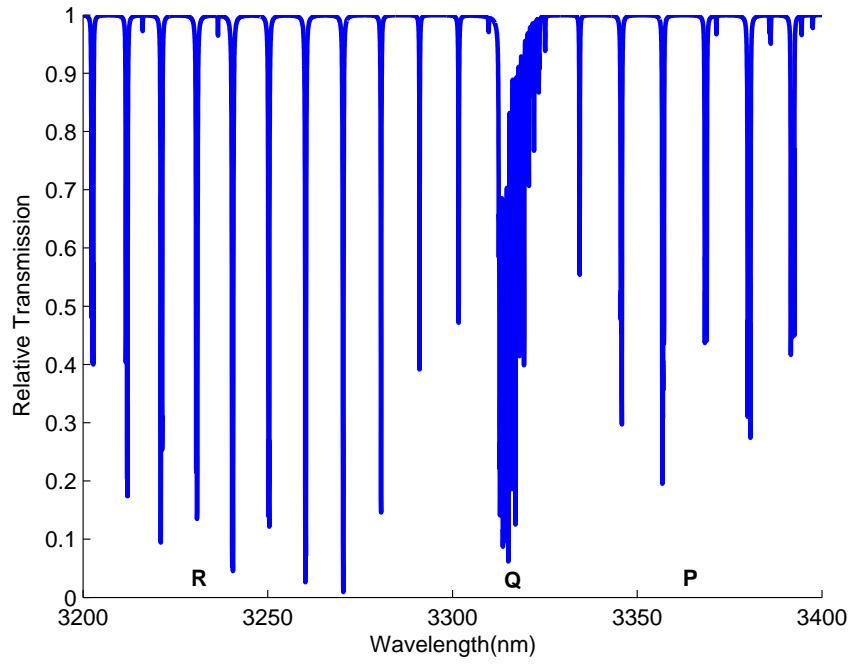


Figure 2.8: Fundamental energy level transitions of  $\text{CH}_4$  at MIR band - 1.02% $\text{CH}_4:\text{N}_2$  at STP and 5.9cm path length

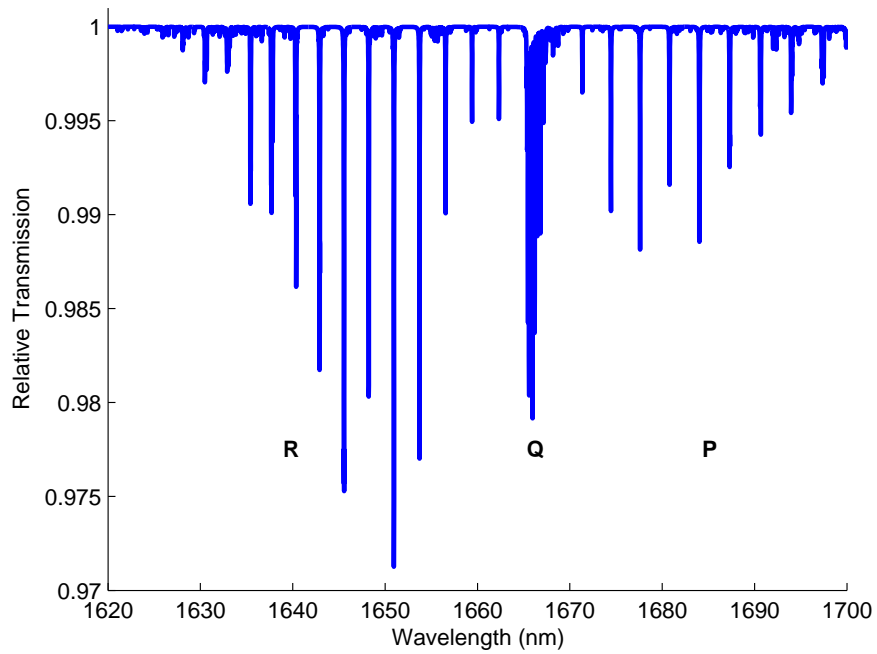


Figure 2.9: 1<sup>st</sup> overtone energy level transitions of  $\text{CH}_4$  at NIR band - 1.02% $\text{CH}_4:\text{N}_2$  at STP and 5.9cm path length

## 2.7 Extracting Gas Concentration and Pressure

### 2.7.1 Overview

This section shows an analytical method for recovering the concentration and pressure of a target gas from the absolute gas absorption line shape and its derivatives. For this the Beer-Lambert Law, equation (2.7), has to be evaluated in more detail to provide a method to recover the gas parameters, concentration and pressure, from the absolute and derivative gas absorption signals.

### 2.7.2 Gas Concentration

Excitation of vibrational/rotational transitions due to the absorption of the target gas at atmospheric pressure is best described by a Lorentzian profile and is a function of frequency, given by [18]:

$$\alpha(\nu) = \frac{N_o S}{\pi \gamma \left\{ \left( \frac{\nu - \nu_o}{\gamma} \right)^2 + 1 \right\}} = \frac{\alpha_o}{(\Delta^2 + 1)} \quad (2.13)$$

where  $N_o$  is the number of molecules at STP,  $S$  is line strength ( $\text{cm} \cdot \text{molecule}^{-1}$ ),  $\gamma$  is the half width half maximum (HWHM) line width ( $\text{cm}^{-1}$ ),  $\nu_o$  is the frequency at line centre and  $\alpha_o$  is the absorption coefficient at line centre. Substituting equation (2.13) into equation (2.7) gives the expression for the absolute gas absorption:

$$1 - \frac{I_{Out}}{I_{In}} = \frac{N_o S}{\pi \gamma (\Delta^2 + 1)} Cl = \frac{\alpha_o}{(\Delta^2 + 1)} Cl \quad (2.14)$$

Equation (2.14) can be arranged to give an expression for  $C$ , then by setting  $\Delta = 0$  results in the expression for concentration at line centre:

$$C = \frac{1 - \frac{I_{Out}}{I_{In}}}{\alpha_o l} \quad (2.15)$$

Equation (2.15) shows that the concentration is proportional to the recovered relative transmission function of the laser signal.

When using WM the method to recover gas concentration is more complex. The concentration can be recovered from the slope through the line centre of the 1<sup>st</sup> derivative and from the amplitude of the 2<sup>nd</sup> derivative. Therefore the simplest method is to measure amplitude at line centre on the 2<sup>nd</sup> derivative signal. The expressions for the 1<sup>st</sup> and 2<sup>nd</sup> harmonic signals are given by [39]:

$$I_{Out\ 1f} = -I_{In} \frac{d\alpha(\nu)}{d\nu} \delta\nu Cl = I_{In} \frac{2\alpha_o\Delta}{\gamma(\Delta^2 + 1)^2} \delta\nu Cl \quad (2.16)$$

$$I_{Out\ 2f} = -I_{In} \frac{2\alpha_o}{\gamma} \frac{d^2\alpha(\nu)}{d\nu^2} \delta\nu Cl = -I_{In} \frac{2\alpha_o(3\Delta^2 - 1)}{\gamma^2(\Delta^2 + 1)^3} \delta\nu^2 Cl \quad (2.17)$$

By examining equation (2.16) it can be seen that there is a dependency on  $\delta\nu/\gamma$ . This coefficient is the modulation index,  $m$ , and is discussed in more detail later. The parameter,  $m$ , becomes more dominant as the harmonics increase, as can be seen in equation (2.17). For the 2<sup>nd</sup> harmonic it's  $\delta\nu^2/\gamma^2$ , for the 3<sup>rd</sup> harmonic it's  $\delta\nu^3/\gamma^3$  and follows the same pattern for higher harmonics. A point to note here is the measured harmonic signal amplitudes are respective derivatives of the gas absorption lines in the limit of small modulation indices ( $m \ll 1$ ). Equation (2.17) can be rearranged to give an expression for  $C$ , then again setting  $\Delta = 0$  results in the expression for concentration at line centre on the 2<sup>nd</sup> harmonic signal.

$$C = \frac{\gamma^2 I_{Out\ 2f}}{2I_{In}\alpha_o\delta\nu^2 l} \quad (2.18)$$

Hence, the concentration is proportional to the amplitude of the 2<sup>nd</sup> harmonic signal, scaled by the input power, absorption coefficient, path length, absorption line width and sinusoid modulation amplitude. Therefore, to recover  $C$ , accurate knowledge of these factors must be known/obtained. The alternative is to use calibration to a known gas concentration, from which, gas measurements can be scaled to recover a value for  $C$ . This is the approach normally adopted but is subject to errors as many of the parameters are subject to change.

### 2.7.3 Gas Pressure

To recover the pressure of the measured gas a number of assumptions have been made: collision broadening dominates, which has been experimentally found to

be above 20millibars, as below 20millibars Doppler broadening dominated and the Beer-Lambert approximation holds. These assumptions have been made to highlight to the reader a number of features affecting the line shape. If the above is true then the relationship between pressure and line width for an absorption feature based on a Lorentzian profile is given by [36]:

$$\gamma = \gamma_o P \left( \frac{T_o}{T} \right)^n \quad (2.19)$$

where  $\gamma_o$  is the typical value for the line width with units  $\text{cm}^{-1}/\text{atm}$  at  $296^\circ\text{K}$  and  $n$  is a temperature dependent coefficient. Gas concentration can be expressed by the following:

$$C = \frac{N}{N_o} \quad (2.20)$$

where  $N$  is the number of gas molecule per unit volume and  $N_o$  is the number of gas molecules at STP per unit volume. Equation (2.20) is substituted into equation (2.15) and taking the expression at line centre for a direct measurement gives:

$$1 - \frac{I_{Out}}{I_{In}} = \frac{NSl}{\pi\gamma} \quad (2.21)$$

Then substituting equation (2.19) into equation (2.21) gives:

$$1 - \frac{I_{Out}}{I_{In}} = \frac{NSl}{\pi\gamma_o P} \left( \frac{T}{T_o} \right)^n \quad (2.22)$$

At a constant temperature equation (2.22) simplifies to:

$$1 - \frac{I_{Out}}{I_{In}} = \frac{NSl}{\pi\gamma_o P} = \frac{NKl}{P} \quad (2.23)$$

where  $K$  is a constant given by  $S/\pi\gamma_o$ . The next section of the analysis requires the use of the Ideal Gas Law:

$$P = \frac{nRT}{V} = NRT \quad (2.24)$$

where  $n$  is the number of moles,  $R$  is the universal gas constant of  $82.0575 \text{ atm.cm}^3/\text{mol.}^\circ\text{K}$ , and  $V$  is the volume. Rearranging equation (2.24) for  $N$  and substituting into equation (2.23) gives:

$$1 - \frac{I_{Out}}{I_{In}} = \frac{PKl}{PRT} = \frac{Kl}{RT} \quad (2.25)$$

By examination of equation (2.25) it can be seen that the amplitude of the absolute absorption line shape is independent of gas pressure and line width changes at atmospheric pressure. At lower than atmospheric pressures, Doppler broadening has an effect and the absolute absorption line amplitude has a small dependence on the line width.

In the case of TDLS with WMS the analysis is again slightly more complex. By examination of the 1<sup>st</sup> and 2<sup>nd</sup> harmonic signals it can be seen that the peaks of the 1<sup>st</sup> harmonic are the zero crossings of the 2<sup>nd</sup> harmonic. By re-examining equation (2.17) and removing the scaling coefficients and setting to zero gives:

$$\frac{2(3\Delta^2 - 1)}{\gamma^2(\Delta^2 + 1)^3} \delta\nu^2 = 0 \quad (2.26)$$

Equation (2.26) solves to  $\Delta^2 = 1/3$ , this can be solved further for  $\nu$  giving the zero crossings on the 2<sup>nd</sup> harmonic signal as  $\nu = \nu_o \pm \gamma/\sqrt{3}$ . This shows that line width information can be extracted from harmonic results.

## 2.8 Modelling Line Spectra

In spectroscopy the most accurate analysis of spectra lines is when more than one method of broadening is considered. For example at pressures greater than 20 millibars collision broadening becomes dominate, hence a Lorentzian profile would be used. However, even at atmospheric pressures there is still a contribution from Doppler broadening. Therefore, it is best to use a Voigt profile to model the broadening of the line width. A Voigt profile is the convolution of the Gaussian and Lorentzian profiles given by [40]:

$$I(\nu) = \int_{-\infty}^{+\infty} G(\nu')L(\nu - \nu')d\nu' \quad (2.27)$$

where the Lorentzian profile is given by:

$$L(\nu) = \frac{a_L}{1 + 4 \left( \frac{\nu}{\gamma_L} \right)^2} \quad (2.28)$$

where  $a_L$  is the absorption coefficient and  $\gamma_L$  is the HWHM. The Gaussian profile is given by:

$$G(\nu) = \frac{1}{\sigma\sqrt{2\pi}} e^{\left(\frac{-\nu^2}{2\sigma^2}\right)} \quad (2.29)$$

where  $\sigma$  is the standard deviation. The Voigt profile produced from equation (2.27) can be approximated as:

$$I(\nu) = \frac{\gamma_L}{\gamma_G} a_L \sqrt{\pi(\ln 2)} V(X, Y) \quad (2.30)$$

where  $\gamma_G$  is the HWHM of the Gaussian profile and  $V(X, Y)$  is given by:

$$V(X, Y) = \sum_{i=1}^4 \frac{C_i(Y - A_i) + D_i(X - B)}{(Y - A_i)^2 + (X - B_i)^2} \quad (2.31)$$

where  $A_i$  to  $D_i$  are constants defined in Table 2.1:

$i$	$A_i$	$B_i$	$C_i$	$D_i$
1	-1.215	1.2359	-0.3085	0.021
2	-1.3509	0.3786	0.5906	-1.1858
3	-1.215	-1.2359	-0.3085	-0.021
4	-1.3509	-0.3786	0.5906	1.1858

Table 2.1: Constants used to generate the Voigt approximation

The parameters  $X$  and  $Y$  are defined by the following expressions:

$$X = \frac{2\sqrt{\ln 2}}{\gamma_G} \nu \quad (2.32)$$

and

$$Y = \frac{\gamma_L}{\gamma_G} \sqrt{\ln 2} \quad (2.33)$$

A Voigt profile based on the above equations is used by modelling software, developed by Dr Michael Lengden [41], to produce ideal absorption results to compare to the experimental data presented in this thesis. The modelling software utilises the High-resolution TRANsmission (HITRAN) molecular absorption database [42], which is a collection of spectroscopic parameters from a number of theoretical and experimental sources, to produce theoretical gas absorption

transmission functions. HITRAN has been made available by Dr Larry Rothman et al. [42] at Harvard University; the database version used in this research was the 2004 release.

The modelling software allows the user to control a number of parameters (including concentration, pressure, temperature, path length and broadening coefficients) to determine the simulated absorption line. With this control, the theoretical absorption can be tailored to closely match the conditions experienced by the test gas in the laboratory. A comparison can then be made with the theoretical and experimental data. This comparison would check the viability of the analysis technique used to experimentally recover the gas absorption line. Part of the modelling software is to perform a curve fitting routine on the theoretical line shape. The routine varies concentration and pressure until it reaches a theoretical line shape that is a close match to the experimental data based on a least squares approach. The resulting values for concentration and pressure are then used as the experimentally measured gas parameters.

## **2.9 Summary**

This chapter has introduced the reader to the basic principals of molecular spectroscopy. The mechanisms affecting the width and intensity of the line spectra have been presented. Importantly, the Beer-Lambert Law underpins the analytical analysis reported in the next chapter. A simplified model of the vibrational/rotational spectroscopy of methane allows the reader to understand the fundamental, 1<sup>st</sup> overtone and 2<sup>nd</sup> overtone transitions resulting from the absorption of photons at the appropriate wavelength. Finally, the approach taken to best model theoretical line shapes accounting for both Doppler and Collision broadening in the form of a Voigt profile has been given.

# Chapter 3

## Analytical Methodology - Conventional Techniques

---

### 3.1 Overview

This chapter introduces the mathematical model used to express the conventional 1<sup>st</sup> harmonic signals in TDLS with WM. It is then further expanded to define the RAM technique [21] and Phasor Decomposition method [20]. The modelling continues with the derivation of expressions that give the power variation on the photo receiver at the peak of the recovered RAM absorption signal (distorted at high  $m$  values) and the 1<sup>st</sup> and 2<sup>nd</sup> harmonic WM/IM signal. At the end of the previous chapter a method to extract the concentration and pressure of a target gas was given, when applying TDLS with WM. However, to achieve this, precise knowledge of the system's parameters were required. Some of these parameters are easily obtained experimentally, however others are difficult to obtain. As there is the possibility that some system parameters drift over time, there is the potential need for frequent calibration and characterisation. Therefore, for practical applications there is a need for calibration free and stable analysis techniques for the extraction of gas concentration and pressure.

Researchers at the University of Strathclyde recently developed two calibration

free analysis techniques for the recovery of gas concentration and pressure, these are the RAM technique and the PD method [20, 21]. Both of these approaches use TDLS with WM, observing the 1<sup>st</sup> harmonic signal to probe the target gas absorption feature. However, as mentioned previously all techniques that utilise the 1<sup>st</sup> harmonic signal for gas composition analysis are restricted by the background RAM [20, 21]. The removal of this unwanted RAM signal, allows signal amplification of the detection equipment to be increased and the detection sensitivity improved. For TDLS with WM, high  $m$  values produce terms from higher harmonics, which distorts the recovered signals, therefore, to recover the true gas absorption line shape correction factors must be applied [20, 21, 43]. At low  $m$  ( $<0.2$ ) values, the distortion terms are negligible and correction is not required.

The following sections introduce the analytical approaches for the above techniques, first, the RAM technique and the PD method. Secondly, the approach taken for an amplitude investigation to compare the variation in power levels at peak absorption on the recovered RAM absorption signals and the 1<sup>st</sup> and 2<sup>nd</sup> harmonic WM/IM signals are given. Finally, the procedure to correct 1<sup>st</sup> harmonic signals from distortion terms due to high  $m$  values, currently being developed by researchers at the University of Strathclyde, is then shown.

## 3.2 RAM Technique

The expression for the 1<sup>st</sup> harmonic signal has to be derived in order to illustrate the principal of the RAM technique. Recalling from chapter 2 the transmission of light through an absorbing gas is described by the Beer-Lambert law (equation (2.7)):

$$I_t(\lambda) = I_o(\lambda)e^{-\alpha(\lambda)Cl} \approx I_o(\lambda)[1 - \alpha(\lambda)Cl] \quad (3.1)$$

where  $I_t(\lambda)$  and  $I_o(\lambda)$  is the transmitted and incident intensity of the laser respectively due to an absorbing medium, which has a wavelength dependent absorption coefficient of  $\alpha(\lambda)$ . Gas concentration as a fraction of the total

molecular density is represented by  $C$  and  $l$  is the path length. Again, the approximation made above holds when  $\alpha(\lambda)Cl \ll 1$ .

In TDLS with WM techniques the laser wavelength ( $\lambda$ ) is slowly scanned through the gas absorption line by a ramp current of a few hertz in frequency up to a few kilohertz depending on the application. Simultaneously, a higher frequency ( $>10\text{kHz}$ ) sinusoidal current modulates both the output intensity and the wavelength. The laser output intensity can be written as:

$$I = I(\lambda_c) + \Delta I(\lambda_c)\cos(\omega t) \quad (3.2)$$

where  $I(\lambda_c)$  is the intensity of the laser at a wavelength of  $\lambda_c$  and  $\Delta I(\lambda_c)$  is the amplitude of the intensity modulation (IM) varying at the modulation frequency,  $\omega$ . The accompanying WM about the centre wavelength,  $\lambda_c$ , as it is slowly scanned over the gas line by the ramp current is given by:

$$[\lambda - \lambda_c] = \delta\lambda(\lambda_c)\cos(\omega t - \psi') \quad (3.3)$$

where  $\delta\lambda(\lambda_c)$  is the peak amplitude wavelength deviation, from  $\lambda_c$ , arising from the WM and  $\psi'$  is the phase separation between the intensity and wavelength modulation [44–46]. Equations (3.1) and (3.2) are combined to give an expression for the intensity at the receiver after going through the absorbing gas:

$$I_o = [I(\lambda) + \Delta I(\lambda)\cos(\omega t)][1 - \alpha(\lambda)Cl] \quad (3.4)$$

The interaction of the WM with the gas absorption feature, as mentioned in chapter 2, gives rise to an IM signal at the fundamental frequency. Higher harmonics are also present due to non-linearity in  $\alpha(\lambda)$  around  $\lambda_c$ . A Taylor series expansion for  $\alpha(\lambda)$  around  $\lambda_c$  can be used to represent all the generated terms:

$$\alpha(\lambda) = \alpha(\lambda_c) + \alpha'(\lambda)|_{\lambda_c}[\lambda - \lambda_c] + \frac{1}{2}\alpha''(\lambda)|_{\lambda_c}[\lambda - \lambda_c]^2 + \dots \quad (3.5)$$

where  $\alpha'(\lambda)$  and  $\alpha''(\lambda)$  are the 1<sup>st</sup> and 2<sup>nd</sup> derivatives of the absorption coefficient respectively. Substitution of equation (3.3) into (3.5) and (3.5) into equation (3.4) gives all of the harmonic frequencies. For small modulation indices, ( $m < 0.2$ ), the Taylor series expansion may be approximated by the first three terms, the full

2<sup>nd</sup> order expansion is presented in appendix B. Implementing the substitutions with this approximation, results in the following expression for the 1<sup>st</sup> harmonic signal at  $\omega$ :

$$I_{\omega} = \Delta I(\lambda_c)\cos(\omega t) - \Delta I(\lambda_c)\alpha(\lambda_c)Cl\cos(\omega t) - I(\lambda_c)\alpha'(\lambda)|_{\lambda_c}Cl\delta\lambda(\lambda_c)\cos(\omega t - \psi') \quad (3.6)$$

In equation (3.6), the first term is the background RAM, which is due to the direct power modulation of the laser and is gas concentration independent. The second term is a gas concentration dependent RAM component. Collectively, these two terms may be written as  $\Delta I(\lambda_c)\cos(\omega t)[1 - \alpha(\lambda_c)Cl]$ , which is simply the RAM signal containing the gas absorption profile. The final term of (3.6) is the 1<sup>st</sup> derivative signal resulting from the interaction of the WM with the gas absorption feature, denoted earlier as the 1<sup>st</sup> harmonic WM/IM signal. As can be seen the RAM and WM/IM terms are separated by  $\psi'$ . Hence, using phase selection on the LIA these signals can be isolated and examined independently.

With the 1<sup>st</sup> harmonic signal now derived, it can be shown how the RAM technique can be implemented to recover the absolute gas absorption line shape through phase selection. In the RAM technique the WM/IM signal is nulled on the X measurement axis of the LIA (aligned to the Y axis) through phase selection, resulting in an isolated projection of the RAM signal onto the X measurement axis of the LIA as illustrated by Figure 3.1 [21]. Note that the WM/IM signal consists of two components of opposite sign representing the positive and negative gradients on either side of the gas absorption line.

Hence, the isolated projection of the RAM signal is recorded on the LIA X measurement axis, shown by Figure 3.2, and the LIA output is given by:

$$RAM = \Delta I(\lambda_c)[1 - \alpha(\lambda_c)Cl]\sin\psi' \quad (3.7)$$

The factor of  $\sin\psi'$  is present due to the recorded signal being a projection of the full RAM signal onto the LIA measurement axis. The unwanted background RAM can clearly be seen on Figure 3.2 with the superposition of the gas absorption profile.

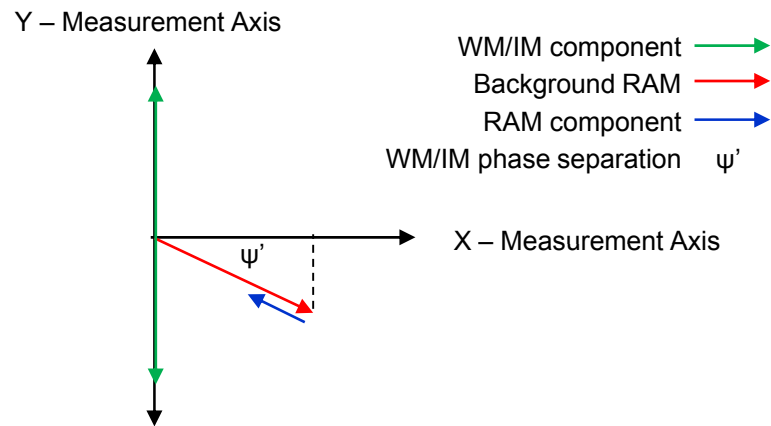


Figure 3.1: Phasor representation of the RAM technique with the detection phase set to null the WM/IM on the X measurement axis, giving an isolated projection of the RAM signal on the X measurement axis

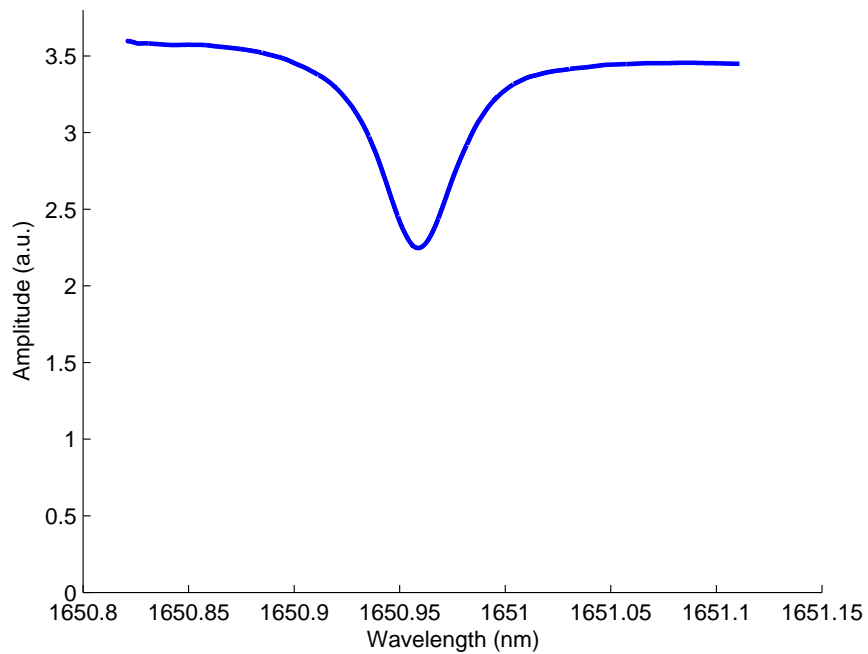


Figure 3.2: Recorded projection of the RAM signal on the LIA, 10.13%CH<sub>4</sub>:N<sub>2</sub> m=0.2

The absolute gas absorption line shape may be obtained by normalisation to the background RAM signal,  $\Delta I(\lambda_c)$ .  $\Delta I(\lambda_c)$  can be obtained by recording a no gas signal using the LIA or through a baseline fitting process to the off-line points of the gas signal (Figure 3.2). Note, for the RAM technique prior knowledge of  $\psi'$  is not required as it is taken into account through the normalisation process. The approximation to the Beer-Lambert law is only made to simplify the mathematical presentation of the 1<sup>st</sup> harmonic signal, enabling the WM/IM signal to be dealt with through a Taylor series expansion. Given that the RAM technique isolates the RAM signal from the WM/IM signal, irrespective of the approximation made, there is no requirement for the approximation when dealing only with the recovered absolute RAM signal, thus the following can be written:

$$\frac{I_t}{I_o} = e^{-\alpha(\lambda)Cl} = \frac{RAM}{\Delta I(\lambda_c)} \quad (3.8)$$

The benefits of the RAM technique are two fold: firstly the measurement sensitivity is improved by using TDLS with WM compared to TDLS with direct detection and secondly the recovery of the absolute gas absorption line shape is achieved through a simple normalisation process. However, a disadvantage of the technique is that it is a projection of the RAM signal that is recorded by the LIA; therefore it is a reduced RAM signal that is recorded. Recording the full RAM signal is achievable if  $\psi' = 90^\circ$  [20, 21], although this is only possible by applying a sinusoidal modulation of  $>1\text{MHz}$  (section 4.5.4 illustrates the relationship between  $\psi'$  and  $\omega$ ). Operating at these conditions is usually not practical due to bandwidth limitations of receiver equipment. This disadvantage is overcome by the PD method, which records the full RAM signal at any value of  $\omega$ .

### 3.3 Phasor Decomposition Method

As well as recovering the full RAM absorption the PD method also recovers the full 1<sup>st</sup> derivative signal simultaneously. This is achieved by recording both measurement axes of the LIA (X and Y channels). The detection phase is set so

a projection of the WM/IM signal is isolated from the RAM on the Y channel. The resulting signal on the X channel is the full RAM signal with a projection of the WM/IM signal. This is clearly illustrated by the phasor diagram of Figure 3.3.

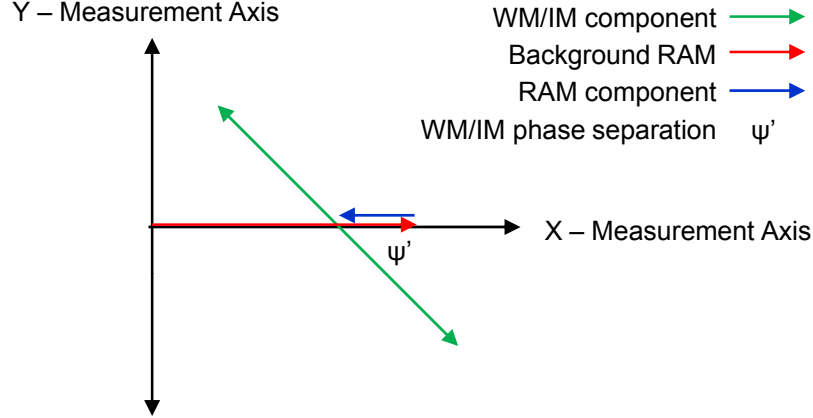


Figure 3.3: Phasor representation of the PD method with the detection phase set to isolate the WM/IM signal from the RAM

In this approach the X and Y outputs ( $OP_x$  and  $OP_y$ ) of the LIA respectively are given as follows:

$$OP_x = \Delta I(\lambda_c)[1 - \alpha(\lambda_c)Cl] - I(\lambda_c)\alpha'(\lambda_c)\delta\lambda(\lambda_c)Cl\cos(\psi') \quad (3.9)$$

and

$$OP_y = -I(\lambda_c)\alpha'(\lambda_c)\delta\lambda(\lambda_c)Cl\sin(\psi') \quad (3.10)$$

Using equations (3.9) and (3.10), the isolated RAM signal, term 1 of equation (3.9) can be found from:

$$RAM = \Delta I(\lambda_c)[1 - \alpha(\lambda_c)Cl] = OP_x - \frac{OP_y}{\tan\psi'} \quad (3.11)$$

Following this decomposition process, the absolute gas absorption line shape may be recovered by normalisation to the background RAM signal in a similar procedure as for the RAM technique. Note, that for the PD method, prior knowledge of  $\psi'$  is required and it may be found by the method reported in [20] and [43] (a review of this is given in section 4.5.4). Again, similar to the RAM technique, the recovered RAM signal can be written as:

$$\frac{I_t}{I_o} = e^{-\alpha(\lambda)Cl} = \frac{RAM}{\Delta I(\lambda_c)} = \frac{OP_x - [OP_y/\tan\psi']}{\Delta I(\lambda_c)} \quad (3.12)$$

The above expression is essentially the same as presented in [20], albeit presented in a different form. In [20] a phasor diagram was used to illustrate the components of the 1<sup>st</sup> harmonic signal and derive the expression given by equation (3.11). By defining the signals at the X and Y outputs of the LIA, the phasor diagram is not necessary and the final decomposition equation (3.11) and absolute gas absorption line shape (3.12) may be derived as above.

To complete the PD method the full 1<sup>st</sup> derivative signal is obtained by using the following:

$$Full\ 1^{st}\ Derivative = \frac{OP_y}{\sin\psi'} \quad (3.13)$$

The result of equation (3.13) would then be normalised to a power reference of the source laser to account for the varying power level during the sweep of the absorption feature.

Figures 3.4 and 3.5 illustrate the recorded signals on the X and Y outputs of the LIA respectively, when using the PD method. Figure 3.6 shows the resulting signals following the decomposition process of the PD method.

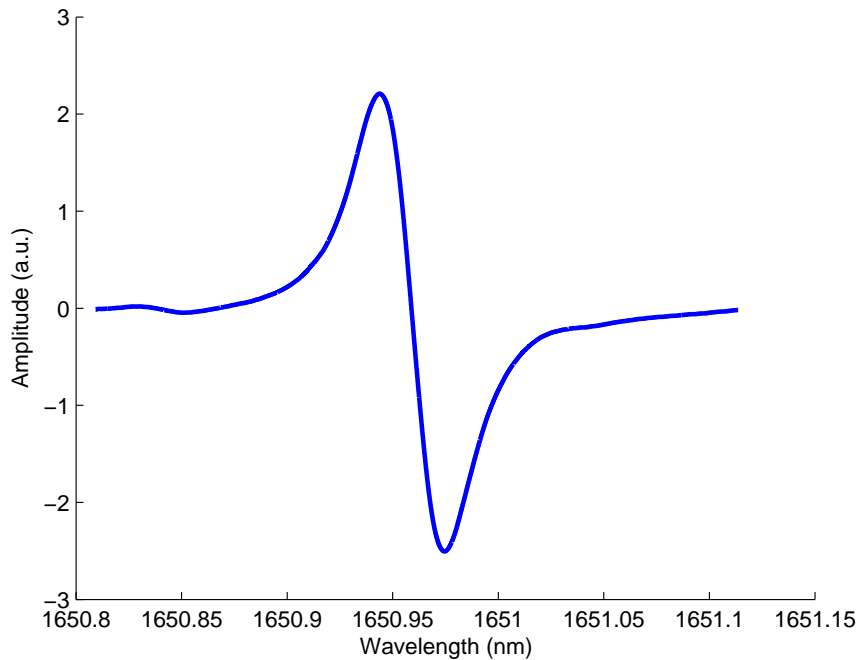


Figure 3.4: Y axis - Recorded projection of WM/IM signal, 10.13%CH<sub>4</sub>:N<sub>2</sub> m=0.2

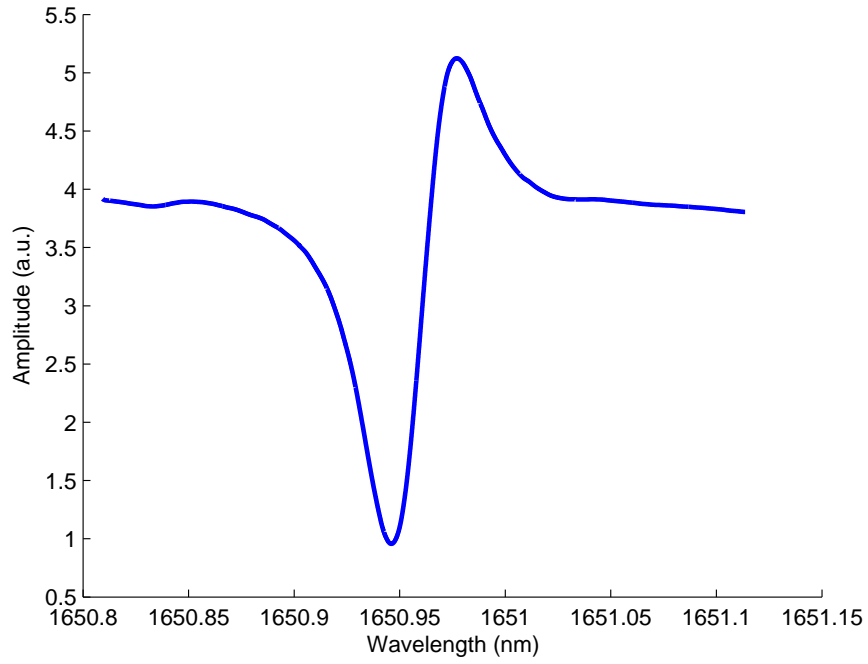


Figure 3.5: X axis - Recorded RAM signal with a projection of WM/IM, 10.13%CH<sub>4</sub>:N<sub>2</sub> m=0.2

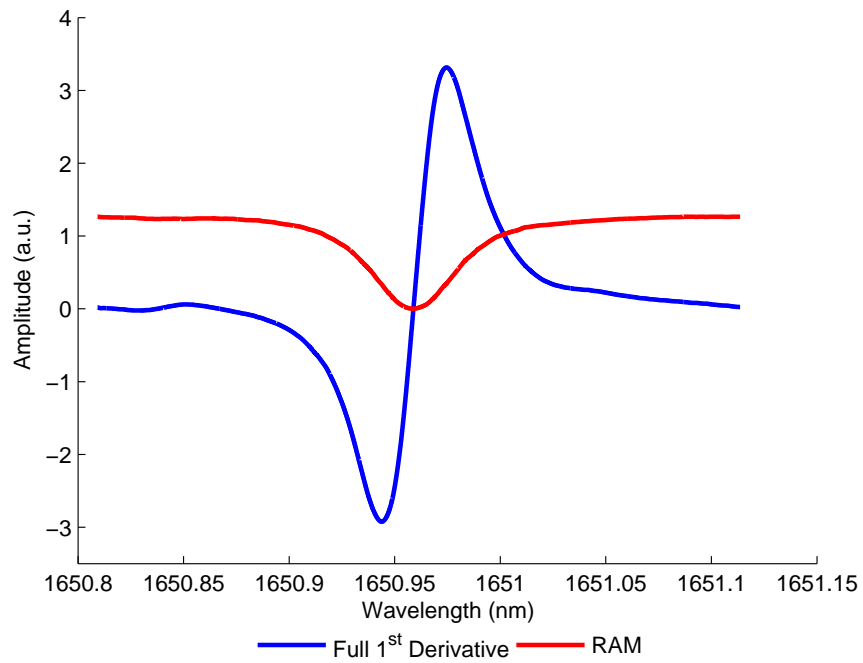


Figure 3.6: Resulting signals using the PD method, 10.13%CH<sub>4</sub>:N<sub>2</sub> m=0.2

The benefits of the PD method is the ability to record the full RAM signal, which allows the absolute gas absorption line shape to be recovered, without the need to operate at high modulation frequencies ( $>1\text{MHz}$ ). However, as with all 1<sup>st</sup> harmonic analysis techniques they each suffer from the presence of background RAM. To improve the detection sensitivity of the PD method or RAM technique the background RAM needs to be suppressed. This can be accomplished by RAM nulling and is demonstrated in chapter 5.

## 3.4 Amplitude Investigation

### 3.4.1 Overview

The previous sections have introduced analytical approaches to recover absolute gas absorption signals from the 1<sup>st</sup> harmonic signal (3.6). From this analysis the absolute gas absorption line shape or the full 1<sup>st</sup> derivative of the absolute gas absorption line shape can be extracted. Another option is to extract the 2<sup>nd</sup> derivative of the absolute gas absorption line shape, from the 2<sup>nd</sup> harmonic signal recorded on the LIA. As mentioned previously, a major benefit of doing 2<sup>nd</sup> harmonic detection is that the recovered signal sits on a zero background and gas concentration can be directly measured from the amplitude of the 2<sup>nd</sup> harmonic signal.

Ideally, it is desirable to use the technique that has the largest recovered signal amplitude, therefore giving the best signal to noise (SNR) and the best achievable measurement sensitivity. This section first describes the analytical methods to determine the absolute power levels of the RAM absorption signal and the 1<sup>st</sup> derivative and 2<sup>nd</sup> derivative signals, based on measured experimental parameters. These can first be used to scale the recovered experimental amplitudes to obtain the experimental power levels, from which a comparison of theory to experiment can then be made. The next step of the investigation is to show the effect on the recovered amplitudes when the sinusoidal modulation frequency,  $\omega$ , is increased.

### 3.4.2 Power of 1<sup>st</sup> Derivative Signal - Conventional TDLS with WM isolated from RAM

To determine the power of the 1<sup>st</sup> derivative signal the Fourier series expansion of the absorption coefficient,  $\alpha(\lambda)$ , has to be derived [47]. The expression for  $\alpha(\lambda)$  can be written as:

$$\alpha(\lambda) = \alpha_o f(\theta) \quad (3.14)$$

where  $f(\theta)$  is given by

$$f(\theta) = \frac{1}{1 + (\Delta + m \cos\theta)^2} \quad (3.15)$$

where, for a Lorentzian profile,  $\alpha_o = N_o S / \pi \gamma$ ,  $m = \delta\nu / \gamma$  is the modulation index,  $\Delta = (\lambda - \lambda_o) / \gamma$  is the deviation from line centre and  $\theta = \omega t - \psi'$ . The Fourier series of  $f(\theta)$  from equation (3.15) is now taken in terms of harmonics of the modulation frequency,  $\omega$ , and the Fourier expansion is given by [48]:

$$f(\theta) = \left\{ a_o + \sum_{n=1}^{\infty} a_n \cos(n\theta) \right\} = \left\{ a_o + \sum_{n=1}^{\infty} a_n \cos(n\omega t - n\psi') \right\} \quad (3.16)$$

where

$$a_0 = \frac{1}{\pi} \int_0^{\pi} f(\theta) d\theta = \frac{1}{\pi} \int_0^{\pi} \frac{1}{1 + (\Delta + m \cos\theta)^2} d\theta \quad (3.17)$$

$$a_n = \frac{2}{\pi} \int_0^{\pi} f(\theta) \cos(n\theta) d\theta = \frac{2}{\pi} \int_0^{\pi} \frac{\cos(n\theta)}{1 + (\Delta + m \cos\theta)^2} d\theta \quad (3.18)$$

where the Fourier coefficient for the 1<sup>st</sup> derivative signal is:

$$a_1 = \frac{2}{\pi} \int_0^{\pi} f(\theta) \cos\theta d\theta = \frac{2}{\pi} \int_0^{\pi} \frac{\cos\theta}{1 + (\Delta + m \cos\theta)^2} d\theta \quad (3.19)$$

Figure 3.7 shows  $a_1$  reaching a maximum when the following condition is met [49]:

$$\Delta = \pm \frac{\sqrt{3m^2 + 4} - 1}{\sqrt{3}} \quad (3.20)$$

From Figure 3.7 it can be seen that  $a_1$  reaches a maximum at  $m = 2$  when  $\Delta = \pm\sqrt{3}$ , resulting in peak values of  $a_1 = \pm 0.5$ . The value of  $m = 2$  for maximum 1<sup>st</sup> derivative signal amplitude is widely accepted in the field of TDLS with WM, confirmed by Figure 3.7.

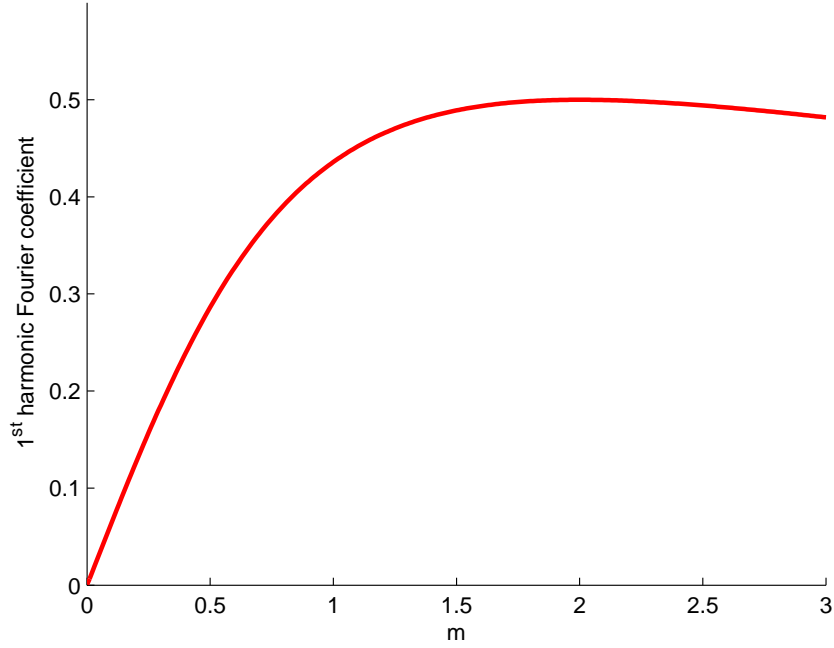


Figure 3.7: 1<sup>st</sup> derivative Fourier coefficient variation with  $m$  at  $\Delta = \pm\sqrt{3}$

The magnitude of the maximum signal power for the 1<sup>st</sup> derivative,  $S_\omega$ , in conventional TDLS with WM is given by the substitution of the Fourier form for  $\alpha(\lambda)$ , equation (3.14), into a truncated version of the Beer-Lambert Law, equation (3.1):

$$S_\omega = 0.5AI_o \quad (3.21)$$

where  $A = \alpha_o Cl$  and  $I_o$  is the laser intensity at line centre. The expression obtained in equation (3.21) is used to scale and compare experimental results to theory, which is presented in chapter 6.

### 3.4.3 Power of 2<sup>nd</sup> Derivative Signal - Conventional TDLS with WM

Before we determine the power of the 2<sup>nd</sup> derivative signal at  $\lambda_c$ , the expression for the 2<sup>nd</sup> harmonic signal has to be derived. Recalling the substitution of equation (3.3) into (3.5) and (3.5) into equation (3.4) and taking the 2<sup>nd</sup> harmonic terms,

the expression for the 2<sup>nd</sup> harmonic signal is given by:

$$I_{2\omega} = -\frac{1}{2}\Delta I(\lambda_c)\alpha'(\lambda)|_{\lambda_c}Cl\delta\lambda(\lambda_c)\cos(2\omega t - \psi') - \frac{1}{4}I(\lambda_c)\alpha''(\lambda)|_{\lambda_c}Cl\delta\lambda^2(\lambda_c)\cos 2(\omega t - \psi') \quad (3.22)$$

where the first term in equation (3.22) is a signal that is proportional to the 1<sup>st</sup> derivative arising from the RAM and the second term is the desired 2<sup>nd</sup> derivative signal. As can be seen from (3.22) the terms are separated by  $\psi'$  similar to the 1<sup>st</sup> harmonic terms. From examination of the 2<sup>nd</sup> derivative signal it can be seen that gas concentration can not be extracted directly from the recovered signal, as it is scaled by system parameters. As mentioned in chapter 1 practical applications of 2<sup>nd</sup> harmonic detection requires calibration to a known concentration of the target gas.

With the recovered 2<sup>nd</sup> harmonic signal defined the expression for the power of the 2<sup>nd</sup> derivative signal can be derived by recalling equation (3.16) and examining the expression for the Fourier coefficient  $a_2$ :

$$a_2 = \frac{2}{\pi} \int_0^\pi f(\theta)\cos 2\theta \, d\theta = \frac{2}{\pi} \int_0^\pi \frac{\cos 2\theta}{1 + (\Delta + m \cos\theta)^2} \, d\theta \quad (3.23)$$

Figure 3.8 illustrates  $a_2$  reaching a maximum when the following condition is met [49]:  $\Delta = 0$ .

From Figure 3.8 it can be seen that  $a_2$  reaches a maximum at  $m = 2.2$ , resulting in peak values of  $a_2 = \pm 0.342$ . The value of  $m = 2.2$  for maximum 2<sup>nd</sup> derivative signal amplitude is widely accepted in the field of TDLS with WM, confirmed by Figure 3.8.

The magnitude of the maximum signal power for the 2<sup>nd</sup> derivative,  $S_{2\omega}$ , in conventional TDLS with WM is given by the substitution of the Fourier form for  $\alpha(\lambda)$ , equation (3.14), into a truncated version of the Beer-Lambert Law, equation (3.1):

$$S_{2\omega} = 0.342AI_o \quad (3.24)$$

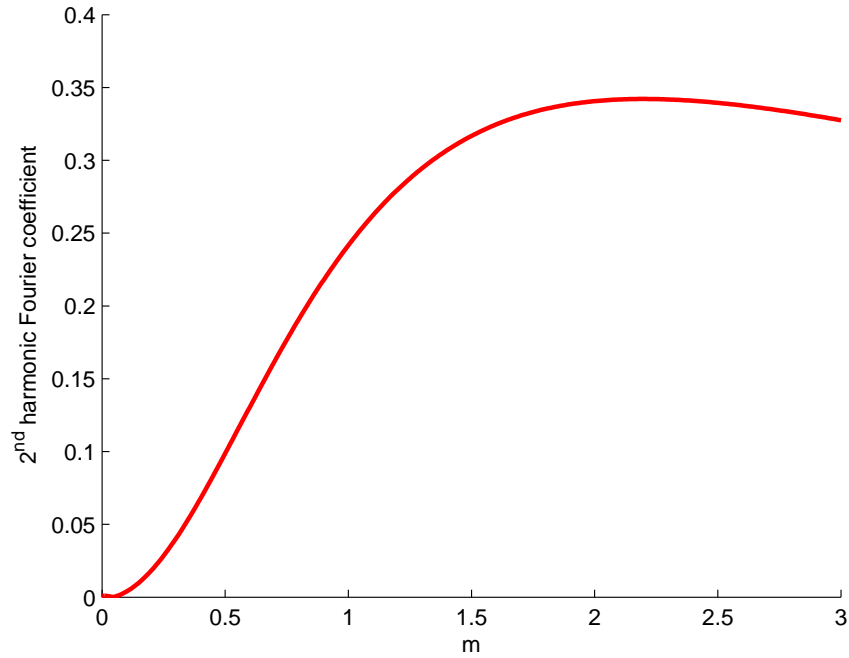


Figure 3.8: 2<sup>nd</sup> derivative Fourier coefficient variation with  $m$  at  $\Delta = 0$

The expression obtained in equation (3.24) is used to scale and compare experimental results to theory, which is presented in chapter 6.

### 3.4.4 Intensity of Absolute Gas Absorption Line Shape

As mentioned, the absolute gas absorption line shape is extracted from the RAM components of the recovered 1<sup>st</sup> harmonic signal of the LIA, using the PD method. For the purpose of this derivation it is known as the *RAM* signal and the expression for the recovered 1<sup>st</sup> harmonic signal is re-defined using Fourier analysis instead of the Taylor series expansion approach. Recalling the expression for the laser intensity at the receiver after interacting with an absorbing gas, equation (3.4), if  $\alpha(\lambda)$  is replaced by the expressions given by equations (3.14) and (3.16), the resulting expression for  $I_o$  using Fourier analysis can be written as:

$$I_o = [I(\lambda) + \Delta I(\lambda)\cos(\omega t)] \left[ 1 - \alpha_o Cl \left\{ a_o + \sum_{n=1}^{\infty} a_n \cos(n\omega t - n\psi') \right\} \right] \quad (3.25)$$

The 1<sup>st</sup> harmonic signal observed at the LIA is given when  $n = 1$  in equation (3.25):

$$I_\omega = \Delta I(\lambda) \cos(\omega t) [1 - A a_o(\lambda)] - A a_1(\lambda_c) I(\lambda) \cos(\omega t - \psi') - \frac{1}{2} A a_2(\lambda) \Delta I(\lambda) \cos(\omega t - 2\psi') \quad (3.26)$$

where  $A = \alpha_o Cl$ . As previously stated: the first term in equation (3.26) is the RAM, consisting of the background RAM and the gas concentration dependent RAM term; the second at a phase of  $\psi'$  is the WM/IM signal and finally, at a phase of  $2\psi$  is a term that arises from the IM of the 2<sup>nd</sup> derivative signal. If the detection phase of the LIA is set to null the WM/IM signal on the X measurement axis of the LIA, this will result in an isolated projection of the RAM signal on the X measurement axis, given by:

$$I_{RAM} = \Delta I(\lambda) \left[ 1 - A \left( a_o(\lambda) - \frac{1}{2} a_2(\lambda) \right) \right] \sin \psi' \quad (3.27)$$

To recover the true line shape,  $f(\lambda)$ , from the measured signal equation (3.27) is re-arranged to:

$$I_{RAM} = \Delta I(\lambda) [1 - A f(\lambda) C_f(\lambda)] \sin \psi' \quad (3.28)$$

where  $C_f(\lambda)$  is known as the normalised shape distortion function, defined by:

$$C_f(\lambda) = \frac{a_o(\lambda) - \frac{1}{2} a_2(\lambda)}{f(\lambda)} = \frac{\int_0^\pi (1 - \cos 2\theta) f(\theta) d\theta}{\pi f(\lambda)} \quad (3.29)$$

The impact of the  $C_f(\lambda)$  on the recovered signal is explained in more detail in section 3.5. The term  $C_f(\lambda)$  can be used to correct the measured signal through division. From this point onwards  $C_f(\lambda)$  is known as a correction function. Taking equations (3.14), (3.16), (3.19) and (3.23), the specific correction function for a Lorentzian line shape is given by:

$$C_f(\Delta, m) = \frac{1 + \Delta^2}{\pi} \int_0^\pi \frac{1 - \cos 2\theta}{1 + (\Delta + m \cos \theta)^2} d\theta \quad (3.30)$$

Therefore, the true line shape function,  $Af(\lambda)$ , can be recovered using equations (3.28), (3.29) and (3.30) from measurements of  $I_{RAM}$ . The recorded line shape from the LIA,  $Af_m(\lambda)$ , after normalisation to the background can be derived from

equations (3.27), (3.28) and (3.29) as it is distorted from the actual line shape by:

$$Af_m(\lambda) = AC_f(\lambda)f(\lambda) = A \left[ a_o(\lambda) - \frac{1}{2} a_2(\lambda) \right] \quad (3.31)$$

the subscript  $m$  is used to show the dependence on the modulation index,  $m$ . Using equation (3.30) gives:

$$Af_m(\lambda) = \frac{A}{\pi} \int_0^\pi \frac{1 - \cos 2\theta}{1 + (\Delta + m \cos \theta)^2} d\theta \quad (3.32)$$

The expression for the power of the recovered *RAM* signal, by using the PD method at line centre ( $\Delta = 0$ ), can now be defined using equations (3.28) and (3.32):

$$S_{RAM} = \Delta I_o \frac{A}{\pi} \int_0^\pi \frac{1 - \cos 2\theta}{1 + m^2 \cos^2 \theta} d\theta \quad (3.33)$$

where  $\Delta I_o$  is the IM at line centre. The factor of  $\sin \psi'$  from equation (3.28) is not present as equation (3.33) assumes that the PD method has been used to recover the full *RAM* signal. The term  $\Delta I_o$  can be related to  $m$ , by the current tuning coefficient,  $\xi(\omega)$ , and the modulation coefficient,  $\kappa$ , of the source laser:

$$\Delta I_o = \frac{\kappa \gamma}{\xi(\omega)} m \quad (3.34)$$

where  $\kappa = \delta I / \delta i$  is the IM coefficient of the source laser,  $\xi = \delta \nu / \delta i$  is the current tuning coefficient of the source laser and recalling  $m = \delta \nu / \gamma$ . Section 4.5.3 shows how  $\kappa$  and  $\xi$  can be experimentally determined. Equation (3.33) becomes:

$$S_{RAM} = A \frac{\kappa \gamma}{\xi(\omega)} \frac{m}{\pi} \int_0^\pi \frac{1 - \cos 2\theta}{1 + m^2 \cos^2 \theta} d\theta \quad (3.35)$$

By inspection of equation (3.35) there are a number of observations to be made. The first is the product of  $m/\pi$  with the integral shows the opposing effects of increasing signal amplitude with  $m$  but reduction in the peak value due to the WM, Figure 3.9 shows how the signal size increases with  $m$ . Also evident, the size of  $S_{RAM}$  is inversely dependent on  $\xi$  implying that better sensitivity can be achieved at higher modulation frequencies, as  $\xi$  decreases with increasing  $\omega$ .

The expression obtained in equation (3.35) is used to scale and compare experimental results to theory, which is presented in chapter 6.

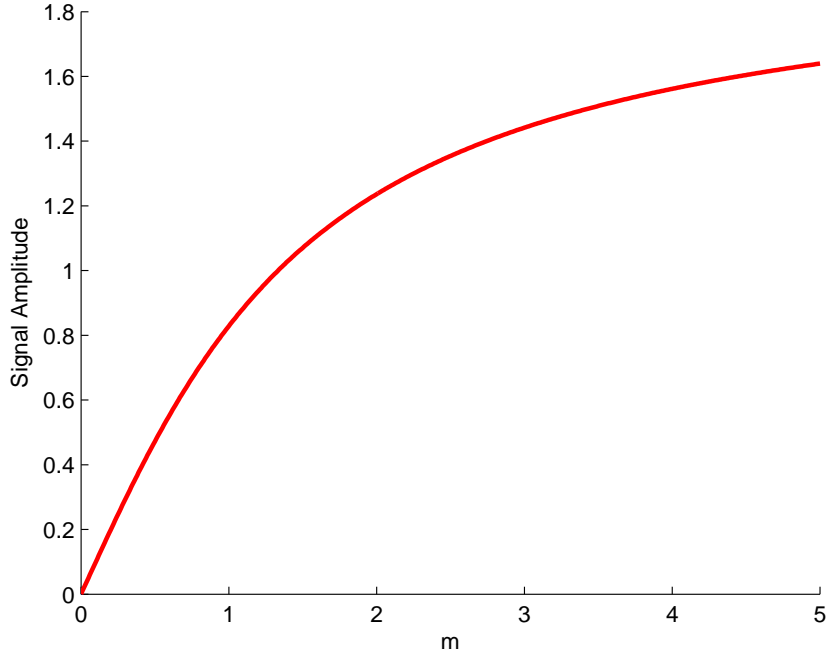


Figure 3.9: Variation of signal size with  $m$  for a Lorentzian line shape at  $\Delta = 0$

### 3.5 Correction Factor Implementation

Correction factor implementation for accurate line shape recovery is currently being investigated by researchers at the University of Strathclyde. This section gives an explanation of the techniques applied to the results presented in chapter 5. As mentioned at the start of this chapter, when applying TDLS with WM, knowledge of  $m$  is required: as  $m$  increases the measured signal from the LIA includes distortion terms, which are a function of  $m$ . Recalling equation (3.29), the normalised shape distortion function:

$$C_f(\lambda_c) = \frac{a_o(\lambda_c) - \frac{1}{2} a_2(\lambda_c)}{f(\lambda_c)} = \frac{\int_0^\pi (1 - \cos 2\theta) f(\theta) d\theta}{\pi f(\lambda_c)}$$

It can clearly be seen that the true line shape is distorted by the  $a_2$  term, which is a superposition of an inverted  $2^{nd}$  derivative signal, that is a result of IM of the  $2^{nd}$  derivative component giving a difference frequency at the first harmonic. Also, there is a distortion from the  $a_o$  term (background RAM), which is a convolution of the laser power spectrum with the line shape. In this analysis the distortion

due to the  $a_2$  is investigated and a method to correct the recorded signal from the LIA to obtain the true line shape profile is given. The contribution from  $a_2$  for the distortion factor added to the recorded signal is given by equation (3.23) and is shown by Figure 3.10. Figure 3.10 shows both  $m = 0.2$  and  $m = 2$  to emphasise the effect of low and high modulation index.

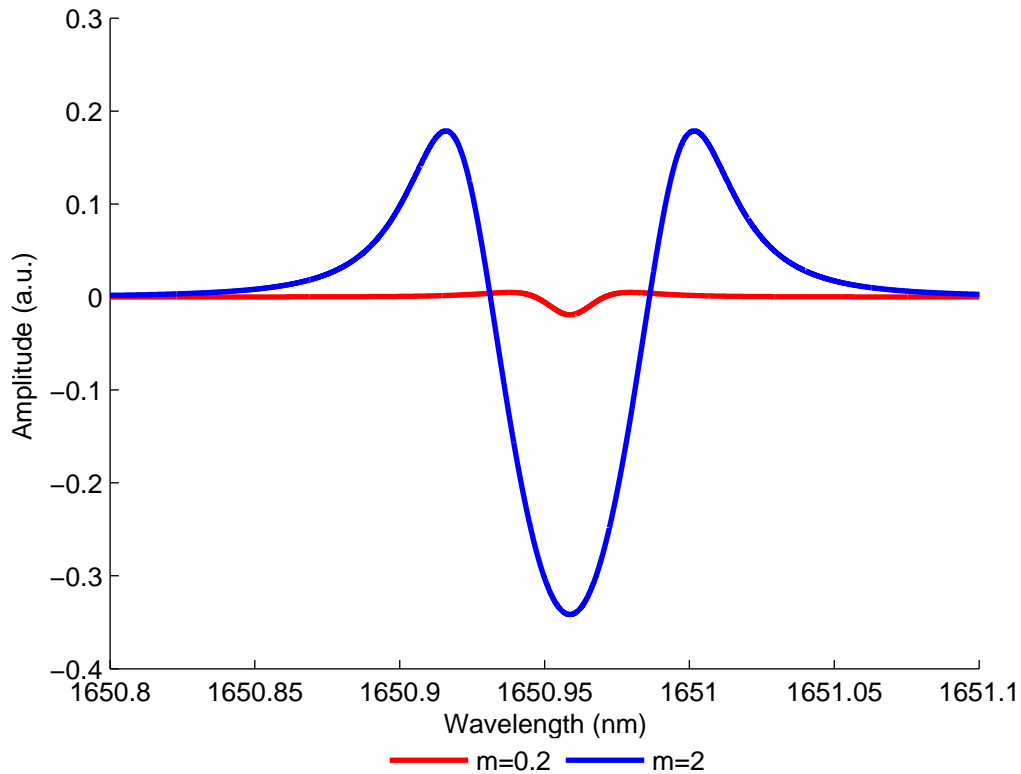


Figure 3.10: Contribution from  $a_2$  on the distortion factor present on the recorded signal for low and high  $m$

To successfully correct a distorted line shape, an accurate value for  $m$  must be obtained. This is achieved by using a ratio method, discussed shortly, which takes a ratio between the distorted and undistorted line shape to extrapolate a value for  $m$ . The calculated value of  $m$  can then be used in the correction factor equations presented at the end of this section to reconstruct the true line shape. The curve fitting process on the theoretical line shape can then be done to find the best fit to the corrected line shape.

Figure 3.11 highlights the difference in peak depth between the undistorted and distorted signals for  $m=0.2$  and  $m=2$  respectively.

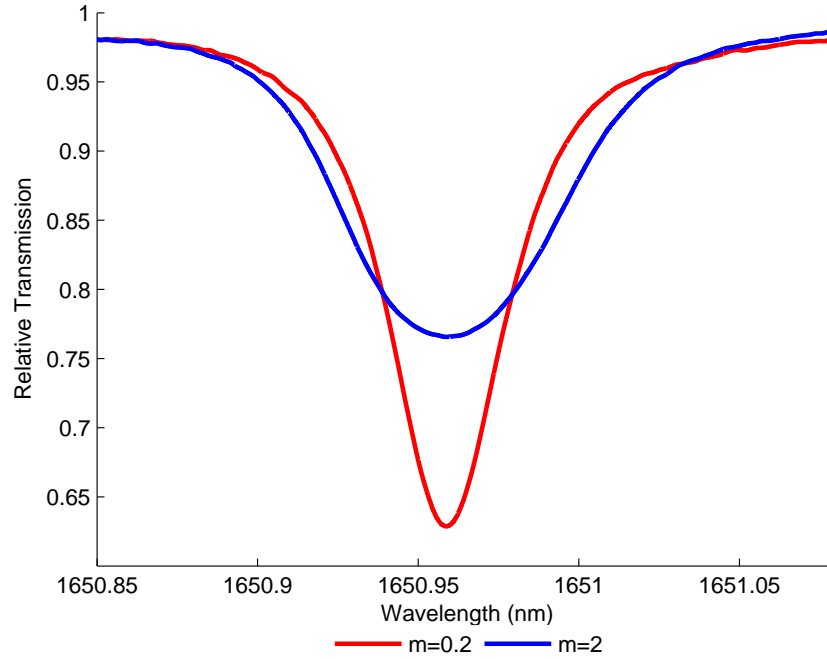


Figure 3.11: Line shape of undistorted ( $m = 0.2$ ) and distorted ( $m = 2$ ) recorded RAM measurements, 10.13%CH<sub>4</sub>:N<sub>2</sub> at STP with 9.9cm path length

The method to determine  $m$ , involves taking a ratio of the experimentally recorded peak depth to the peak depth of the low  $m$  signal (unaffected by the distortion). The following analysis assumes the recorded signals have been normalised to the background RAM or curve fitted baseline. Firstly, the ratio is calculated by:

$$ratio = \frac{1 - Ap(m)}{A_{Ref.}} \quad (3.36)$$

where  $Ap(m)$  is the peak depth at line centre of the distorted signal and  $A_{Ref.} = -\log(A)$ , where  $A$  is the peak depth at line centre of the undistorted signal, both these signals can be measured from the recorded signals. The next step is to determine the value of  $m$  on the distorted signal. This is accomplished by using the following expression to produce a value that can be compared to equation (3.36):

$$p(m, A) = \frac{2}{\pi A} \int_0^\pi \sin^2\theta \left\{ 1 - \exp\left(\frac{-A}{1 + m^2 \cos^2\theta}\right) \right\} d\theta \quad (3.37)$$

The expression given by equation (3.37) is applied to a large range of  $m$  values to construct a look up table, which can then be used to estimate the value of  $m$  for the distorted signal. This is done by taking the value of *ratio* and subtracting it from each value of  $P(m, A)$  in the table. The smallest resulting value of  $P(m, A)$  is located within the table and the corresponding value of  $m$  is the approximated value of  $m$  for the distorted signal. Identifying the best value for  $m$  is crucial as it determines the size of the correction factor.

The next stage is to use the calculated value for  $m$  to produce the desired correction factor to correct the distorted signal. For low concentrations where the Beer-Lambert approximation holds the correction factor is given by equation (3.30). However, at high concentrations, where  $\alpha \ll Cl$  is not valid, the correction is given by:

$$C_f(\lambda_c) = \frac{\int_0^\pi (1 - \cos 2\theta) f_e \theta \, d\theta}{\pi f_e(\lambda_c)} \quad (3.38)$$

where

$$f_e(\lambda_c) = \frac{1 - \exp(-Af(\lambda))}{A} \quad (3.39)$$

For a Lorentzian profile  $f_e(\theta)$  and  $f_e(\lambda_c)$  become:

$$f_e(\theta) = \frac{1 - \exp\left\{\frac{-A}{1 + (\Delta + m \cos\theta)^2}\right\}}{A} \quad (3.40)$$

$$f_e(\lambda_c) = \frac{1 - \exp\left\{\frac{-A}{1 + \Delta^2}\right\}}{A} \quad (3.41)$$

The distorted signal is then divided by the correction function using either equations (3.30) or (3.38) to gain the true gas absorption line shape. Correction factor implementation is part of ongoing research with refinements and improvements to the described methods planned.

## 3.6 Summary

This chapter has derived the analytical models used by the PD method and RAM techniques, to extract the absolute gas absorption line shape from the recorded

LIA output signals. This was followed by the derivation of theoretical expressions for power variations in the recovered RAM absorption signal and the 1<sup>st</sup> and 2<sup>nd</sup> harmonic signals. Finally, the analytical approach used to correct recovered line shapes distorted by high  $m$  values was given.

# Chapter 4

## Experimental Methodology

---

### 4.1 Overview

This chapter gives a detailed description of the experimental system. The description is broken down into its three main areas: laser and drive electronics; gas cell and delay fibre (i.e. optical components) and receiver electronics. The system and laser characterisation are then described in order to obtain the results given in chapters 5 and 6. The experimental system used to suppress the background RAM whilst using the PD method and RAM technique to recover the absolute gas absorption line shape is shown in Figure 4.1. A modified version of the system was used for the amplitude investigation. The required modification was the disconnection of the fibre delay line. The system given in Figure 4.1 is an adaptation of a system originally designed and built by researchers at the University of Strathclyde [39], used in the development of the RAM technique. The author has added RAM nulling capabilities to the system along with updated characterisation methods and results.

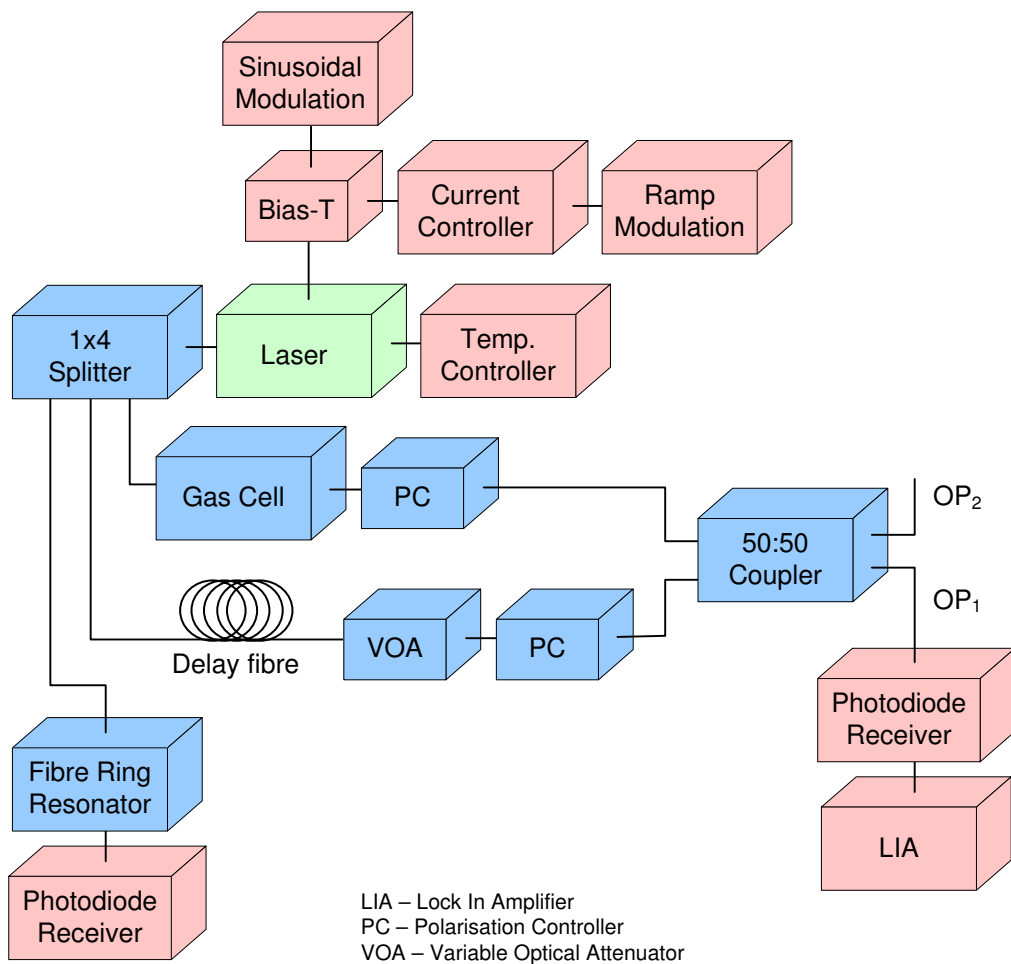


Figure 4.1: Schematic diagram of the experimental system for TDLS with WM and RAM nulling

The DFB laser shown in Figure 4.1 is first temperature tuned to the absorption feature. The feature is then scanned and interrogated by a dual modulation of laser current using a ramp and sinusoid, achieved using the bias-T. The output of the laser is then split using the splitter into three active paths. The first is to the gas cell, where the target gas can interact with the laser radiation. The next component on this branch is a polarisation controller (PC), which is used to minimise optical interference between the gas branch and delay branch. The second path from the splitter contains a fibre reel that introduces the necessary  $\pi$  phase shift in the modulated laser signal to achieve background RAM suppression. The variable optical attenuator (VOA) is used to match the amplitude of the intensity on the delay branch to that on the gas branch. Again, the PC is used

to minimise optical interference by aligning the optical axes of the branches to be orthogonal to each other. The branches are then combined and the output at OP<sub>1</sub> is recorded by the receiver and processed by the lock in amplifier (LIA). With the system optimised for RAM nulling the resulting output from the LIA is free of background RAM. OP<sub>2</sub> of the combiner is used in the signal normalisation procedure. The final path of the splitter goes to a fibre ring resonator. The recorded output of the resonator on the receiver is used to apply a wavelength scale to the recorded absorption signals.

Methane (CH<sub>4</sub>) is used as the target gas, as it is readily available and has well defined absorption lines in the NIR range. Also, methane measurements are in demand by industry for a variety of applications including methane monitoring inside a fuel cell. The 1<sup>st</sup> overtone transitions of the rotational/vibrational states of methane can be accessed in the 1620-1700nm range, and this work focuses on the 1650.96nm line, which is part of the R branch (see Figure 2.9) specifically R4 [50]. The main absorption feature is a combination of four absorption lines and at pressures above atmospheric they merge resulting in a single absorption feature that is well isolated and ideal for research purposes.

## 4.2 Laser and Drive Electronics

The laser source was a 1650nm isolated DFB laser (Model No. OL6109L-10B) manufactured by OKI. The laser was constructed in a 14 pin butterfly package, with an optical isolator and a Peltier for thermal control. The laser was mounted on a PCB allowing connections to a LDC 210 laser controller and a TED 200C temperature controller, both from Thorlabs. The butterfly package was connectorised with a FC/APC (ferrule connector/angled physical connection) pigtail and this allowed the laser to be connected to the optical splitter. For the laser output wavelength to be close to the absorption feature both current and temperature tuning is required. Temperature tuning provides a coarse range of tuning and a feedback loop maintains the desired temperature. The thermistor,

which measures the temperature of the laser, has an associated resistance that is displayed on the front panel of the TED 200C. To convert this resistance ( $k\Omega$ ) into a temperature ( $^{\circ}\text{C}$ ) the following expression was used [51]:

$$T = \left[ \frac{3892}{\ln\left(\frac{R}{2.142 \times 10^{-5}}\right)} \right] - 273.15 \quad (4.1)$$

where  $R$  was recorded as  $6.591k\Omega$  and using equation (4.1) gave  $T$  a value of  $34.837^{\circ}\text{C}$ .

Laser power is a function of the laser current and Figure 4.2 shows the laser power/current curve, for the operating range of  $10\text{mA}$  to  $150\text{mA}$  (the power was measured at the photodiode detector with the delay branch disconnected). For maximum utilisation of the laser the injection current was set to  $80\text{mA}$  on the LDC 210.

As described in chapter 1 a double modulation is applied to the laser current, in the form of a low frequency ramp and a high frequency sinusoid, both provided by Agilent 33250A signal generators. The ramp was set to  $5\text{Hz}$ , i.e. scanning the gas feature every  $0.2\text{s}$ , with an amplitude of  $300\text{mV}_{pk-pk}$ , giving a current sweep of  $50\text{mA}$  to  $110\text{mA}$  to the laser diode. The sinusoid was set to the desired frequency and amplitude. The required frequency for RAM nulling is described in section 4.3 and the procedure for determining the required amplitude is described in section 4.5.3. The ramp and sinusoid both have to modulate the laser current. This is achieved by using a bias-T, which allows the superposition of an AC signal onto a DC signal without any deterioration on either signal. The circuit diagram of the bias-T is shown by Figure 4.3.

The ramp signal is presented with zero resistance at low frequencies due to the inductors; this therefore allows the ramp current from the LDC 210 to pass unchanged. The capacitor blocks DC signals and allows the sinusoidal signal through. The  $50\Omega$  resistor was used to match the output impedance ( $50\Omega$ ) of the Agilent 33250A. The resulting output from the bias-T to the laser was a superposition of a large low frequency ramp with a small high frequency sinusoid.

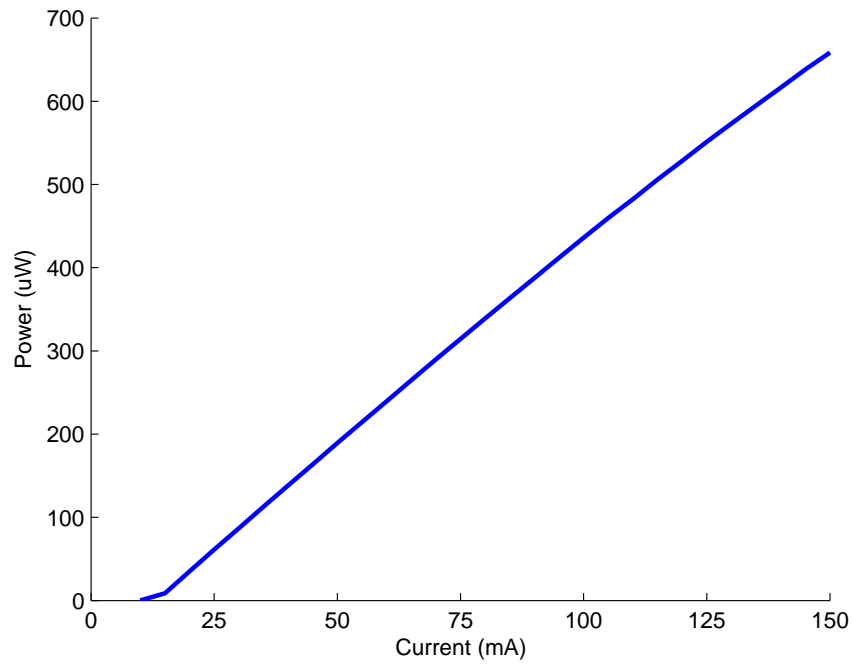


Figure 4.2: Illustration of power vs. current for DFB laser

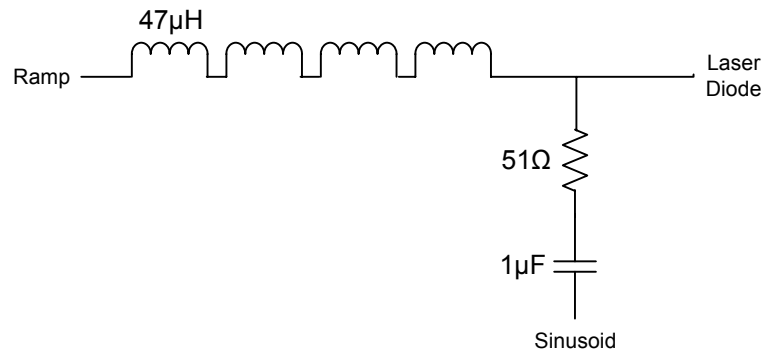


Figure 4.3: Circuit diagram for the bias-T, providing the superposition of the ramp and sinusoid modulation signals to the DFB laser

## 4.3 Delay Fibre and Gas Cell

### 4.3.1 Overview

As mentioned previously (in chapter 1 and section 4.1) and shown in Figure 4.1, implementation of the novel optical RAM nulling technique requires that the source laser output is split with equal power being fed to a branch with a gas cell and a branch with a delay fibre. The laser power is split using an optical 1x4 splitter from Sifam Fibre Optics. This section gives details of the design and construction of each branch. Standard single mode fibre was used for all optical connections.

### 4.3.2 Delay Line Branch

The primary component of the delay line branch was a reel of SMF 28 fibre. The purpose of the fibre reel was to introduce a  $\pi$  phase change in the modulated signal, so that when the two branches were re-combined the signals were in anti-phase. The length of fibre required was determined by the following expression:

$$Fibre\ Length = \frac{c}{2n_e f} \quad (4.2)$$

where  $c$  is the speed of light,  $n_e$  is the effective index for light propagation in the fibre (1.451 for SMF 28) and  $f$  is the sinusoid modulation frequency. A value of 100kHz was chosen, for  $f$ , as this is the upper end of conventional TDLS with WM. Using equation (4.2) gave a fibre length of approximately 1km and in practice, a fibre reel of nominal length 1km was used and the modulation frequency was adjusted until the anti-phase condition was achieved. A further consideration in the selection of the fibre length is that it had to be much greater than the coherence length of the laser, to minimise optical interference noise. For the laser used, which had a full width half maximum (FWHM) bandwidth of 8MHz, the coherence length is  $\approx 38$ m, very much less than that of the 1km fibre.

To balance the IM signals on both branches a variable optical attenuator (VOA

- Thorlabs VOA50-APC) was placed in the delay branch after the fibre reel. The VOA was adjusted until the IM amplitudes were matched at the combiner output  $OP_1$ , thereby effecting cancellation. The final component was a polarization controller (PC), which allowed the polarisation states of both IM signals to be aligned orthogonal, reducing system noise to a level comparable to the receiver noise. The benefits of using the PCs are shown in the next section.

### 4.3.3 Gas Cell Branch

The gas branch primarily consisted of the gas cell, shown in Figure 4.4, used to hold the methane so the laser radiation could interact with the gas. The cell was made from a cylindrical piece of plastic that was 37.5cm in length with a diameter of 9cm, and an enclosed volume of approximately  $2385\text{cm}^3$  (2.4litres). The ends of the cell were sealed with screw caps that had rubber gaskets to make the cell airtight. The screw caps provided connections for gas supplies, fibre connections and a pressure gauge. The first cap had three Swagelok valves: the first was used as an inlet for methane at the desired concentration; the second was an inlet for nitrogen ( $N_2$ ) used either to purge the cell of methane or dilute the methane to create a lower concentration; the final valve was connected to a rotary vacuum pump, which allowed all gases to be removed from the cell. The outlet of the pump was passed into a fume cupboard for the safe extraction of the gas from the lab. Also on the cap was a thermocouple, which had been passed through and sealed to the inside of the cell, which was then connected to a monitor giving a reading of temperature inside the cell.



Figure 4.4: Photograph of the gas cell enclosure

The other screw cap had two fibre feed-throughs, this allowed two lengths of fibre each with a FC/APC connector at each end into the cell, the connectors inside were attached to a micro-optic cell, discussed shortly, and the connectors outside were used to connect to one of the outputs of the splitter and a PC. Also connected to the cap was a LEO-2 digital pressure gauge, from Omni Instruments, used to monitor the pressure inside the cell to an accuracy of 0.001Bar.

The gas measurement region was defined by the micro-optic cell, which had an open path length of 9.9cm between two focussing C lenses that allowed the gas to interact with the laser, shown in Figure 4.5. C lenses have a spherical face and were used instead of gradient index (GRIN) lenses because they provided lower insertion loss at lower cost [52]. The lenses had equal focal lengths and were placed in a concentric arrangement in order to reduce interferometric noise due to light oscillating between the lenses. The lenses had an anti-reflection coating at 1650nm to minimise reflections. The cell was constructed by placing the two lenses in a jig approximately 10cm apart. The jig was adjusted in the  $x$ ,  $y$  and  $z$  direction until the measured loss through the lenses was minimal. With the lenses still in the jig a ceramic base was offered up to the underside of the lenses, UV curing glue was used to attached each lens to the tile. After completion the total loss through the cell was measured to be 1.8dB, where 0.8dB was the insertion loss of the lenses and the remaining 1dB was due to misalignment of the lenses. Both lenses had a FC/APC pigtail and were connected to the fibre in the cell cap feed-through using a bulkhead.

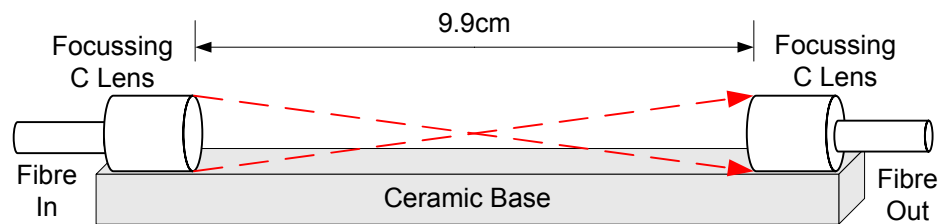


Figure 4.5: Design of 9.9cm micro-optic cell

A PC was attached to the gas cell branch and used in partnership with a PC on the delay branch to minimise optical noise due to interference at the re-combiner, illustrated in Figure 4.6. The red trace in Figure 4.6 shows the

receiver output / noise when the delay line is disconnected and no modulation is applied. The blue trace is the receiver output with the delay line connected, no applied modulation and the PCs adjusted to show the maximum interference noise i.e. the polarisation states from both branches aligned. The black trace is the receiver output with the delay line connected, no applied modulation and the PCs adjusted to minimise the interference noise i.e. the polarisation states from both branches are orthogonal. Therefore, it can be seen from Figure 4.6, using the PCs the optical noise on the system was reduced to a level that is similar to the recorded receiver noise.

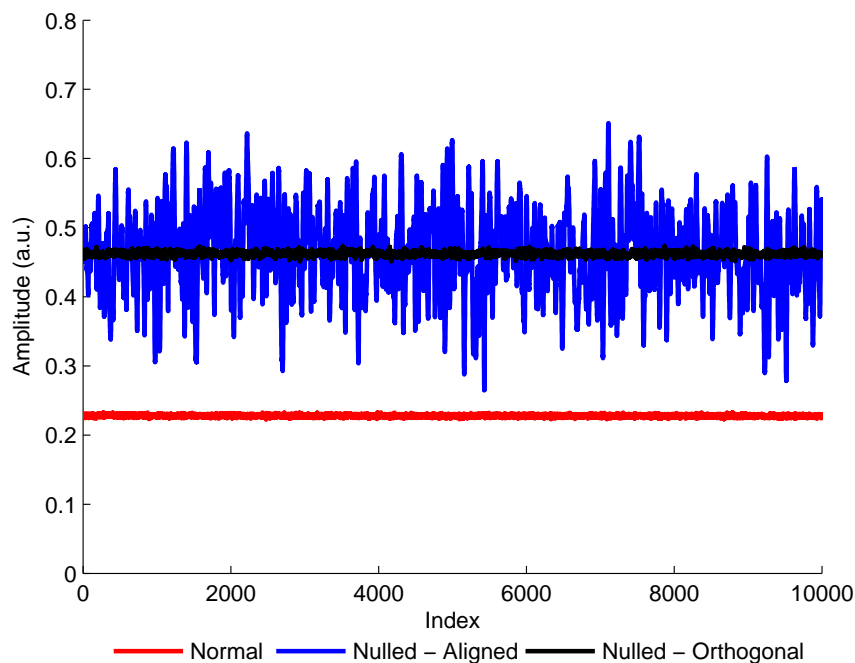


Figure 4.6: Receiver output - no modulation applied. The red trace is the receiver output with the delay branch disconnected. The blue trace is the output with the delay branch connected and the optical axes of the branches aligned parallel. The black trace is the output with the delay branch connected and the optical axes of the branches aligned orthogonal. The black trace is double in amplitude due to the addition of the DC terms.

Figure 4.7 shows the effect of applying the sinusoidal modulation. The red trace is the receiver output with the delay line disconnected and sinusoidal modulation applied. The black trace is the receiver output with the delay line connected, sinusoid modulation applied, the VOA adjusted to balance the power from the two branches to achieve RAM nulling and the PCs adjusted for minimum interference noise. Clearly, it can be seen that when the delay line is connected the sinusoidal modulation is suppressed, which results in the background RAM being suppressed. The increase in the DC level is a result of the addition of the DC terms (equation (B.7)) from both branches.

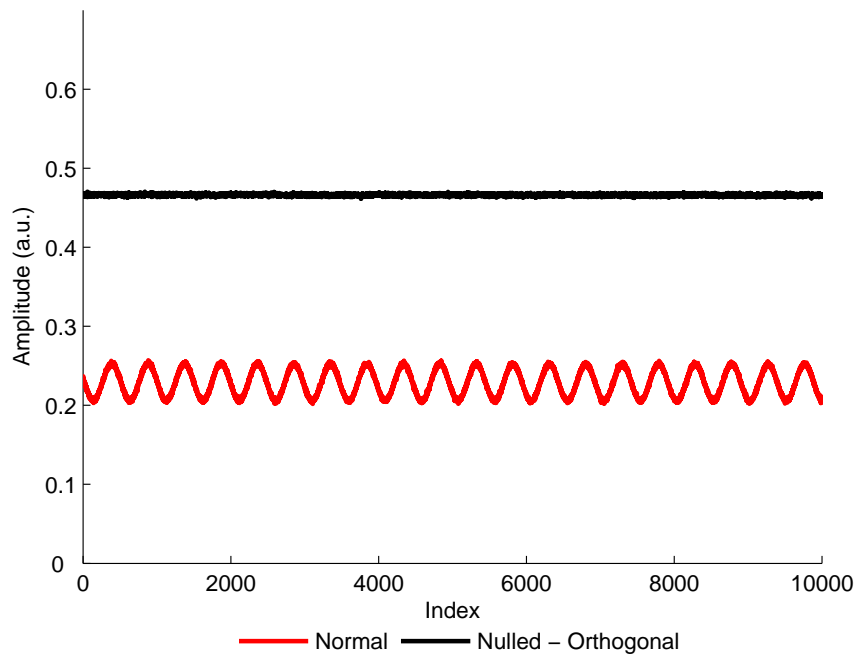


Figure 4.7: Receiver output - sinusoid modulation applied. The red trace is the receiver output with the delay branch disconnected. The black trace is the output with the delay branch connected, showing the successful suppression of the background RAM component on the modulated laser signal. Again, the black trace is double in amplitude due to the addition of the DC terms.

## 4.4 Receiver Electronics

The output of the re-combiner was connected to an InGaAs photodiode receiver, from OptoSci Ltd., (model LNP-2). The receiver had a 1MHz bandwidth, with two adjustable gain settings, which were set to their lowest to maximise bandwidth. The output of the photodiode was connected to a Perkin Elmer 7280 LIA, in order to recover the harmonic signals of the gas transmission function. As mentioned earlier the LIA measures the variation in the input amplitude at a specific frequency taken from the reference input of the LIA. The function of a LIA is that it can extract small signals within high backgrounds. Figure 4.8 shows a basic schematic of a LIA.

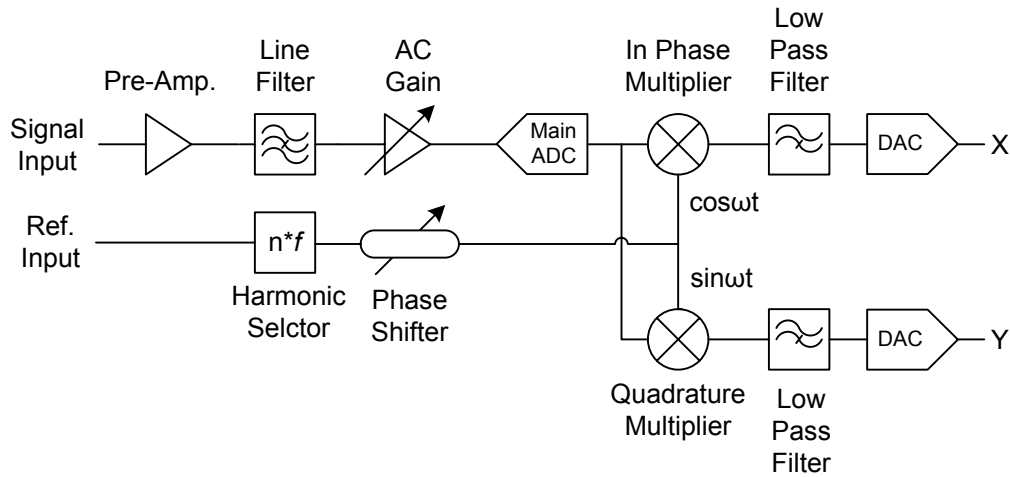


Figure 4.8: Schematic block diagram of the Perkin Elmer 7280 LIA

The input signal first goes through a pre-amplifier stage, then a line frequency rejection filter to remove any presence of a 50Hz signal. The signal goes through an AC gain stage to increase the target signal against background noise. The AC gain is controlled by the user and is adjusted to maximise the signal seen by the main analogue to digital converter (ADC), but not to a level that overloads the ADC. The signal is then split with the in-phase multiplier and the quadrature multiplier both being fed. The second input to the multipliers was provided by the reference signal. The in-phase multiplier is supplied with the  $\cos(\omega t)$  version of the reference signal and the quadrature multiplier is supplied with the  $\sin(\omega t)$  version of the reference signal. These multiplication processes produces

two demodulated signals, the in-phase and quadrature, X and Y output of the LIA respectively, where X and Y are separated by  $90^\circ$ .

The reference signal is taken from the 5V TTL *Sync* output of the Agilent signal generator, that provides the high frequency sinusoid. By using the signal generator as an external reference source allows the LIA to track any fluctuations in the modulation signal to the laser. The first stage of the reference component in the LIA is the harmonic selector, which allows the user to select what harmonic signal to view. The reference signal is multiplied by the value set by the user. A phase-locked loop (PLL) is used by the LIA to lock onto the reference signal and track any changes in frequency. The reference signal is then multiplied by the digitised signals as mentioned earlier to generate the two demodulated signals.

The final stages of the LIA are a low pass filter and a digital to analogue converter (ADC). The purpose of the filter is to produce a DC signal that is proportional to the amplitude of the chosen harmonic signal. The passband of the filter is controlled by the time constant of the LIA. When selecting a time constant there is a trade off between SNR and accurate signal recovery: too large a time constant over averages the signal and too small introduces additional noise. The filtered analogue signal was then viewed on a Tektronix TDS3014B oscilloscope, with 100MHz bandwidth and a sampling rate of 1.25GSa/s. Connection between the oscilloscope and a computer was achieved using a GPIB cable, with the computer running LabView for data capture.

## 4.5 System Characterisation

### 4.5.1 Overview

To accurately recover the true line shape from the recorded gas absorption signals knowledge of a number of system parameters is crucial. The following sections present the developed procedures used.

### 4.5.2 Wavelength Referencing

This section gives an overview of the fibre ring resonator [21] developed for wavelength referencing. There was a need for accurate wavelength referencing as there was a non-linear relationship between laser current and output wavelength. Therefore, the assignment of a wavelength scale onto the time axis of the recorded signals was needed.

The design of fibre resonators can take a number of forms [53,54]. A configuration that used two optical fibre couplers was used to give better SNR and strong resonance peaks on a zero background [53]. The fibre resonator can be used in situ; therefore changes in laser wavelength due to non-linearity or drift can be tracked and applied to the recorded signals in a field deployed system. The construction of the fibre resonator used is shown in Figure 4.9.

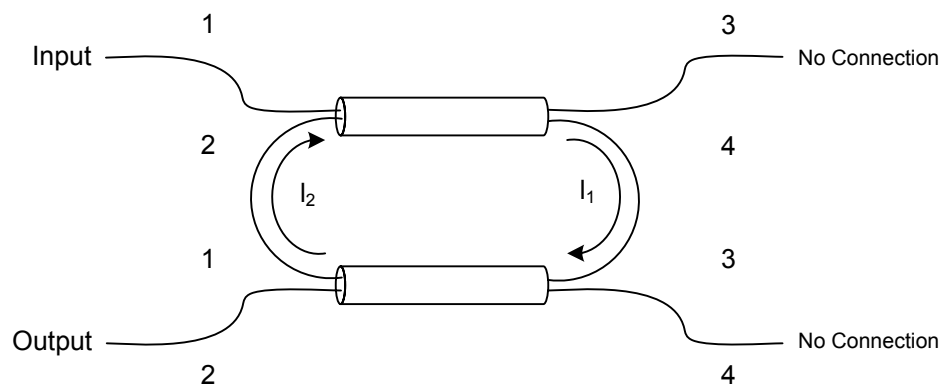


Figure 4.9: Design of fibre ring resonator using a two optical coupler configuration

The principal of the resonator is that light enters port 1 of the first coupler, entering the ring. Light travels round the ring, which has a length of  $l_1 + l_2$ , and enters the first coupler now at port 2. On resonance, the light entering ports 1 and 2 of the first coupler interferes constructively, resulting in a maximum signal on the ring. Off resonance, the light entering ports 1 and 2 interferes destructively. The signal level on the ring is sampled from port 2 of the second coupler. The output of the fibre resonator is the classic Fabry-Perot response with resonance peaks on a zero background when the laser current is ramped, which

can be modelled using Urquhart's equations [53, 55]:

$$\frac{Output}{Input} = \frac{(\varepsilon'_1 \varepsilon'_2)^2 / e^{-2\alpha(l_1 + 2l_2)}}{(1 - \varepsilon_1 \varepsilon_2)^2 + 4\varepsilon_1 \varepsilon_2 \sin_2(\beta[l_1 + l_2])} \quad (4.3)$$

where

$$\varepsilon_j = (1 - K_j)^{\frac{1}{2}} (1 - \gamma_j)^{\frac{1}{2}} e^{-2\alpha l_j} \quad (j = 1, 2) \quad (4.4)$$

and

$$\varepsilon'_j = K_j^{\frac{1}{2}} (1 - \gamma_j)^{\frac{1}{2}} e^{-2\alpha l_j} \quad (j = 1, 2) \quad (4.5)$$

$\alpha$  is the field loss in the fibre (typically 0.22dB/km for standard SMF),  $K_1$ ,  $K_2$ ,  $\gamma_1$  and  $\gamma_2$  are the coupling ratios and excess losses of the couplers respectively and  $\beta$  is the propagation constant, given by:

$$\beta = \frac{2\pi}{\lambda} n_e \quad (4.6)$$

where  $n_e$  is the effective refractive index of the fibre and  $\lambda$  is wavelength.

From inspection of equation (4.3) it can be seen that the main factors that affect frequency response are ring length and coupling ratio. An important parameter of the fibre resonator is the finesse, which is set by the coupling ratio. The finesse is the ratio of the frequency separation between the peaks to the full width half maximum (FWHM) of the peaks. Therefore, the higher the finesse the sharper the resonance peaks are. However, there is a trade off between the finesse and the resolution of the data logging software. The resonator ring length determines the frequency spacing between the resonance peaks, also known as the free spectral range (FSR). The expression relating resonator finesse and FSR is given by:

$$Finesse = \frac{FSR}{FWHM} \quad (4.7)$$

There are practical considerations when deciding the ring length along with the trade off with the number of resonance peaks and the resolution of the data logging software. The ring length of the constructed resonator was 47cm. A number of coupling ratios were modelled [21] to evaluate the performance of the resonator. It was decided that two 40:60 couplers would be used, with 40% being directed into the ring. This gave an acceptable finesse and contrast ratio, so

that the locations of the resonance peaks could be extracted, the output of the fibre resonator is shown by Figure 4.10. The amplitude of the resonance peaks in Figure 4.10 increase with the scan due to the increasing laser intensity as the current is ramped.

The fibre resonator was characterised using a 1665nm DFB laser by observing 3 methane absorption lines, in order to obtain the FSR. The observed lines aren't isolated but the peak positions are well documented in the HITRAN database. The scan of the 1665nm laser and the resonator output is shown in Figure 4.11.

Three peak positions, gives two sets of absolute wavelength references, which allows two calculations of the FSR to be made. By inspection of Figure 4.11, the spacing between points A and B was 10.167GHz and 24 resonance peaks giving an FSR of 0.424GHz. The spacing between points B and C was 12.956GHz and 28 resonance peaks giving a FSR of 0.462GHz, this gave an average value of 0.443GHz for the FSR. The FSR of a resonator is also given by the following:

$$FSR = \frac{c}{n_e L} \quad (4.8)$$

where  $c$  is the speed of light in a vacuum,  $n_e$  is the effective refractive index of the medium (1.45 for standard SMF) and  $L$  is the optical path length, in this case the fibre ring.

With knowledge of the resonator FSR and the frequency of the absorption peak feature at line centre an accurate wavelength scale can be applied to the recorded signals. The following procedure, illustrated by Figure 4.12, assumes that the normalised gas absorption signal is recorded in the same time domain as the resonator output. Firstly, the peaks of the resonator scan are identified; a polynomial fit is then applied to the peak points to generate a relative frequency scale for the entire sweep. The peak position of the gas absorption line on the relative scale,  $f_c$ , is identified. A scaling factor is then calculated that moves  $f_c$  to the absolute frequency at line centre, in this case  $1.82 \times 10^{14}$ Hz (1650.96nm). This factor is then applied to the rest of the relative scale, generating an absolute frequency scale. It was then converted to an absolute wavelength scale, using  $\lambda = c/f$ , and applied to the normalised gas absorption line shape.

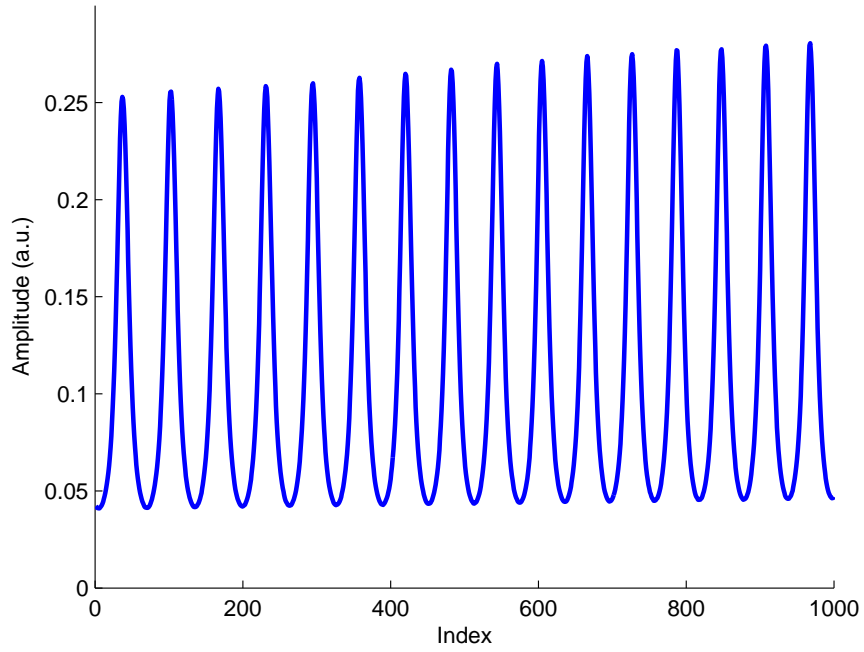


Figure 4.10: Fibre ring resonator output as the laser current is ramped

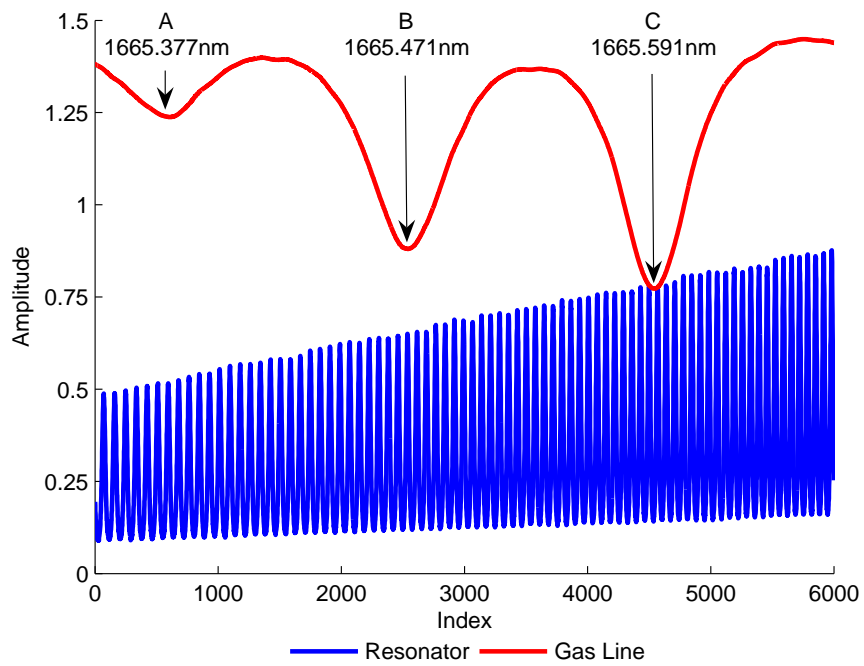


Figure 4.11: Scan of 1665nm laser observing 3 methane lines overlaid with the fibre resonator output

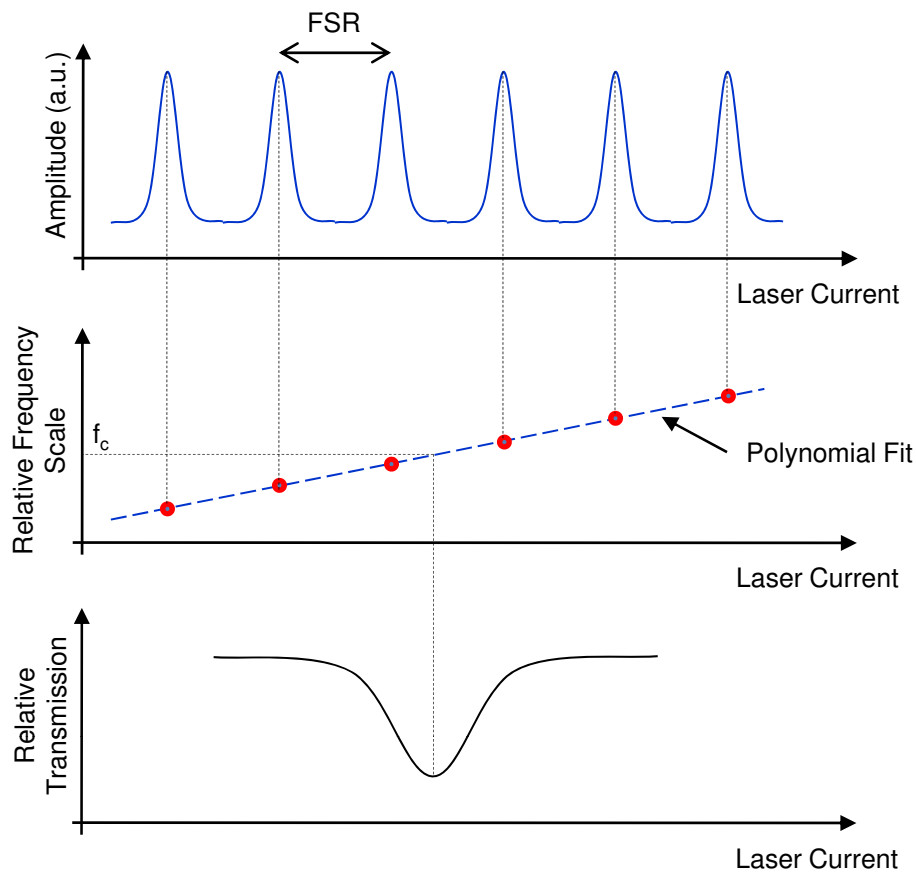


Figure 4.12: Using fibre resonator to build a absolute wavelength scale

A recent advance has been made in the determination of the FSR of the resonator. For the new technique the output of the resonator is recorded along with a gas absorption signal that contains two absorption peaks. The gas signal is wavelength referenced using the resonator output using the above method, however the FSR is varied using an iterative process. The resulting series of wavelength referenced gas signals are compared to theory by determining the error in the peak positions of the experimental data. The correct value of FSR is given by the result that has the lowest least square error in peak positions compared to theory. The results presented later in this thesis were wavelength referenced using the original technique involving the three known absorption features. Future work will use the new technique as it appears to give a more accurate value for FSR.

### 4.5.3 Laser Tuning and Modulation Coefficients

The amplitude of the sinusoid modulation for TDLS with WM is dependent on the desired  $m$  value, recalling  $m = \delta\nu/\gamma$ . A value for  $\gamma$  can be estimated by measuring the HWHM of a normalised direct detection result at the same concentration and pressure, as the intended TDLS with WM measurement, for example at STP using 10.13%CH<sub>4</sub>:N<sub>2</sub>  $\gamma=2.2511$ GHz. The typical values for  $m$  used in this work were  $m = 0.2, 0.5, 1, 1.5, 2, 2.2$ . With prior knowledge of  $m$  and  $\gamma$ , values for  $\delta\nu$  could be calculated, given in table 4.1 for the stated value of  $\gamma$ .

$m$	$\delta\nu$ (GHz)
0.2	0.45022
0.5	1.1255
1	2.2511
1.5	3.37665
2	4.5022
2.2	4.95242

Table 4.1: Calculated values for  $\delta\nu$  based on a value of 2.2511GHz for  $\gamma$

The resulting frequency deviation has to be converted into a current deviation in order to set the required sinusoid amplitude. This conversion required characterisation of the laser current tuning coefficient,  $\xi$ , which has the units GHz/mA. To determine  $\xi$  the following experimental procedure was carried out.

The laser is solely modulated by the sinusoid at the desired frequency. The output of the laser is connected to the fibre ring resonator (described in section 4.5.2), the output of the resonator is connected to the photodiode receiver, with the output of the receiver being connected to the oscilloscope. The sinusoidal output from the signal generator is also observed on the scope. Figure 4.13 shows a typical screen shot from the oscilloscope using this setup, showing that for a certain applied amplitude there is a resulting frequency deviation given by the number of peaks between the large troughs. The phase difference between the signals is the phase separation between the IM and WM components of the laser.

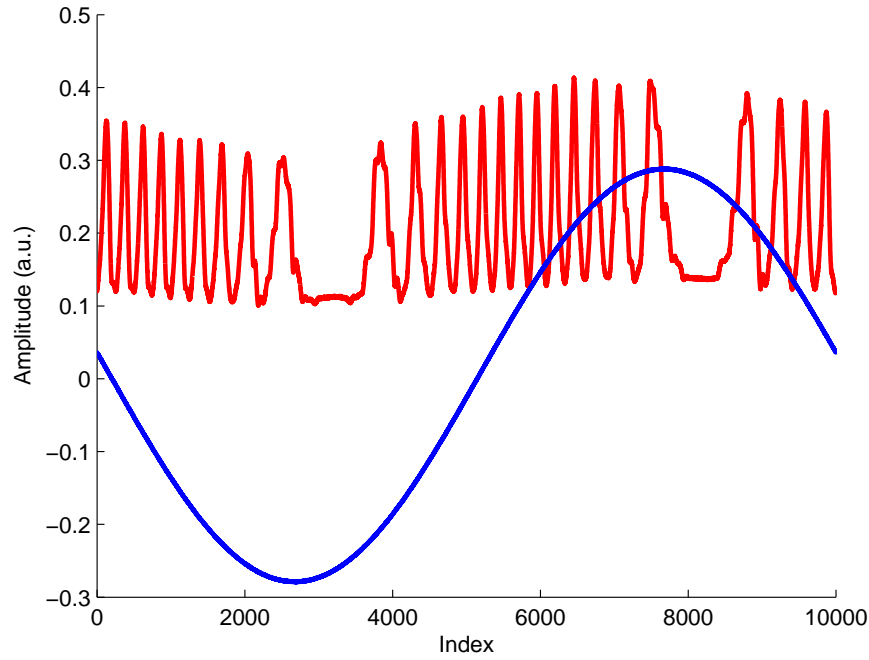


Figure 4.13: Determining the tuning coefficient,  $\xi$ , of the laser by measuring the frequency deviation (red trace) for a given voltage modulation (blue trace)

As the amplitude of the sinusoid is increased the number of resonator peaks also increases due to the increased frequency deviation. As the frequency spacing between the peaks is the FSR of the resonator, a value for peak frequency deviation in terms of applied peak voltage can be determined. To find  $\xi$ , the amplitude frequency deviation,  $\delta\nu$  was found by multiplying the number of resonator peaks by 0.443GHz (resonator FSR), then dividing the value by 2.

The amplitude current deviation,  $\delta i$ , was found by dividing the peak-to-peak voltage from the signal generator by 100: a factor of 50 arising from the  $50\Omega$  resistor in the bias-T seen by the signal generator output and a further factor of 2 to get the value in terms of an amplitude. The value of  $\delta\nu$  was then divided by  $\delta i$  to gain  $\xi$ . With knowledge of  $\xi$  the value for  $\delta i$  could be calculated for any given value of  $\delta\nu$ . Using the values given in table 4.1 the corresponding values for  $\delta i$  can be calculated followed by the required peak-to-peak voltage,  $\Delta V$ , from the signal generator. Table 4.2 gives the values for  $\delta i$  and  $\Delta V$  for 100kHz based on  $\xi=0.124\text{GHz}/\text{mA}$ . The values for  $\Delta V$  are calculated by multiplying  $\delta i$  by

100, again a factor of 50 represents the  $50\Omega$  resistor in the bias-T seen by the signal generator output and a further factor of 2 is to convert from amplitude to peak-to-peak value. Values for  $\Delta V$  and  $\delta i$  had to be calculated as  $\Delta V$  is applied on the signal generator and  $\delta i$  is required for the correction factor implementation. The dither values given in table 4.2 increase linearly with increasing  $m$ , therefore the dither value for any  $m$  is easily obtainable.

$m$	$\delta i$ (mA)	$\Delta V$ (mV)
0.2	3.625	362.5
0.5	9.062	906.2
1	18.124	1812.4
1.5	27.185	2719
2	36.247	3625
2.2	39.872	3987

Table 4.2: Calculated dither voltages and currents for 100kHz sinusoid modulation frequency

The above procedure was carried out for a number of modulation frequencies ranging from 10kHz to 1.2MHz, Figure 4.14 shows the results of tuning coefficient against modulation frequency,  $f$ , as can be seen the value of  $\xi$  decreases with  $f$ .

Another important laser parameter that needs to be determined is the modulation coefficient,  $\kappa$ , which is the power deviation,  $\delta I$ , of the laser for a given current deviation,  $\delta i$ , experimentally determined using the power/current curve (Figure 4.2) of the source laser. A modified version of the power/current curve is given by Figure 4.15, where by using a polynomial interpolation of the power/current curve  $\delta I$  can be read off for any given value of  $\delta i$ .  $\kappa$  was recorded for all  $\delta i$  used in this research and the results are shown by Figures 4.16 and 4.17. As can be seen there is little variation in  $\kappa$ , therefore an average value was taken,  $\kappa=4.896\mu\text{W}/\text{mA}$ .

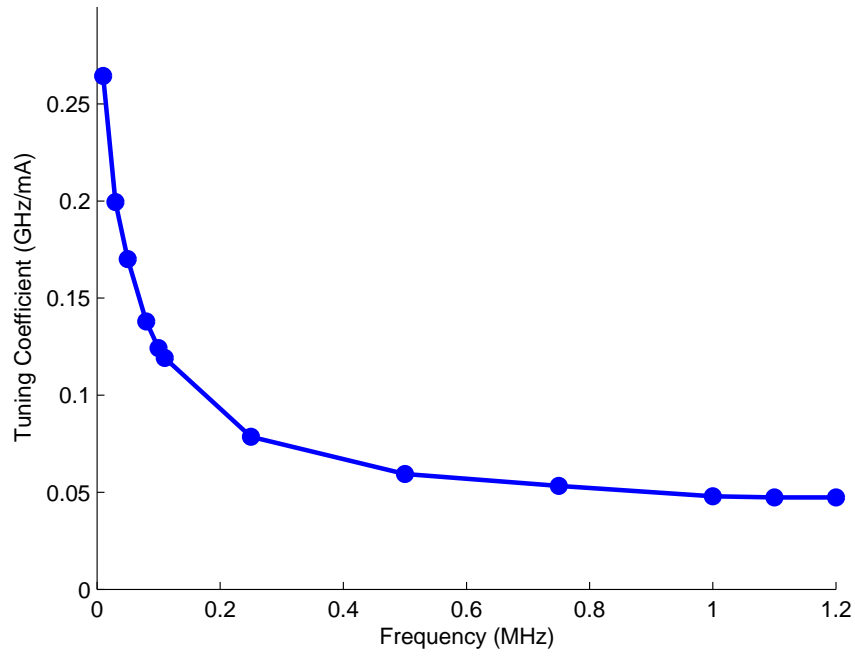


Figure 4.14: Experimental results of  $f$  against  $\xi$

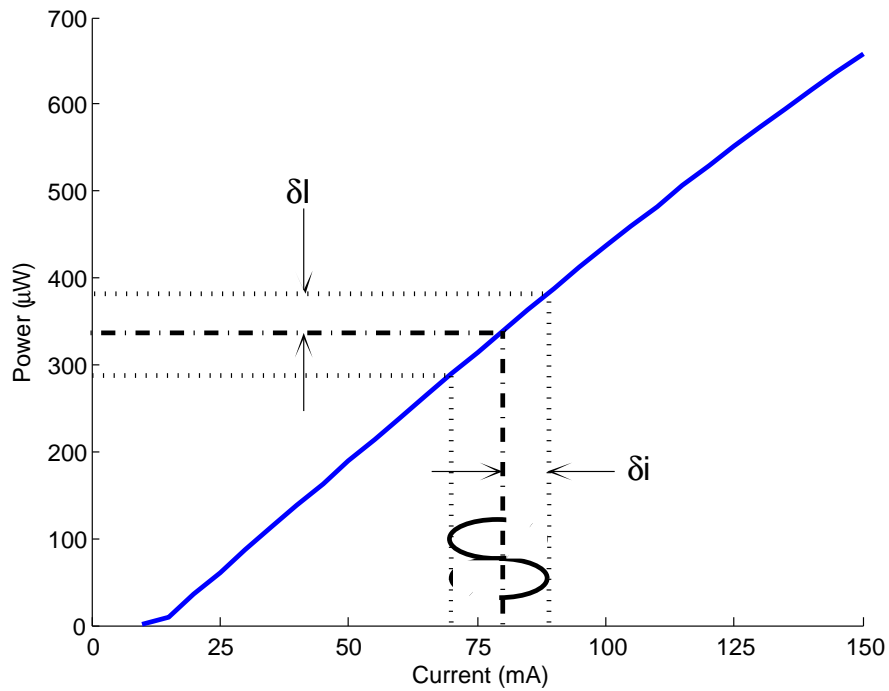


Figure 4.15: Power/current curve highlighting the resulting power deviation due to the applied current deviation

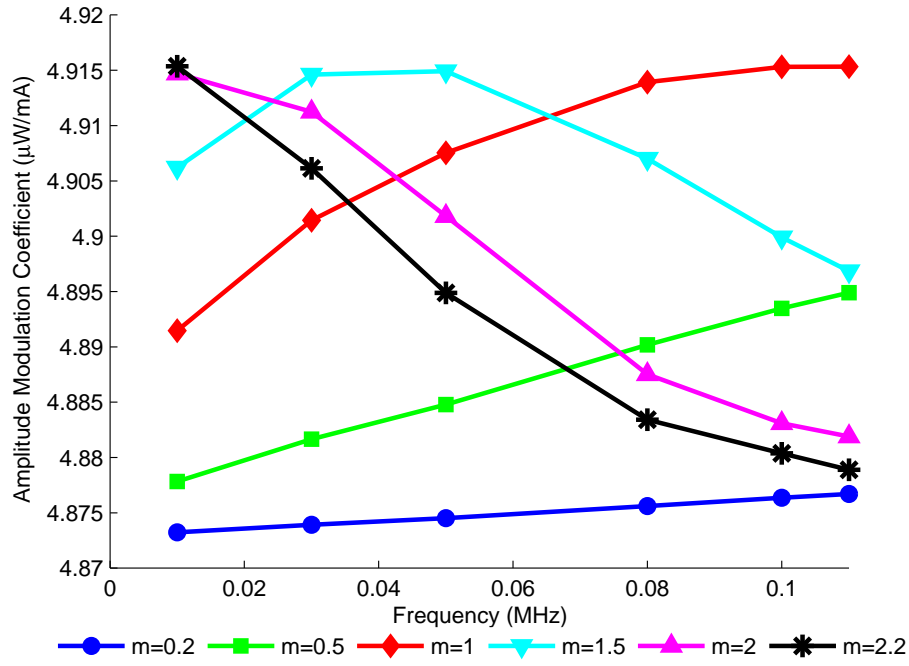


Figure 4.16: Results for  $\kappa$  as sinusoidal modulation frequency and  $m$  are varied between 10kHz and 100kHz

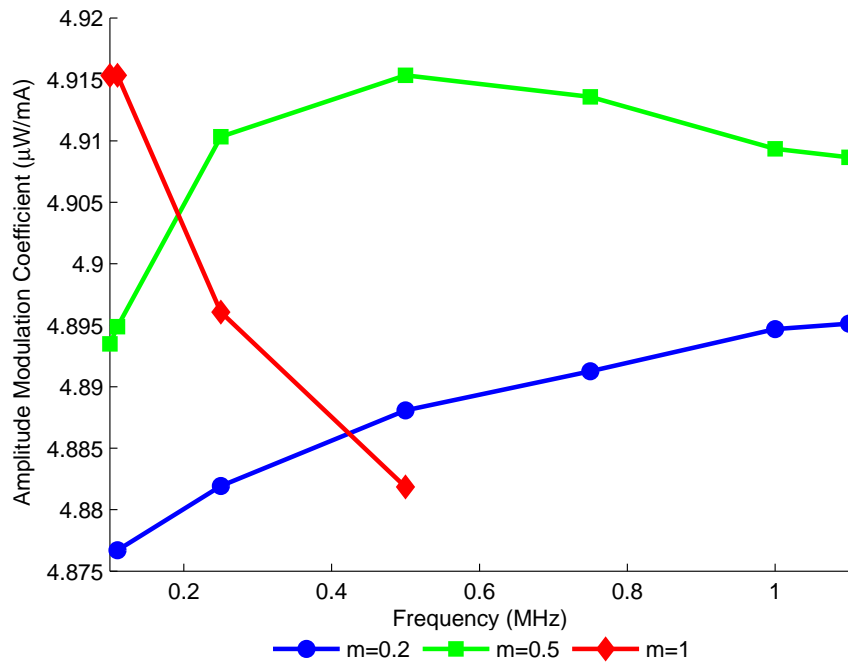


Figure 4.17: Results for  $\kappa$  as sinusoidal modulation frequency and  $m$  are varied varied between 110kHz and 1.1MHz

#### 4.5.4 IM and WM Phase Separation

As mentioned in section 3.2 there is a phase separation between the WM and IM components of the 1<sup>st</sup> harmonic signal. The RAM components due to the IM on the laser are aligned in phase to the applied current. Laser WM arises from a combination of fast carrier injection and slow thermal mechanisms as a result of current modulation [20]. The refractive index of the material decreases due to the carrier injection, thus increasing the optical frequency and decreasing the wavelength. The WM arising purely from carrier injection is in anti-phase with the modulation current and the RAM components [20]. The thermal effect, which causes expansion of the optical path in the DFB laser grating period dominates at low modulation frequencies and hence decreases the optical frequency and increases the wavelength with increasing temperature and current. Therefore, the thermally driven WM and RAM are intrinsically in phase, but with the addition of a phase lag,  $\psi'$ , arising from the thermal impedance of the system and the vector addition of the smaller carrier effects [20]. Note, that, as in previous work [20, 43]  $\psi'$  is defined as the phase shift between the WM and the IM and  $\psi$  is the FM/IM phase shift ( $\psi = \psi' + 180^\circ$ ). The procedure used to obtain  $\psi'$  present when applying TDLS with WM are reported in [20, 43], a description of the process is given in this section.

The process for obtaining  $\psi'$  is incorporated into the PD method. Recalling from section 3.3, when using the PD method the RAM components are aligned to the X measurement axis and nulled on the Y measurement axis. There is a projection of the IM/WM signal also on the X axis. The Y measurement axis contains the projection of the IM/WM signal isolated from the RAM components. These signals are represented on a phasor diagram in Figure 4.18.

The phasor diagram in Figure 4.18 can be manipulated to show a right angled triangle, basic trigonometry can then be applied to obtain  $\psi'$ .

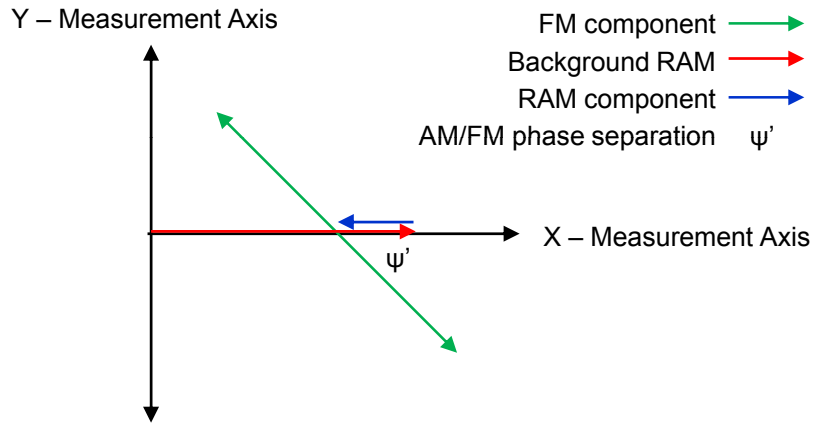


Figure 4.18: Phasor representation of the PD method

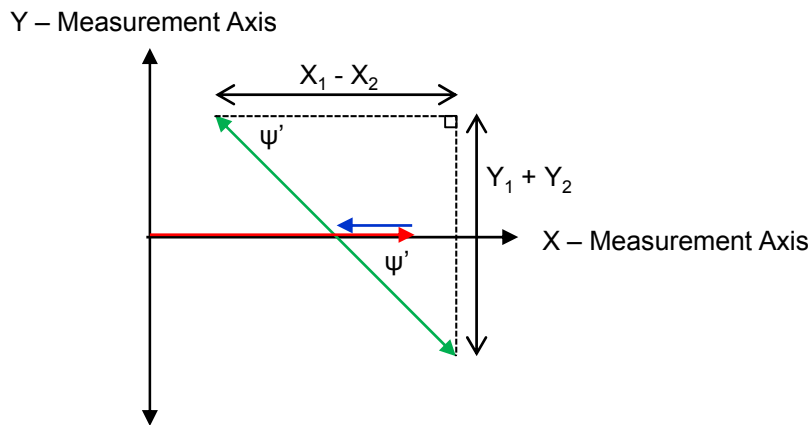


Figure 4.19: Revised - Phasor representation of the PD method

The maximum ( $Y_2$ ) and minimum ( $Y_1$ ) are obtained from the output of CH2 of the LIA, similarly the maximum ( $X_2$ ) and minimum ( $X_1$ ) from the output of CH1 of the LIA are obtained. With reference to Figure 4.19 the obtained values for  $Y_2$ ,  $Y_1$ ,  $X_2$  and  $X_1$  can be used to calculate  $\psi'$  by applying the following expression:

$$\psi' = \tan^{-1} \frac{|Y_2| + |Y_1|}{|X_1| - |X_2|} \quad (4.9)$$

The sinusoid modulation frequency was varied from 10kHz to 1.1MHz and the above procedure was used to calculate the variation in  $\psi'$ , shown in Figure 4.20. A phasor diagram is used to represent the variation in  $\psi'$ , given in Figure 4.21. As can be seen,  $\psi'$  approaches the  $90^\circ$  separation point, the RAM and WM signals

are isolated from each other on the X and Y measurement axis respectively as the modulation frequency approaches 1.1MHz. The increase in phase lag of  $\psi'$  as the modulation frequency is increased, is a result of the carrier effect becoming dominant over thermal effects.

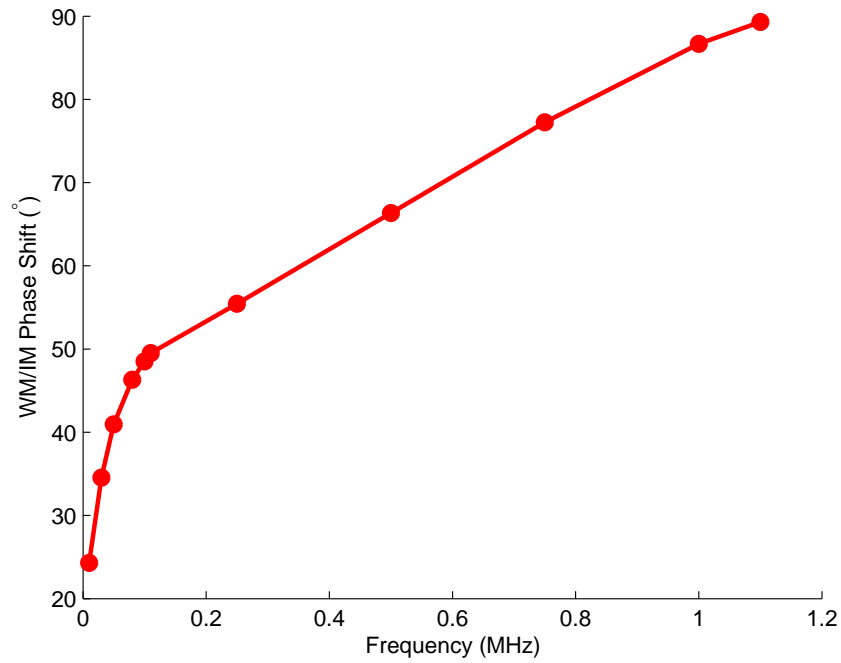


Figure 4.20: Result of the magnitude of  $\psi'$  against modulation frequency

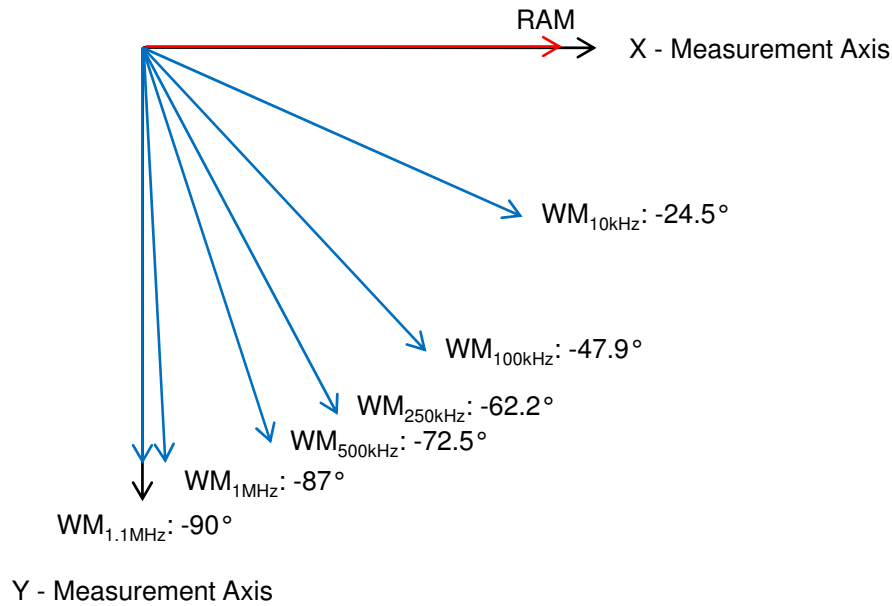


Figure 4.21: Illustration of the variation of  $\psi'$  with modulation frequency - the RAM signal is aligned with the X measurement axis

## 4.6 Summary

This chapter has introduced the various components that make up the experimental system used to perform RAM nulling and the amplitude investigation. The description of the system was split into three main sections: laser and drive electronics, delay fibre and gas cell and receiver electronics. Issues regarding minimising noise of the system were addressed through the use of polarization controllers. A range of procedures were documented, which allowed the following laser/system parameters to be characterised:  $m$ , resonator FSR,  $\xi$ ,  $\Delta V$ ,  $\delta i$ ,  $\kappa$  and  $\psi'$ . These parameters were necessary to identify correctly the operating conditions of the DFB laser.

# Chapter 5

## Validation of RAM Nulling for 1<sup>st</sup> Harmonic TDLS with RAM

---

### 5.1 Overview

This chapter presents experimental results that validate the RAM nulling technique along with the proposed correction factor implementation. The results are split into two main sections: RAM technique with RAM nulling and PD method with RAM nulling. Within each section the results are further divided by gas concentration: 10.13%CH<sub>4</sub> and 1.02%CH<sub>4</sub> in OFN (gas provided and certified by BOC Ltd.); for each concentration gas measurements at  $m = 0.2, 0.5, 1, 1.5$  and  $2$  are given. As a measure of accuracy the associated error in measured concentration and pressure extracted from the recovered absolute gas absorption line shape compared to the certified gas concentration and pressure as measured by the LEO-2 digital pressure gauge are presented.

Before the RAM nulling results are presented, a typical result using TDLS with direct detection is given by Figure 5.1. This shows the recorded signals from the oscilloscope with the delay branch disconnected and only the ramp modulation applied to the laser current. As mentioned in chapter 1 it can easily be seen from Figure 5.1 that to recover the absolute gas absorption line shape the gas

measurement is normalised to the no gas measurement. The normalisation process could also be carried out by taking a polynomial fit to the off line points of the gas signal. A theoretical line shape generated from HITRAN 2004 data was curve fitted by varying the concentration and pressure, until a best fit to the normalised experimental line shape was found in terms of least squares. The resulting values for concentration and pressure were then used as the experimentally determined gas parameters. Figure 5.2 shows the recovered absolute gas absorption line shape for 10.13% methane in nitrogen at a pressure of 0.995 bar as measured by the digital pressure gauge. The experimentally determined gas parameters from the curve fitting approach were 10.04%CH<sub>4</sub>:N<sub>2</sub> and 0.939Bar, thus giving errors of 0.93% and 5.61% respectively.

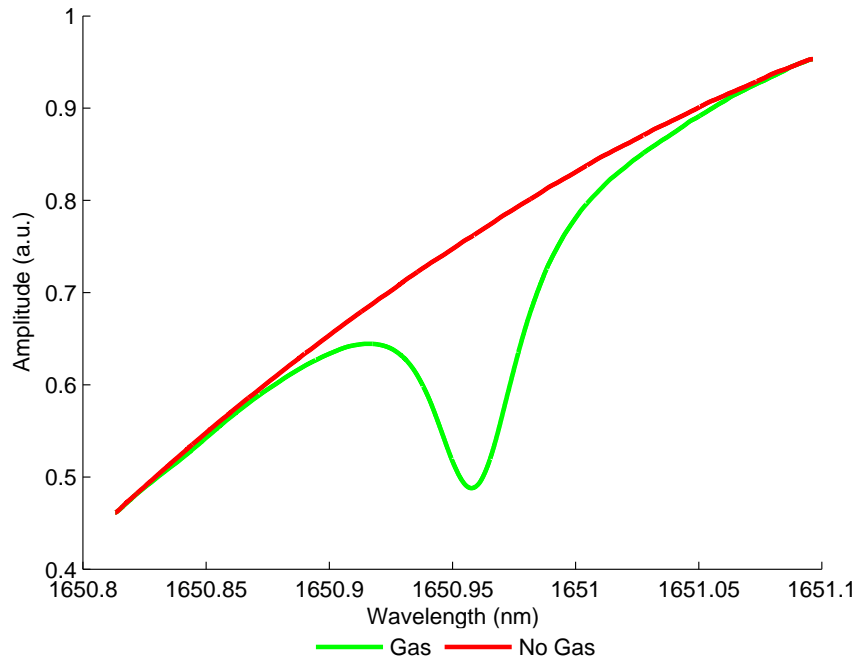


Figure 5.1: Raw measurements for TDLS with direct detection - 10.13%CH<sub>4</sub>:N<sub>2</sub>, 0.995Bar and 16.9°C

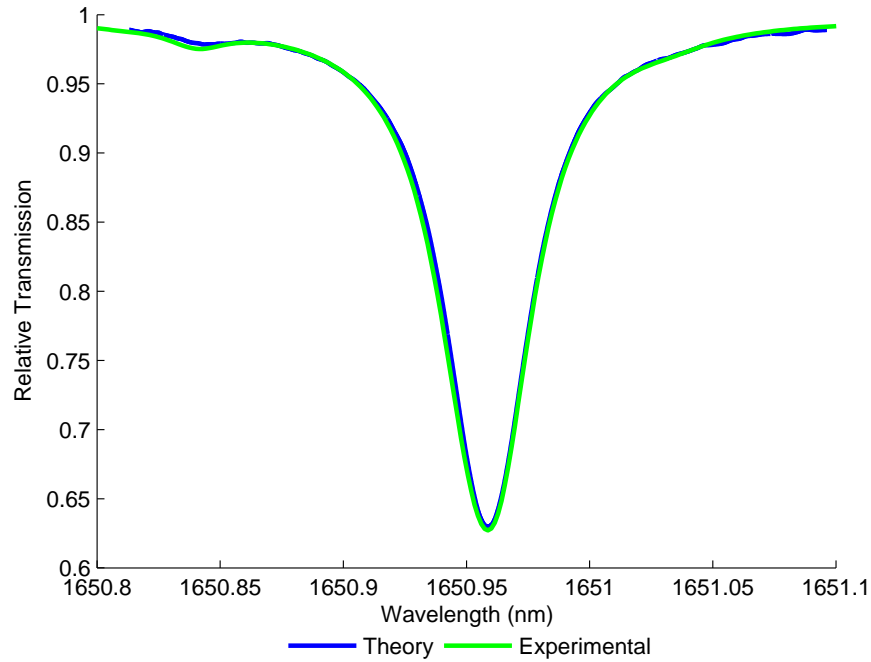


Figure 5.2: Recovered absolute gas absorption line shape using TDLS with direct detection - 10.13%CH<sub>4</sub>:N<sub>2</sub>, 0.995Bar and 16.9°C

## 5.2 RAM Technique with RAM Nulling

### 5.2.1 Overview

The presence of background RAM determines the dynamic range of the LIA, thereby limiting the resolution in recovery of the small gas absorption signal contained therein. The low amplitude resolution in turn places an instrument limit on the sensitivity of the system. To improve measurement sensitivity the high background must be suppressed and a novel optical approach has been developed that successfully achieves this. The following sections go through the analytical approach to show how the RAM background can be removed successfully prior to the receiver electronics.

## 5.2.2 Revised Analytical Methodology

The presented analysis makes reference to a simplified experimental system schematic, shown in Figure 5.3 (the full system schematic is given by Figure 4.1 on page 57). The method is to split the modulated laser output power into two branches, one through the gas cell and the other through a fibre reel, and recombine them before the photodiode detector. To null the background two conditions have to be met: the signals must be equal in intensity and be in anti-phase when they are recombined. The sinusoidal modulation frequency / fibre reel length was chosen to ensure a  $\pi$  phase separation between the IM of the two components at the re-combiner, the procedure for specifying the fibre length was detailed in section 4.3.2. The intensity of the signals are balanced using a variable optical attenuator (VOA), which forms part of the delay branch (not shown in Figure 5.3).

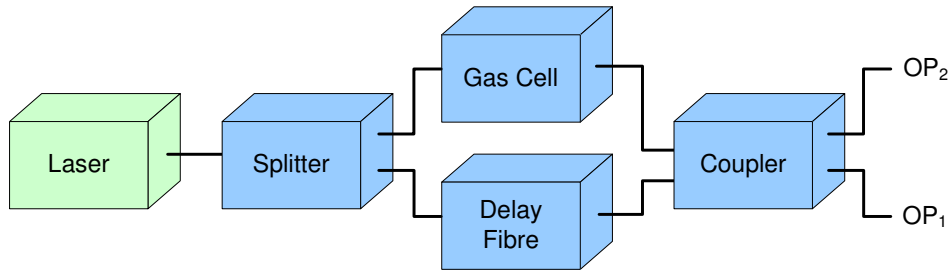


Figure 5.3: Simplified schematic of RAM Nulling implementation

The laser signal on the gas branch is given by a slightly modified version of equation (3.2):

$$I_1 = I_1(\lambda_c) + \Delta I_1(\lambda_c) \cos(\omega t) \quad (5.1)$$

The laser intensity on the delay branch is given by:

$$\begin{aligned} I_2 &= I_2(\lambda_c) + \Delta I_2(\lambda_c) \cos(\omega t - \pi) \\ &= I_2(\lambda_c) - \Delta I_2(\lambda_c) \cos(\omega t) \end{aligned} \quad (5.2)$$

where the  $\pi$  phase difference is the result of the fibre reel. Firstly, in the absence of gas in the cell or off-line in the presence of gas, the output at OP<sub>1</sub> (Figure 5.3), can be written as the combination of equations (5.1) and (5.2) (the DC terms are

neglected as they are rejected by the LIA):

$$\begin{aligned} OP_{1 (no\ gas)} &= \Delta I_1(\lambda_c)\cos(\omega t) - \Delta I_2(\lambda_c)\cos(\omega t) \\ &= [\Delta I_1(\lambda_c) - \Delta I_2(\lambda_c)]\cos(\omega t) \end{aligned} \quad (5.3)$$

where,  $I_1(\lambda_c)$  and  $I_2(\lambda_c)$  are the individual contributions from the gas branch and delay branch respectively and include the different wavelength dependencies of the different paths through the couplers. The VOA is adjusted to balance the intensity levels at a particular frequency and are approximately equal over the entire wavelength range of an interrogated gas line, giving a near zero background signal. Secondly, in the presence of gas in the cell, the output at  $OP_1$  is given by:

$$\begin{aligned} OP_{1 (gas)} &= \Delta I_1(\lambda_c)\cos(\omega t)[1 - \alpha(\lambda_c)Cl] - \Delta I_2(\lambda_c)\cos(\omega t) \\ &\quad - \Delta I_1(\lambda_c)\alpha'(\lambda_c)Cl\delta\lambda(\lambda_c)\cos(\omega t - \psi') \end{aligned} \quad (5.4)$$

Again, it can be seen that  $OP_{1(gas)}$  sits on a near-zero background, since, off-line or with no gas present, the term in the square brackets equals 1 and  $\Delta I_1(\lambda) \approx \Delta I_2(\lambda)$  over the scan range. If truly wavelength flattened couplers were used, then  $\Delta I_1(\lambda)$  could equal  $\Delta I_2(\lambda)$  over the scan and the background signal would be zero over the entire scan. In practice, it is not possible to completely remove all the wavelength dependences of the couplers and the recorded signals sit on a very small sloping background, passing through line centre,  $\lambda_c$ , at which the intensities from both branches are matched. However, this is not an issue as regards to dynamic range, resolution and sensitivity as the background slope is so small and, as detailed below, can be dealt with at the signal processing stage of the recorded signals. The analysis of the implementation of RAM nulling using the RAM technique and PD method are now given.

For the RAM technique with RAM nulling the detection phase of the LIA is such that the isolated IM/WM is aligned to the Y measurement axis of the LIA, resulting in a projection of the isolated RAM signal on the X measurement axis of the LIA. Figure 5.4 shows a revised phasor diagram showing the contribution from the delay branch.

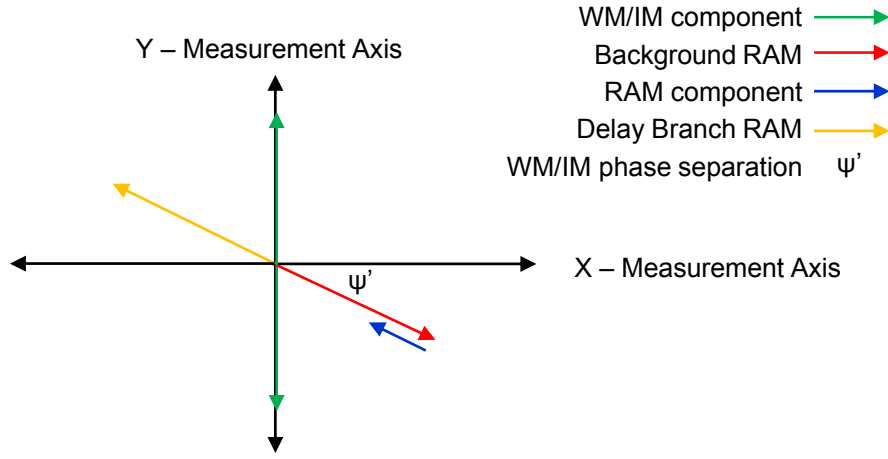


Figure 5.4: Phasor representation of the RAM technique with RAM nulling

The signal at the output of the LIA with the background RAM suppressed becomes:

$$OP_1 (gas) = \Delta I_1(\lambda_c)[1 - \alpha(\lambda_c)Cl] \sin \psi' - \Delta I_2(\lambda_c) \sin \psi' \quad (5.5)$$

$$OP_1 (no gas) = \Delta I_1(\lambda_c) \sin \psi' - \Delta I_2(\lambda_c) \sin \psi' \quad (5.6)$$

The expression given in equation (5.6) is recorded when there is no gas in the cell or can be obtained from a baseline fit to the recorded signal with gas in the cell. This expression is needed to remove the small sloping background present on the gas signal due to the wavelength dependences of the couplers. Using equations (5.5) and (5.6), the expression for the absolute gas absorption line shape is easily derived:

$$\frac{I_t}{I_o} = e^{-\alpha(\lambda)Cl} = 1 + \frac{OP_1 (gas) - OP_1 (no gas)}{\Delta I_1(\lambda_c)} \quad (5.7)$$

The denominator of equation (5.7) is simply the no gas output of the LIA with the delay branch disconnected from the coupler, i.e. the background RAM signal. As well as being crucial to recovering the gas absorption line shape, it also serves as a convenient normalisation factor that accounts for any changes in background laser intensity and the wavelength dependencies of the laser output. However, this term is not present at  $OP_1$  when the system is fully connected, because it is suppressed due to the RAM nulling. A method to normalise the signal from (5.7), which utilised the signal at the second arm of the fibre combiner,  $OP_2$ , is

used to find  $\Delta I_1(\lambda_c)$ :

$$\Delta I_1(\lambda_c) = OP_2 (no\ gas)K(\lambda_c) \quad (5.8)$$

where  $OP_2 (no\ gas)$  is the signal recorded at the second arm of the fibre combiner with no gas in the cell. The signal could equally be obtained by doing a curve fit to the recorded signal when gas is in the cell.  $K(\lambda_c)$  is a scaling factor that represents the behavior of the fibre combiner and needs only to be measured once. The factor is the ratio between  $OP_1 (no\ gas)$  measured with the delay branch disconnected to  $OP_2 (no\ gas)$  measured with the delay branch connected over the full wavelength range of a scan. Equations (5.7) and (5.8) form the basis of the RAM technique with RAM nulling.

### 5.2.3 Experimental Methodology

The result shown in Figure 5.2 can be used as a comparison with the results obtained using the RAM technique or the PD method, to show that similar accuracy can be achieved without the limitation of operating at DC. All recovered line shapes are compared to a theoretical Voigt line shape generated from the HITRAN 2004 database. Before the main results are shown for the RAM technique using RAM nulling, a number of results illustrating the successful suppression of the background RAM are shown.

Figure 5.5 shows the output of the photodiode receiver, with 10.13%CH<sub>4</sub>:N<sub>2</sub> at 0.998Bar and 18.2°C in the cell, with the delay line disconnected and both the ramp and sinusoidal modulation applied to the laser current. From inspection of Figure 5.5 the modulation of the laser current along with the superposition of the absorption signal can be clearly seen. Figure 5.6 now shows the output with the delay branch connected and the system optimised to achieve RAM nulling by adjustment of the sinusoid frequency to achieve anti-phase and IM balancing using the VOA between the two branches. By inspection of the off line points in Figure 5.6, it can be seen that the sinusoidal modulation has been suppressed by the RAM nulling. The resulting off line signal is processed by the LIA as DC, thus producing a zero background signal at the output of the LIA. The DC

level has doubled compared to Figure 5.5 due to the addition of the DC terms (Appendix B B.7) from both branches.

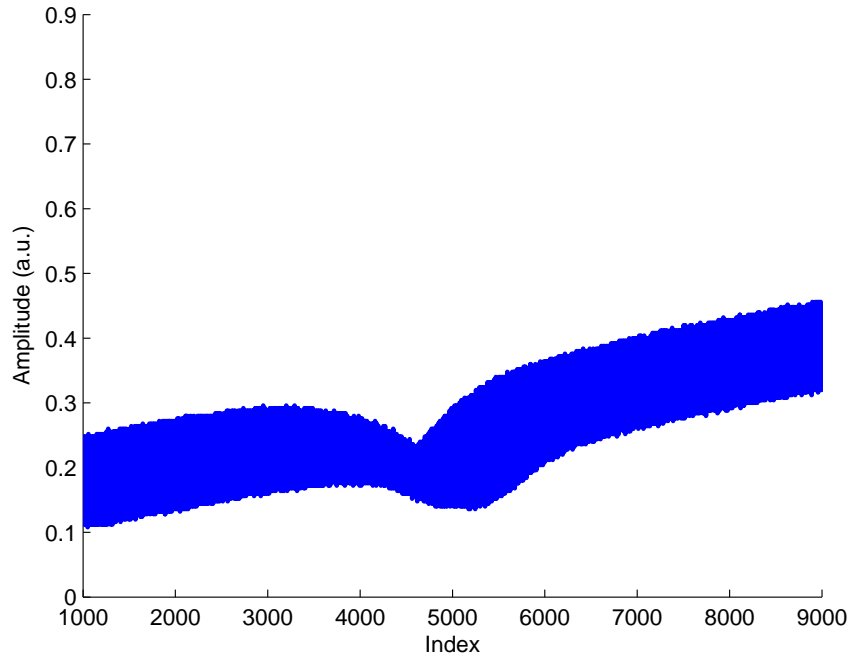


Figure 5.5: Recorded output from photodiode receiver - delay branch disconnected (10.13%CH<sub>4</sub>:N<sub>2</sub>, 0.998Bar and 18.2°C)

Another illustration of RAM nulling is shown by Figure 5.7. Here the output of the X measurement axis (CH1) is shown with and without the delay branch connected, the suppression of the background RAM can clearly be seen when the delay branch is connected and the system was optimised for RAM nulling. In this case the RAM technique has been applied and CH1 of the LIA is aligned to the RAM components isolated from the WM/IM signal.

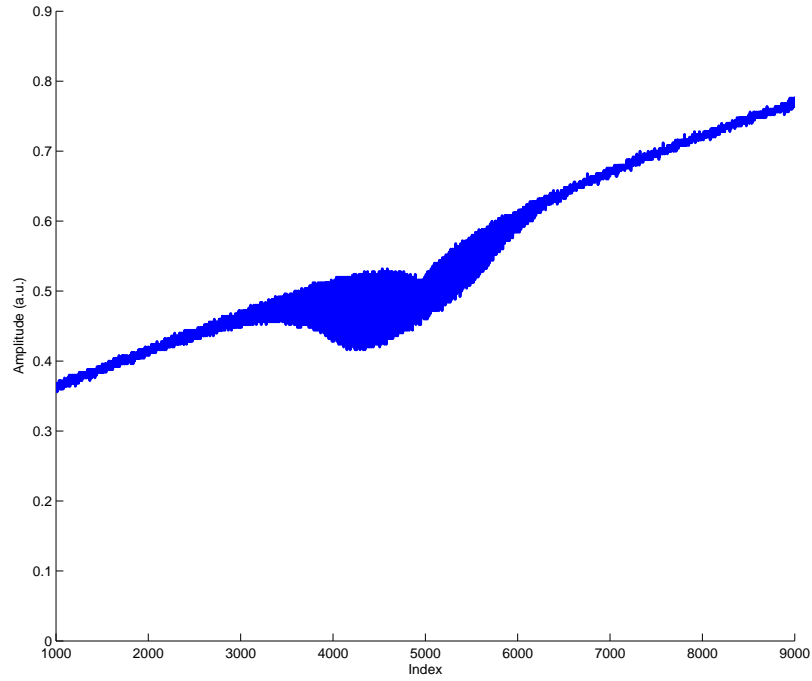


Figure 5.6: Recorded output from photodiode receiver - delay branch connected and system optimised for RAM nulling (10.13%CH<sub>4</sub>:N<sub>2</sub>, 0.998Bar and 18.2°C)

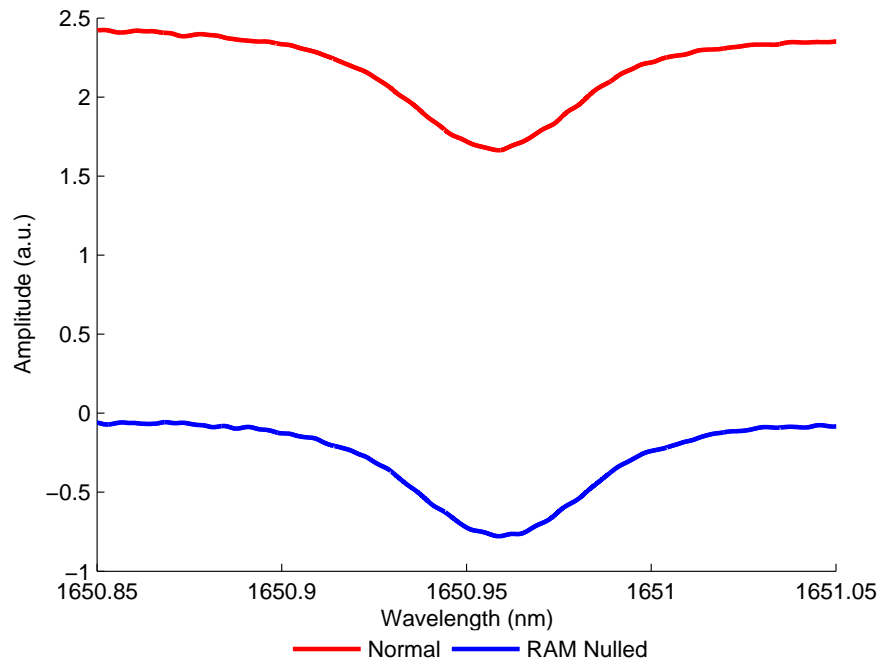


Figure 5.7: Recorded output from CH1 of the LIA - delay branch disconnected and connected (10.13%CH<sub>4</sub>:N<sub>2</sub>, 0.998Bar and 18.2°C)

The general procedure used to recover the absolute gas absorption line shape using the RAM technique with RAM nulling is documented below:

1. The gas cell was purged with OFN and then evacuated using the vacuum pump.
2. The gas cell was filled with the desired concentration of methane to atmospheric pressure.
3. With the delay branch disconnected and OP<sub>1</sub> of the re-combiner connected to the photodiode receiver, the LIA detection phase was adjusted so that the RAM components were isolated from the WM/IM component on CH1 of the LIA. The detection phase was set to minimise the RAM absorption depth relative to the off line points (no absorption), the procedure is documented fully in [21]. When the RAM absorption is minimised the interference from the WM/IM signal is minimised.
4. The delay branch was then connected and the sinusoid modulation frequency was adjusted to achieve anti-phase, with the specified delay fibre,  $f=101.28\text{kHz}$ . The VOA was then used to balance the IM between the two branches until the off line points of the LIA output were on a zero background. Finally, the PCs were adjusted to minimise any optical interference noise.
5. The output of CH1 of the LIA, which shows the RAM absorption on a zero background is recorded on the oscilloscope.
6. The cell was then purged with OFN and the signals from OP<sub>2</sub> and OP<sub>1</sub> with the delay branch connected and disconnected respectively were recorded.
7. The output of the fibre ring resonator was recorded so that it could be used for wavelength referencing.
8. The four recorded signals mentioned in the previous three steps were then used by the procedure documented in section 5.2.2 to recover the absolute gas absorption line shape, accomplished by a MATLAB program given

in Appendix C. The MATLAB program returns a result for the derived expression for the absolute gas absorption line shape given by equation 5.7:

$$\frac{I_t}{I_o} = e^{-\alpha(\lambda)Cl} = 1 + \frac{OP_1 (gas) - OP_1 (no gas)}{\Delta I_1(\lambda_c)}$$

### 5.2.4 10.13%CH<sub>4</sub>:N<sub>2</sub> Results

This section gives the results for the RAM technique with RAM nulling using 10.13%CH<sub>4</sub> in OFN. Each result shows the recovered gas absorption line shape as measured by the receiver equipment. However, as mentioned earlier, as the sinusoidal amplitude is increased, distortion terms are introduced to the recovered signals. Therefore, the second trace on each measurement is the corrected absolute gas absorption line shape using the correction factor implementation in section 3.5. The third and final trace is a theoretical absorption line shape generated from the HITRAN 2004 database. The results given by Figures 5.8 to 5.12 on pages 93–95 are for measurements made at  $m = 0.2, 0.5, 1, 1.5$  and  $2$  with 10.13%CH<sub>4</sub>:N<sub>2</sub> at 0.995Bar and 16.4°C in the cell. All measurements had the following key system parameters: ramp modulation of 5Hz at 300mV<sub>pk-pk</sub>;  $I_{LD}=80\text{mA}$  and  $T_{ACT}=6.591\text{k}\Omega$ . The LIA parameters are given in Table 5.1. For all measurements the LIA AC Gain and Time Constant were 6dB and 500 $\mu\text{s}$  respectively.

m	Sensitivity OP <sub>1</sub> Nulled	Sensitivity OP <sub>1</sub> Normal	Sensitivity. OP <sub>2</sub> Nulled	Detection Phase (°)	DR (dB) Nulled	DR (dB) Normal
0.2	1mV	5mV	500 $\mu\text{V}$	29.5	55	41
0.5	2mV	10mV	1mV	29	49	35
1	5mV	20mV	1mV	29	41	29
1.5	5mV	50mV	2mV	28.5	41	21
2	10mV	50mV	5mV	26.5	35	21

Table 5.1: LIA parameters for RAM technique with RAM nulling at 10.13%CH<sub>4</sub>:N<sub>2</sub>

Also shown in Table 5.1 is an increase in Dynamic Reserve (DR) of the LIA achieved using RAM nulling. DR is a measure of the LIA abilities to measure

accurately in the presence of interfering signals, usually expressed in dBs. For example, if the full scale sensitivity was 1 $\mu$ V and the DR was 40dB, this would mean that a input limit of 0.1mV could be tolerated without overloading the LIA. DR is given by the following expression:

$$DR = 20 \log_{10} \left( 0.7 \frac{Input\ Limit}{LIA\ Sensitivity} \right) \quad (5.9)$$

where  $20 \log_{10}$  converts DR to dBs, the 0.7 factor is a conversion from peak to r.m.s, the *Input Limit* is a function of the AC Gain, for 6dBs *Input Limit*=800mV and *LIA Sensitivity* is set by the user to increase the vertical resolution of the recovered signals without overloading the LIA output.

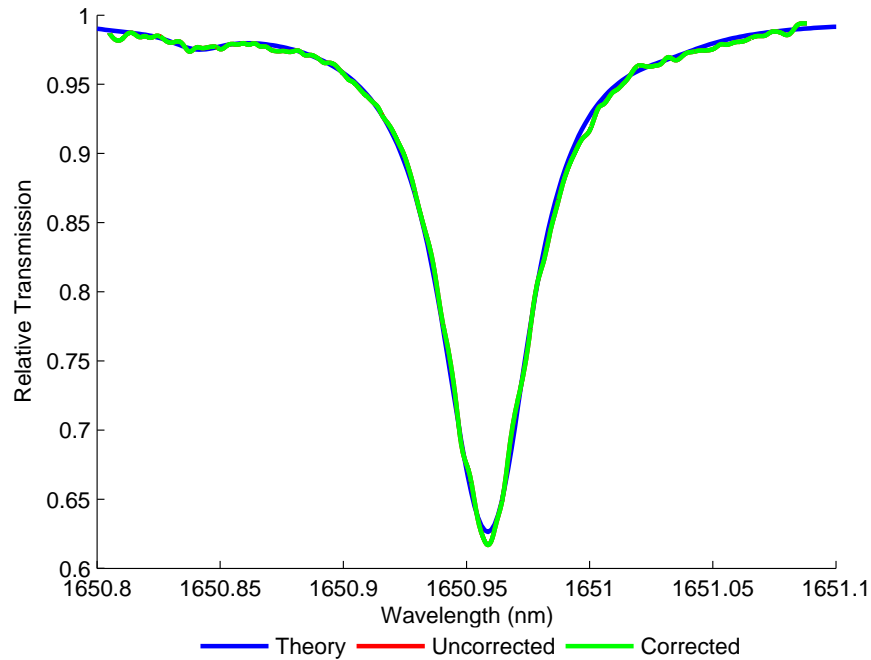


Figure 5.8: 10.13%CH<sub>4</sub>:N<sub>2</sub> at 0.995Bar and 16.4°C with m=0.2 - Recovered absolute gas absorption line shape compared to theory

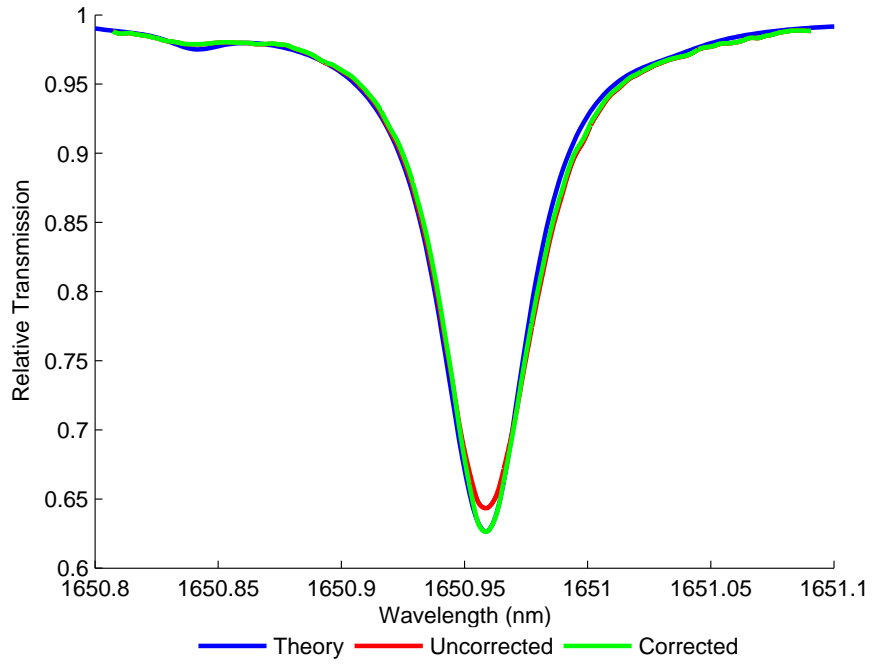


Figure 5.9: 10.13%CH<sub>4</sub>:N<sub>2</sub> at 0.995Bar and 16.4°C with m=0.5 - Recovered absolute gas absorption line shape compared to theory

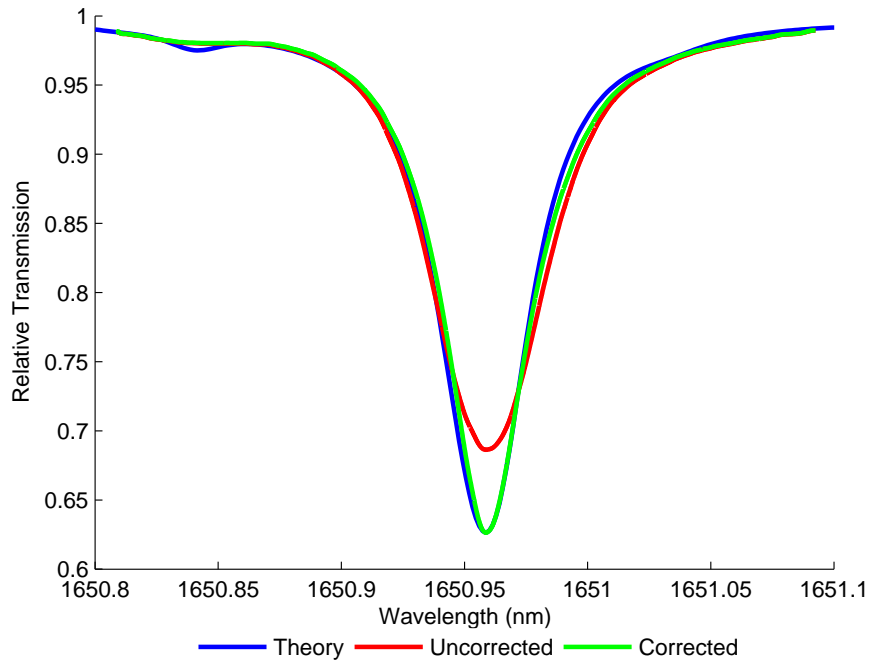


Figure 5.10: 10.13%CH<sub>4</sub>:N<sub>2</sub> at 0.995Bar and 16.4°C with m=1 - Recovered absolute gas absorption line shape compared to theory

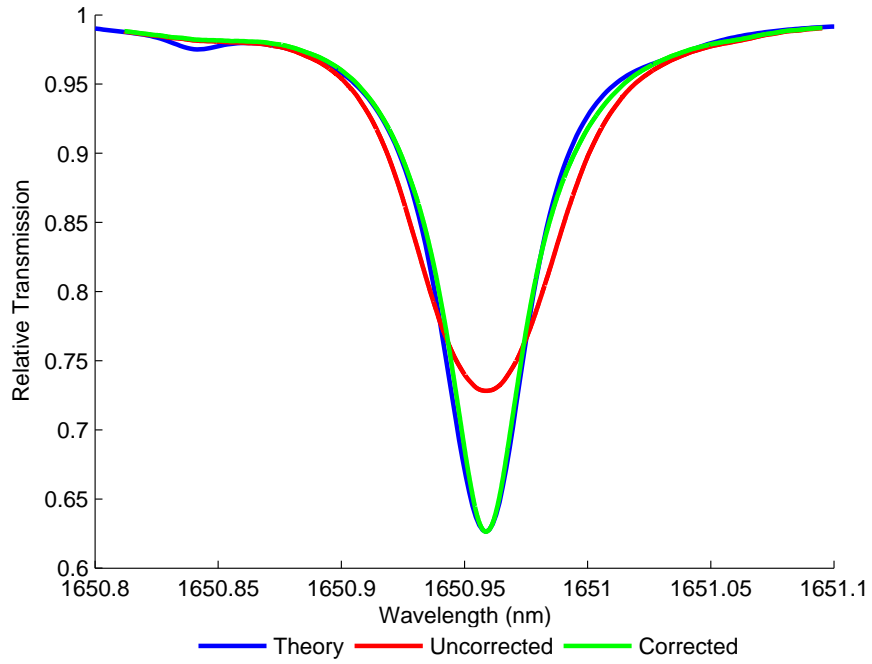


Figure 5.11: 10.13%CH<sub>4</sub>:N<sub>2</sub> at 0.995Bar and 16.4°C with m=1.5 - Recovered absolute gas absorption line shape compared to theory

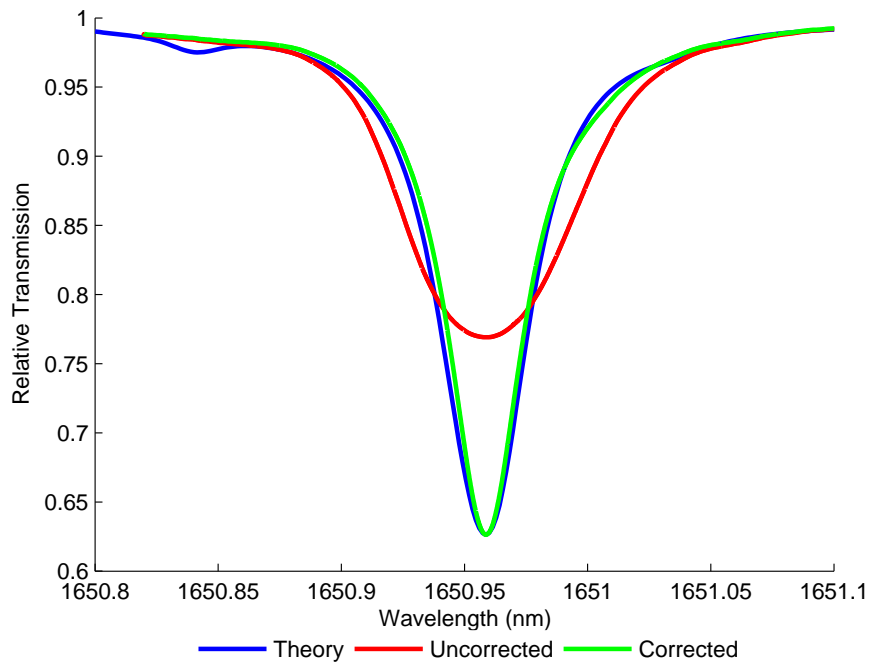


Figure 5.12: 10.13%CH<sub>4</sub>:N<sub>2</sub> at 0.995Bar and 16.4°C with m=2 - Recovered absolute gas absorption line shape compared to theory

### 5.2.5 Measurement of Concentration and Pressure

In this investigation curve fitting the theoretical line shape by varying the gas concentration and pressure to find a best fit to the experimentally recovered line shape, was carried out to determine the experimental gas parameters (concentration and pressure). Table 5.2 shows the known and recovered concentrations and pressures for the results given in Figures 5.8 to 5.12 on pages 93–95, for  $m$  values 0.2 to 2. Also given in the table are the associated errors in concentration and pressure values. It can be seen that the error in concentration is relatively low for all  $m$  values, whereas the errors in pressure are higher. The main source of error in the pressure is believed to be due to the correction factor. As the correction factor implementation is still under development, it is hoped that advances are made in the accurate recovery of the true width of the gas line shape, which determines the recovered pressure. Another observation from Table 5.1 that the RAM nulling approach has enabled the LIA sensitivity and DR to be improved significantly.

$m$	Known Conc. (%)	Recovered Conc. (%)	Conc. Error (%)	Known Pres. (Bar)	Recovered Pres. (Bar)	Pres. Error (%)
0.2	10.13	10.03	0.97	0.995	0.952	4.36
0.5	10.13	10.07	0.57	0.995	0.993	0.21
1	10.13	10.02	1.07	0.995	0.947	4.78
1.5	10.13	10.11	0.2	0.995	0.902	9.35
2	10.13	10	1.29	0.995	0.894	10.18

Table 5.2: Calculated errors in concentration and pressure using RAM technique with RAM nulling at 10.13%CH<sub>4</sub>:N<sub>2</sub>

### 5.2.6 1.02%CH<sub>4</sub>:N<sub>2</sub> Results

This section gives the results for the RAM technique with RAM nulling using 1.02%CH<sub>4</sub> in OFN. Each result shows the recovered gas absorption line shape as measured by the receiver equipment. However, as mentioned earlier, the second trace on each measurement is the corrected absolute gas absorption line shape using the correction factor implementation mentioned in section 3.5. The third and final trace is a theoretical absorption line shape generated from the HITRAN 2004 database.

The results given by Figures 5.13 to 5.17 on pages 98–100 are for measurements made at  $m = 0.2, 0.5, 1, 1.5$  and 2 with 1.02%CH<sub>4</sub>:N<sub>2</sub> at 0.994Bar and 16.7°C in the cell. All measurements had the following key system parameters: ramp modulation of 5Hz at 300mV<sub>pk-pk</sub>; I<sub>LD</sub>=80mA and T<sub>ACT</sub>=6.591kΩ. The LIA parameters are given in Table 5.3, for all measurements the LIA AC Gain and Time Constant were 6dB and 500μs respectively. Also shown in Table 5.3 is the increase in Dynamic Reserve (DR) of the LIA achieved using RAM nulling.

m	Sensitivity OP <sub>1</sub> Nulled	Sensitivity OP <sub>1</sub> Normal	Sensitivity. OP <sub>2</sub> Nulled	Detection Phase (°)	DR (dB) Nulled	DR (dB) Normal
0.2	200μV	5mV	200μV	29.5	69	41
0.5	500μV	10mV	500μV	29.5	61	35
1	500μV	20mV	2mV	27	61	29
1.5	1mV	20mV	2mV	26.5	55	29
2	1mV	50mV	5mV	25	55	21

Table 5.3: LIA parameters for RAM technique with RAM nulling at 1.02%CH<sub>4</sub>:N<sub>2</sub>

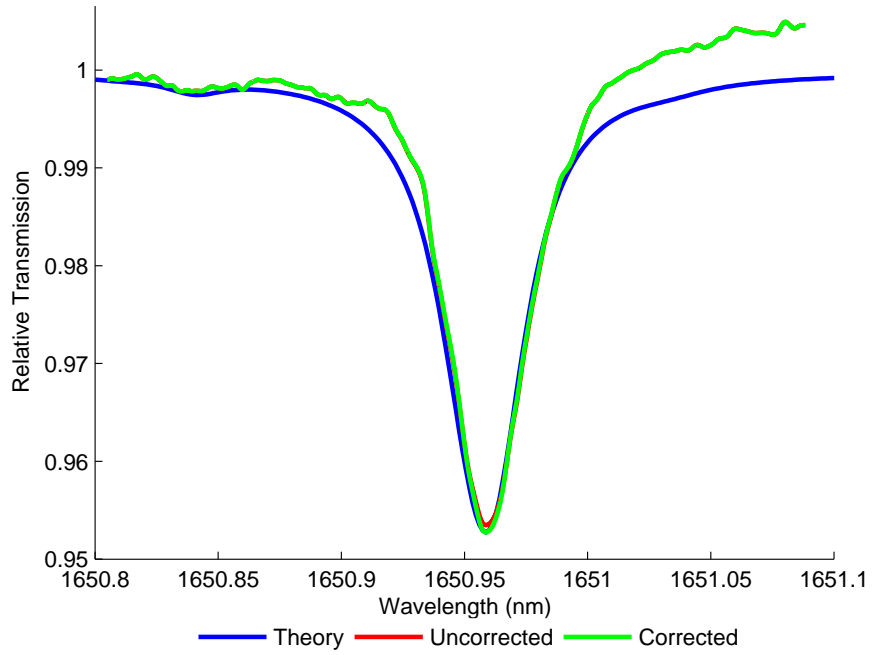


Figure 5.13: 1.02%CH<sub>4</sub>:N<sub>2</sub> at 0.994Bar and 16.7°C with m=0.2 - Recovered absolute gas absorption line shape compared to theory

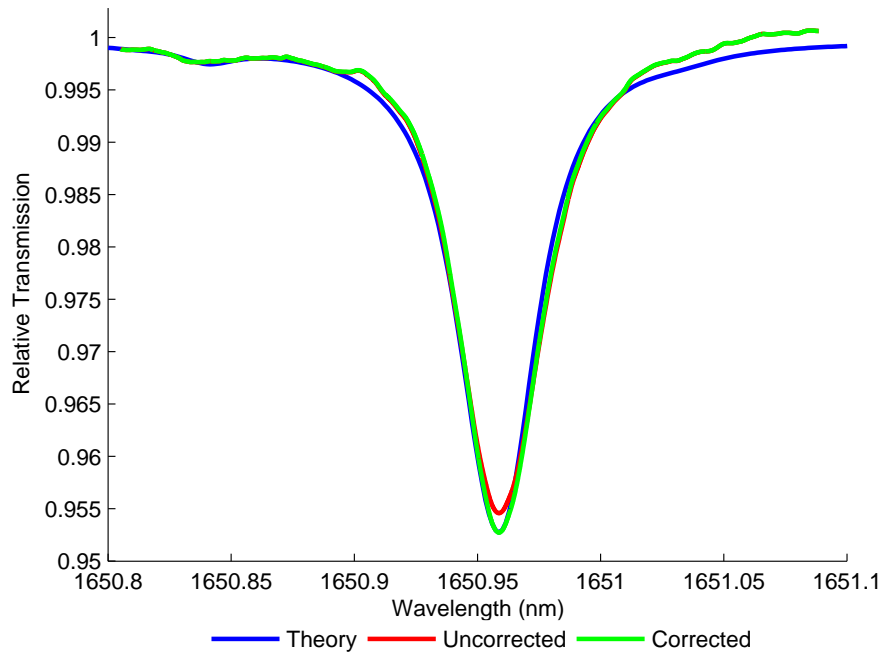


Figure 5.14: 1.02%CH<sub>4</sub>:N<sub>2</sub> at 0.994Bar and 16.7°C with m=0.5 - Recovered absolute gas absorption line shape compared to theory

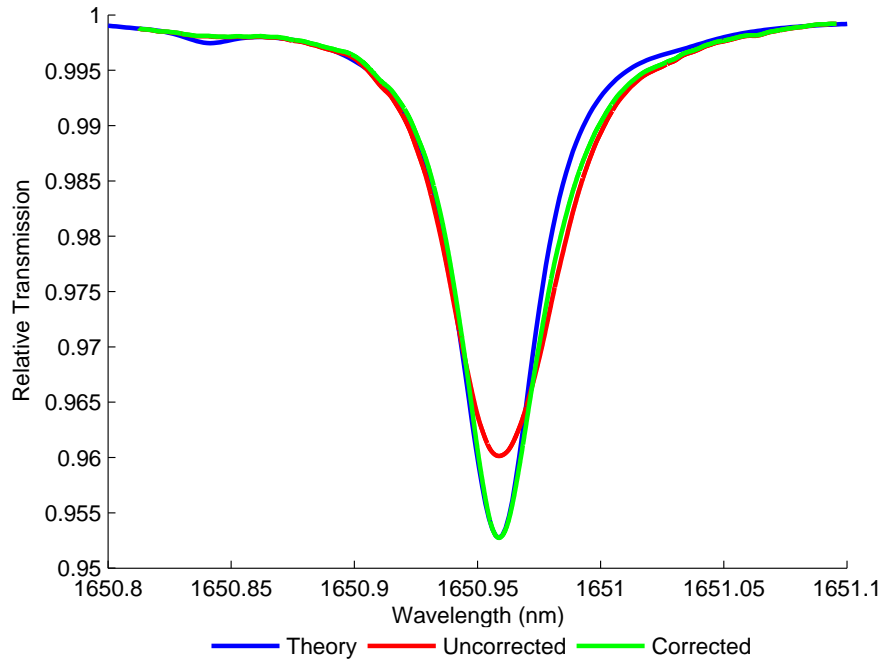


Figure 5.15: 1.02%CH<sub>4</sub>:N<sub>2</sub> at 0.994Bar and 16.7°C with m=1 - Recovered absolute gas absorption line shape compared to theory

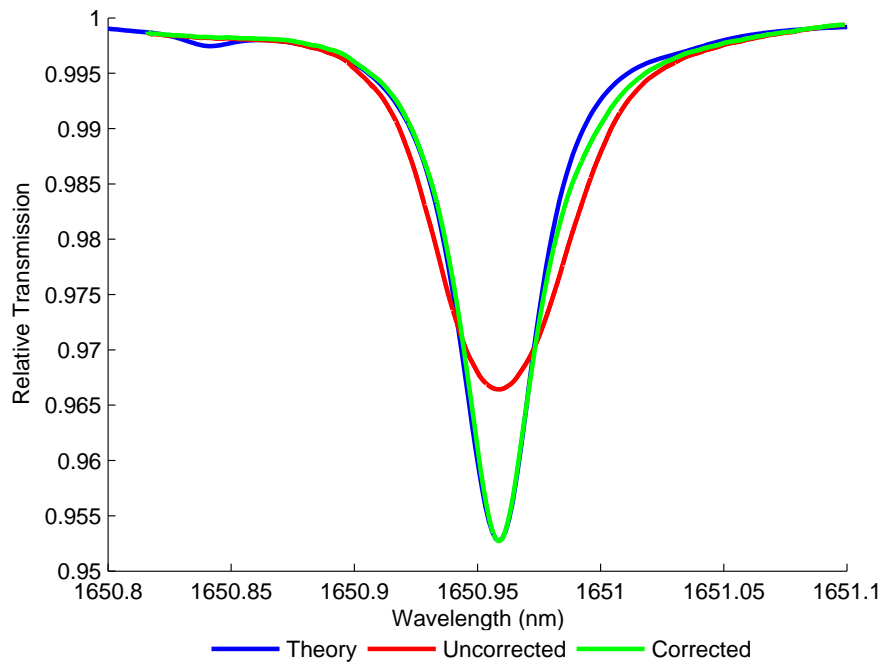


Figure 5.16: 1.02%CH<sub>4</sub>:N<sub>2</sub> at 0.994Bar and 16.7°C with m=1.5 - Recovered absolute gas absorption line shape compared to theory

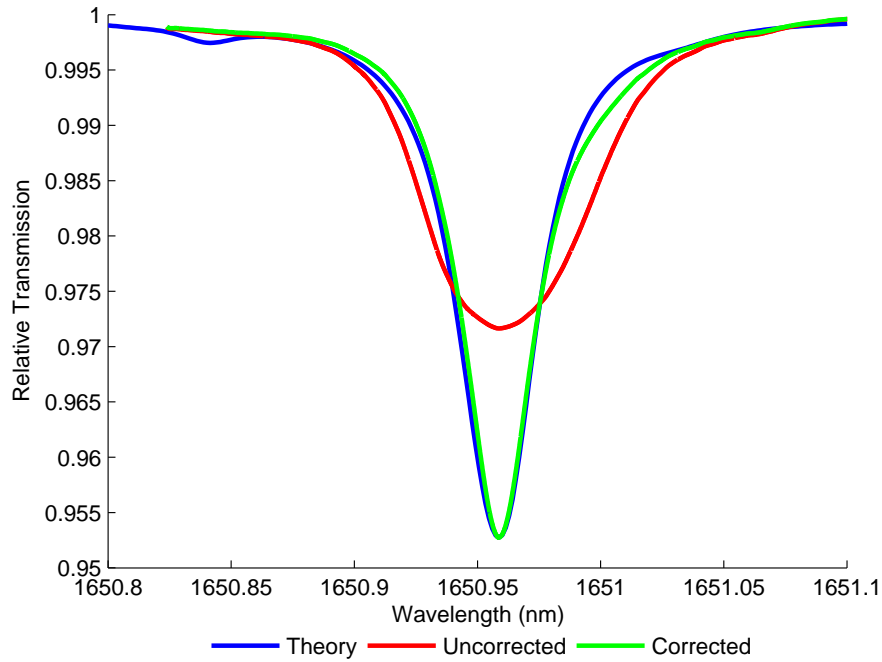


Figure 5.17: 1.02%CH<sub>4</sub>:N<sub>2</sub> at 0.994Bar and 16.7°C with  $m=2$  - Recovered absolute gas absorption line shape compared to theory

### 5.2.7 Measurement of Concentration and Pressure

The curve fitting procedure to extract measured values for concentration and pressure were applied to the experimental absolute gas absorption line shapes in Figures 5.13 to 5.17 on pages 98–100 for  $m$  values 0.2 to 2. Table 5.4 shows the known and recovered concentrations and pressures for the results along with their associated error. It can be seen again that the error in concentration is relatively low for all  $m$  values, whereas the errors in pressure are higher. Again, the main source of error in the pressure is believed to be due to the correction factor. Table 5.4 again illustrates the improvement in LIA sensitivity and DR.

m	Known Conc. (%)	Recovered Conc. (%)	Conc. Error (%)	Known Pres. (Bar)	Recovered Pres. (Bar)	Pres. Error (%)
0.2	1.02	1.017	0.3	0.994	0.942	5.2
0.5	1.02	1.013	0.7	0.994	0.926	6.87
1	1.02	1.01	1.02	0.994	0.922	7.28
1.5	1.02	1.015	0.5	0.994	0.984	1.04
2	1.02	1.018	0.15	0.994	0.926	6.87

Table 5.4: Calculated errors in concentration and pressure using RAM technique with RAM nulling at 1.02%CH<sub>4</sub>:N<sub>2</sub>

## 5.2.8 Summary of Results

For both concentrations, 10.13% and 1.02%, and all  $m$  values used, the gas absorption line shapes, generated by applying the newly formalised correction factors on the directly recovered RAM signals, closely match the theoretical Voigt line shapes generated from HITRAN data (see Figures 5.8 to 5.12 on pages 93–95 and Figures 5.13 to 5.17 on pages 98–100). In addition, the concentration extracted by curve fitting a Voigt profile (generated from HITRAN data), using concentration and pressure as parameters, agrees extremely well with the known certified concentration (see the low errors in Tables 5.2 and 5.4). Finally, in all measurements of the RAM signals with RAM nulling both the sensitivity and the dynamic reserve of the LIA were improved dramatically relative to the recovery of signals without nulling, the former by a factor in the range 10 to 50 and the latter by 14dB in all cases

As mentioned earlier, the RAM absorption component recovered by the LIA is attenuated by a factor of  $\sin\psi'$ , due to the component being a projection onto the measurement axis. To recover the full RAM absorption component on the LIA the laser has to be operating at the 90° separation point (i.e.  $\psi' = 90^\circ$ ). However, to accomplish this experimental investigations have found that laser modulation of 1.1MHz was required, which could be impractical due to bandwidth limitations

of receiver equipment. This leads onto the PD method, from which, through a decomposition process of the recovered signals from the LIA, the full RAM absorption is recovered. Results using the PD method with RAM nulling are given in the following section.

## 5.3 PD Method with RAM Nulling

### 5.3.1 Revised Analytical Methodology

For the PD method with RAM nulling, the LIA is set as described in section 3.3, with the WM/IM isolated from the RAM signals on the Y measurement axis and the RAM signal aligned in phase with the X measurement axis the recovery of the RAM signal is maximised at the X axis output and nulled on the Y axis output. Figure 5.18 shows a revised phasor diagram showing the contribution from the delay branch.

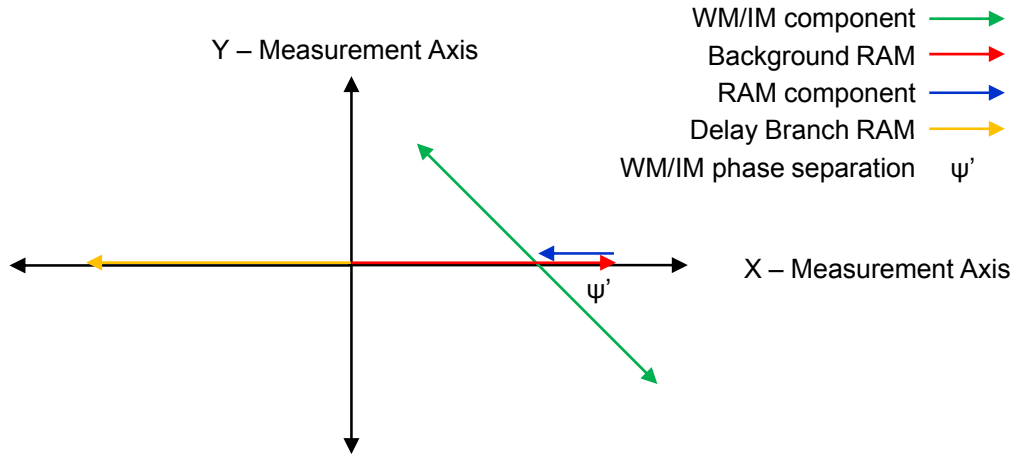


Figure 5.18: Phasor representation of the PD method with RAM nulling

Both X and Y channels of the LIA are recorded with gas in the cell and the relevant  $OP_1$  signals can be written as:

$$OP_{1x (gas)} = \Delta I_1(\lambda_c)[1 - \alpha(\lambda_c)Cl] - \Delta I_2(\lambda_c) - I_1(\lambda_c)\alpha'(\lambda_c)Cl\delta\lambda(\lambda_c)\cos\psi' \quad (5.10)$$

$$OP_{1y (gas)} = -I_1(\lambda_c)\alpha'(\lambda_c)Cl\delta\lambda(\lambda_c)\sin\psi' \quad (5.11)$$

$$OP_{1x (no\ gas)} = \Delta I_1(\lambda_c) - \Delta I_2(\lambda_c) \quad (5.12)$$

Again, the reason for recording  $OP_{1x (no\ gas)}$  is so it can be used in the signal processing to remove the small sloping background due to the wavelength dependencies of the couplers. Applying the PD method (3.12) to equations (5.10), (5.11) and (5.12) an expression for the absolute gas transmission function can easily be derived:

$$\frac{I_t}{I_o} = e^{-\alpha(\lambda)Cl} = 1 + \frac{OP_{1x (gas)} - OP_{1x (no\ gas)} - [OP_{1y (gas)}/\tan\psi']}{\Delta I_1(\lambda_c)} \quad (5.13)$$

The process to normalise the expression given by (5.13) is the same as in section 5.2, utilising the signal at the second output,  $OP_2$ , of the fibre combiner.

### 5.3.2 Experimental Methodology

This section gives a range of results using the PD method with RAM nulling to recover the corrected absolute gas absorption line shape. All recovered line shapes are compared to a theoretical line shape generated from the HITRAN 2004 database. Before the main results are shown, a number of results illustrating the successful suppression of the background RAM are shown. Figure 5.19 shows the output of CH1 (X measurement axis) of the LIA with and without the delay branch connected with 10.13%CH<sub>4</sub>:N<sub>2</sub> at 0.998Bar and 18.2°C in the cell. The signals contain the RAM components along with a projection of the WM/IM signal, the suppression of the background RAM can clearly be seen when the delay branch was connected and the system was optimised for RAM nulling. Figure 5.20 shows the output of CH2 (Y measurement axis) of the LIA with and without the delay branch connected. The output shows the isolated projection of the WM/IM signal. As this signal is isolated from the RAM, RAM nulling has no affect on it. The PD method has been applied by adjusting the detection phase of the LIA until the output of CH2 was on a zero background.

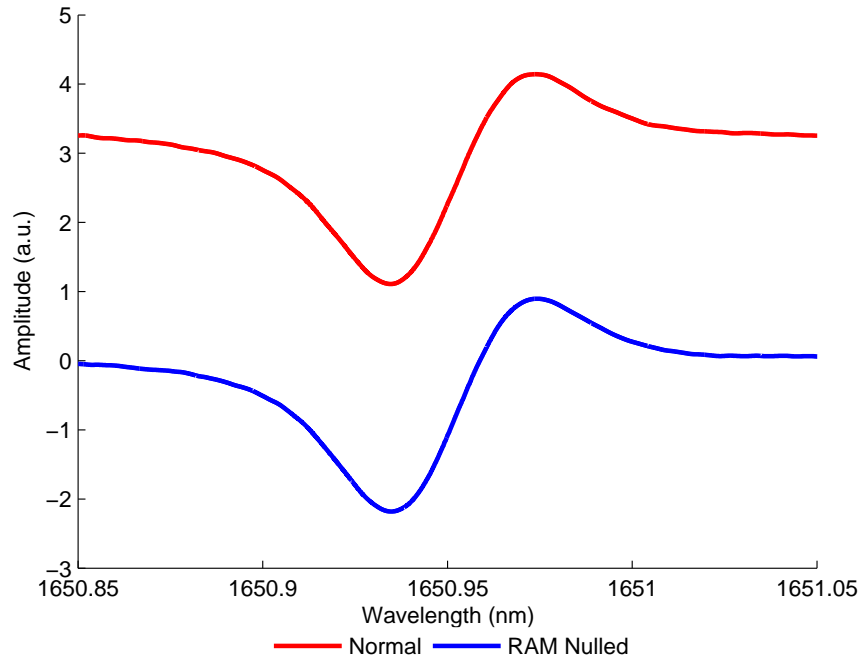


Figure 5.19: Recorded output from CH1 (X axis) of the LIA - delay branch disconnected and connected (10.13%CH<sub>4</sub>:N<sub>2</sub> at 0.998Bar and 18.2°C)

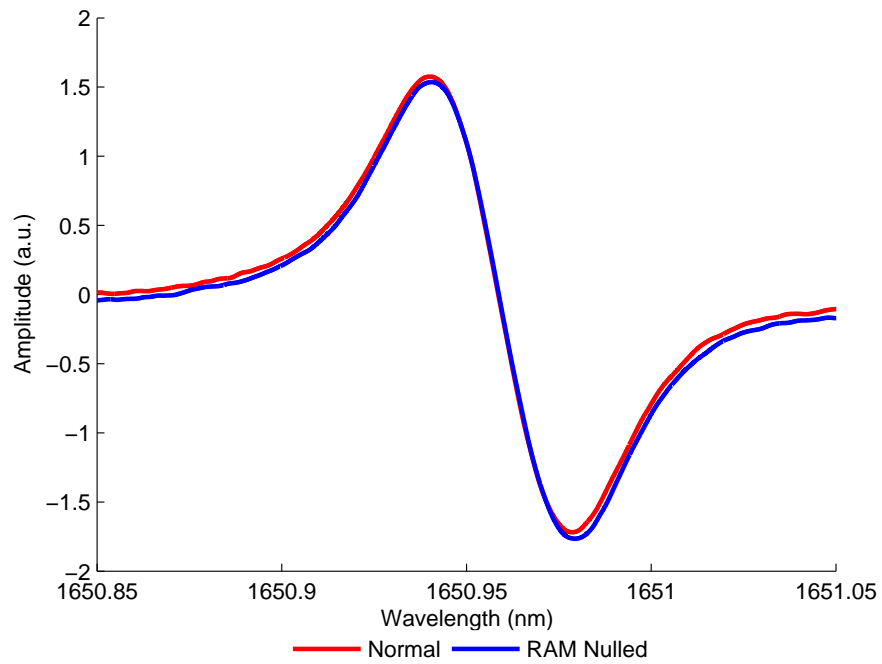


Figure 5.20: Recorded output from CH2 (Y axis) of the LIA - delay branch disconnected and connected (10.13%CH<sub>4</sub>:N<sub>2</sub> at 0.998Bar and 18.2°C)

The process for extracting the full 1<sup>st</sup> derivative signal is the same as described in section 3.3 (equation (3.13)). As expected the 1<sup>st</sup> derivative signal is unaffected by RAM nulling, due the phase separation,  $\psi'$ , between the WM/IM and RAM signals.

The general procedure used to recover the absolute gas absorption line shape using the PD method with RAM nulling is documented below:

1. The gas cell was purged with OFN and then evacuated using the vacuum pump.
2. The gas cell was filled with the desired concentration of methane to atmospheric pressure.
3. With the delay branch disconnected and OP<sub>1</sub> of the re-combiner connected to the photodiode receiver, the LIA detection phase was adjusted so that the output of CH2 of the LIA was on a zero background, isolated from the RAM components.
4. The delay branch was then connected and the sinusoid modulation frequency was adjusted to achieve anti-phase, with the specified delay fibre,  $f=101.28\text{kHz}$ . The VOA was then used to balance the IM between the two branches until the off line points of the CH1 output of the LIA was on a zero background. Finally, the PCs were adjusted to minimise optical interference noise.
5. The output of CH1 of the LIA, which shows the RAM absorption on a zero background with a projection of the WM/IM and the output of CH2 showing an isolated projection of the WM/IM signal are recorded on the oscilloscope.
6. The cell was then purged with OFN and the signals from OP<sub>2</sub> and OP<sub>1</sub> with the delay branch connected and disconnected respectively were recorded.
7. The output of the fibre ring resonator was recorded so that it could be used for wavelength referencing.

8. The recorded signals mentioned in the previous three steps were then used in the procedure documented in section 5.3 to recover the absolute gas absorption line shape, accomplished by a MATLAB program given in Appendix D. The MATLAB program returns a result for the derived expression for the absolute gas absorption line shape given by equation (5.13):

$$\frac{I_t}{I_o} = e^{-\alpha(\lambda)Cl} = 1 + \frac{OP_{1x} (gas) - OP_{1x} (no gas) - [OP_{1y} (gas)/\tan\psi]}{\Delta I_1(\lambda_c)}$$

### 5.3.3 10.13%CH<sub>4</sub>:N<sub>2</sub> Results

This section gives the results for the PD method with RAM nulling using 10.13%CH<sub>4</sub> in OFN. Each result shows the recovered absolute gas absorption line shape as measured by the receiver equipment. The second trace on each measurement is the corrected absolute gas absorption line shape using the correction factor mentioned in section 3.5. The third and final trace is a theoretical absorption line shape generated from the HITRAN 2004 database.

The results given by Figures 5.21 to 5.25 on pages 107–109 are for measurements made at  $m = 0.2, 0.5, 1, 1.5$  and  $2$  with 10.13%CH<sub>4</sub>:N<sub>2</sub> at 0.995Bar and 14.2°C in the cell. All measurements had the following key system parameters: ramp modulation of 5Hz and 300mV<sub>pk-pk</sub>; I<sub>LD</sub>=80mA and T<sub>ACT</sub>=6.591kΩ. The LIA parameters are given in Table 5.1, for all measurements the LIA AC Gain and Time Constant were 6dB and 500μs respectively. Also shown in Table 5.5 is the increase in Dynamic Reserve (DR) of the LIA achieved using RAM nulling.

m	Sensitivity OP <sub>1</sub> Nulled	Sensitivity OP <sub>1</sub> Normal	Sensitivity. OP <sub>2</sub> Nulled	Detection Phase (°)	DR (dB) Nulled	DR (dB) Normal
0.2	5mV	5mV	500μV	-13.6	41	41
0.5	10mV	20mV	2mV	-13.4	49	35
1	10mV	20mV	5mV	-13.4	41	29
1.5	20mV	50mV	5mV	-13.4	41	21
2	20mV	50mV	5mV	-13.6	35	21

Table 5.5: LIA parameters for PD method with RAM nulling at 10.13%CH<sub>4</sub>:N<sub>2</sub>

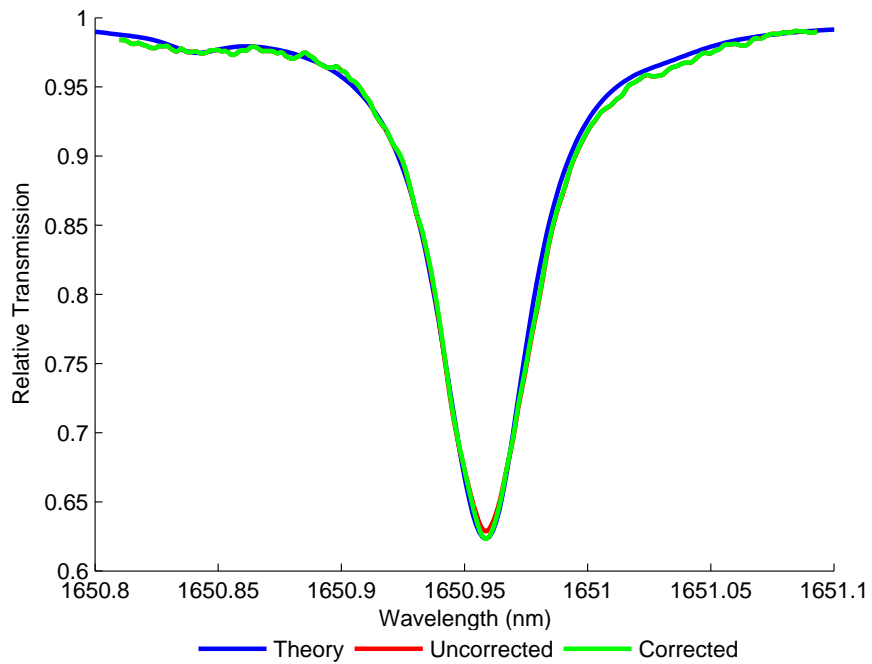


Figure 5.21: 10.13%CH<sub>4</sub>:N<sub>2</sub> at 0.995Bar and 14.2°C with m=0.2 - Recovered absolute gas absorption line shape compared to theory

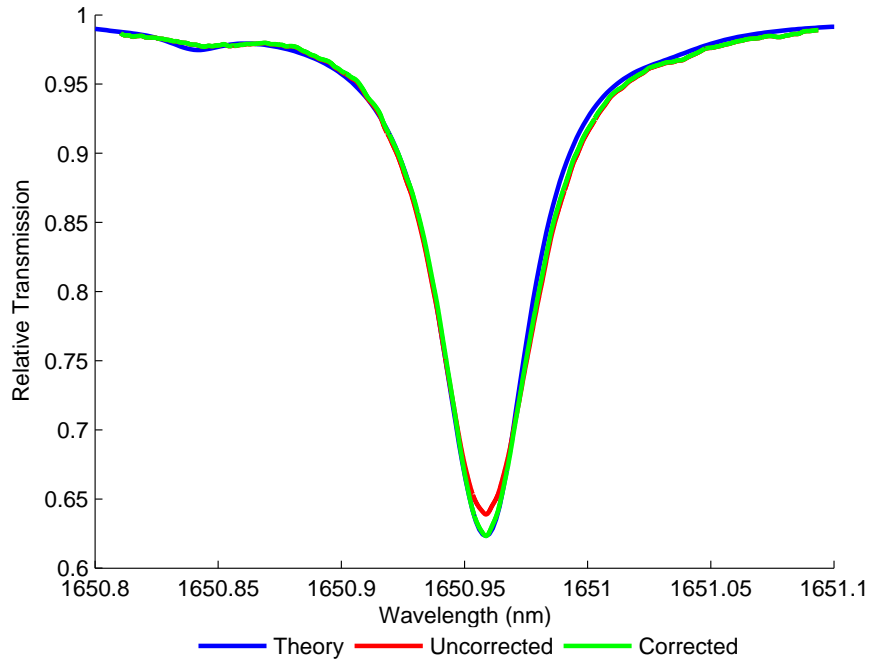


Figure 5.22: 10.13%CH<sub>4</sub>:N<sub>2</sub> at 0.995Bar and 14.2°C with m=0.5 - Recovered absolute gas absorption line shape compared to theory

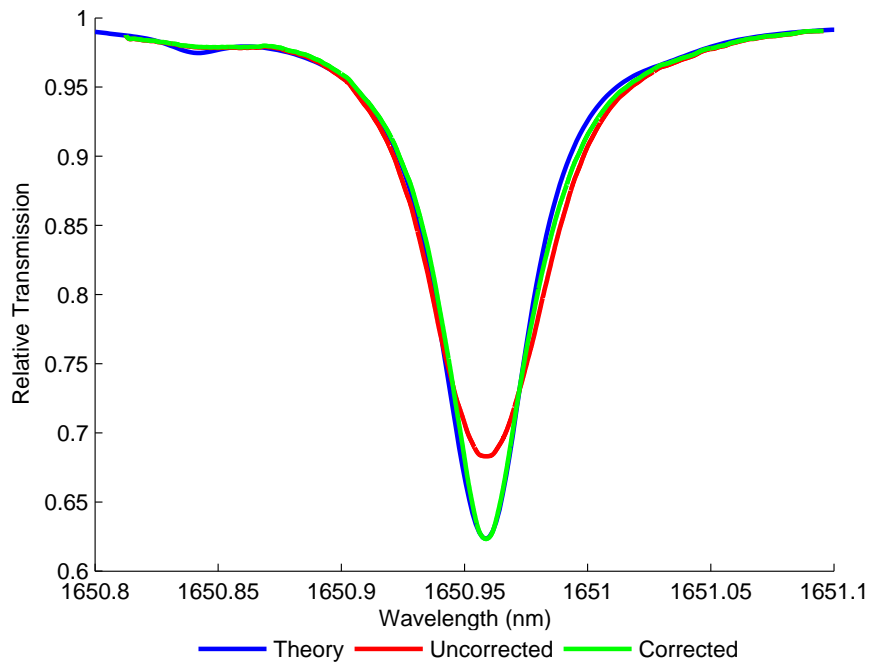


Figure 5.23: 10.13%CH<sub>4</sub>:N<sub>2</sub> at 0.995Bar and 14.2°C with m=1 - Recovered absolute gas absorption line shape compared to theory

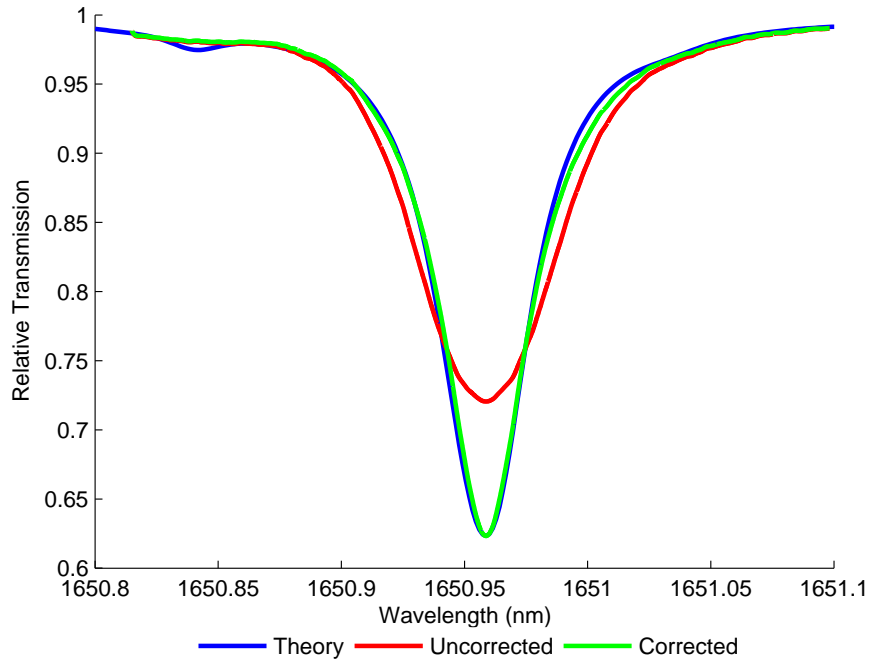


Figure 5.24: 10.13%CH<sub>4</sub>:N<sub>2</sub> at 0.995Bar and 14.2°C with m=1.5 - Recovered absolute gas absorption line shape compared to theory

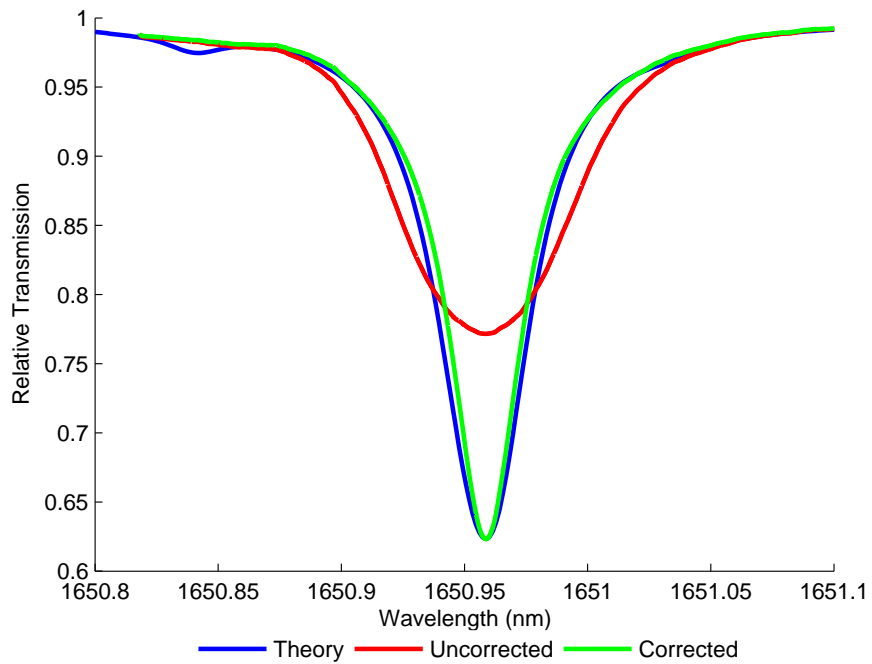


Figure 5.25: 10.13%CH<sub>4</sub>:N<sub>2</sub> at 0.995Bar and 14.2°C with m=2 - Recovered absolute gas absorption line shape compared to theory

### 5.3.4 Measurement of Concentration and Pressure

The curve fitting procedure was again used to extract the measured gas concentration and pressure from the corrected signals given in Figures 5.21 to 5.25 on pages 107–109. Table 5.6 shows the known and measured concentrations and pressures for  $m$  value range 0.2 to 2, along with their associated error. It can be seen that the error in concentration is relatively low for all  $m$  values, whereas before, the errors in pressure are higher. The main source of error in the pressure is believed to be due to the correction factor. As the correction factor implementation is still under development, it is hoped that advances are made in the accurate recover of the true width of the gas line shape, which determines the recovered pressure. Again, the increase in LIA sensitivity and DR is shown in Table 5.5.

$m$	Known Conc. (%)	Recovered Conc. (%)	Conc. Error (%)	Known Pres. (Bar)	Recovered Pres. (Bar)	Pres. Error (%)
0.2	10.13	9.95	1.74	0.995	0.923	7.27
0.5	10.13	10.05	0.79	0.995	0.947	4.78
1	10.13	10.06	0.7	0.995	0.952	4.36
1.5	10.13	10.05	0.79	0.995	0.956	3.95
2	10.13	9.77	3.55	0.995	0.894	10.18

Table 5.6: Calculated errors in concentration and pressure using PD method with RAM nulling at 10.13%CH<sub>4</sub>:N<sub>2</sub>

### 5.3.5 1.02%CH<sub>4</sub>:N<sub>2</sub> Results

This section gives the results for the PD method with RAM nulling using 1.02%CH<sub>4</sub> in OFN. Each result shows the recovered absolute gas absorption line shape as measured from the receiver equipment. The second trace on each measurement is the corrected absolute gas absorption line shape using the correction factor implementation in section 3.5. The third and final trace is a

theoretical absorption line shape generated from the HITRAN 2004 database.

The results given by Figures 5.26 to 5.30 on pages 112–114 are for measurements made at  $m = 0.2, 0.5, 1, 1.5$  and 2 with 1.02%CH<sub>4</sub>:N<sub>2</sub> at 0.995Bar and 15.5°C in the cell. All measurements had the following key system parameters: ramp modulation of 5Hz and 300mV<sub>*pk-pk*</sub>; I<sub>LD</sub>=80mA and T<sub>ACT</sub>=6.591kΩ. The LIA parameters are given in Table 5.7, for all measurements the LIA AC Gain and Time Constant were 6dB and 500μs respectively. Also shown in Table 5.7 is the increase in Dynamic Reserve (DR) of the LIA achieved using RAM nulling.

m	Sensitivity OP <sub>1</sub> Nulled	Sensitivity OP <sub>1</sub> Normal	Sensitivity. OP <sub>2</sub> Nulled	Detection Phase (°)	DR (dB) Nulled	DR (dB) Normal
0.2	500μV	5mV	500μV	-13.87	61	41
0.5	1mV	10mV	1mV	-13.87	55	35
1	2mV	20mV	2mV	-13.91	49	29
1.5	2mV	50mV	5mV	-13.91	49	21
2	2mV	50mV	5mV	-13.99	49	21

Table 5.7: LIA parameters for PD method with RAM nulling at 1.02%CH<sub>4</sub>:N<sub>2</sub>

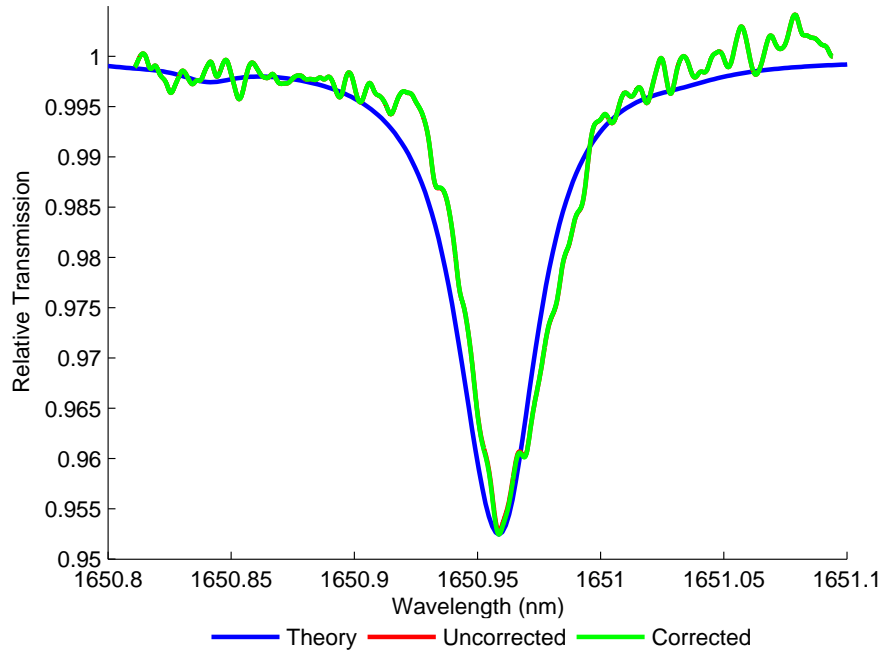


Figure 5.26: 1.02%CH<sub>4</sub>:N<sub>2</sub> at 0.995Bar and 15.5°C with m=0.2 - Recovered absolute gas absorption line shape compared to theory

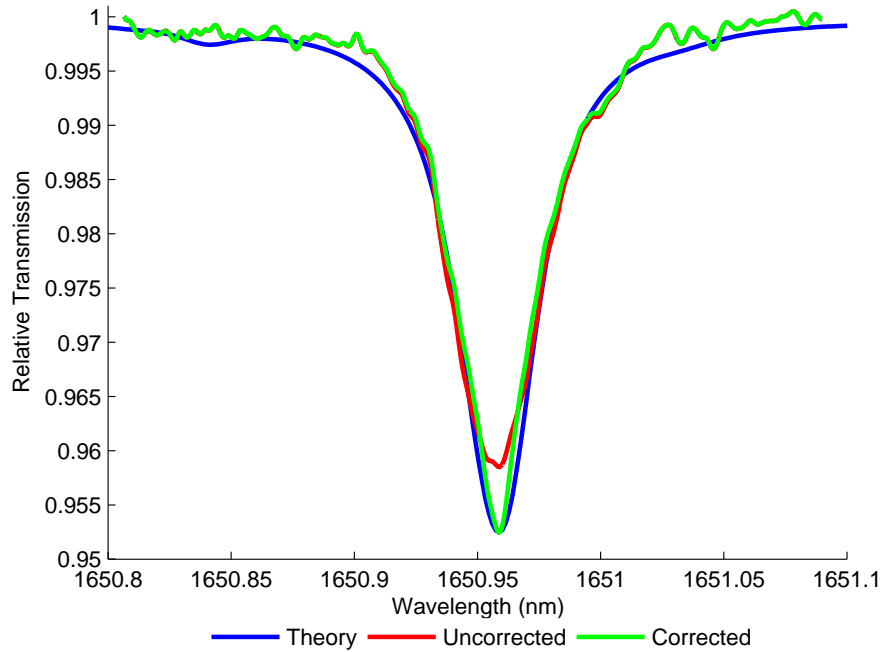


Figure 5.27: 1.02%CH<sub>4</sub>:N<sub>2</sub> at 0.995Bar and 15.5°C with m=0.5 - Recovered absolute gas absorption line shape compared to theory

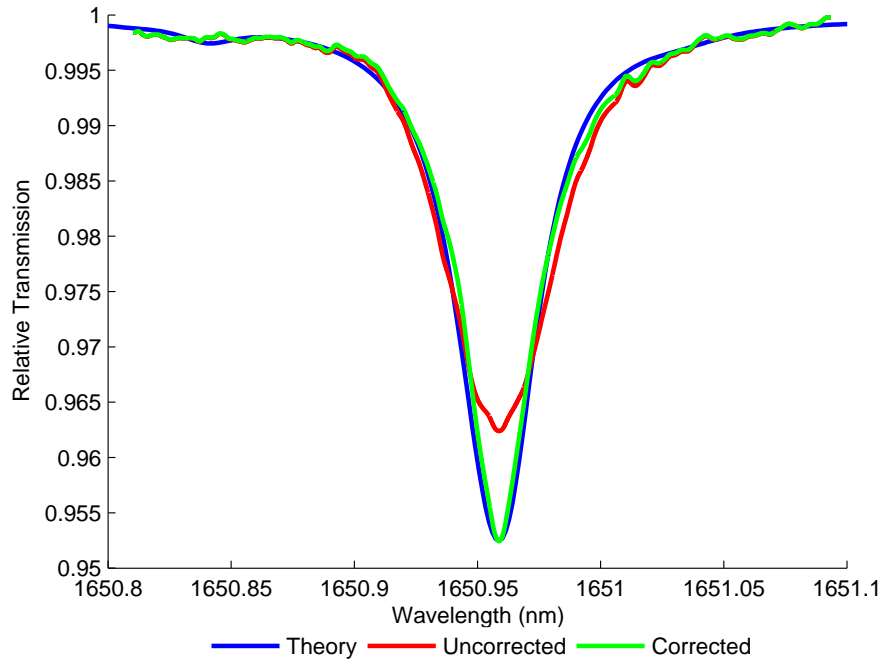


Figure 5.28: 1.02%CH<sub>4</sub>:N<sub>2</sub> at 0.995Bar and 15.5°C with m=1 - Recovered absolute gas absorption line shape compared to theory

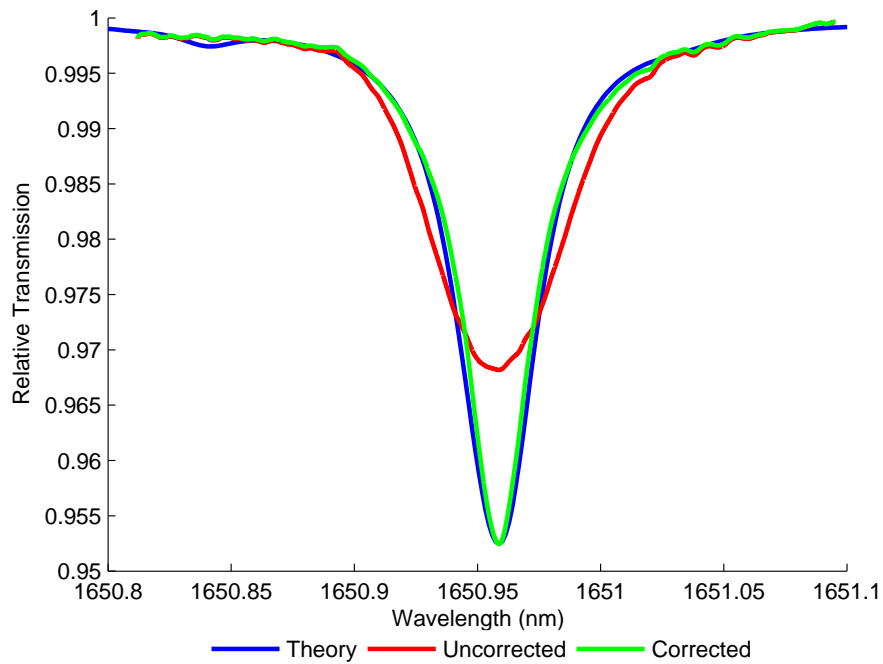


Figure 5.29: 1.02%CH<sub>4</sub>:N<sub>2</sub> at 0.995Bar and 15.5°C with m=1.5 - Recovered absolute gas absorption line shape compared to theory

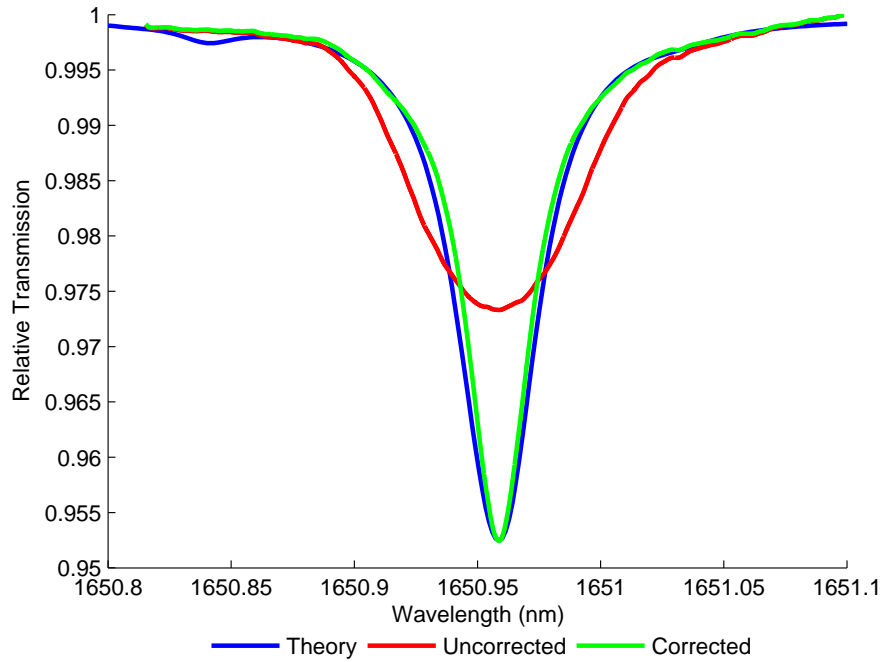


Figure 5.30: 1.02%CH<sub>4</sub>:N<sub>2</sub> at 0.995Bar and 15.5°C with  $m=2$  - Recovered absolute gas absorption line shape compared to theory

### 5.3.6 Measurement of Concentration and Pressure

Once more, the curve fitting procedure was again used to extract the measured gas concentration and pressure from the corrected signals given in Figures 5.26 to 5.30 on pages 112–114. Table 5.6 shows the known and measured concentrations and pressures for  $m$  value range 0.2 to 2, along with their associated error. It can be seen again that the error in concentration is relatively low for all  $m$  values, whereas the errors in pressure are higher. Again, the main source of error in the pressure is believed to be due to the correction factor. As the correction factor implementation is still under development, it is hoped that advances are made in the accurate recovery of the true width of the gas line shape, which determines the recovered pressure. As can be seen from the results with low  $m$  values i.e. Figures 5.26 to 5.27 on page 112, the SNR is lower. This is a result of the decomposition process combining the noise from both outputs of the LIA. Again, the increase in LIA sensitivity and DR is shown in Table 5.7.

m	Known Conc. (%)	Recovered Conc. (%)	Conc. Error (%)	Known Pres. (Bar)	Recovered Pres. (Bar)	Pres. Error (%)
0.2	1.02	0.954	6.44	0.995	0.931	6.44
0.5	1.02	0.988	3.24	0.995	0.898	9.77
1	1.02	1.004	1.55	0.995	0.894	10.18
1.5	1.02	1.002	1.75	0.995	0.894	10.18
2	1.02	0.991	2.84	0.995	0.894	10.18

Table 5.8: Calculated errors in concentration and pressure using RAM technique with RAM nulling at 1.02%CH<sub>4</sub>:N<sub>2</sub>

### 5.3.7 Summary of Results

The results presented using the PD method with RAM nulling reinforces the observations made section 5.2.8. As mentioned earlier the PD method recovers the full RAM absorption along with the full 1<sup>st</sup> derivative of the absolute gas absorption. Results of the 1<sup>st</sup> derivative have not been shown as gas concentration can not be directly extracted from the recovered 1<sup>st</sup> derivative signal. The extraction of gas pressure is not possible from the 1<sup>st</sup> derivative signal.

## 5.4 Overall Summary and Conclusions

Revised analytical models and procedures for the recovery of signals in the RAM and PD techniques with RAM nulling were presented in chapter 5 and then used to recover the distorted RAM signals in Figures 5.8 to 5.17 (using the RAM technique) and in 5.21 to 5.30 (using the PD method). A new theoretical model of the directly recovered (distorted) RAM signal has been developed and presented in chapter 3. This model provided a correction factor to enable the absolute gas absorption line shape to be recovered from the distorted RAM signal at high  $m$  values. The close agreement between the absolute gas absorption line shapes recovered in this way and the theoretical Voigt line shapes generated from HITRAN data in all of the results presented in Figures 5.8 to 5.17 and Figures

5.21 to 5.30 fully validate:

- the new experimental RAM nulling approach used in conjunction with the RAM and PD techniques
- the revised analytical model and procedures for extracting the RAM signal from the RAM and PD measurement processes used with RAM nulling
- the new model of the recovered RAM signal and the correction factor and procedures to generate the absolute gas absorption line shape from it at high  $m$  values

Finally, the curve fitting procedure described in chapter 3 was used to extract measurements of concentration and pressure from the absolute gas absorption line shape in this way and the low errors in the results compared to the certified concentrations supplied by BOC further confirms validation of the measurement process.

In addition to the above, the removal of the large background RAM enabled a large increase in the LIA dynamic reserve and a significant improvement in the LIA sensitivity (see Tables 5.1, 5.3, 5.5 and 5.7). In an ideal situation the experimental system would be limited by receiver noise. Therefore, increasing the DR and improving the sensitivity of the LIA should automatically increase measurement sensitivity. Indeed, as indicated by the DR and sensitivity improvement we believe that the inherent sensitivity of the system has been significantly improved. However, the experimental system used for this research was limited by etalon fringes due to oscillations between the faces of the C lens in the micro-optic cell. Due to this limitation a complete investigation of the increase of measurement sensitivity from using RAM nulling could not be carried out.

# Chapter 6

## Optimisation of 1<sup>st</sup> Harmonic TDLS with RAM

---

### 6.1 Overview

This chapter presents the experimental results for the amplitude investigation described in section 3.4. When using conventional TDLS with WM techniques, the user recovers the 1<sup>st</sup> or 2<sup>nd</sup> harmonic WM/IM signal, which is proportional to the 1<sup>st</sup> and 2<sup>nd</sup> derivatives of absolute gas absorption line shape respectively. A measure of concentration of the target gas can be extracted from the recovered harmonic WM/IM signals. When using conventional techniques a concentration measurement is made from a relative measurement of the harmonic WM/IM signal amplitude in conjunction with a calibration procedure. On the other hand, with the RAM technique or PD method, the recovered absolute transmission profile of the gas absorption line shape is used along with the curve fitting of a theoretical line shape to find the best match to the experimental line shape in terms of least square errors to obtain a value for concentration. Therefore, the amplitudes of the harmonic WM/IM signals and the recovered transmission profile (referred to as the RAM signal from this point as the profile is recovered from the RAM absorption in either the RAM technique or the PD method) can

not be directly compared. The amplitudes of the 1<sup>st</sup> and 2<sup>nd</sup> harmonic WM/IM signals can not be directly compared either as they undergo different scaling factors through the LIA as a result of the different signal frequencies involved.

To enable meaningful comparisons of the absolute amplitudes of the 1<sup>st</sup> and 2<sup>nd</sup> harmonic WM/IM signal and the RAM signal, appropriate scaling factors must be determined to allow signals at the output of the LIA (in units of Volts) to be converted to optical power variations incident on the receiver (in units of  $\mu\text{W}$ ) under the conditions of recovery for each type of signal. Once the signals are suitably scaled the comparisons are made at line centre,  $\lambda_c$ , for the 2<sup>nd</sup> harmonic WM/IM and RAM signals. For the 1<sup>st</sup> harmonic WM/IM signal an average amplitude value between the maximum and minimum is used.

The purpose of the investigation was to evaluate the change in signal amplitudes in terms of laser power as the sinusoidal modulation frequency was increased beyond conventional values. At each frequency a range of modulation indices,  $m$ , was applied. The investigation was carried out in two parts. The first section looked at conventional modulation frequencies ranging from 10kHz to 110kHz with  $m$  values of 0.2, 0.5, 1, 1.5, 2 and 2.2 for each frequency, results were obtained with 10.13%CH<sub>4</sub>:N<sub>2</sub> and 1.02%CH<sub>4</sub>:N<sub>2</sub> in the cell. The second section of the investigation looked at the behaviour of the RAM signal as the modulation frequency was varied from 100kHz to 1.2MHz with  $m$  set to 0.2 and 0.5. Only two  $m$  values were used, as to operate at higher  $m$  values in this frequency range would overload the laser, which could damage the laser or shorten its operating lifetime. Again, measurements were made with 10.13%CH<sub>4</sub>:N<sub>2</sub> and 1.02%CH<sub>4</sub>:N<sub>2</sub> in the cell.

The following sections describe how the scaling factors for the various signals were obtained and then applied. The RAM and 1<sup>st</sup> harmonic WM/IM signals were recovered using the PD method and the 2<sup>nd</sup> harmonic WM/IM signal was recovered using conventional methods. The approximately scaled signals are compared relatively to one another and to the theoretical amplitudes. For this investigation the system setup given in Figure 4.1 was modified by disconnecting

the delay branch and replacing the LNP2 photodiode receiver with a Thorlabs PDA10CS-EC detector, which had a bandwidth of 17MHz at zero gain. The amplitude investigation examined signals at modulation frequencies >1MHz. The LNP2 receiver has a bandwidth of only 1MHz and hence the need for the replacement. Also, for the high frequency part of the investigation only the 1<sup>st</sup> harmonic WM/IM and RAM signal are examined, due to the bandwidth of the LIA being only 2MHz.

## 6.2 Scaling Factor Calculations

The purpose of the scaling factors were to determine signal levels as an absolute deviation in power ( $\mu\text{W}$ ) of the transmitted laser beam. Before the scaling factors are calculated the procedure for determining the theoretical amplitudes of the various absorption signals must first be calculated. The theoretical amplitudes can be calculated by using equations (3.18), (3.21), (3.24) and (3.35) for the 1<sup>st</sup> harmonic WM/IM ( $S_\omega$ ), 2<sup>nd</sup> harmonic WM/IM ( $S_{2\omega}$ ) and RAM ( $S_{RAM}$ ) absorption signals respectively, recalled below:

$$S_\omega = AI_o \frac{2}{\pi} \int_0^\pi \frac{\cos\theta}{1 + (\Delta + m \cos\theta)^2} d\theta$$

$$S_{2\omega} = AI_o \frac{2}{\pi} \int_0^\pi \frac{\cos(2\theta)}{1 + (\Delta + m \cos\theta)^2} d\theta$$

$$S_{RAM} = A \frac{\kappa\gamma}{\xi(\omega)} \frac{m}{\pi} \int_0^\pi \frac{1 - \cos 2\theta}{1 + m^2 \cos^2 \theta} d\theta$$

The expression for the 1<sup>st</sup> and 2<sup>nd</sup> harmonic WM/IM signals are at a maximum when  $m$  is 2 and 2.2 respectively. The RAM amplitude increases monotonically with  $m$ . A number of system parameters must be obtained to allow the use of the above expression for the theoretical power at  $\lambda_c$ . With regards to the 1<sup>st</sup> and 2<sup>nd</sup> harmonic WM/IM signals the term  $I_o$  is the power at  $\lambda_c$ , measured to be  $339\mu\text{W}$  and kept constant during the entire investigation. The expression  $A = \alpha_o Cl$  is given by calculating  $\alpha_o$ ,  $0.4705\text{cm}^{-1}$ , using spectroscopic parameters.  $C$  in this

investigation is either going to be 0.1013 or 0.0102 and  $l$  was measured as 9.9cm. For the RAM signal, knowledge of the following parameters are required  $\kappa$ ,  $\gamma$  and  $\xi(\omega)$ . The procedures for determining these parameters was given in section 4.5.3.

To obtain the scaling factors for the experimental 1<sup>st</sup> and 2<sup>nd</sup> harmonic WM/IM and RAM signals, the theoretical maxima in units of  $\mu\text{W}$  for each signal were divided by the corresponding experimental maxima in units of volts for the conditions of recovery for each type of signal. The resulting scaling factors were then used to suitably scale the experimental signals for all values of  $m$ . With all the experimental signals scaled to an absolute power variation they could now be directly compared. The following sections give a range of results, which compare the experimental absorption signals at  $\lambda_c$  to theory.

The process given above to calculate the scaling factors was devised after an initial approach was investigated. To obtain the scaling factor for the RAM signals it was believed that the term  $\Delta I$  could be determined by first measuring power levels then by recording a *nogas* signal to obtain the background RAM signal. These two approaches would give a value for  $\Delta I$  in terms of  $\mu\text{W}$  and volts, which could then be used to calculate the scaling factor. It was then thought that this scaling factor could be applied to the 1<sup>st</sup> harmonic WM/IM signal. For the 2<sup>nd</sup> harmonic WM/IM signal a similar approach was taken, however, a slightly different approach was needed as the background signal on the 2<sup>nd</sup> harmonic WM/IM is negligible. The laser was modulated at  $2f$ , but the LIA had a reference signal of  $f$  and the LIA set to recover the 2<sup>nd</sup> harmonic WM/IM. This setup produced a signal at the LIA output that could be used along with the earlier power level measurements to gain the scaling factor. The scaling factors generated from this method were consistent with the factors produced from the above technique. Therefore, the technique utilising the theoretical amplitudes was used to obtain the scaling factors.

## 6.3 Signal Amplitude Investigation: Low Modulation Frequency Range

### 6.3.1 Overview

This section of results is for the modulation frequency range of 10kHz to 110kHz. This range would be classed as conventional modulation frequencies. The purpose is to examine the behaviour of the signals as the frequency and  $m$  value are changed. The results given had the following key system parameters: ramp modulation of 5Hz and  $300\text{mV}_{pk-pk}$ ;  $I_{LD}=80\text{mA}$  and  $T_{ACT}=6.591\text{k}\Omega$ . For all measurements the LIA AC Gain and Time Constant were 6dB and  $500\mu\text{s}$  respectively. The PD method was used to recover the (distorted) RAM signal and the direct 1<sup>st</sup> harmonic WM/IM signal scaled by  $\sin\psi'$  (using the MATLAB program in appendix D). Conventional TDLS with WM techniques were used to record the direct 2<sup>nd</sup> harmonic WM/IM signal, with the 2<sup>nd</sup> harmonic amplitude taken from the recorded signal. The signals were processed using a MATLAB program, given in appendix E, to illustrate the different signal amplitudes varying with modulation index for a range of modulation frequencies. The signals were then processed by a second MATLAB program, given in appendix F, to illustrate the amplitude variations against modulation frequency for the range of modulation indices.

### 6.3.2 10.13%CH<sub>4</sub>:N<sub>2</sub> Results

In this section, each result for a particular applied modulation frequency shows the variation of theoretical signal amplitude with  $m$  for the 1<sup>st</sup> and 2<sup>nd</sup> harmonic WM/IM and RAM signals expressed as a power variation. In addition to the theoretical amplitudes, each plot shows the variation in the experimental signal amplitudes with  $m$  for the 1<sup>st</sup> and 2<sup>nd</sup> harmonic WM/IM and RAM signals expressed as a power variation. The results were obtained and are presented for several frequencies in the range 10 to 110kHz. The same results are then plotted as signal amplitudes versus modulation frequency for several fixed values of  $m$  in the range of 0.2 to 2. The results given by Figures 6.1 to 6.6 on pages 124–129 were obtained when 10.13%CH<sub>4</sub>:N<sub>2</sub> at 1.022Bar and 17.5°C was in the cell. The LIA parameters for these results are given in Table 6.1.

	Modulation Frequency											
	10kHz		30kHz		50kHz		80kHz		100kHz		110kHz	
$m$	Sens. (mV)	Phase (°)	Sens. (mV)	Phase (°)	Sens. (mV)	Phase (°)	Sens. (mV)	Phase (°)	Sens. (mV)	Phase (°)	Sens. (mV)	Phase (°)
<i>1<sup>st</sup> Harmonic Detection</i>												
0.2	5	+1	10	+9	10	+4.8	10	+1	10	-0.5	10	-1.5
0.5	20	0	20	+9	20	+4.5	20	+0.3	20	-1.5	20	-2.2
1	20	+0.3	50	+10	50	+3.5	50	-0.6	50	-2.5	50	-3.4
1.5	50	-0.1	50	+9.5	50	+3.1	50	0	50	-2.8	50	-3.7
2	50	-0.3	50	+9.1	50	+2.8	50	-0.4	50	-2.2	50	-3.1
2.2	50	-0.3	50	+9.1	50	+2.8	50	-0.5	50	-2.4	50	-3.3
<i>2<sup>nd</sup> Harmonic Detection</i>												
0.2	0.5	-147	0.5	-162	0.5	+160	0.5	+126	0.5	+104	0.5	+94
0.5	5	-147	5	-162	5	+162	5	+126	5	+104	5	+95
1	10	-147	10	-160	10	+163	10	+128	10	+107	10	+97
1.5	10	-147	10	-160	10	+164	10	+129	10	+110	10	+101
2	20	-147	20	-160	20	+165	20	+134	20	+116	20	+107
2.2	20	-147	20	-160	20	+166	20	+135	20	+117	20	+109

Table 6.1: LIA parameters for amplitude investigation low frequency range - 10.13%CH<sub>4</sub>:N<sub>2</sub>

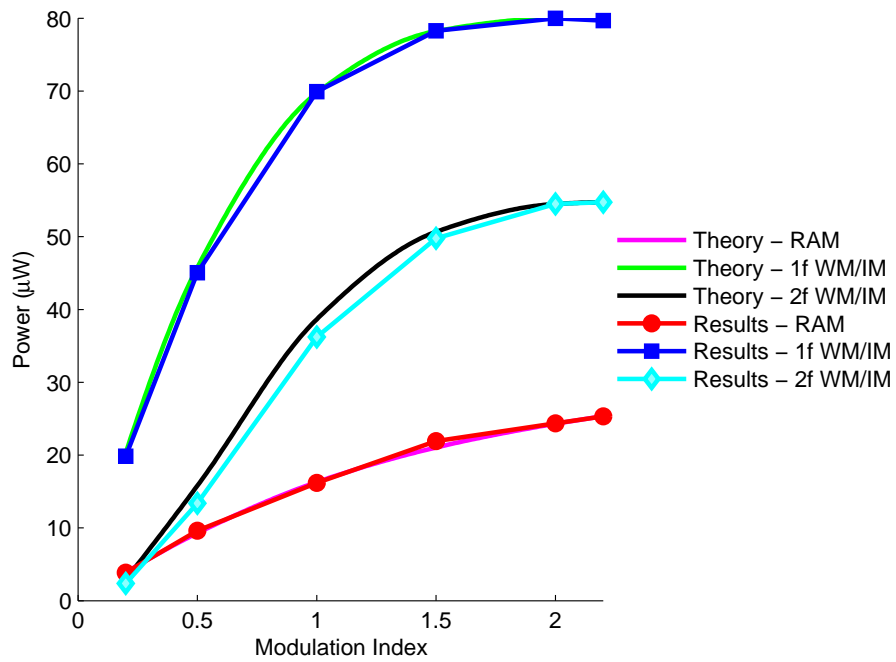


Figure 6.1: 10.13%CH<sub>4</sub>:N<sub>2</sub> at 1.022Bar and 17.5°C at 10kHz - Theoretical power variations at,  $\lambda_c$ , for 1<sup>st</sup> and 2<sup>nd</sup> harmonic WM/IM and RAM signals compared to scaled experimental power variations at,  $\lambda_c$ , for 1<sup>st</sup> and 2<sup>nd</sup> harmonic WM/IM and RAM signals

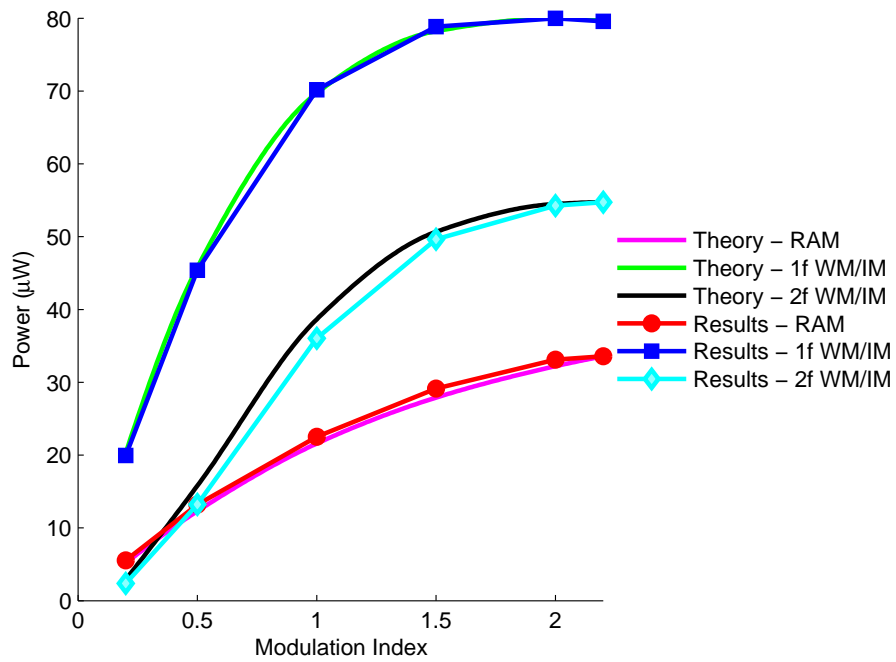


Figure 6.2: 10.13%CH<sub>4</sub>:N<sub>2</sub> at 1.022Bar and 17.5°C at 30kHz - Theoretical power variations at,  $\lambda_c$ , for 1<sup>st</sup> and 2<sup>nd</sup> harmonic WM/IM and RAM signals compared to scaled experimental power variations at,  $\lambda_c$ , for 1<sup>st</sup> and 2<sup>nd</sup> harmonic WM/IM and RAM signals

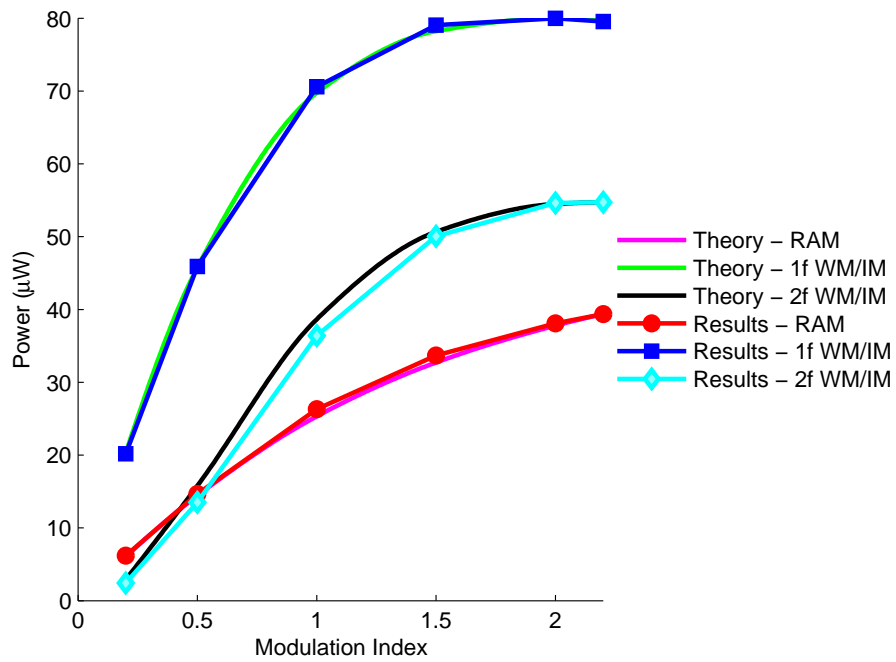


Figure 6.3: 10.13%CH<sub>4</sub>:N<sub>2</sub> at 1.022Bar and 17.5°C at 50kHz - Theoretical power variations at,  $\lambda_c$ , for 1<sup>st</sup> and 2<sup>nd</sup> harmonic WM/IM and RAM signals compared to scaled experimental power variations at,  $\lambda_c$ , for 1<sup>st</sup> and 2<sup>nd</sup> harmonic WM/IM and RAM signals

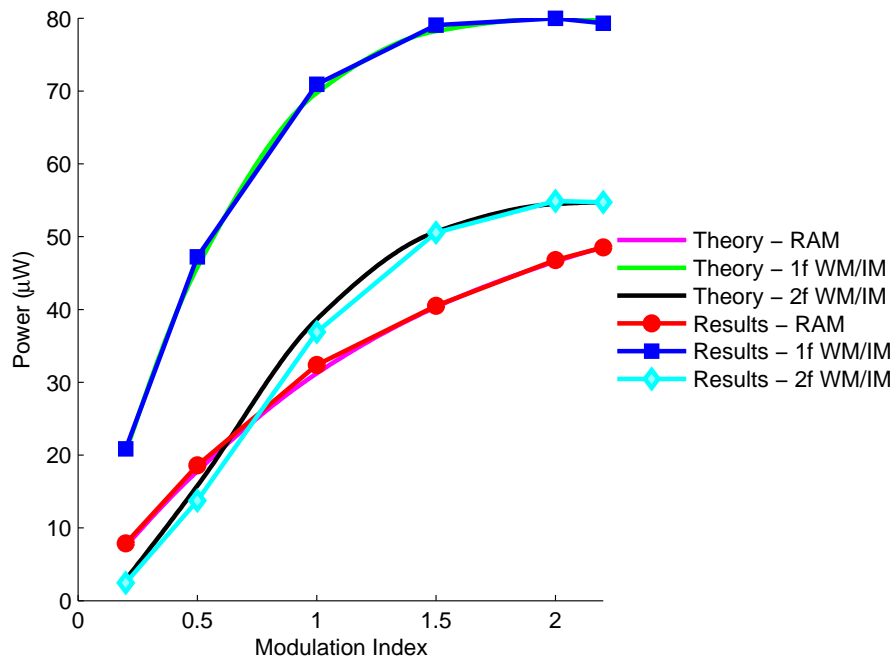


Figure 6.4: 10.13%CH<sub>4</sub>:N<sub>2</sub> at 1.022Bar and 17.5°C at 80kHz - Theoretical power variations at,  $\lambda_c$ , for 1<sup>st</sup> and 2<sup>nd</sup> harmonic WM/IM and RAM signals compared to scaled experimental power variations at,  $\lambda_c$ , for 1<sup>st</sup> and 2<sup>nd</sup> harmonic WM/IM and RAM signals

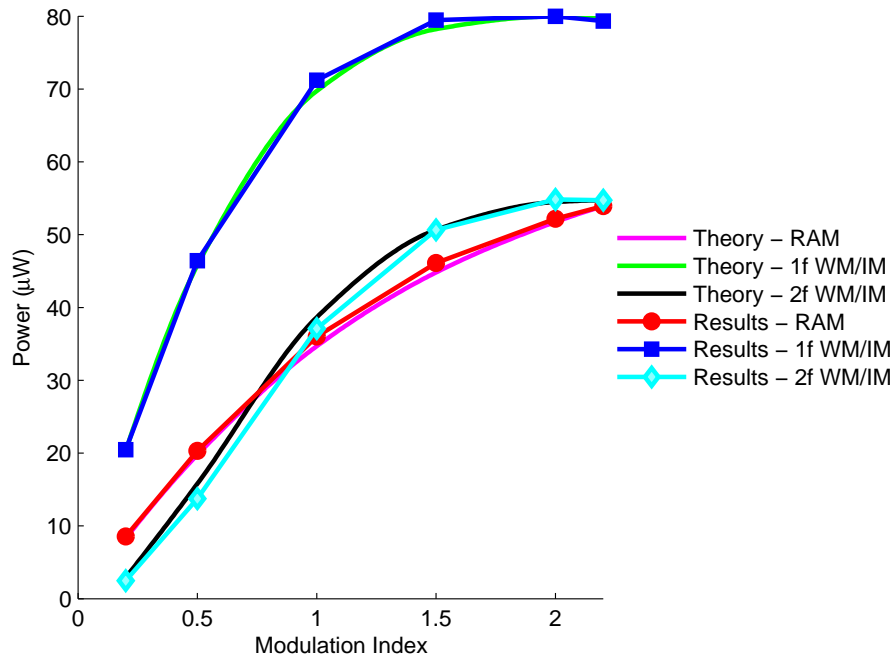


Figure 6.5: 10.13%CH<sub>4</sub>:N<sub>2</sub> at 1.022Bar and 17.5°C at 100kHz - Theoretical power variations at,  $\lambda_c$ , for 1<sup>st</sup> and 2<sup>nd</sup> harmonic WM/IM and RAM signals compared to scaled experimental power variations at,  $\lambda_c$ , for 1<sup>st</sup> and 2<sup>nd</sup> harmonic WM/IM and RAM signals

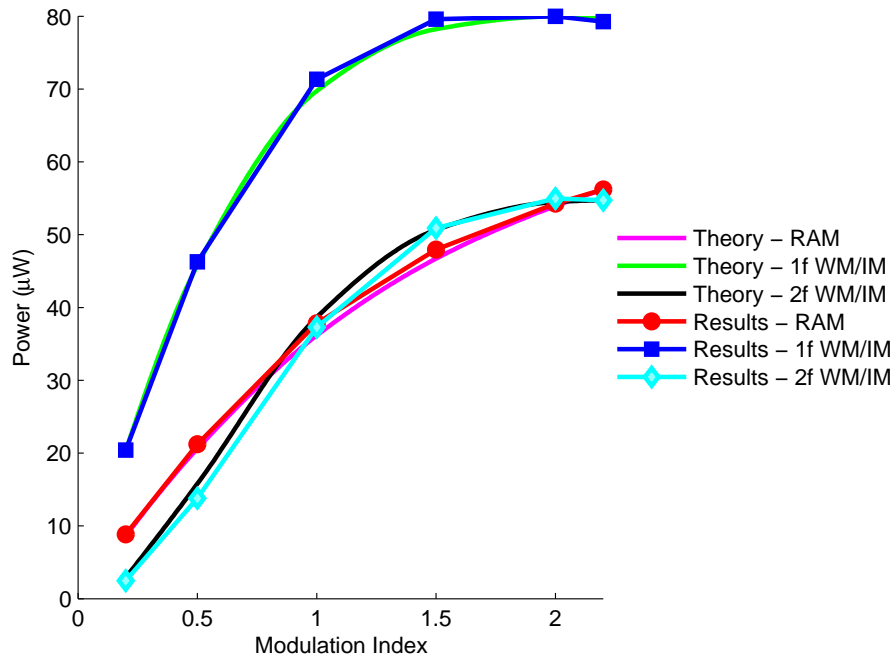


Figure 6.6: 10.13%CH<sub>4</sub>:N<sub>2</sub> at 1.022Bar and 17.5°C at 110kHz - Theoretical power variations at,  $\lambda_c$ , for 1<sup>st</sup> and 2<sup>nd</sup> harmonic WM/IM and RAM signals compared to scaled experimental power variations at,  $\lambda_c$ , for 1<sup>st</sup> and 2<sup>nd</sup> harmonic WM/IM and RAM signals

The experimental results given by Figures 6.1 to 6.6 on pages 124–129 show good comparison to theory. As can be seen from the results the amplitudes of the 1<sup>st</sup> and 2<sup>nd</sup> harmonic WM/IM signals are not affected by the modulation frequency. However, as expected, the RAM signals increase with increasing modulation frequency. Also, from Figures 6.1 to 6.6 on pages 124–129 there is a small discrepancy in the 2<sup>nd</sup> harmonic WM/IM comparison. The source couldn't be identified, but it is believed to be systematic and is relatively constant as  $m$  varies.

The results shown in Figures 6.1 to 6.6 on pages 124–129 present the comparison of theory to experiment in terms of power variation against  $m$  for the modulation frequency range 10kHz to 110kHz. To illustrate the variation in power better Figures 6.7 to 6.12 on pages 130–133 show the same results but for power variation against modulation frequency for the  $m$  range 0.2 to 2.2.

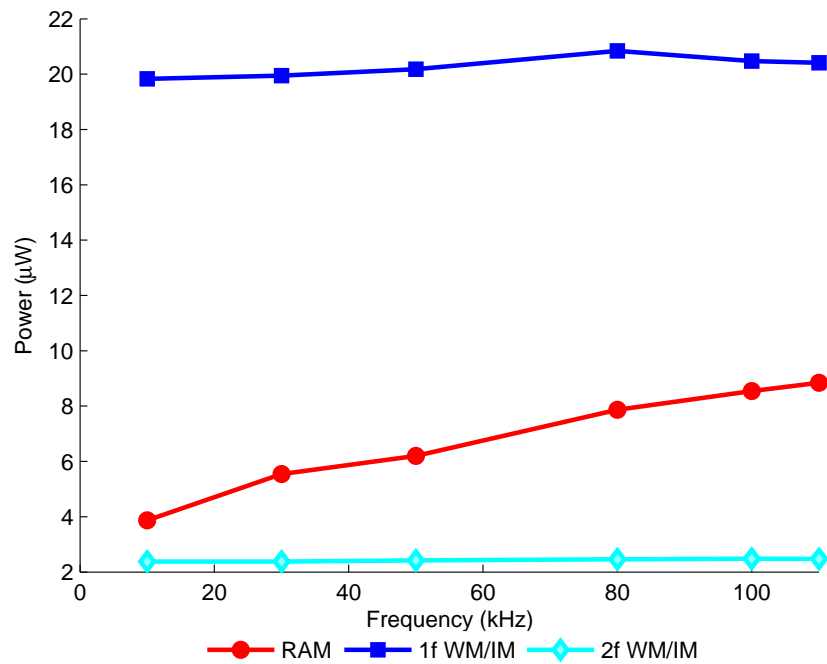


Figure 6.7: 10.13%CH<sub>4</sub>:N<sub>2</sub> at 1.022Bar and 17.5°C at m=0.2 - comparison of power variations for 1<sup>st</sup> and 2<sup>nd</sup> harmonic WM/IM and RAM signals

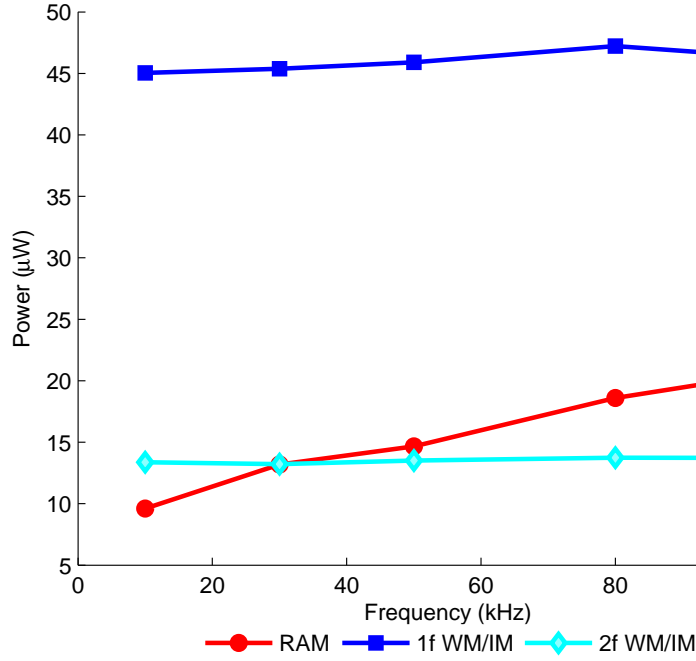


Figure 6.8: 10.13%CH<sub>4</sub>:N<sub>2</sub> at 1.022Bar and 17.5°C at m=0.5 - comparison of power variations for 1<sup>st</sup> and 2<sup>nd</sup> harmonic WM/IM and RAM signals

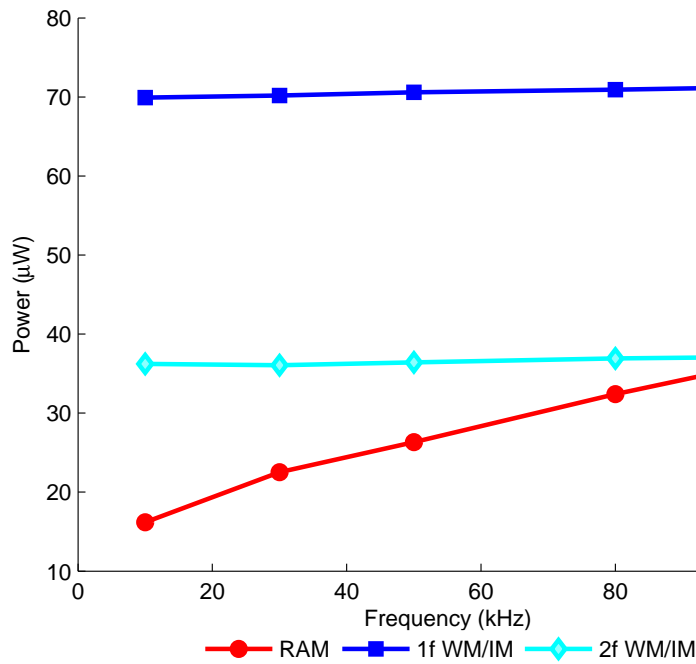


Figure 6.9: 10.13%CH<sub>4</sub>:N<sub>2</sub> at 1.022Bar and 17.5°C at m=1 - comparison of power variations at 1<sup>st</sup> and 2<sup>nd</sup> harmonic WM/IM and RAM signals

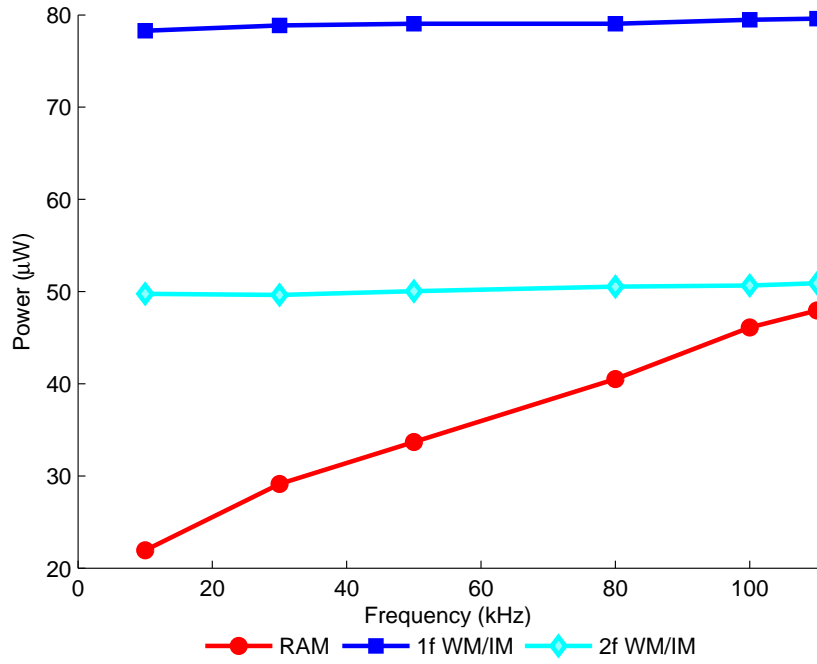


Figure 6.10: 10.13%CH<sub>4</sub>:N<sub>2</sub> at 1.022Bar and 17.5°C at m=1.5 - comparison of power variations for 1<sup>st</sup> and 2<sup>nd</sup> harmonic WM/IM and RAM signals

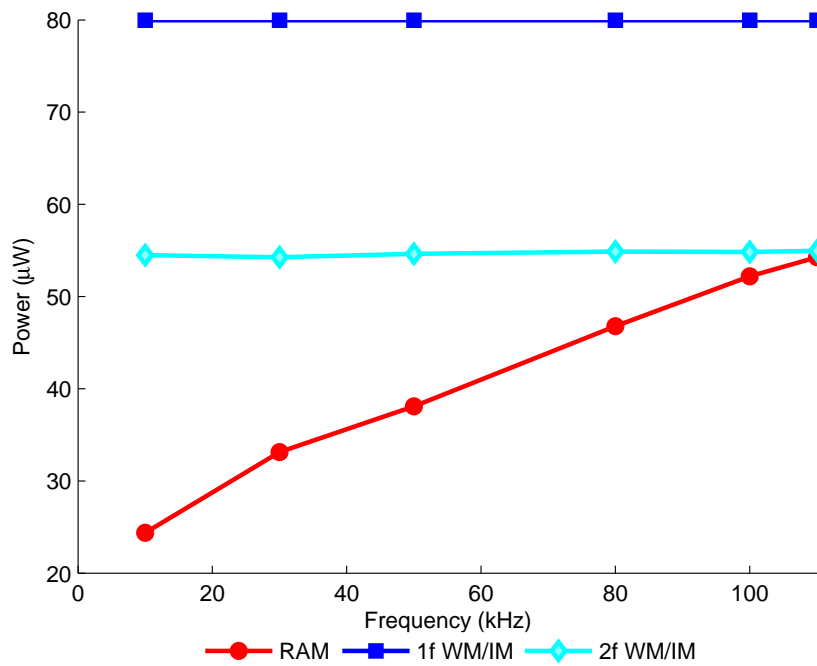


Figure 6.11: 10.13%CH<sub>4</sub>:N<sub>2</sub> at 1.022Bar and 17.5°C at m=2 - comparison of power variations for 1<sup>st</sup> and 2<sup>nd</sup> harmonic WM/IM and RAM signals

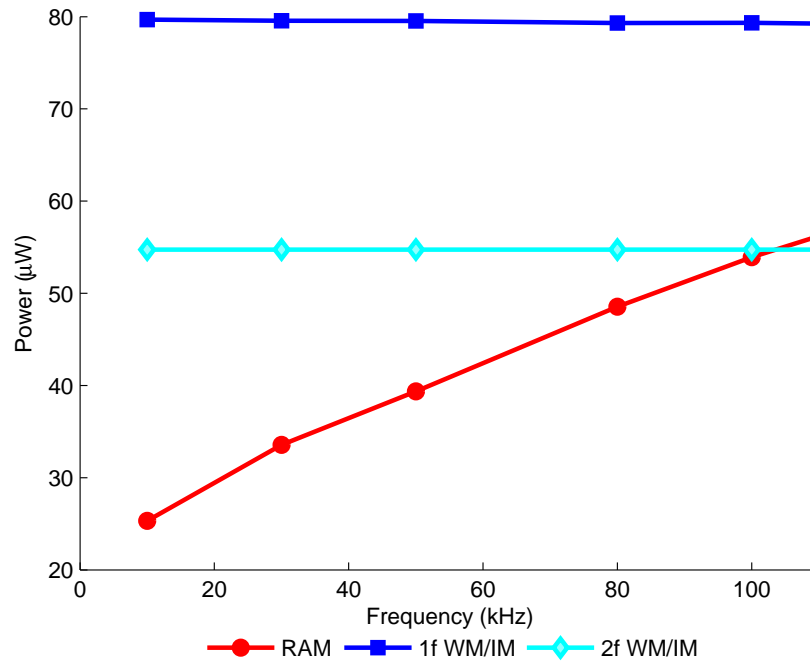


Figure 6.12: 10.13%CH<sub>4</sub>:N<sub>2</sub> at 1.022Bar and 17.5°C at  $m=2.2$  - comparison of power variations for 1<sup>st</sup> and 2<sup>nd</sup> harmonic WM/IM and RAM signals

From examination of Figures 6.7 to 6.12 on pages 130–133 it can be seen that for a given  $m$  value the amplitudes of the 1<sup>st</sup> and 2<sup>nd</sup> harmonic WM/IM signals are relatively constant over the frequency range. However, the amplitude of the RAM signal is increasing with modulation frequency, and as can be seen, the RAM signal becomes comparable with or exceeds the 2<sup>nd</sup> harmonic WM/IM signal at corresponding  $m$  values as the modulation frequency is increased. At  $m = 2.2$  and a modulation frequency of 110kHz the amplitude of the RAM signal is comparable to the 2<sup>nd</sup> harmonic WM/IM signal amplitude

### 6.3.3 1.02%CH<sub>4</sub>:N<sub>2</sub> Results

In this section, the same set of measurements were obtained in the same way as for 10.13%CH<sub>4</sub>:N<sub>2</sub> and now presented for 1.02%CH<sub>4</sub>:N<sub>2</sub>. The LIA parameters for these results are given in Table 6.2.

	Modulation Frequency											
	10kHz		30kHz		50kHz		80kHz		100kHz		110kHz	
$m$	Sens. (mV)	Phase (°)	Sens. (mV)	Phase (°)	Sens. (mV)	Phase (°)	Sens. (mV)	Phase (°)	Sens. (mV)	Phase (°)	Sens. (mV)	Phase (°)
1 <sup>st</sup> Harmonic Detection												
0.2	5	-0.4	5	+9.1	5	+2.72	5	-1.5	5	-3.23	5	-4.13
0.5	10	-0.5	10	+9.1	10	+2.72	10	-1.46	20	-3.18	20	-4.07
1	10	-0.5	20	+9.1	20	+2.66	20	-1.51	50	-3.21	50	-4.09
1.5	20	-0.4	20	+9.1	50	+2.68	50	-1.48	50	-3.26	50	-4.17
2	20	-0.5	50	+9.1	50	+2.66	50	-1.53	50	-3.32	50	-4.24
2.2	50	-0.4	50	+9.1	50	+2.66	50	-1.53	50	-3.35	50	-4.24
2 <sup>nd</sup> Harmonic Detection												
0.2	0.1	-145.7	0.1	-158.9	0.1	+163.7	0.1	+126	0.1	+108.5	0.1	+99.5
0.5	0.5	-146.6	0.5	-160.5	0.5	+162.7	0.5	+126	0.5	+105.5	0.5	+96.5
1	2	-146.8	2	-159.9	2	+163.3	2	+128	2	+106.5	2	+97.4
1.5	2	-146.6	2	-160	2	+163	2	+129	2	+107	2	+98
2	2	-147	2	-160.6	2	+162.4	2	+134	2	+109.1	2	+99.7
2.2	2	-147.1	2	-161	2	+162.1	2	+135	2	+109.5	2	+100.1

Table 6.2: LIA parameters for amplitude investigation low frequency range - 1.02%CH<sub>4</sub>:N<sub>2</sub>

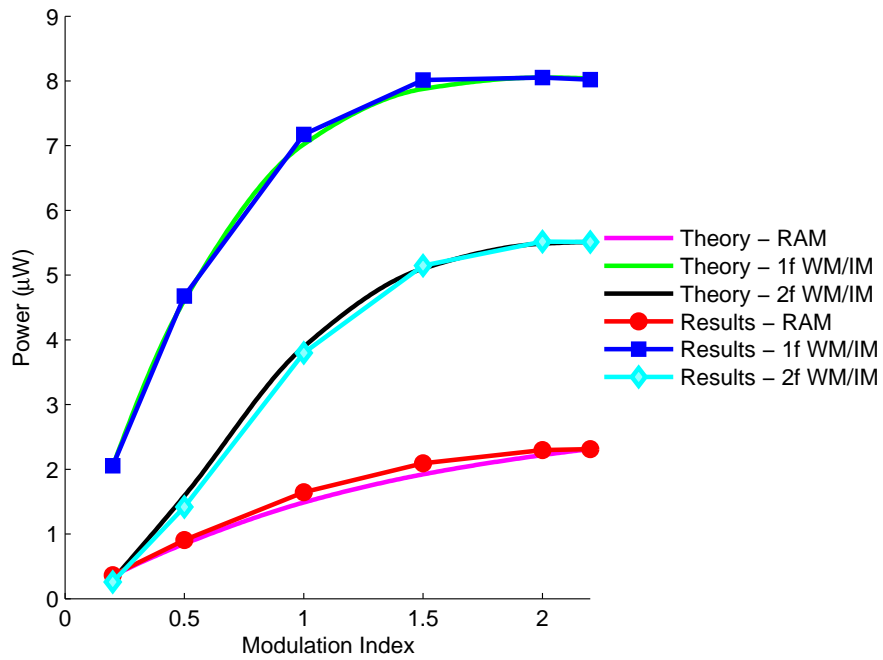


Figure 6.13: 1.02%CH<sub>4</sub>:N<sub>2</sub> at 1.007Bar and 18.1°C at 10kHz - Theoretical power variations at,  $\lambda_c$ , for 1<sup>st</sup> and 2<sup>nd</sup> harmonic WM/IM and RAM signals compared to scaled experimental power variations at,  $\lambda_c$ , for 1<sup>st</sup> and 2<sup>nd</sup> harmonic WM/IM and RAM signals

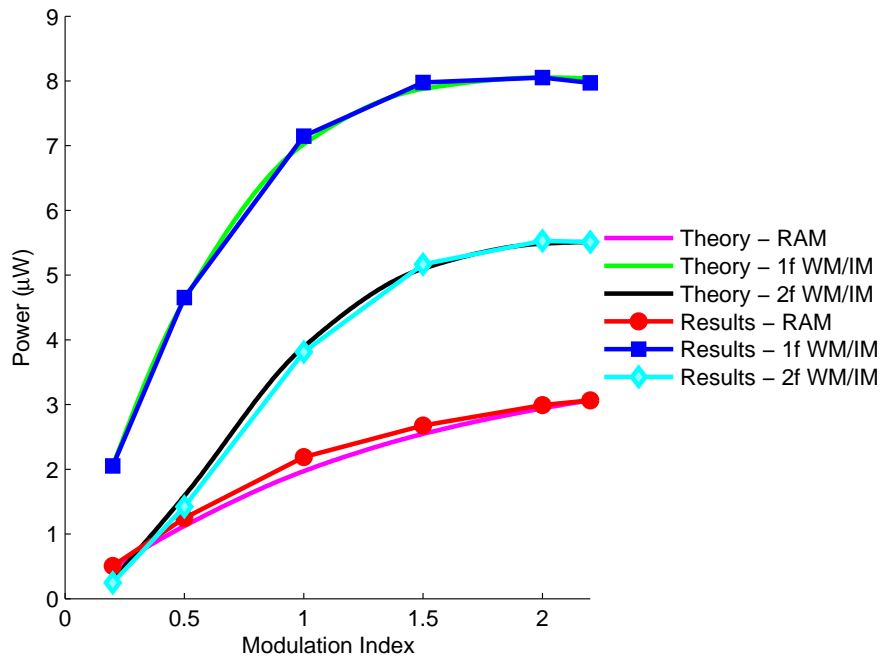


Figure 6.14: 1.02%CH<sub>4</sub>:N<sub>2</sub> at 1.007Bar and 18.1°C at 30kHz - Theoretical power variations at,  $\lambda_c$ , for 1<sup>st</sup> and 2<sup>nd</sup> harmonic WM/IM and RAM signals compared to scaled experimental power variations at,  $\lambda_c$ , for 1<sup>st</sup> and 2<sup>nd</sup> harmonic WM/IM and RAM signals

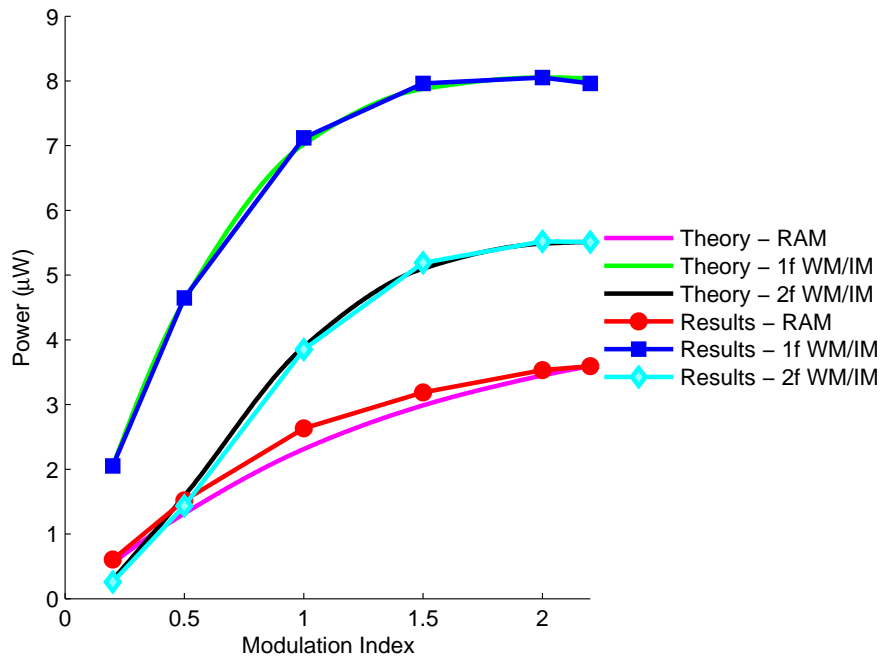


Figure 6.15: 1.02%CH<sub>4</sub>:N<sub>2</sub> at 1.007Bar and 18.1°C at 50kHz - Theoretical power variations at,  $\lambda_c$ , for 1<sup>st</sup> and 2<sup>nd</sup> harmonic WM/IM and RAM signals compared to scaled experimental power variations at,  $\lambda_c$ , for 1<sup>st</sup> and 2<sup>nd</sup> harmonic WM/IM and RAM signals

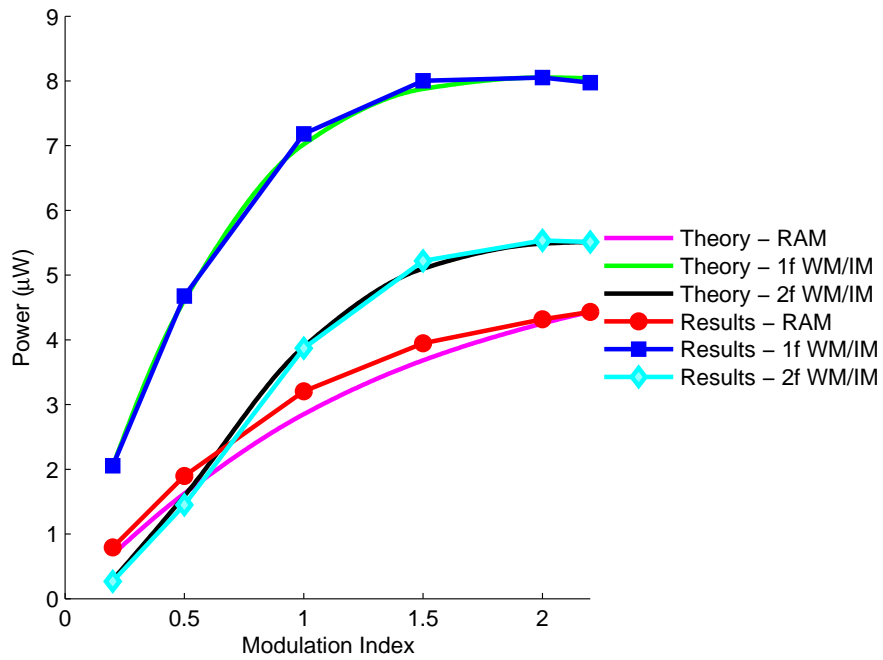


Figure 6.16: 1.02%CH<sub>4</sub>:N<sub>2</sub> at 1.007Bar and 18.1°C at 80kHz - Theoretical power variations at,  $\lambda_c$ , for 1<sup>st</sup> and 2<sup>nd</sup> harmonic WM/IM and RAM signals compared to scaled experimental power variations at,  $\lambda_c$ , for 1<sup>st</sup> and 2<sup>nd</sup> harmonic WM/IM and RAM signals

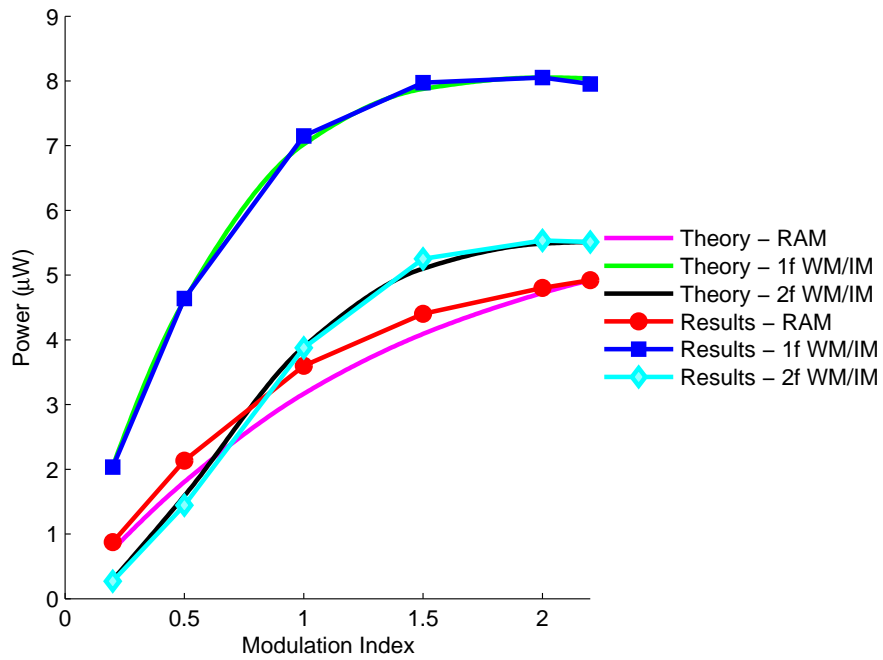


Figure 6.17: 1.02%CH<sub>4</sub>:N<sub>2</sub> at 1.007Bar and 18.1°C at 100kHz - Theoretical power variations at,  $\lambda_c$ , for 1<sup>st</sup> and 2<sup>nd</sup> harmonic WM/IM and RAM signals compared to scaled experimental power variations at,  $\lambda_c$ , for 1<sup>st</sup> and 2<sup>nd</sup> harmonic WM/IM and RAM signals

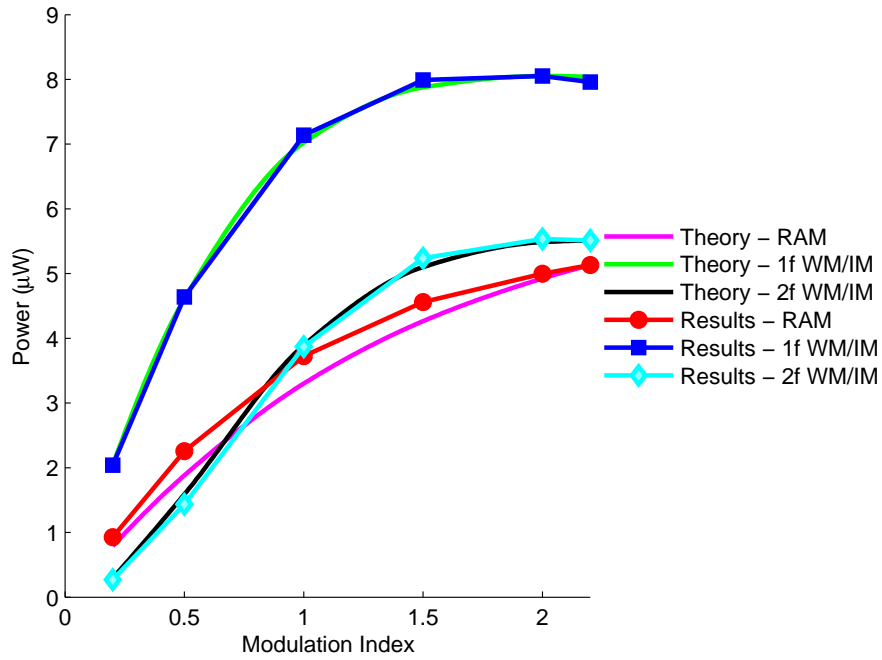


Figure 6.18: 1.02%CH<sub>4</sub>:N<sub>2</sub> at 1.007Bar and 18.1°C at 110kHz - Theoretical power variations at,  $\lambda_c$ , for 1<sup>st</sup> and 2<sup>nd</sup> harmonic WM/IM and RAM signals compared to scaled experimental power variations at,  $\lambda_c$ , for 1<sup>st</sup> and 2<sup>nd</sup> harmonic WM/IM and RAM signals

The experimental results given by Figures 6.13 to 6.18 on pages 135–140 show good comparison to theory. However, unlike the 10.13%CH<sub>4</sub>:N<sub>2</sub> results, there is a discrepancy in the experimental RAM results that is increasing with modulation frequency. As can be seen from the results the amplitudes of the 1<sup>st</sup> and 2<sup>nd</sup> harmonic WM/IM signal are not affected by the modulation frequency. However, as expected, the RAM signals increase with increasing modulation frequency.

The results shown in Figures 6.13 to 6.18 on pages 135–140 present the comparison of theory to experiment in terms of power variation against  $m$  for the modulation frequency range 10kHz to 110kHz. To illustrate the variation in power better Figures 6.19 to 6.24 on pages 141–143 show the same results but for power variation against modulation frequency for the  $m$  range 0.2 to 2.2.

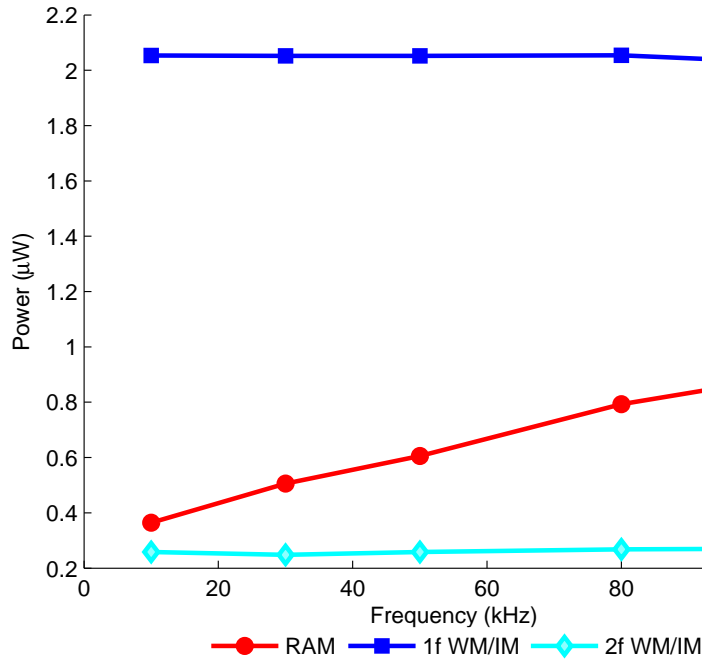


Figure 6.19: 1.02%CH<sub>4</sub>:N<sub>2</sub> at 1.007Bar and 18.1°C at m=0.2 - comparison of power variations for 1<sup>st</sup> and 2<sup>nd</sup> harmonic WM/IM and RAM signals

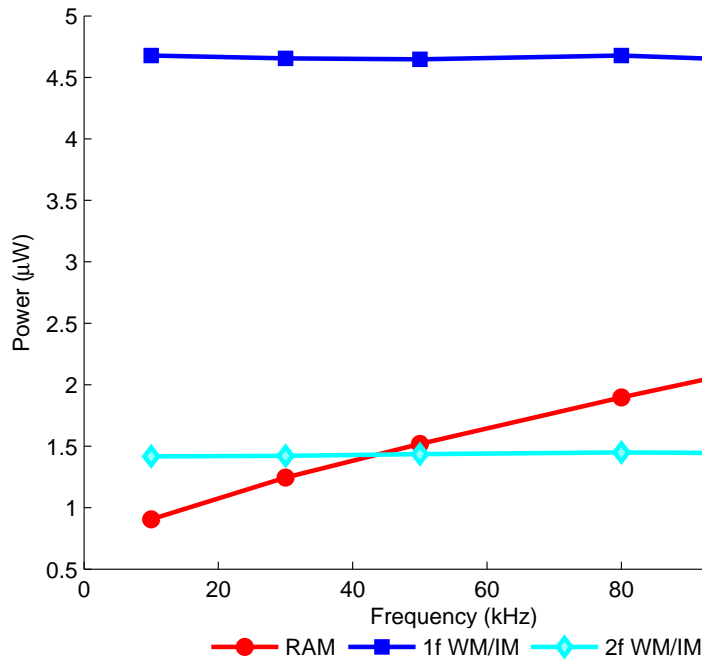


Figure 6.20: 1.02%CH<sub>4</sub>:N<sub>2</sub> at 1.007Bar and 18.1°C at m=0.5 - comparison of power variations for 1<sup>st</sup> and 2<sup>nd</sup> harmonic WM/IM and RAM signals

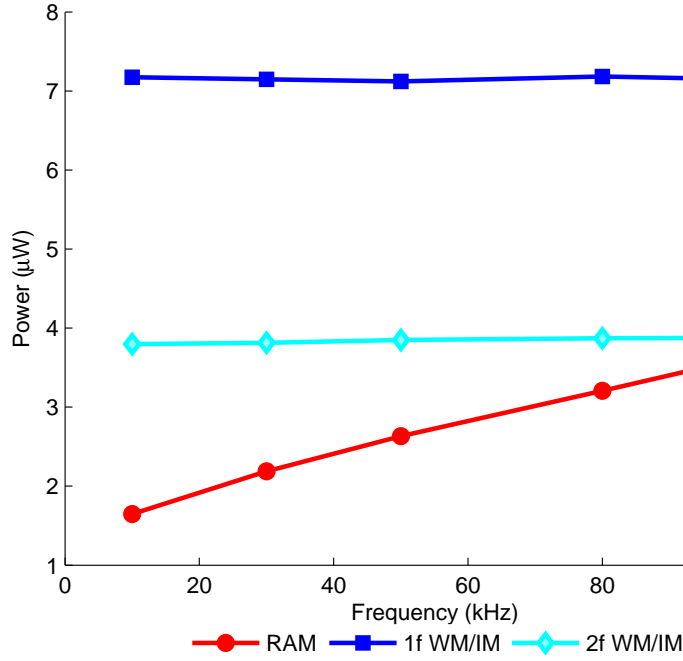


Figure 6.21: 1.02%CH<sub>4</sub>:N<sub>2</sub> at 1.007Bar and 18.1°C at m=1 - comparison of power variations for 1<sup>st</sup> and 2<sup>nd</sup> harmonic WM/IM and RAM signals

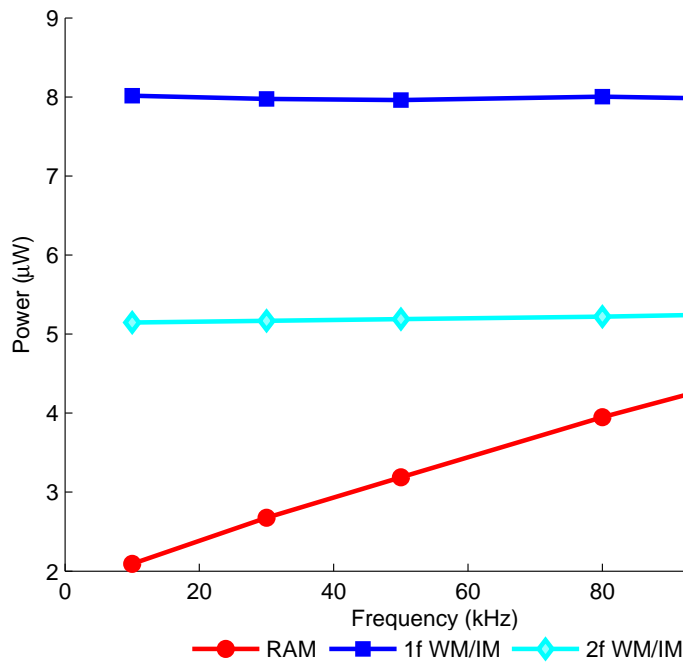


Figure 6.22: 1.02%CH<sub>4</sub>:N<sub>2</sub> at 1.007Bar and 18.1°C at m=1.5 - comparison of power variations for 1<sup>st</sup> and 2<sup>nd</sup> harmonic WM/IM and RAM signals

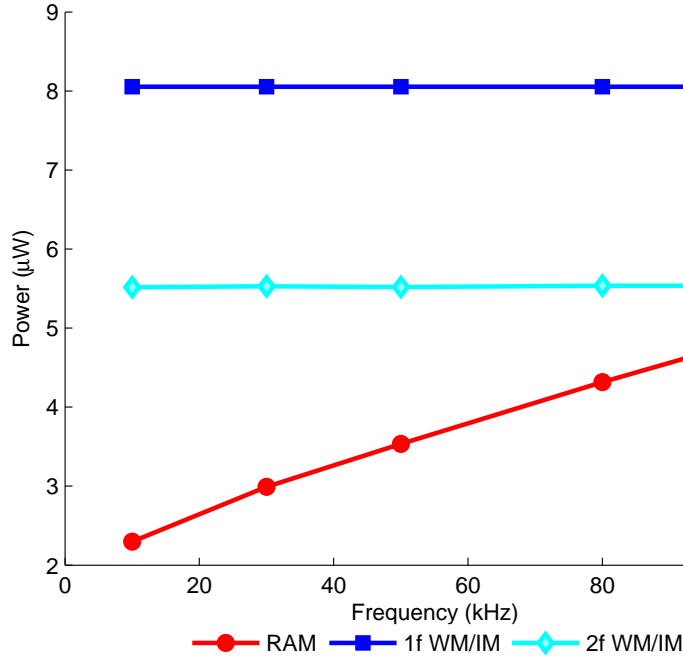


Figure 6.23: 1.02%CH<sub>4</sub>:N<sub>2</sub> at 1.007Bar and 18.1°C at m=2 - comparison of power variations for 1<sup>st</sup> and 2<sup>nd</sup> harmonic WM/IM and RAM signals

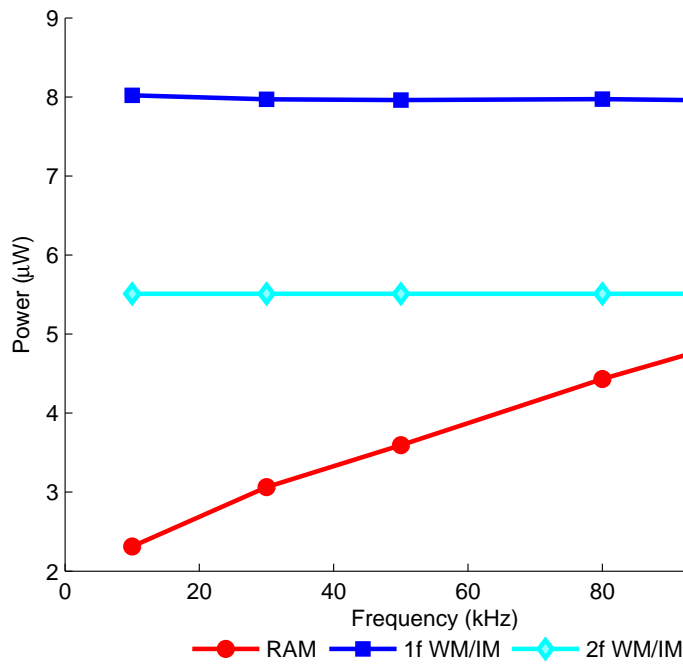


Figure 6.24: 1.02%CH<sub>4</sub>:N<sub>2</sub> at 1.007Bar and 18.1°C at m=2.2 - comparison of power variations 1<sup>st</sup> and 2<sup>nd</sup> harmonic WM/IM and RAM signals

From examination of Figures 6.19 to 6.24 on pages 141–143 it can be seen that for a given  $m$  value the amplitudes of the 1<sup>st</sup> and 2<sup>nd</sup> harmonic WM/IM signals are relatively constant over the frequency range and the amplitude of the RAM signal is increasing with modulation frequency.

### 6.3.4 Discussion of Results

This concludes the results for modulation frequencies in the range 10kHz to 110kHz. The above results validate the approaches and techniques that were used to obtain the scaling factors and applying them to the experimental results to allow direct comparisons of the 1<sup>st</sup> and 2<sup>nd</sup> harmonic WM/IM signals with the RAM signal. As mentioned previously the RAM signal increases with increasing modulation frequency, therefore there is a point when the RAM signal is larger in amplitude compared to the 1<sup>st</sup> harmonic WM/IM. The second part of the investigation evaluates when this point occurs. The results presented in this section support the observations made in the 10.13%CH<sub>4</sub>:N<sub>2</sub> results in the previous section.

## 6.4 Signal Amplitude Investigation: High Modulation Frequency Range

### 6.4.1 Overview

For this section of results an extended range of modulation frequency was used, 100kHz to 1.2MHz, with the purpose of finding the operating condition where the power of the RAM signal was greater than the 1<sup>st</sup> harmonic WM/IM signal power. The range of  $m$  values was reduced to 0.2 and 0.5. To achieve higher  $m$  values requires current modulations that would overload the source causing damage and shortening the operational life time of the laser.

The procedure for calculating the scaling factor was similar to section 6.3,

however, the point where the scaling factor was calculated was changed to  $m = 0.5$ , also only the 1<sup>st</sup> harmonic WM/IM and RAM signal were observed. This was done because the upper end of the 2<sup>nd</sup> harmonic WM/IM signals would not be detectable due to the LIA bandwidth limitations

### 6.4.2 10.13%CH<sub>4</sub>:N<sub>2</sub> Results

The results presented in this section were obtained when 10.13%CH<sub>4</sub>:N<sub>2</sub> at 1.022Bar and 17.5°C was in the cell for the modulation frequency range of 100kHz to 1.2MHz. The LIA parameters for these results are given in Table 6.3. To illustrate the variation in power Figures 6.25 to 6.26 on page 147 show the scaled experimental results in terms of power variation plotted against modulation frequency for  $m$  equal to 0.2 and 0.5 respectively. To emphasise the importance of the results given in Figures 6.25 to 6.26 on page 147, Figure 6.27 shows the experimental RAM signals at  $m$  equal to 0.2 and 0.5 compared to the maximum possible 1<sup>st</sup> harmonic WM/IM at  $m=2$  and the maximum possible 2<sup>nd</sup> harmonic WM/IM at  $m=2.2$ .

	Modulation Frequency														
	100kHz		250kHz		500kHz		750kHz		1MHz		1.1MHz		1.2MHz		
$m$	Sens. (mV)	Phase (°)	Sens. (mV)	Phase (°)	Sens. (mV)	Phase (°)	Sens. (mV)	Phase (°)	Sens. (mV)	Phase (°)	Sens. (mV)	Phase (°)	Sens. (mV)	Phase (°)	
$1^{st}$ Harmonic Detection															
0.2	10	-0.5	10	-9.8	10	-19.8	10	-26.6	20	-32	20	-33.4	20	-35	
0.5	20	-1.5	20	-10.4	50	-21.7	50	-29.2	50	-34.6	50	-36.4	50	-38.1	

Table 6.3: LIA parameters for amplitude investigation high frequency range - 10.13%CH<sub>4</sub>:N<sub>2</sub>

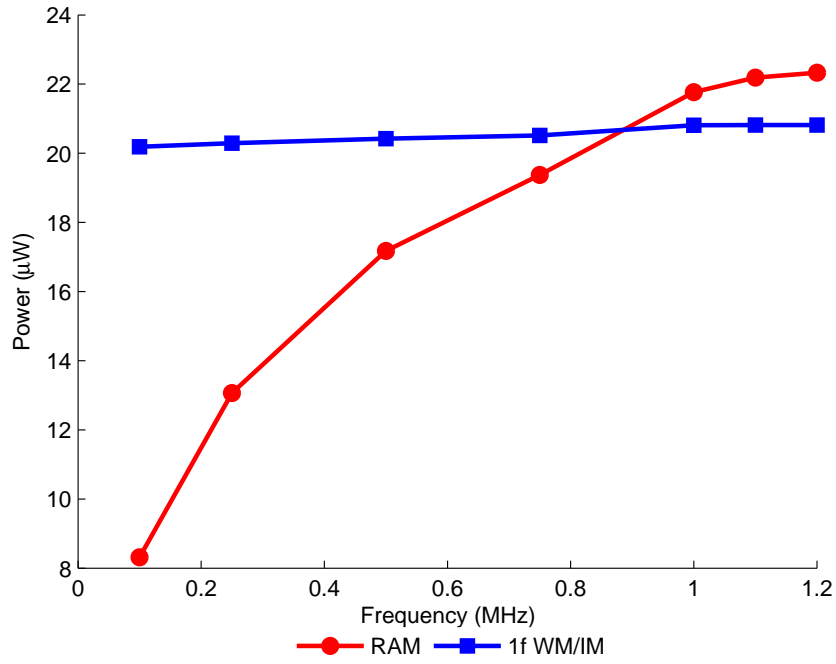


Figure 6.25: 10.13%CH<sub>4</sub>:N<sub>2</sub> at 1.022Bar and 17.5°C at m=0.2 - comparison of power variations at,  $\lambda_c$ , for 1<sup>st</sup> harmonic WM/IM and RAM signals

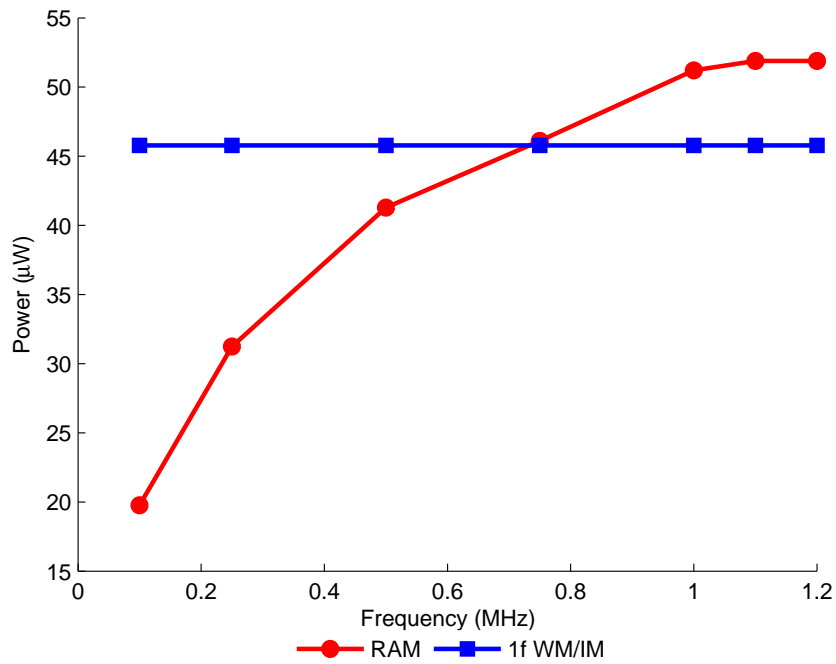


Figure 6.26: 10.13%CH<sub>4</sub>:N<sub>2</sub> at 1.022Bar and 17.5°C at m=0.5 - comparison of power variations at,  $\lambda_c$ , for 1<sup>st</sup> harmonic WM/IM and RAM signals

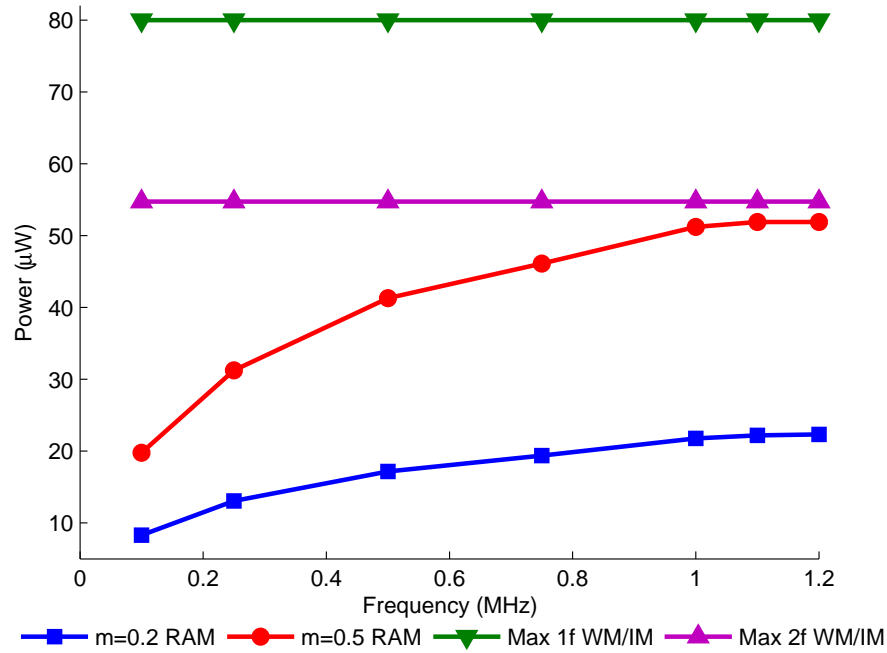


Figure 6.27: 10.13%CH<sub>4</sub>:N<sub>2</sub> at 1.022Bar and 17.5°C - comparison of power variations at  $m=0.2$  and  $m=0.5$  with maximum possible 1<sup>st</sup> and 2<sup>nd</sup> harmonic WM/IM signals

The main observation that can be made from Figure 6.27 is that at  $m=0.2$  the RAM signal reaches approximately 40% of the 2<sup>nd</sup> harmonic WM/IM at  $m=2.2$  and that at  $m=0.5$  the RAM becomes comparable with the 2<sup>nd</sup> harmonic WM/IM at  $m=2.2$  as we approach the higher frequencies. To further illustrate the results, Figures 6.28 to 6.29 on the following page illustrate the variation in power at 1.2MHz for the 1<sup>st</sup> harmonic WM/IM and RAM signals for the entire wavelength sweep of the laser at  $m=0.2$  and  $m=0.5$  respectively. The presented 1<sup>st</sup> harmonic WM/IM signals are the full 1<sup>st</sup> derivative of the absolute gas absorption line shape, as the directly recovered signal projection on the LIA output was scaled by a factor of  $\sin\psi'$ .

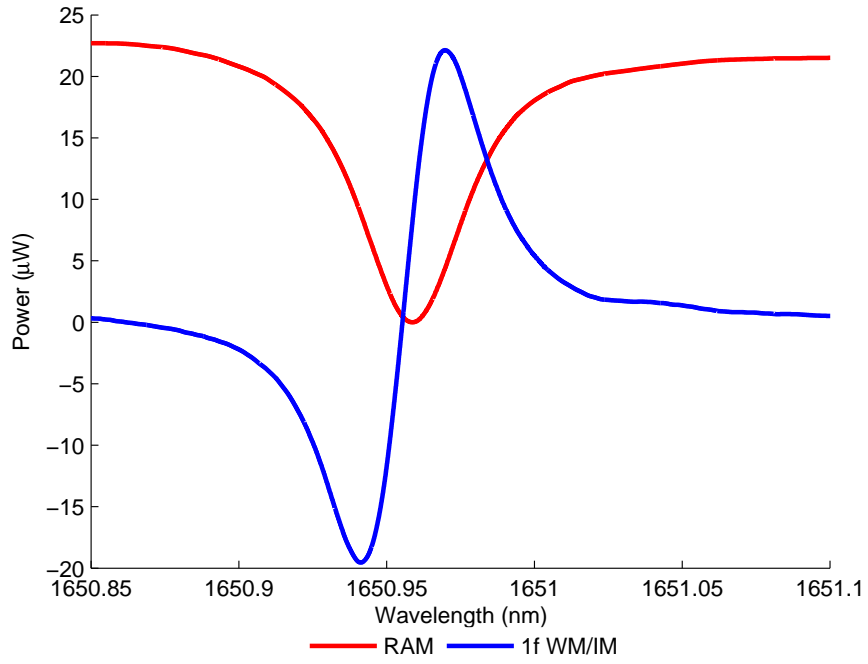


Figure 6.28: 10.13%CH<sub>4</sub>:N<sub>2</sub> at 1.022Bar and 17.5°C at m=0.2 - comparison of 1<sup>st</sup> harmonic WM/IM and RAM signals at 1.2MHz

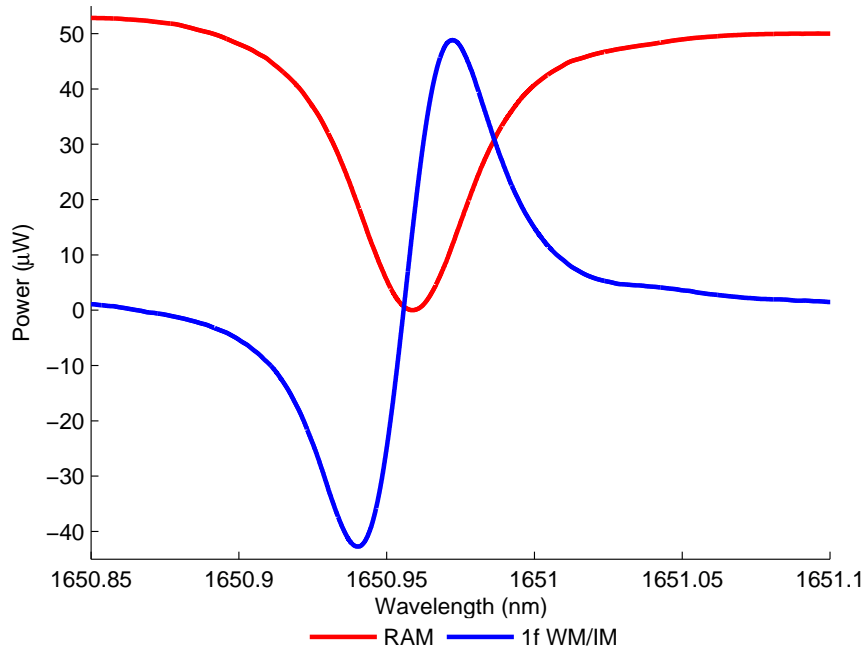


Figure 6.29: 10.13%CH<sub>4</sub>:N<sub>2</sub> at 1.022Bar and 17.5°C at m=0.5 - comparison of 1<sup>st</sup> harmonic WM/IM and RAM signals at 1.2MHz

The results given by Figures 6.25 to 6.26 on page 147 were processed using the MATLAB program given in appendix F. From examination of Figures 6.25 to 6.26 on page 147 it can be seen that for a given  $m$  value the amplitudes of the 1<sup>st</sup> harmonic WM/IM signal is relatively constant over the frequency range and the amplitude of the RAM signal is increasing with modulation frequency. From Figures 6.25 to 6.26 on page 147, it can be seen that the RAM signal is typically bigger than the 1<sup>st</sup> harmonic WM/IM at modulation frequencies  $> 800\text{kHz}$ . Most importantly, from Figure 6.27 it can be seen that at  $m=0.5$  the RAM signal at 1.2MHz is comparable than the 2<sup>nd</sup> harmonic WM/IM signal at  $m=2.2$ .

### 6.4.3 1.02%CH<sub>4</sub>:N<sub>2</sub> Results

The results presented in this section were obtained when 1.02%CH<sub>4</sub>:N<sub>2</sub> at 1.007Bar and 18.1°C was in the cell for the modulation frequency range of 100kHz to 1.2MHz. The LIA parameters for these results are given in Table 6.4. To illustrate the variation in power Figures 6.30 to 6.31 on page 152 show the scaled experimental results in terms of power variation against modulation frequency for  $m$  equal to 0.2 and 0.5.

	Modulation Frequency														
	100kHz		250kHz		500kHz		750kHz		1MHz		1.1MHz		1.2MHz		
$m$	Sens. (mV)	Phase (°)	Sens. (mV)	Phase (°)	Sens. (mV)	Phase (°)	Sens. (mV)	Phase (°)	Sens. (mV)	Phase (°)	Sens. (mV)	Phase (°)	Sens. (mV)	Phase (°)	
$1^{st}$ Harmonic Detection															
0.2	5	-3.23	10	-12.77	10	-24.42	10	-33.14	20	-40.02	20	-42.23	20	-44.56	
0.5	20	-3.18	20	-12.86	50	-24.51	50	-33.41	50	-41.01	50	-43.38	50	-45.94	

Table 6.4: LIA parameters for amplitude investigation high frequency range - 1.02%CH<sub>4</sub>:N<sub>2</sub>

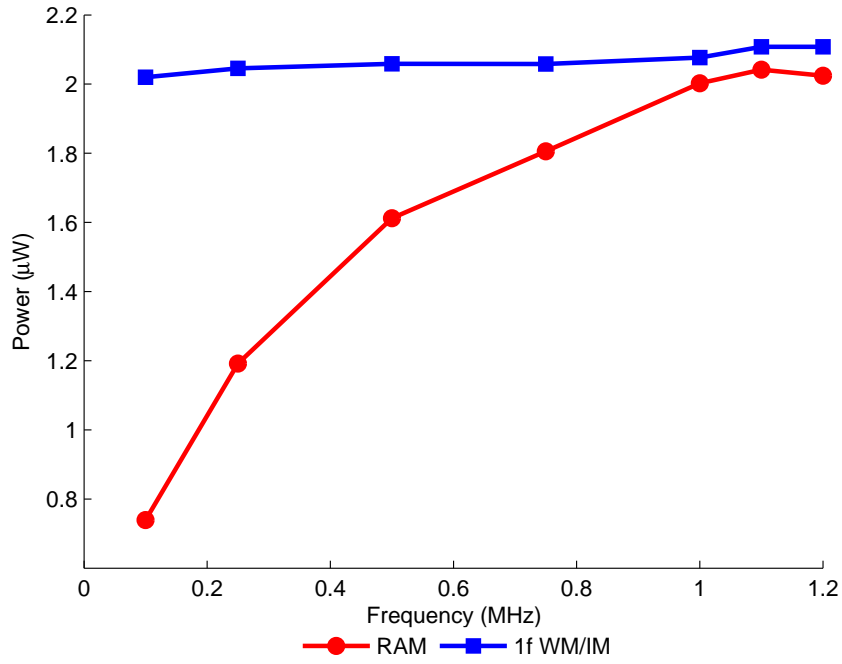


Figure 6.30: 1.02%CH<sub>4</sub>:N<sub>2</sub> at 1.007Bar and 18.1°C at m=0.2 - comparison of power variations at,  $\lambda_c$ , for 1<sup>st</sup> harmonic WM/IM and RAM signals

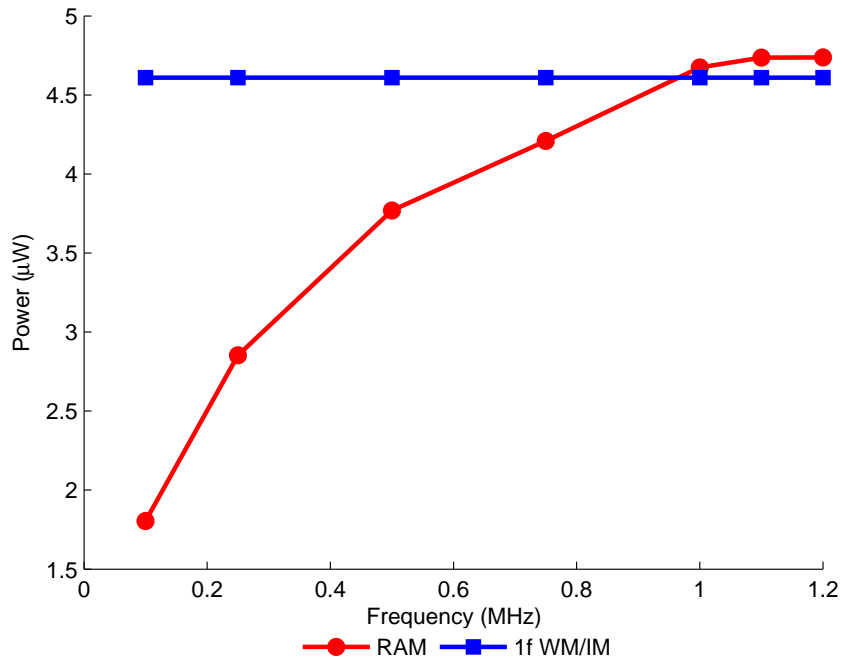


Figure 6.31: 1.02%CH<sub>4</sub>:N<sub>2</sub> at 1.007Bar and 18.1°C at m=0.5 - comparison of power variations at,  $\lambda_c$ , for 1<sup>st</sup> harmonic WM/IM and RAM signals

#### 6.4.4 Discussion of Results

From examination of Figures 6.30 to 6.31 on the previous page it can be seen that for a given  $m$  value the amplitudes of the 1<sup>st</sup> harmonic WM/IM signal is relatively constant over the frequency range and the amplitude of the RAM signal is increasing with modulation frequency, with the RAM bigger than the 1<sup>st</sup> harmonic WM/IM signal at frequencies  $> 1\text{MHz}$ . This concludes the results for the range of 100kHz to 1MHz for modulation frequency, the above results validates the approaches and techniques that were used to obtain the scaling factors and applying them to the experimental results allowing direct comparisons of the 1<sup>st</sup> and 2<sup>nd</sup> harmonic WM/IM signals with the RAM signal at  $\lambda_c$ . Furthermore, the results presented in this section support observations made in the previous 10.13%CH<sub>4</sub>:N<sub>2</sub> results section.

### 6.5 Overall Summary and Conclusions

The results presented in this chapter show excellent agreement between experiment and theory and have further validated the mathematical modelling that describes the RAM and the 1<sup>st</sup> and 2<sup>nd</sup> harmonic WM/IM signals derived in section 3.4. The models were used to compare the amplitudes of theoretical signals with experimental scaled signals in terms of power variation of the transmitted laser beam. A number of initial observations were made. Firstly, the recognised maxima of the 1<sup>st</sup> and 2<sup>st</sup> harmonic WM/IM signals were shown to be  $m=2$  and  $m=2.2$  respectively. Through the mathematical modelling it was shown that the RAM signal amplitudes increased monotonically with  $m$ . Secondly, the devised procedure to scale the experimental signals so that they could be compared to theoretical power variation amplitudes was validated.

Finally, a wide range of results were produced to validate the mathematical expressions and scaling factors. From the results in this chapter it was shown that the 1<sup>st</sup> and 2<sup>nd</sup> harmonic WM/IM signals are dependent on  $m$  and independent of modulation frequency. The RAM signal is both dependent on  $m$  and modulation

frequency. In the low frequency investigation it was clearly demonstrated that the RAM signal amplitude became comparable with (and then exceeded) the 2<sup>nd</sup> harmonic WM/IM signal amplitude at modulation frequencies around 100kHz at all corresponding  $m$  values. At high frequencies ( $>1\text{MHz}$ ) the RAM signal was found to surpass both the 1<sup>st</sup> and 2<sup>nd</sup> harmonic WM/IM signals in terms of power variation. Also of significance, is the RAM signal at  $m=0.5$  becomes comparable with the maximum possible 2<sup>nd</sup> harmonic WM/IM signal, discussed at the end of section 6.4.2. This shows that when using the RAM technique or the PD method under certain operating conditions achievable signal strength and SNRs can be comparable to or even better than conventional WM/IM analysis techniques. Applications, where operating at higher modulation frequencies is needed for better time resolution, include intake/outtake monitoring of aero engines.

# Chapter 7

## Conclusions and Further Work

---

### 7.1 Conclusions

The principal aim of this research was to improve the PD method and RAM technique by incorporating a novel optical approach to suppress the background RAM present on the recovered 1<sup>st</sup> harmonic signals when applying TDLS with WM. The background RAM was suppressed by the implementation of a fibre delay branch placed in parallel with the gas cell, that introduced a  $\pi$  phase shift in the modulated laser signal. The delay branch also consisted of a VOA, used to match the IM of the laser on both branches. When the output of the branches were combined and the system optimised for RAM nulling the effect was a DC signal that when interrupted by the LIA resulted in a zero output, thus, if gas was present the resulting absorption signal was on a zero background. The length of the fibre was specified to give the necessary phase shift at a sinusoidal modulation frequency of approximately 100kHz, this is regarded as the upper limit of conventional TDLS with WM, however other modulation frequencies could be used with appropriate adjustment of the delay fibre length.

New procedures and analytical processes to recover the absolute gas absorption line shape using the RAM and PD methods with RAM nulling have been developed and detailed in chapter 5. The extracted RAM signals suffered from

distortion terms at  $m > 0.2$  due to the presence of higher order Fourier terms of the line shape function. The new model presented in chapter 3 provided correction factors that allowed the absolute gas absorption line shapes to be recovered from the extracted RAM signals at arbitrary  $m$  values up to  $m = 2.2$ .

The outcomes and key conclusions from chapter 5 can be summarised as follows

- A simple investigation of the nature of the signals involved in the RAM nulling process (section 5.2.3) clearly illustrated the nulling process and the use of polarisation controllers to minimise interferometric noise.
- The results presented for the investigation of the 1650.96nm methane line (chapter 5) clearly demonstrate the close agreement between the experimentally recovered and corrected RAM signals (absolute gas absorption line shapes) and the theoretical line shape derived from HITRAN data. This was true for both the RAM technique and the PD method, for all  $m$  values used in the range 0.2 to 2.2 and for both gas concentrations used.
- These results validate the new RAM nulling technique and the measurement procedures and signal analysis techniques developed for use with the RAM and PD methods.
- The results also fully validate the new model of the directly recovered RAM signals that provides correction factors to be applied to distorted line shapes up to  $m = 2.2$ . The use of these correction factors is also validated.

To conclude, the developed processes and procedures presented allow for the successful recovery of the absolute gas absorption line shape using the RAM or PD methods in conjunction with the new RAM nulling technique for  $m$  values up to 2.2. As a result of suppressing the RAM background the dynamic reserve of the LIA is increased and the sensitivity is improved giving rise to increased SNR and measurement sensitivity in principle.

The second aim was the investigation into the amplitudes of the recovered 1<sup>st</sup> and 2<sup>nd</sup> harmonic WM/IM signals and the RAM signal (extracted from

the concentration dependent RAM term of the 1<sup>st</sup> harmonic). As discussed previously, these signals could not be directly compared, as the harmonic signals were relative measurements, whereas the RAM signal was a measure of absolute transmission. The difference in signal recovery scaling factors between the harmonic signals was also an issue. To overcome these issues, the experimental signals were first scaled so they could be expressed as variations in optical power incident on the receiver. This enabled them to be directly compared with theoretical amplitudes generated from recently developed mathematical expressions and with each other.

The outcomes and key conclusions from Chapter 6 can be summarised as follows:

- These results further confirm validation of the new theoretical RAM signal model, particularly the expression for the peak RAM signal amplitude.
- It is clearly demonstrated that the 1<sup>st</sup> and 2<sup>nd</sup> harmonic WM/IM signal amplitudes are dependent on  $m$  and independent of modulation frequency and the RAM signal amplitude is dependent on both  $m$  and modulation frequency.
- In addition, the results validate the process used to generate scaling factors so the experimental signal amplitudes can be expressed in terms of absolute power variation as incident on the receiver.
- At modulation frequencies  $>100\text{kHz}$  the RAM signal is greater than/comparable to the 2<sup>nd</sup> harmonic WM/IM signal at all corresponding  $m$  values.
- At high modulation frequencies around 1MHz the RAM signal at  $m=0.5$  becomes comparable to the maximum possible 2<sup>nd</sup> harmonic WM/IM signal at  $m=2.2$ .

The main conclusion to take from the amplitude investigation is that at high modulation frequencies ( $>1\text{MHz}$ ) the recovered RAM signal offers the benefits of direct detection in terms of recovering the absolute gas absorption line shape complete with the high SNRs of a TDLS with WM system. Importantly, it can

offer high SNRs at low  $m$  values, which are comparable to the maximum possible 2<sup>nd</sup> harmonic WM/IM signal. Due to the low  $m$  values distortion effects are not present or minimal and can be corrected with little error.

## 7.2 Further Work

There are a number of possible areas for further work based on the research presented in this thesis. A natural next step would be the transfer of the developed RAM nulling analysis techniques to systems that use a different type of source laser. For example a quantum cascade laser (QCL) could be used to address the fundamental absorption lines in the MIR, a vertical cavity surface emitting laser (VCSEL) or vertical external cavity surface emitting laser (VECSEL) could be used to target the absorption lines in the NIR. These types of laser have their own advantages and disadvantages compared to the distributed feedback laser (DFB) used in this work. For example, the cost of a QCL is considerable greater compared to a DFB, however by using a QCL detection limits are greatly improved, important if trace gas emissions are the intended applications. A crucial element in the transfer of using a different laser compared to the DFB would be the ability to accurately characterise the new laser, as the above techniques require accurate knowledge of the laser operating parameters to successfully recover the absolute gas absorption line shapes.

A possible new direction for RAM nulling could be the development of a multi point and/or multi species detection system. As most practical applications using TDLS based system utilise more than one sensor, development would be required to engineer a solution that would allow the implementation of a number of sensors but possible only one delay branch used to achieve RAM nulling, to improve measurement sensitivity. Also, multi species applications are also in demand and work could be carried out on the implementation of a system that uses RAM nulling with a range of laser types to target the various gas species. By using a range of laser types, each laser would have its own set of characteristics, these

would have to be well evaluated and procedures devised that allowed integration of all lasers to work under the one system.

The RAM nulling technique presented is an optical approach to reduce noise on the system by suppressing the background RAM. There are areas for development including the automation of the VOA and PCs, through the use of feedback; this would make the system more applicable to practical applications as the system would be able to automatically adapt to fluctuations in the measurement signals. Another option to remove common noise and the background RAM is electrical cancellation. This could be implemented by using a balanced photo receiver arrangement.

Finally, a number of areas could be investigated with the aim of improving system performance of the existing experimental system. The first part would be an in depth investigation into noise effects on the experimental system. This would include identification of possible noise sources including  $1/f$  noise (laser), photodiode shot noise and thermal amplifier noise (both photodiode detector). Included in the investigation would be the development of procedures for measuring the level of noise present on the experimental signals, which would lead to quantifying the SNR of the system at different operating conditions. The aim of the investigation would be to identify if anything could be done to reduce the noise present on the system and to identify the optimum practical operating condition, which minimised the noise present on the recovered absorption signals. Another avenue of improvement would be the development of the correction factor implementation. As mentioned previous there are still some issues regarding the process in the accurate determination of  $m$  and recovering the correct line shape. These issues should hopefully be resolved in the near future as progress is currently being made on the correction factor implementation.

# References

- [1] D. S. Bomse, A. C. Stanton, and J. A. Silver, “Frequency modulation and wavelength modulation spectroscopies: comparison of experimental methods using a lead–salt diode laser,” *Applied Optics*, vol. 31, no. 6, pp. 718–731, 1992.
- [2] D. T. Cassidy and J. Reid, “Atmospheric pressure monitoring of trace gases using tunable diode lasers,” *Applied Optics*, vol. 21, no. 7, pp. 1185–1190, 1982.
- [3] E. D. Hinkley, “High–resolution infrared spectroscopy with a tunable diode laser,” *Applied Physics Letters*, vol. 16, no. 9, pp. 351–354, 1970.
- [4] M. Loewenstein, “Diode laser harmonic spectroscopy applied to in situ measurements of atmospheric trace molecules,” *Journal of Quantitative Spectroscopy and Radiative Transfer*, vol. 40, no. 3, pp. 249–256, 1988.
- [5] J. Reid, B. K. Garside, J. Shewchun, M. El-Sherbiny, and E. A. Ballik, “High sensitivity point monitoring of atmospheric gases employing tunable diode lasers,” *Applied Optics*, vol. 17, no. 11, pp. 1806–1810, 1978.
- [6] J. Reid, J. Shewchun, B. K. Garside, and E. A. Ballik, “High sensitivity pollution detection employing tunable diode lasers,” *Applied Optics*, vol. 17, no. 2, pp. 300–307, 1978.
- [7] P. Werle, F. Slemr, K. Maurer, R. Kormann, R. Mücke, and B. Jänker, “Near– and mid–infrared laser–optical sensors for gas analysis,” *Optics and Lasers in Engineering*, vol. 37, no. 2-3, pp. 101 – 114, 2002.

- [8] C. R. Webster, G. J. Flesch, D. C. Scott, J. E. Swanson, R. D. May, W. S. Woodward, C. Gmachl, F. Capasso, D. L. Sivco, J. N. Baillargeon, A. L. Hutchinson, and A. Y. Cho, “Quantum-cascade laser measurements of stratospheric methane and nitrous oxide,” *Applied Optics*, vol. 40, no. 3, pp. 321–326, 2001.
- [9] Q. Shi, D. D. Nelson, J. B. McManus, M. S. Zahniser, M. E. Parrish, R. E. Baren, K. H. Shafer, and C. N. Harward, “Quantum cascade infrared laser spectroscopy for real-time cigarette smoke analysis,” *Analytical Chemistry*, vol. 75, no. 19, pp. 5180–5190, 2003.
- [10] A. Lucchesini, I. Longo, C. Gabbanini, S. Gozzini, and L. Moi, “Diode laser spectroscopy of methane overtone transitions,” *Applied Optics*, vol. 32, no. 27, pp. 5211–5216, 1993.
- [11] A. Lucchesini, M. D. Rosa, D. Pelliccia, A. Ciucci, C. Gabbanini, and S. Gozzini, “Diode laser spectroscopy of overtone bands of acetylene,” *Applied Physics B: Lasers and Optics*, vol. 63, no. 3, pp. 277–282, 1996.
- [12] F. S. Pavone and M. Inguscio, “Frequency- and wavelength-modulation spectroscopies: Comparison of experimental methods using an algaas diode laser,” *Applied Physics B: Lasers and Optics*, vol. 56, no. 2, pp. 118–122, 1993.
- [13] X. Zhu and D. T. Cassidy, “Modulation spectroscopy with a semiconductor diode laser by injection-current modulation,” *Journal of the Optical Society of America B*, vol. 14, no. 8, pp. 1945–1950, 1997.
- [14] B. Culshaw, G. Stewart, F. Dong, C. Tandy, and D. Moodie, “Fibre optic techniques for remote spectroscopic methane detection—from concept to system realisation,” *Sensors and Actuators B: Chemical*, vol. 51, no. 1-3, pp. 25–37, 1998.
- [15] D. T. Cassidy and L. J. Bonnell, “Trace gas detection with short-external-cavity ingaasp diode laser transmitter modules operating at  $1.58\mu\text{m}$ ,” *Applied Optics*, vol. 27, no. 13, pp. 2688–2693, 1988.

## References

- [16] M. Gabrysch, C. Corsi, F. S. Pavone, and M. Inguscio, “Simultaneous detection of CO and CO<sub>2</sub> using a semiconductor DFB diode laser at 1.578 $\mu$ m,” *Applied Physics B: Lasers and Optics*, vol. 65, no. 1, pp. 75–79, 1997.
- [17] P. Werle, “A review of recent advances in semiconductor laser based gas monitors,” *Spectrochimica Acta Part A: Molecular and Biomolecular Spectroscopy*, vol. 54, no. 2, pp. 197–236, 1998.
- [18] G. Stewart, C. Tandy, D. Moodie, M. A. Morante, and F. Dong, “Design of a fibre optic multi-point sensor for gas detection,” *Sensors and Actuators B: Chemical*, vol. 51, no. 1-3, pp. 227–232, 1998.
- [19] W. Lenth, “Optical heterodyne spectroscopy with frequency- and amplitude-modulated semiconductor lasers,” *Optics Letters*, vol. 8, no. 11, pp. 575–577, 1983.
- [20] A. J. McGettrick, K. Duffin, W. Johnstone, G. Stewart, and D. G. Moodie, “Tunable diode laser spectroscopy with wavelength modulation: A phasor decomposition method for calibration-free measurements of gas concentration and pressure,” *Journal of Lightwave Technology*, vol. 26, no. 4, pp. 432–440, 2008.
- [21] K. Duffin, A. J. McGettrick, W. Johnstone, G. Stewart, and D. G. Moodie, “Tunable diode-laser spectroscopy with wavelength modulation: A calibration-free approach to the recovery of absolute gas absorption line shapes,” *Journal of Lightwave Technology*, vol. 25, no. 10, pp. 3114–3125, 2007.
- [22] P. Kluczynski and O. Axner, “Theoretical description based on fourier analysis of wavelength-modulation spectrometry in terms of analytical and background signals,” *Applied Optics*, vol. 38, no. 27, pp. 5803–5815, 1999.
- [23] S. Schilt, L. Thévenaz, and P. Robert, “Wavelength modulation spectroscopy: Combined frequency and intensity laser modulation,” *Applied Optics*, vol. 42, no. 33, pp. 6728–6738, 2003.

- [24] I. Linnerud, P. Kaspersen, and T. Jaeger, “Gas monitoring in the process industry using diode laser spectroscopy,” *Applied Physics B: Lasers and Optics*, vol. 67, no. 3, pp. 297–305, 1998.
- [25] J. T. C. Liu, J. B. Jeffries, and R. K. Hanson, “Large-modulation-depth 2f spectroscopy with diode lasers for rapid temperature and species measurements in gases with blended and broadened spectra,” *Applied Optics*, vol. 43, no. 35, pp. 6500–6509, 2004.
- [26] J. T. Liu, J. B. Jeffries, and R. K. Hanson, “Wavelength modulation absorption spectroscopy with 2f detection using multiplexed diode lasers for rapid temperature measurements in gaseous flows,” *Applied Physics B: Lasers and Optics*, vol. 78, no. 3, pp. 503–511, 2004.
- [27] L. C. Philippe and R. K. Hanson, “Laser diode wavelength-modulation spectroscopy for simultaneous measurement of temperature, pressure and velocity in shock-heated oxygen flows,” *Applied Optics*, vol. 32, no. 30, pp. 6090–6103, 1993.
- [28] G. B. Rieker, J. B. Jeffries, and R. K. Hanson, “Calibration-free wavelength-modulation spectroscopy for measurements of gas temperature and concentration in harsh environments,” *Applied Optics*, vol. 48, no. 29, pp. 5546–5560, 2009.
- [29] C. B. Carlisle and D. E. Cooper, “Tunable diode laser frequency modulation spectroscopy through an optical fiber: High-sensitivity detection of water vapor,” *Applied Physics Letters*, vol. 56, no. 9, pp. 805–807, 1990.
- [30] P. C. D. Hobbs, “Shot noise limited optical measurements at baseband with noisy lasers (proceedings only),” in *Laser Noise*, vol. 1376, (Boston, MA, USA), pp. 216–221, SPIE, 1991.
- [31] P. C. Hobbs, “Ultrasensitive laser measurements without tears,” *Appl. Opt.*, vol. 36, no. 4, pp. 903–920, 1997.
- [32] X. Zhu and D. T. Cassidy, “Electronic subtracter for trace-gas detection

## References

- with InGaAsP diode lasers,” *Applied Optics*, vol. 34, no. 36, pp. 8303–8308, 1995.
- [33] C. N. Banwell and E. M. McCash, *Fundamentals of Molecular Spectroscopy: Fourth Edition*. McGraw-Hill, 1994.
- [34] B. P. Straughan and S. Walker, *Spectroscopy Volume Two: Molecular, Microwave, Infrared, Far-infrared and Raman Spectroscopy, Force Constants, Group Theory, and Thermodynamic Functions*. Chapman and Hall Ltd., 1976.
- [35] G. M. Barrow, *Introduction to Molecular Spectroscopy, International Student Edition*. McGraw Hill Kogakusha Ltd., 1962.
- [36] E. D. Hinkley, *Laser Monitoring of the Atmosphere: Topics in Applied Optics, Volume 14*. Springer Verlag Berlin Heidelberg, New York, 1976.
- [37] U. L. A. Thorne and S. Johansson, *Spectrophysics: Principles and Applications*. Springer Verlag Berlin Heidelberg, New York, 1999.
- [38] B. Bransden and C. Joachain, *Physics of Atoms and Molecules: Second Edition*. Benjamin Cummings, 2003.
- [39] K. Duffin, *Wavelength Modulation Spectroscopy with Tunable Diode Lasers: a Calibration-Free Approach to the Recovery of Absolute Gas Absorption Line-Shapes*. PhD thesis, University of Strathclyde, 2007.
- [40] A. McLean, C. Mitchell, and D. Swanston, “Implementation of an efficient analytical approximation to the voigt function for photoemission lineshape analysis,” *Journal of Electron Spectroscopy and Related Phenomena*, vol. 69, no. 2, pp. 125–132, 1994.
- [41] Private communication between Dr Michael Lengden and the author.
- [42] L. S. Rothman, D. Jacquemart, A. Barbe, D. Chris Benner, M. Birk, L. R. Brown, M. R. Carleer, J. C. Chackerian, K. Chance, L. H. Coudert, V. Dana, V. M. Devi, J. M. Flaud, R. R. Gamache, A. Goldman, J. M. Hartmann, K. W. Jucks, A. G. Maki, J. Y. Mandin, S. T. Massie, J. Orphal, A. Perrin,

## References

- C. P. Rinsland, M. A. H. Smith, J. Tennyson, R. N. Tolchenov, R. A. Toth, J. Vander Auwera, P. Varanasi, and G. Wagner, “The hitran 2004 molecular spectroscopic database,” *Journal of Quantitative Spectroscopy and Radiative Transfer*, vol. 96, no. 2, pp. 139–204, 2005.
- [43] W. Johnstone, A. J. McGettrick, K. Duffin, A. Cheung, and G. Stewart, “Tunable diode laser spectroscopy for industrial process applications: System characterization in conventional and new approaches,” *IEEE Sensors Journal*, vol. 8, no. 7, pp. 1079–1088, 2008.
- [44] G. Jacobsen, H. Olesen, F. Birkedal, and B. Tromborg, “Current/frequency-modulation characteristics for directly optical frequency-modulated injection lasers at 830nm and 1.3 $\mu$ m,” *Electronics Letters*, vol. 18, no. 20, pp. 874–876, 1982.
- [45] S. Kobayashi, Y. Yamamoto, M. Ito, and T. Kimura, “Direct frequency modulation in algaas semiconductor lasers,” *IEEE Journal of Quantum Electronics*, vol. QE-18, no. 4, pp. 582–595, 1982.
- [46] M. Ito and T. Kimura, “Carrier density dependence of refractive index in algaas semiconductor lasers,” *IEEE Journal of Quantum Electronics: Quantum Electronics Letters*, vol. QE-16, no. 9, pp. 910–911, 1980.
- [47] Private communication between Prof. George Stewart and the author.
- [48] E. Kreyszig, *Advanced Engineering Mathematics*. John Wiley and Sons, 1967.
- [49] R. Arndt, “Analytical line shapes for lorentzian signals broadened by modulation,” *Journal of Applied Physics*, vol. 36, no. 8, pp. 2522–2524, 1965.
- [50] J. S. Margolis, “Measured line positions and strengths of methane between 5500 and 6180 cm<sup>-1</sup>,” *Applied Optics*, vol. 27, no. 19, pp. 4038–4051, 1988.
- [51] JDS Uniphase, *Butterfly Laser Modules: DC Operating Instructions*, August 2000.
- [52] Red Optronics, *C-Lens*. <http://www.redoptronics.com/c-lens.html>.

## *References*

- [53] P. Urquhart, “Compound optical-fiber-based resonators,” *Journal of the Optical Society of America A*, vol. 5, no. 6, pp. 803–812, 1988.
- [54] L. F. Stokes, M. Chodorow, and H. J. Shaw, “All-single-mode fiber resonator,” *Optics Letters*, vol. 7, no. 6, pp. 288–290, 1982.
- [55] P. Urquhart, “Transversely coupled fiber fabry-perot resonator: theory,” *Applied Optics*, vol. 26, no. 3, pp. 456–463, 1987.

# Appendix A

## Publications

### Journal Publications

G. Stewart, W. Johnstone, J. R. P. Bain, K. Ruxton and K. Duffin, “*Recovery of Absolute Gas Absorption Line Shapes Using Tuneable Diode Laser Spectroscopy with Wavelength Modulation Part I: Theoretical Analysis*”, Submitted to IEEE Journal of Lightwave Technology, August 2010.

J. R. P. Bain, W. Johnstone , K. Ruxton, G. Stewart, M. Lengden and K. Duffin, “*Recovery of Absolute Gas Absorption Line Shapes Using Tuneable Diode Laser Spectroscopy with Wavelength Modulation Part 2: Experimental Investigation*”, Submitted to IEEE Journal of Lightwave Technology, August 2010.

M. Lengden, W. Johnstone, J. Black, J. R. P. Bain, I. Armstrong, K. Ruxton and R. Cunningham, “*Investigations into high temperature methane spectra around 6060cm<sup>-1</sup> for gas sensing applications*”, Submitted to Applied Optics, June 2010.

K. Ruxton, A. L. Chakraborty, W. Johnstone, M. Lengden, G. Stewart, K. Duffin, “*Tunable Diode Laser Spectroscopy with Wavelength Modulation: Elimination of Residual Amplitude Modulation in a Phasor Decomposition Approach*”, Sensors and Actuators B: Chemical, Vol. 150, No. 1, pp367-375, September 2010. DOI: 10.1016/j.snb.2010.06.058.

## Appendix A. Publications

A. L. Chakraborty, K. Ruxton and W. Johnstone, “*Suppression of intensity modulation contributions to signals in second harmonic wavelength modulation spectroscopy*”, Optics Letters, Vol. 35, No. 14 pp2400-2402, July 2010. DOI: 10.1364/OL.35.002400.

I. Armstrong, W. Johnstone, K. Duffin, M. Lengden, A. L. Chakraborty and K. Ruxton, “*Detection of CH<sub>4</sub> in the Mid-IR using Difference Frequency Generation with Tunable Diode Laser Spectroscopy*”, IEEE Journal of Lightwave Technology, Vol. 28, No. 10, pp1435-1442, February 2010. DOI: 10.1109/JLT.2010.2042789.

A. L. Chakraborty, K. Ruxton and W. Johnstone, “*Influence of the wavelength-dependence of fiber couplers on the background signal in wavelength modulation spectroscopy with RAM-nulling*”, Optics Express, vol. 18, no. 1, pp267-280, January 2010. DOI: 10.1364/OE.18.000267.

A. L. Chakraborty, K. Ruxton, W. Johnstone, M. Lengden and K. Duffin, “*Elimination of residual amplitude modulation in tunable diode laser wavelength modulation spectroscopy using an optical fiber delay line*”, Optics Express, vol. 17, no. 12, pp9602-9607, June 2009. DOI: 10.1364/OE.17.009602.

## Conference Publications

K. Ruxton, A. L. Chakraborty, W. Johnstone and G. Stewart, “*Tunable diode laser spectroscopy with wavelength modulation: an overview of current techniques and motivations*”, Photon10, Southampton, UK, 23-26 August 2010.

K. Ruxton, A.L. Chakraborty, A.J. McGettrick, K. Duffin, W. Johnstone and G. Stewart, “*Recent advance in tunable diode-laser spectroscopy with background RAM nulling for industrial applications*”, Twentieth Conference on Optical Fibre Sensors, Edinburgh, UK, 5-9 October 2009. DOI: 10.1117/12.833000.

A.L. Chakraborty, K. Ruxton and W. Johnstone, “*Tunable diode laser spectroscopy with RAM nulling current status and future possibilities*”, International Conference on Field Laser Applications in Industry and Research,

*Appendix A. Publications*

Grainau, Germany, 6-11 September 2009.

J.R.P. Bain, G. Stewart, K. Duffin, M. Lengden, K. Ruxton and W. Johnstone, “*Recovery of absolute gas absorption lineshapes using TDLS at arbitrary modulation indices*”, International Conference on Field Laser Applications in Industry and Research, Grainau, Germany, 6-11 September 2009.

I. Armstrong, A. Chakraborty, K. Ruxton, and W. Johnstone, “*An investigation of TDLS modulation schemes as applied to the Mid-IR spectral region by difference frequency generation in PPLN*”, 7th International Conference on Tunable Diode Laser Spectroscopy (TDLS), Zermatt, Switzerland, 13-17 July 2009.

K. Ruxton, A. L. Chakraborty, A. J. McGettrick, K. Duffin, W. Johnstone and G. Stewart, “*Diode laser spectroscopy using a calibration free phasor decomposition approach with RAM nulling*”, 7th International Conference on Tunable Diode Laser Spectroscopy (TDLS), Zermatt, Switzerland, 13-17 July 2009.

A. L. Chakraborty, K. Ruxton, W. Johnstone, M. Lengden and K. Duffin, “*Elimination of residual amplitude modulation in TDLS-WMS*”, Conference on Lasers and Electro-Optics/ European Quantum Electronics Conference (CLEO Europe/EQEC-2009), Munich, Germany, 14-19 June 2009.

# Appendix B

## $2^{nd}$ order Taylor series expansion of Lorentzian line shape

The laser output intensity can be written as:

$$I = I(\lambda_c) + \Delta I(\lambda_c)\cos(\omega t) \quad (\text{B.1})$$

The intensity at the receiver after going through an absorbing gas:

$$I_o = [I(\lambda) + \Delta I(\lambda)\cos(\omega t)][1 - \alpha(\lambda)Cl] \quad (\text{B.2})$$

A Taylor series expansion for  $\alpha(\lambda)$  around  $\lambda_c$  is given by:

$$\alpha(\lambda) = \alpha(\lambda_c) + \alpha'(\lambda)|_{\lambda_c}[\lambda - \lambda_c] + \frac{1}{2} \alpha''|_{\lambda_c}[\lambda - \lambda_c]^2 + \dots \quad (\text{B.3})$$

Therefore:

$$\begin{aligned} I_o \approx & [I(\lambda_c) + \Delta I(\lambda_c)\cos(\omega t)] \\ & [1 - \alpha(\lambda_c)Cl - \alpha'(\lambda)|_{\lambda_c}Cl\delta\lambda(\lambda_c)(\cos(\omega t - \psi) \\ & - \frac{1}{2} \alpha''(\lambda)|_{\lambda_c}Cl\delta\lambda^2(\lambda_c)\cos^2(\omega t - \psi)] \end{aligned} \quad (\text{B.4})$$

Multiplying out the bracketed terms in equation (B.4) gives:

$$\begin{aligned} I_o = & I(\lambda_c) + \Delta I(\lambda_c)\cos(\omega t) - I(\lambda_c)\alpha(\lambda_c)Cl - \Delta I(\lambda_c)\alpha(\lambda_c)Cl\cos(\omega t) \\ & - I(\lambda_c)\alpha'(\lambda)|_{\lambda_c}Cl\cos(\omega t - \psi) - \Delta I(\lambda_c)\alpha'(\lambda)|_{\lambda_c}Cl\delta\lambda(\lambda_c)\cos(\omega t)\cos(\omega t - \psi) \\ & - \frac{1}{2} I(\lambda_c)\alpha''(\lambda)|_{\lambda_c}Cl\delta\lambda^2(\lambda_c)\cos^2(\omega t - \psi) \\ & - \frac{1}{2} \Delta I(\lambda_c)\alpha''(\lambda)|_{\lambda_c}Cl\delta\lambda^2(\lambda_c)\cos(\omega t)\cos^2(\omega t - \psi) \end{aligned} \quad (\text{B.5})$$

Using the trigonometric identities:

$$\begin{aligned}\cos(\omega t)\cos(\omega t - \psi) &= \frac{1}{2} [\cos(2\omega t - \psi) + \cos\psi] \\ \cos^2(\omega t - \psi) &= \frac{1}{2} [1 + \cos 2(\omega t - \psi)]\end{aligned}$$

Equation (B.5) becomes:

$$\begin{aligned}I_o &= I(\lambda_c) + \Delta(\lambda_c)\cos(\omega t) - I(\lambda_c)\alpha(\lambda_c)Cl - \Delta I(\lambda_c)\alpha(\lambda_c)Cl\cos(\omega t) \\ &\quad - I(\lambda_c)\alpha'(\lambda)|_{\lambda_c}Cl\delta\lambda(\lambda_c)(\omega t - \psi) \\ &\quad - \frac{1}{2} \Delta I(\lambda_c)\alpha'(\lambda)|_{\lambda_c}Cl\delta\lambda(\lambda_c)[\cos(2\omega t - \psi) + \cos\psi] \\ &\quad - \frac{1}{4} I(\lambda_c)\alpha''(\lambda)|_{\lambda_c}Cl\delta\lambda^2(\lambda_c)[1 + \cos 2(\omega t - \psi)] \\ &\quad - \frac{1}{4} \Delta I(\lambda_c)\alpha''(\lambda)|_{\lambda_c}Cl\delta\lambda^2(\lambda_c) \left[ \cos(\omega t) + \frac{1}{2} \{ \cos(3\omega t - 2\psi) + \cos(2\psi - \omega t) \} \right]\end{aligned}\tag{B.6}$$

The DC component is given by:

$$I_{DC} = I(\lambda_c)[1 - \alpha(\lambda_c)Cl]\tag{B.7}$$

The  $1^{st}$  harmonic expression is given by:

$$\begin{aligned}I_\omega &= \Delta I(\lambda_c)\cos(\omega t) - \Delta I(\lambda_c)Cl\cos(\omega t) \\ &\quad - I(\lambda_c)\alpha'(\lambda)|_{\lambda_c}Cl\delta\lambda(\lambda_c)\cos(\omega t - \psi)\end{aligned}\tag{B.8}$$

The  $2^{nd}$  harmonic expression is given by:

$$\begin{aligned}I_{2\omega} &= -\frac{1}{2} \Delta I(\lambda_c)\alpha'(\lambda)|_{\lambda_c}Cl\delta\lambda(\lambda_c)\cos(2\omega t - \psi) \\ &\quad - \frac{1}{4} I(\lambda_c)\alpha''(\lambda)|_{\lambda_c}Cl\delta\lambda^2(\lambda_c)\cos 2(\omega t - \psi)\end{aligned}\tag{B.9}$$

The remaining terms are considered negligible for small  $\delta\lambda(\lambda_c)$ :

$$\begin{aligned}I &= -\frac{1}{2} \Delta I(\lambda_c)\alpha'(\lambda)|_{\lambda_c}Cl\delta\lambda(\lambda_c)\cos\psi \\ &\quad - \frac{1}{4} I(\lambda_c)\alpha''(\lambda)|_{\lambda_c}Cl\delta\lambda^2(\lambda_c) \\ &\quad - \frac{1}{4} \Delta I(\lambda_c)\alpha''(\lambda)|_{\lambda_c}Cl\delta\lambda(\lambda_c) \left[ \cos(\omega t) + \frac{1}{2} \{ \cos(3\omega t - 2\psi) + \cos(2\psi - \omega t) \} \right]\end{aligned}\tag{B.10}$$

# Appendix C

## MATLAB code - RAM technique with RAM Nulling

```
%-----  
%   RAM technique with RAM nulling  
%   Andrew J McGettrick, Kevin Duffin, Michael Lengden, Keith Ruxton  
%   and James Bain  
%-----  
  
clc  
clear  
close all  
format long  
  
c_AIR = 0.91; % Broadening coefficient for nitrogen  
  
starttrim = 501;  
stoptrim = 8500;  
  
% reading in all user data  
[inputnumber,inputtext] = xlsread('parameters_RAM_null.xls', 'a1:b19');  
input_text = char(inputtext);  
  
%-----  
%   Generate theory file  
%-----  
  
% 1.1 Reading in Hitran Data for region of interest  
methanelines = xlsread('methanelines.xls');  
z = length(methanelines);  
  
% 1.2 Defining all constants  
k = 1.3806503e-23; %Boltzmann  
M = 16; %Mass  
c = 299792458e2; %Speed of light  
h = 6.626e-34; %Planck
```

### Appendix C. MATLAB code - RAM technique with RAM Nulling

```
L = 9.9; %Length of cell

% 1.3 Defining temperature
T_0 = 296; % Reference Temperature in Kelvin
T_K = 273.15; %0 degrees celcius in Kelvin
degreeT = inputnumber(15); %input('\n Temperature in Celsius: ');
T = degreeT+T_K; %Converting to Kelvin

% 1.4 Reading in pressure and converting from bar to atm
pressure = inputnumber(14)*0.986926; %atm

    %1.4.1 Pressure range for fitting loop
    coeff = linspace(pressure-0.1,pressure+0.1,50);

    %1.4.2 Defining Start Concentrations
    actual_methane_concentration=[0,0.5,1];

    %1.4.2 Defining Start Concentrations
    methane_concentration = inputnumber(16)/100;%0.1013;
    nitrogen_concentration = 1-methane_concentration;

% 1.5 Frequency Range
vsteps = 2000;
v = linspace(6054,6064,vsteps); %theory frequency range
lambda = 1./v.*1e7;

% 1.6 Calculation of individual line-strengths
Q_T0 = (7.0192e-9*T_0^4)-(3.6651e-6*T_0^3)+(0.0031476*T_0^2)+(1.4428*T_0)-71.184;
Q_T = (7.0192e-9*T^4)-(3.6651e-6*T^3)+(0.0031476*T^2)+(1.4428*T)-71.184;
S1 = 1-exp(-(h*c.*methanelines(:,1))/(k*T));
S2 = 1-exp(-(h*c.*methanelines(:,1))/(k*T_0));
S3 = S1./S2;
S4 = Q_T0./Q_T;
S5 = T_0/T;
S6 = exp((-h*c*methanelines(:,5)/k)*((1/T)-(1/T_0)));
S7 = S3.*S4.*S5.*S6;
S_T=S7.*methanelines(:,2); %Total linestrength

% 1.7 Calculation of Broadening Parameters

    %1.7.1 Gaussian Broadening
    gammag = 7.1625e-7.*methanelines(:,1).*(T/16)^0.5;
    gammag = gammag';

    %1.7.2 Air broadening parameter
    air_broadening_parameter = c_AIR*methanelines(:,3).*(T_0/T).^0.73;

    %1.7.3 Self Broadening parameter
    self_broadening_parameter = methanelines(:,4).*(T_0/T)^0.8;

    %1.7.4 Lorentzian Broadening
    gammal = 2*pressure.*((air_broadening_parameter*nitrogen_concentration)
    +(self_broadening_parameter*methane_concentration));
    gammal = gammal';

% 1.8 X values for Voigt Profile
```

### Appendix C. MATLAB code - RAM technique with RAM Nulling

```
for j = 1:z
    X(:,j) = 2*sqrt(log(2))*(v-methanelines(j,1)-methanelines(j,7))./gammag(j);
end

% 1.9 A-D values for Voigt Profile
A = [-1.2150 -1.3509 -1.2150 -1.3509];
B = [1.2359 0.3786 -1.2359 -0.3786];
C = [-0.3085 0.5906 -0.3085 0.5906];
D = [0.0210 -1.1858 -0.0210 1.1858];

% 1.10 Final voigt Y-value
Y = (gammal./gammag)*sqrt(log(2));

% 1.11 final voigt V-value
for j = 1:z
    for i = 1:4
        V_top(i,:) = (C(i)*(Y(j)-A(i)))+(D(i)*(X(:,j)-B(i)));
        V_bottom(i,:) = (Y(j)-A(i))^2+(X(:,j)-B(i)).^2;
    end

    V = V_top./V_bottom;
    Vfinal(:,j) = (2/gammag(j))*(log(2)/pi)^0.5*methane_concentration
        *(7.339e21/T_0)*S_T(j)*sum(V);
end

% 1.12 Final spectral absorption coefficient
kv = pressure*sum(Vfinal');

% 1.13 Final fractional transmission
T = exp(-kv.*L);

theory_lambda = lambda;
theory_amps = T;

%-----
%           Data Input, Filtering and Processing
%-----

% Input of resonator signal and trimming ends of data
res = dlmread('res');
res=res(starttrim:stoptrim);

% Filtering reonator to remove spurious peaks
[b1 a1] = ellip(2,0.1,90,0.02);
res_avg = filtfilt(b1,a1,res);

[b2 a2] = ellip(2,0.00002,60,0.001);

sep_FM_sens = inputnumber(1,2);

% Reading in Channel 1 of LIA data is filterd and trimmed
AM_FM1 = dlmread(input_text(1,:));
AM_FM2 = AM_FM1(starttrim:stoptrim);
AM_FM = filtfilt(b2,a2,AM_FM2);
xx=length(AM_FM2);
```

*Appendix C. MATLAB code - RAM technique with RAM Nulling*

```
AM_FM3 = dlmread(input_text(2,:));
AM_FM_nogas = AM_FM3(starttrim:stoptrim);
AM_FM_nogas = filtfilt(b2,a2,AM_FM_nogas);

AM_whole = AM_FM - AM_FM_nogas;

figure
hold on;
plot(AM_FM,'r')
plot(AM_FM_nogas,'g')
plot(AM_whole,'b')
title('RAM')

X_LIA_sens = sep_FM_sens;

%-----code to base fit the OP2 data-----
nogas_OP2 = dlmread(input_text(10,:));
nogas_OP2 = nogas_OP2(starttrim:stoptrim);
nogas_OP2 = filtfilt(b2,a2,nogas_OP2);

b = nogas_OP2;
OP2_nogas_sens = inputnumber(8,2);
%-----

%-----fitting for OP1 no gas break arm 2-----
no_gas_OP1 = dlmread(input_text(6,:));
no_gas_OP1 = no_gas_OP1(starttrim:stoptrim);
no_gas_OP1 = filtfilt(b2,a2,no_gas_OP1);

cc = no_gas_OP1;

OP1_nogas_sens = inputnumber(4,2);
%-----end-----

% Create array with all signal sensitivities
sens_factors = [sep_FM_sens X_LIA_sens OP2_nogas_sens OP1_nogas_sens];
max_sens = max(sens_factors); % Find maximum sensitivity

% Scale all signals to match sensitivity
direct_absorption_signal_amps = direct_absorption_signal_amps / (max_sens / X_LIA_sens);
cc = cc / (max_sens / OP1_nogas_sens);
b = b / (max_sens / OP2_nogas_sens);

% 5.4 Trim O/P2 No gas
OP2_nogas_trim = [b];

% 5.5 Trim O/P1 No gas Break Arm 2
OP1_nogas_trim = [cc];

% 5.6 Calculate ratio to scale O/P1 gas
ratio1 = OP2_nogas_trim ./ OP1_nogas_trim;
min_ratio1 = mean(ratio1);
)

part1 = direct_absorption_signal_amps ./ OP2_nogas_trim;%nogas_OP2;
part2 = part1 .* min_ratio1;
```

### Appendix C. MATLAB code - RAM technique with RAM Nulling

```
gas = part2;

RAM_no_gas_amps = AM_FM_nogas;

%-----
%      Wavelength Referencing
%-----

% 3.1 Find Peaks
diff_res = diff(res_avg);
peak      = [];

for n = 1:length(diff_res)-1
    if ( ne(sign(diff_res(n)),sign(diff_res(n+1))) && (diff_res(n) > diff_res(n+1)) )
        peak = [peak n+1];
    end
end

% 3.2 Define x and y values of peaks
JJ = peak;
resonator_peak(:,:)=res_avg(JJ(:,:));

% 3.3 Plot the Resonator scan and show the identified peaks
% figure
% hold on
% plot(JJ,resonator_peak,'o')
% plot(res_avg,'r')
% plot(res)

% 3.4 Defining the peak line centre in wavelength and frequency
Line_Cent_Wave = 1.650958773750263e+003;
Line_Cent_Freq = 3e8./(Line_Cent_Wave);

% 3.5 Find the line centre index from the experimental plot
Q = min(gas);
Q_Index = find(gas == Q);
Line_Cent_Index = Q_Index(1);

% 3.6 Find resonator peak location of closest resonator peak to the line
%       centre of the experimental plot
[error1, closest_peak]=min(abs(JJ-Line_Cent_Index));

% 3.7 Convert resonator peak indices to frequencies
% 3.7.1 Frequency spacing
delta_f= 0.4275;

% 3.7.2 Declare vector for storing frquencies
Res_Peak_Wave = [];
Res_Peak_Wave(closest_peak)=150000;

FF=length(JJ)+1;
nn=1;

while nn < FF
    if nn<closest_peak
        Res_Peak_Wave(nn)=[150000+((closest_peak-nn)*delta_f)];
    end
    nn=nn+1;
end
```

### Appendix C. MATLAB code - RAM technique with RAM Nulling

```
end;

if nn>closest_peak
    Res_Peak_Wave(nn)=[150000-((nn-closest_peak)*delta_f)];
end;
nn=nn+1;
end;

% 3.7.3 resonator frequencies
P=polyfit(JJ,Res_Peak_Wave,2);
x=[1:1:xx];
YYY=polyval(P, x);

% 3.8 Shift this polynomial to match the experimental plot at line centre and outwards
shift = Line_Cent_Freq-YYY(Line_Cent_Index);
YYY = YYY+shift;

% 3.9 Wavelength values for each data channel
YYY_wavelength = 3e8./YYY;

% 3.9 Wavelength values for each data channel
XXX = 3e8./YYY;
% sep_FM = [XXX' sep_FM];
%
% figure
% plot(gas)
% title('before shift')

% 5.4.7 Find indices for the theoretical wavelengths that match two ends of
% experimental data
IND1 = find(lambda <= YYY_wavelength(1));
IND1 = IND1(1);
IND2 = find(lambda <= YYY_wavelength(xx));
IND2 = IND2(1);
% 5.4.8 Calculate the wavelengths and amplitudes of the theory data in range
% of experimental data
cut_theory_lambda = linspace(lambda(IND2),lambda(IND1),IND1-IND2+1);
cut_theory_amps = theory_amps(IND2:IND1);
% 5.4.9 Interpolating theory data over length of experimental
% data, making sets of data over equal range and equal length
amps_chopped = interp1(cut_theory_lambda,cut_theory_amps,YYY_wavelength,'linear','extrap');

% 5.4.10 Setting the experimental baseline to theoretical
% baseline
gap = gas(1800) - amps_chopped(1800);

normalised_direct_absorption = gas+abs(gap);

% [error1, RAM_Start_Index] = min(abs(theory_lambda - XXX(1)));
% Vertical_Shift = abs(theory_amps(RAM_Start_Index) - normalised_direct_absorption(1));
%
% if normalised_direct_absorption(1) > theory_amps(RAM_Start_Index)
%     % 10.1.1 If Experiment above Theory shift Experimental values down
%     normalised_direct_absorption = normalised_direct_absorption - Vertical_Shift;
% else
%     % 10.1.2 If Experiment below Theory shift Experimental values up
```

### Appendix C. MATLAB code - RAM technique with RAM Nulling

```
%    normalised_direct_absorption = normalised_direct_absorption + Vertical_Shift;
% end

% figure
% plot(normalised_direct_absorption);
% title('Plot of calculated RAM');

% 1.5 Read in channel X
X_LIA_axis = AM_whole;
X_LIA_axis = [XXX' X_LIA_axis];

% 1.6 Separate the files into frequencies and amplitudes
X_LIA_axis_amps = X_LIA_axis(:,2)';

% convert from wavelength to frequency
X_LIA_axis_frequencies = 3e8 ./ (X_LIA_axis(:,1)' * 1e-9)';
% sep_FM_amps = sep_FM(:,2)';
% sep_FM_amps = sep_FM_amps * -1;

% convert from wavelength to frequency
sep_FM_frequencies = 3e8 ./ (X_LIA_axis(:,1)' * 1e-9)';

%-----
%          Correction Factors
%-----

% 10.2.3 Ask user for current dither size
current_dither_size= inputnumber(6)/2;

% 10.2.5 separate frequencies and amplitudes into different vectors
sep_AM_freqs = YYY * 1e9; %sep_FM_frequencies;
sep_AM_amps = gas;
sep_AM_waves = 1e9*(3e8./sep_AM_freqs);

% 10.2.6 Read in delta_nu/delta_i value,obtained previously from laser
% characterisation procedure
del_nu= inputnumber(9);
del_nu = del_nu * current_dither_size;
del_nu = del_nu * 1e9;
del_nu_cm = del_nu/3e10;

% Assume constant gamma (GHz)
% Probably best going for 2.1-2.2 GHz for 1% CH_4 and 2.4-2.5 GHz for 10%
gamma = 2.2511;
gamma = 1e9*gamma;
gamma_cm = 1e9*gamma/3e10;

% Calculate HWHM magnitude as frequency difference between FWHM_freq and line centre
line_cent_index_1=find(sep_AM_amps==min(sep_AM_amps));
line_cent_freq=sep_AM_freqs(line_cent_index_1(1));
line_cent_freq=line_cent_freq(1);

% Set up correction integral
I_min = min(sep_AM_amps);
sep_AM_amps_corrected(:,1) = normalised_direct_absorption;
multiplier1 = linspace(1,1,length(normalised_direct_absorption));
multiplier2 = linspace(1,1,360);
```

### Appendix C. MATLAB code - RAM technique with RAM Nulling

```
theta = linspace(0,pi,360);
theta_x = theta';
theta_x = theta_x*multiplier1;

% -----determining m-----
if inputnumber(11) == 1
    %-----start of m code least squares method-----
    % Define arbitrary Lorentzian on which to apply distortions
    m_ref = 0.1;
    ref_peak_depth = 0.997;
    A_2 = -log(ref_peak_depth);

    % Calculate line centre frequency
    line_cent_index_1=find(sep_AM_amps==min(sep_AM_amps));
    line_cent_freq=sep_AM_freqs(line_cent_index_1(1));
    line_cent_freq=line_cent_freq(1);

    % Define delta for reference signal
    % HWHM_ref = gamma*1e9;
    HWHM_ref = del_nu/m_ref;
    delta_0_ref = (sep_AM_freqs-line_cent_freq)./HWHM_ref;
    delta_ref = delta_0_ref;
    delta_ref = delta_ref'*multiplier2;
    delta_ref = delta_ref';

    % Define a_0
    y_0 = 1./(1+((delta_ref+m_ref.*cos(theta_x)).^2));
    z_0 = trapz(theta,y_0);
    a_0 = (1./pi).*z_0;

    % Define a_2
    y_2 = cos(2.*theta_x)./(1+((delta_ref+m_ref.*cos(theta_x)).^2));
    z_2 = trapz(theta,y_2);
    a_2 = (2./pi).*z_2;

    % Define simulated first harmonic signal amplitudes
    I_ref(:,1) = 1-A_2.*(a_0-(a_2./2));
    I_ref_min = min(I_ref);

    % Normalising the reference Lorentzian to the signal to be corrected
    ratio = (1-I_min)./(1-I_ref_min);
    I_ref = (1-I_ref).*ratio;
    I_ref = 1-I_ref;

    % Define arbitrarily high initial value for 'sum_errors' for implementing a
    % while loop
    sum_errors = 100;

    % Measure the amplitude error between the corrected signal and the
    % equivalent simulated Lorentzian, then take the square and sum over many
    % points around line-centre.
    errors = I_ref-sep_AM_amps_corrected;
    errors = errors.^2;
    sum_errors(:,2) = sum(errors);

    % Open while loop to do additional iterations. By defining an artificially
```

Appendix C. MATLAB code - RAM technique with RAM Nulling

```

% high initial value for sum_errors, the loop can be terminated when the
% sum of squared errors reaches a minimum value (i.e. when the corrected
% signal most closely approximates a pure Lorentzian)
i = 2;
while sum_errors(:,i)<sum_errors(:,i-1)
    % 10.3.5 Define incremental m values from previously obtained m and then
    % calculate the equivalent HWHM
    m_ref(:,i) = m_ref(:,i-1)+0.05;
    HWHM_ref = del_nu/m_ref(:,i);
    delta_0_ref = (sep_AM_freqs-line_cent_freq)/HWHM_ref;
    delta_ref = delta_0_ref;
    delta_ref = delta_ref'*multiplier2;
    delta_ref = delta_ref';

    % Define a_0
    y_0 = 1./(1+((delta_ref+m_ref(:,i)).*cos(theta_x)).^2));
    z_0 = trapz(theta,y_0);
    a_0 = (1./pi).*z_0;

    % Define a_2
    y_2 = cos(2.*theta_x)./(1+((delta_ref+m_ref(:,i)).*cos(theta_x)).^2));
    z_2 = trapz(theta,y_2);
    a_2 = (2./pi).*z_2;

    % Define simulated first harmonic signal amplitudes
    I_ref(:,i) = 1-A_2.*(a_0-(a_2./2));
    I_ref_min(:,i) = min(I_ref(:,i));

    % Normalising the reference Lorentzian to the signal to be corrected
    ratio(:,i) = (1-I_min)./(1-I_ref_min(:,i));
    I_ref(:,i) = (1-I_ref(:,i)).*ratio(:,i);
    I_ref(:,i) = 1-I_ref(:,i);

    errors = I_ref(:,i)-sep_AM_amps_corrected;
    errors = errors.^2;
    sum_errors(:,i+1) = sum(errors);

    i = i+1;
end

m_ref(:,i-2)
m = m_ref(:,i-2);

% Split reference into wavelengths and amplitudes
point2_waves = theory_lambda;
point2_amps = theory_amps;

point2_min = min(point2_amps);
A = -log(point2_min);

% figure
% plot(m_ref, sum_errors(2:i))
% title('Plot of Summed Squared Errors with m (Simulated Lorentzian at Low Conc)')
% xlabel('m')
% ylabel('Summed Square Errors')
%-----end of m code least squares method-----

```

Appendix C. MATLAB code - RAM technique with RAM Nulling

```

else
    % -----start of m code ratio method-----
    % ref file
    % point2 = xlsread('direct_result.xls');

    % Split into wavelengths and amplitudes
    point2_waves = theory_lambda;
    point2_amps = theory_amps;

    point2_min = min(point2_amps);
    distorted_min = min(sep_AM_amps_corrected(:,1));
    % Calculate 'A' factor; A=alphaCl
    A = -log(point2_min);
    % Calculate ratio
    ratio = (1-distorted_min)/A;
    % Define number of reference points in look-up table
    n_increments =1000;

    for n = 1:n_increments
        bbb = 2.5/n_increments;
        m(:,n) = 0+(bbb*n);

        y = (sin(theta).^2).*(1-exp(-A./(1+(m(:,n)^2).*(cos(theta).^2))));
        z_corr = trapz(theta,y);
        P_m(:,n) = (2/(pi*A))*z_corr;
    end

    % figure
    % plot(m, P_m)

    look_up_table = [m' P_m'];
    look_up_table = look_up_table';
    [zero look_up_index] = min(abs(ratio-look_up_table(2,:)));
    m = look_up_table(1,look_up_index)
    % -----end of m code ratio method-----
end

% Define HWHM for delta, based on new m
HWHM = del_nu/m;

% 10.3.6 Calculating Correction Factors, start with delta values
delta = (abs(sep_AM_freqs)-line_cent_freq)/HWHM;
delta_i = delta'*multiplier2;
delta_i = delta_i';

%-----correction equation codes-----
if inputnumber(12) == 1 % from excel file
    %-----start of correction equations for high concentrations-----
    % y is the integrand of the correction factor
    y = (1-cos(2*theta_x)).*(1-(exp(-A./(1+((delta_i+(m.*cos(theta_x)).^2))))));

    % Use 'trapz' function to approximate definite integral 'trapz' derived
    % from 'trapz' gives approximation of integral of 'y' with respect to
    % 'theta', which was previously defined between 0 and pi.
    % 'trapz.m' downloaded from: http://www.mathworks.com/matlabcentral/fileexchange
    % Alternatively use 'trapz' as before.

```

Appendix C. MATLAB code - RAM technique with RAM Nulling

```

z_corr = trapz(theta,y);

% Obtain correction factor
correction_factor = (1./(pi.*(1-exp(-A./(1+(delta.^2)))))).*z_corr;
%-----end of correction equation for high concentrations-----
else
%-- start of correction equations for low concentrations-----
% y is the integrand of the correction factor
y = (1-cos(2*theta_x))./(1+(delta_i+(m_ref(:,i-2)*cos(theta_x))).^2);
z_corr = trapz(theta,y);

% 10.3.6.2 Obtain correction factor
correction_factor = ((1+delta.^2)./pi).*z_corr;
%-----end of correction equation for low concentrations-----
end

correction_factor = 1./correction_factor;

% Apply each new correction factor to original data and record in new column
sep_AM_amps_corrected(:,2) = (1-sep_AM_amps_corrected(:,1)).*correction_factor';
sep_AM_amps_corrected(:,2) = 1-sep_AM_amps_corrected(:,2);

% Find the minimum amplitude in the experimental plot
K_1 = min(theory_amps);
K_Index_1 = find(theory_amps == K_1);
Line_Cent_Wave_1 = theory_lambda(K_Index_1);

K_2 = min(sep_AM_amps_corrected(:,2));
K_Index_2 = find(sep_AM_amps_corrected(:,2) == K_2);
Line_Cent_Wave_2 = sep_AM_waves(K_Index_2);
% The lateral shift at high modulation indices is calculated and corrected
line_centre_shift = Line_Cent_Wave_2 - Line_Cent_Wave_1;
sep_AM_waves = sep_AM_waves - line_centre_shift;

LLL = min(point2_amps) - 0.005;
LL = max(point2_amps) + 0.01;

figure
hold on
plot(point2_waves,point2_amps, '--','LineWidth',2)
plot(sep_AM_waves,sep_AM_amps_corrected(:,1), 'r','LineWidth',2)
plot(sep_AM_waves,sep_AM_amps_corrected(:,2),'g','LineWidth',2)
xlabel('Wavelength (nm)')
ylabel('Transmission')
title(input_text(12,:))
axis([1650.8 1651.1 LLL 1])
legend('Theory','Uncorrected','Corrected','Location','SouthEast')

saveas(gcf,input_text(19,:))

gas = sep_AM_amps_corrected(:,2);
%%%%%%%%%%%%%%%%%%%%%%%%%%%%%%%%%%%%%%%%%%%%%%%%%%%%%%%%%%%%%%%%%%%%%%%%
% 4.0 Reading in of all spectroscopic constants and variables
%%%%%%%%%%%%%%%%%%%%%%%%%%%%%%%%%%%%%%%%%%%%%%%%%%%%%%%%%%%%%%%%%%%%%%%%
% 4.2 Defining temperature
T_0 = 296; % Reference Temperature in Kelvin

```

### Appendix C. MATLAB code - RAM technique with RAM Nulling

```
T_K = 273.15; %0 degrees celcius in Kelvin
degreeT = inputnumber(15); %input('\n Temperature in Celsius: ');
T = degreeT+T_K; %Converting to Kelvin

% 4.3 Reading in pressure and converting from bar to atm
% pressure = input('\n Initial Pressure: '); %bar
pressure = inputnumber(14)*0.986926; %atm

    %4.3.1 Pressure range for fitting loop
    coeff = linspace(pressure-0.1,pressure+0.1,50);

    %4.3.2 Defining Start Concentrations
    actual_methane_concentration=[0,0.5,1];

% 4.4 Frequency Range
vsteps = 2000;
v = linspace(6054,6064,vsteps); %theory frequency range
lambda = 1./v.*1e7;

% 4.5 Calculation of individual line-strengths
Q_T0 = (7.0192e-9*T_0^4)-(3.6651e-6*T_0^3)+(0.0031476*T_0^2)+(1.4428*T_0)-71.184;
Q_T = (7.0192e-9*T^4)-(3.6651e-6*T^3)+(0.0031476*T^2)+(1.4428*T)-71.184;
S1 = 1-exp(-(h*c.*methanelines(:,1))/(k*T));
S2 = 1-exp(-(h*c.*methanelines(:,1))/(k*T_0));
S3 = S1./S2;
S4 = Q_T0./Q_T;
S5 = T_0/T;
S6 = exp((-h*c.*methanelines(:,5)/k)*((1/T)-(1/T_0)));
S7 = S3.*S4.*S5.*S6;
S_T=S7.*methanelines(:,2); %Total linestrength

% 4.6 Calculation of Broadening Parameters

    %4.6.1 Gaussian Broadening
    gammag = 7.1625e-7.*methanelines(:,1).*(T/16)^0.5;
    gammag = gammag';

    % 4.6.2 Air broadening parameter
    air_broadening_parameter = c_AIR.*methanelines(:,3).*(T_0/T).^0.73;

    % 4.6.3 Self Broadening parameter
    self_broadening_parameter = methanelines(:,4).*(T_0/T)^0.8;

% 4.7 X values for Voigt Profile
for j = 1:z
X(:,j) = 2*sqrt(log(2))*(v-methanelines(j,1)-methanelines(j,7))./gammag(j);
end

% 4.8 A-D values for Voigt Profile
A = [-1.2150 -1.3509 -1.2150 -1.3509];
B = [1.2359 0.3786 -1.2359 -0.3786];
C = [-0.3085 0.5906 -0.3085 0.5906];
D = [0.0210 -1.1858 -0.0210 1.1858];

%%%%%%%%%%%%%%%%%%%%%%%%%%%%%%%%%%%%%%%%%%%%%%%%%%%%%%%%%%%%%%%%%%%%%%%%%%%%%%
% 5.0 Pressure Loop and Golden Section Search
```

%%%

```

for why = 1:2
why
    % 5.1 Constants for Golden Section Search
        tol=0.001;
        Ce = (3-sqrt(5))/2;
        R = 1-Ce;

    % 5.2 Pressure and Concentration Variables
        total_pressure = coeff(why);
        x0 = actual_methane_concentration(1);
        x3 = actual_methane_concentration(3);

    % 5.3 Defining Initial Values for methane concentrations
        if (abs(actual_methane_concentration(3)-actual_methane_concentration(2))
            > abs(actual_methane_concentration(2)-actual_methane_concentration(1))),
            x1 = actual_methane_concentration(2);
            x2 = actual_methane_concentration(2)
                + Ce*(actual_methane_concentration(3)-actual_methane_concentration(2));
        else
            x2 = actual_methane_concentration(2);
            x1 = actual_methane_concentration(2)
                - Ce*(actual_methane_concentration(2)-actual_methane_concentration(1));
        end

    % 5.4 GOLDEN SECTION SEARCH
        while abs(x3-x0) > tol*(abs(x1)+abs(x2)),

            % 5.4.1 Concentrations
                methane_concentration(1) = x1;
                methane_concentration(2) = x2;
                nitrogen_concentration = 1-methane_concentration;

            % 5.4.2 Lorentzian Broadening
                gammal = 2*total_pressure.*((air_broadening_parameter*nitrogen_concentration)
                    +(self_broadening_parameter*methane_concentration));
                gammal = gammal';

            % 5.4.3 Voigt Y values
                Y1 = (gammal(1,:)./gammag)*sqrt(log(2));
                Y2 = (gammal(2,:)./gammag)*sqrt(log(2));

            % 5.4.4 Creating Voigt V Values
                for j = 1:z
                    for i = 1:4
                        V_top1(i,:) = (C(i)*(Y1(j)-A(i)))+(D(i)*(X(:,j)-B(i)));
                        V_bottom1(i,:) = (Y1(j)-A(i))^2+(X(:,j)-B(i)).^2;
                        V_top2(i,:) = (C(i)*(Y2(j)-A(i)))+(D(i)*(X(:,j)-B(i)));
                        V_bottom2(i,:) = (Y2(j)-A(i))^2+(X(:,j)-B(i)).^2;
                    end
                    V1 = V_top1./V_bottom1;
                    V12(:,j) = (2/gammag(j))*(log(2)/pi)^0.5*methane_concentration(1)
                        *(7.339e21/T_0)*S_T(j)*sum(V1);
                    V2 = V_top2./V_bottom2;
                    V22(:,j) = (2/gammag(j))*(log(2)/pi)^0.5*methane_concentration(2)

```

```

*(7.339e21/T_0)*S_T(j)*sum(V2);
end

% 5.4.5 Spectral Absorption Coefficients
kv1 = total_pressure*sum(V12');
kv2 = total_pressure*sum(V22');

% 5.4.6 Fractional Transmission
T1 = exp(-kv1.*L);
T2 = exp(-kv2.*L);

% 5.4.7 Find indices for the theoretical wavelengths that match two ends of
%       experimental data
IND1 = find(lambda <= YYY_wavelength(1));
IND1 = IND1(1);

IND2 = find(lambda <= YYY_wavelength(xx));
IND2 = IND2(1);

% 5.4.8 Calculate the wavelengths and amplitudes of the theory data in range
%       of experimental data
cut_theory_lambda = linspace(lambda(IND2),lambda(IND1),IND1-IND2+1);
cut_theory_amps1 = T1(IND2:IND1);
cut_theory_amps2 = T2(IND2:IND1);

% 5.4.9 Interpolating theory data over length of experimental
%       data, making sets of data over equal range and equal length
amps_chopped1 = interp1(cut_theory_lambda,cut_theory_amps1,YYY_wavelength,
'linear','extrap');
amps_chopped2 = interp1(cut_theory_lambda,cut_theory_amps2,YYY_wavelength,
'linear','extrap');

% 5.4.10 Setting the experimental baseline to theoretical
%       baseline
gap1 = gas(1800) - amps_chopped1(1800);
gap2 = gas(1800) - amps_chopped2(1800);

norm_amps1 = gas-gap1;
norm_amps2 = gas-gap2;

% 5.4.11 Least squares fit of theory and experimental
f1=sum((amps_chopped1(Line_Cent_Index-500:Line_Cent_Index+500)-
norm_amps1(Line_Cent_Index-500:Line_Cent_Index+500)).^2);

f2=sum((amps_chopped2(Line_Cent_Index-500:Line_Cent_Index+500)-
norm_amps2(Line_Cent_Index-500:Line_Cent_Index+500)).^2);

% 5.4.12 New values for the Golden Section Search
if f2 < f1,
    x0 = x1;
    x1 = x2;
    x2 = R*x1 + Ce*x3;
    f1 = f2;
    concentration = methane_concentration(2);
    finalvalue(1,why) = f1;
    finalvalue(2,why) = f2;

```

Appendix C. MATLAB code - RAM technique with RAM Nulling

```

        finalvalue(3,why) = concentration;
        finalvalue(4,why) = total_pressure;
    else
        x3 = x2;
        x2 = x1;
        x1 = R*x2 + Ce*x0;
        f2 = f1;
        concentration = methane_concentration(2);
        finalvalue(1,why) = f1;
        finalvalue(2,why) = f2;
        finalvalue(3,why) = concentration;
        finalvalue(4,why) = total_pressure;
    end
end
end

%%%%%%%%%%%%%%%%%%%%%%%%%%%%%%%%%%%%%%%%%%%%%%%%%%%%%%%%%%%%%%%%%%%%%%%%
% 6.0 Finding final concentration
%%%%%%%%%%%%%%%%%%%%%%%%%%%%%%%%%%%%%%%%%%%%%%%%%%%%%%%%%%%%%%%%%%%%%%%%

% 6.1 Finding data set with minimum lsq fit
min_index = min(finalvalue(1,:));
min_index = find(finalvalue(1,:) == min_index);

% 6.2 Final concentration, error, and pressure
final_methane_conc = finalvalue(3,min_index);
final_press = finalvalue(4,min_index);
error = abs((((final_methane_conc*100)-inputnumber(16))/inputnumber(16))*100);
final_nitrogen_conc = 1-final_methane_conc;

% 6.3 Final Lorentzian Broadening
gammal=2*final_press.*((air_broadening_parameter*final_nitrogen_conc)
+(self_broadening_parameter*final_methane_conc));
gammal=gammal';

% 6.4 Final voigt Y-value
Y = (gammal./gammag)*sqrt(log(2));

% 6.5 final voigt V-value
for j = 1:z
    for i = 1:4
        V_top(i,:) = (C(i)*(Y(j)-A(i)))+(D(i)*(X(:,j)-B(i)));
        V_bottom(i,:) = (Y(j)-A(i))^2+(X(:,j)-B(i)).^2;
    end
    V = V_top./V_bottom;
    Vfinal(:,j) = (2/gammag(j))*(log(2)/pi)^0.5*final_methane_conc
*(7.339e21/T_0)*S_T(j)*sum(V);
end

% 6.6 Final spectral absorption coefficient
kv = final_press*sum(Vfinal');

% 6.7 Final fractional transmission
T = exp(-kv.*L);

% 6.8 Changing range of theory data to the range of experimental data

```

### Appendix C. MATLAB code - RAM technique with RAM Nulling

```
cut_theory_amps = T(IND2:IND1);
amps_chopped = interp1(cut_theory_lambda,cut_theory_amps,YYY_wavelength,
'linear','extrap');

% 6.9 Setting the experimental baseline to theoretical
% baseline
gap = gas(1800)-amps_chopped(1800);
gas = gas-gap;

% 6.10 Calculating theory/experimental residual
residual = amps_chopped-gas';

% 6.11 Stating final concentration
final_methane_conc = (final_methane_conc*100)
final_press = final_press/0.986926
error_press = abs((((final_press)-(pressure/0.986926))/(pressure/0.986926))*100);

%% 6.12 Plots comparisons of the experimental data and the Matlab theory file, and
%% also a residual subtraction of the two sets of data
figure
axes('position',[.1 .1 .8 .5])
hold on
plot (YYY_wavelength,gas,'linewidth',1.5)
% plot (YYY_wavelength,gas2,'m','linewidth',1.5)
plot(cut_theory_lambda,cut_theory_amps,'r','linewidth',1.5)
xlabel('Wavelength, nm')
ylabel('Relative Transmission')
title({'Methane Absorption Spectra at ', num2str(degreeT),'^{o}C'];
['Calculated Concentration ',num2str(final_methane_conc),'% (error ',num2str(error),'%)'];
['Calculated Pressure ',num2str(final_press),'bar (error ',num2str(error_press),'%)']})
legend('Experimental Data', 'Theoretical Fit',4)
axes('position',[.1 .75 .8 .2])
plot(YYY_wavelength,residual)
xlabel('Wavelength, nm')
ylabel('Residual')

% theory(:,1) = cut_theory_lambda;
% theory(:,2) = cut_theory_amps;
% waves = YYY_wavelength;

sheetname = input_text(15,:);
sheetname = sheetname(1:6);
result = [YYY_wavelength' gas sep_AM_waves' sep_AM_amps_corrected(:,2)];
xlswrite(input_text(9,:),result,sheetname);

theory = [theory_lambda' theory_amps'];
xlswrite('theory.xls',theory);
figure(3);
```

# Appendix D

## MATLAB code - PD method with RAM Nulling

```
%-----  
% PD method with RAM nulling  
% Andrew J McGettrick, Kevin Duffin, Michael Lengden, Keith Ruxton  
% and James Bain  
%-----  
clc  
clear  
close all  
format long  
  
c_AIR = 0.91; % Broadening coefficient for nitrogen  
  
starttrim = 501;  
stoptrim = 8500;  
  
% reading in all user data  
[inputnumber,inputtext] = xlsread('parameters_PDM_null.xls', 'a1:b19');  
input_text = char(inputtext);  
  
%-----  
% Generate theory file  
%-----  
  
% 1.1 Reading in Hitran Data for region of interest  
methanelines = xlsread('methanelines.xls');  
z = length(methanelines);  
  
% 1.2 Defining all constants  
k = 1.3806503e-23; %Boltzmann  
M = 16; %Mass  
c = 299792458e2; %Speed of light  
h = 6.626e-34; %Planck  
L = 9.9; %Length of cell  
  
% 1.3 Defining temperature  
T_0 = 296; % Reference Temperature in Kelvin  
T_K = 273.15; %0 degrees celcius in Kelvin
```

#### Appendix D. MATLAB code - PD method with RAM Nulling

```
degreeT = inputnumber(15); %input('\n Temperature in Celsius: ');
T = degreeT+T_K; %Converting to Kelvin

% 1.4 Reading in pressure and converting from bar to atm
pressure = inputnumber(14)*0.986926; %atm

    %1.4.1 Pressure range for fitting loop
    coeff = linspace(pressure-0.1,pressure+0.1,50);

    %1.4.2 Defining Start Concentrations
    actual_methane_concentration=[0,0.5,1];

    %1.4.2 Defining Start Concentrations
    methane_concentration = inputnumber(16)/100;%0.1013;
    nitrogen_concentration = 1-methane_concentration;

% 1.5 Frequency Range
vsteps = 2000;
v = linspace(6054,6064,vsteps); %theory frequency range
lambda = 1./v.*1e7;

% 1.6 Calculation of individual line-strengths
Q_T0 = (7.0192e-9*T_0^4)-(3.6651e-6*T_0^3)+(0.0031476*T_0^2)+(1.4428*T_0)-71.184;
Q_T = (7.0192e-9*T^4)-(3.6651e-6*T^3)+(0.0031476*T^2)+(1.4428*T)-71.184;
S1 = 1-exp(-(h*c.*methanelines(:,1))/(k*T));
S2 = 1-exp(-(h*c.*methanelines(:,1))/(k*T_0));
S3 = S1./S2;
S4 = Q_T0./Q_T;
S5 = T_0/T;
S6 = exp((-h*c*methanelines(:,5)/k)*((1/T)-(1/T_0)));
S7 = S3.*S4.*S5.*S6;
S_T=S7.*methanelines(:,2); %Total linestrength

% 1.7 Calculation of Broadening Parameters

    %1.7.1 Gaussian Broadening
    gammag = 7.1625e-7.*methanelines(:,1).*(T/16)^0.5;
    gammag = gammag';

    %1.7.2 Air broadening parameter
    air_broadening_parameter = c_AIR*methanelines(:,3).*(T_0/T).^0.73;

    %1.7.3 Self Broadening parameter
    self_broadening_parameter = methanelines(:,4)*(T_0/T)^0.8;

    %1.7.4 Lorentzian Broadening
    gammal = 2*pressure.*((air_broadening_parameter*nitrogen_concentration)
    +(self_broadening_parameter*methane_concentration));
    gammal = gammal';

% 1.8 X values for Voigt Profile
for j = 1:z
    X(:,j) = 2*sqrt(log(2))*(v-methanelines(j,1)-methanelines(j,7))./gammag(j);
end

% 1.9 A-D values for Voigt Profile
```

*Appendix D. MATLAB code - PD method with RAM Nulling*

```
A = [-1.2150 -1.3509 -1.2150 -1.3509];
B = [1.2359 0.3786 -1.2359 -0.3786];
C = [-0.3085 0.5906 -0.3085 0.5906];
D = [0.0210 -1.1858 -0.0210 1.1858];

% 1.10 Final voigt Y-value
Y = (gammal./gammag)*sqrt(log(2));

% 1.11 final voigt V-value
for j = 1:z
    for i = 1:4
        V_top(i,:) = (C(i)*(Y(j)-A(i)))+(D(i)*(X(:,j)-B(i)));
        V_bottom(i,:) = (Y(j)-A(i))^2+(X(:,j)-B(i)).^2;
    end

    V = V_top./V_bottom;
    Vfinal(:,j) = (2/gammag(j))*(log(2)/pi)^0.5*methane_concentration
        *(7.339e21/T_0)*S_T(j)*sum(V);
end

% 1.12 Final spectral absorption coefficient
kv = pressure*sum(Vfinal');

% 1.13 Final fractional transmission
T = exp(-kv.*L);

theory_lambda = lambda;
theory_amps = T;

%-----
% Data Input, Filtering and Processing
%-----
% Input of resonator signal and trimming ends of data
res = dlmread('res');
res=res(starttrim:stoptrim);

% Filtering reonator to remove spurious peaks
[b1 a1] = ellip(2,0.1,90,0.02);
res_avg = filtfilt(b1,a1,res);

[b2 a2] = ellip(2,0.00002,60,0.001);

sep_FM_sens = inputnumber(1,2); %input('\n Input CH2 sensitivity in volts: ');

%-----start of mick's code-----
% The sep FM is inputted the "wrong way round" (ie +ve peak occuring 1st)
%with regard to time for PDM measurements
sep_FM1 = dlmread(input_text(3,:));
sep_FM2 = sep_FM1(starttrim:stoptrim);
sep_FM = filtfilt(b2,a2,sep_FM2);
xx=length(sep_FM2);

sep_FM3 = dlmread(input_text(4,:));
sep_FM_nogas = sep_FM3(starttrim:stoptrim);
sep_FM_nogas = filtfilt(b2,a2,sep_FM_nogas);
```

*Appendix D. MATLAB code - PD method with RAM Nulling*

```

% Reading in Channel 1 of LIA
% data is filtered and trimmed
AM_FM1 = dlmread(input_text(1,:));
AM_FM2 = AM_FM1(starttrim:stoptrim);
AM_FM = filtfilt(b2,a2,AM_FM2);

AM_FM3 = dlmread(input_text(2,:));
AM_FM_nogas = AM_FM3(starttrim:stoptrim);
AM_FM_nogas = filtfilt(b2,a2,AM_FM_nogas);

moveAM = AM_FM_nogas(end) - AM_FM(end);
AM_FM_nogas = AM_FM_nogas - moveAM;
% AM_FM_orig = AM_FM;
% AM_FM = AM_FM;% - AM_FM_nogas;

figure
hold on;
plot(AM_FM);
plot(AM_FM_nogas, 'r');
% plot(AM_FM_orig, 'g');
title('CH1');

% ***** CALCULATION OF PHI - AM/WM PHASE SHIFT *****
% Locate +ive & -ive peaks on ch Y to calculate AM/WM phase shift
y1 = min(sep_FM); % amplitude of negative peak of sep_FM = y1
y1_index = find(sep_FM == y1); % index of neg peak

y2 = max(sep_FM); % amplitude of positive peak of sep_FM = y2
y2_index = find(sep_FM == y2); % index of pos peak

% Calculate x1, x2 corresponding to indices for y2 and y2 - note "corresponding"
min_AM_FM = AM_FM(y2_index); % not necessarily min (or max) of AM_FM_amps...
max_AM_FM = AM_FM(y1_index); % ..min (or max) of sep_FM

% Therefore, actual values of x1 and x2...
x1 = max_AM_FM(1);% - RAM_negative_peak(1));
x2 = min_AM_FM(1);% - RAM_positive_peak(1));

% FINALLY...Calculate phi = AM_WM_phase_shift in degrees - therefore (180/pi)
phi = (180/pi) * atan((abs(y2)+abs(y1))/abs((x1-x2)))

% Calculate direct absorption signal using phasor decomposition method
AM_whole = AM_FM - AM_FM_nogas + (sep_FM./tan(phi)* pi/180);

% Calculate full first derivative signal
sep_FM_whole = sep_FM/sin(phi*pi/180);
% recall that recorded sep_FM was 180 deg shifted. Therefore * (-1)
sep_FM_whole = sep_FM_whole * -1; %

direct_absorption_signal_amps = AM_whole;
sep_FM = sep_FM_whole;

X_LIA_sens = sep_FM_sens;

%-----code to base fit the OP2 data-----
nogas_OP2 = dlmread(input_text(10,:));

```

*Appendix D. MATLAB code - PD method with RAM Nulling*

```
nogas_OP2 = nogas_OP2(starttrim:stoptrim);
nogas_OP2 = filtfilt(b2,a2,nogas_OP2);

b = nogas_OP2;
OP2_nogas_sens = inputnumber(8,2);
%-----

%-----fitting for OP1 no gas break arm 2-----
no_gas_OP1 = dlmread(input_text(6,:));
no_gas_OP1 = no_gas_OP1(starttrim:stoptrim);
no_gas_OP1 = filtfilt(b2,a2,no_gas_OP1);

cc = no_gas_OP1;

OP1_nogas_sens = inputnumber(4,2);
%-----end-----

% Create array with all signal sensitivities
sens_factors = [sep_FM_sens X_LIA_sens OP2_nogas_sens OP1_nogas_sens];
max_sens = max(sens_factors); % Find maximum sensitivity

% 5.3 Scale all signals to match sensitivity
direct_absorption_signal_amps = direct_absorption_signal_amps / (max_sens / X_LIA_sens);
cc = cc / (max_sens / OP1_nogas_sens);
b = b / (max_sens / OP2_nogas_sens);

% 5.4 Trim O/P2 No gas
OP2_nogas_trim = [b];

% 5.5 Trim O/P1 No gas Break Arm 2
OP1_nogas_trim = [cc];

% 5.6 Calculate ratio to scale O/P1 gas
ratio1 = OP2_nogas_trim ./ OP1_nogas_trim;
min_ratio1 = mean(ratio1);

% 5.8 Normalise Gas signal using George's equation
part1 = direct_absorption_signal_amps ./ OP2_nogas_trim;%nogas_OP2;
part2 = part1 .* min_ratio1;
gas = part2;

sep_FM = sep_FM_whole;
RAM_no_gas_amps = AM_FM_nogas;
% gas = normalised_direct_absorption;

%-----
Wavelength Referencing
%-----

% 3.1 Find Peaks
diff_res = diff(res_avg);
peak = [];

for n = 1:length(diff_res)-1
    if ( ne(sign(diff_res(n)),sign(diff_res(n+1))) && (diff_res(n) > diff_res(n+1)) )
```

*Appendix D. MATLAB code - PD method with RAM Nulling*

```
        peak = [peak n+1];
    end
end

% 3.2 Define x and y values of peaks
JJ = peak;
resonator_peak(:,:)=res_avg(JJ(:,:));

% 3.3 Plot the Resonator scan and show the identified peaks
% figure
% hold on
% plot(JJ,resonator_peak,'o')
% plot(res_avg,'r')
% plot(res)

% 3.4 Defining the peak line centre in wavelength and frequency
Line_Cent_Wave = 1.650958773750263e+003;
Line_Cent_Freq = 3e8./(Line_Cent_Wave);

% 3.5 Find the line centre index from the experimental plot
Q = min(gas);
Q_Index = find(gas == Q);
Line_Cent_Index = Q_Index(1);

% 3.6 Find resonator peak location of closest resonator peak to the line
% centre of the experimental plot
[error1, closest_peak]=min(abs(JJ-Line_Cent_Index));

% 3.7 Convert resonator peak indices to frequencies
% 3.7.1 Frequency spacing
delta_f= 0.4275;

% 3.7.2 Declare vector for storing frquencies
Res_Peak_Wave = [];
Res_Peak_Wave(closest_peak)=150000;

FF=length(JJ)+1;
nn=1;

while nn < FF
    if nn<closest_peak
        Res_Peak_Wave(nn)=[150000+((closest_peak-nn)*delta_f)];
    end;

    if nn>closest_peak
        Res_Peak_Wave(nn)=[150000-((nn-closest_peak)*delta_f)];
    end;
    nn=nn+1;
end;

% 3.7.3 resonator frequencies
P=polyfit(JJ,Res_Peak_Wave,2);
x=[1:1:xx];
YYY=polyval(P, x);

% 3.8 Shift this polynomial to match the experimental plot at line centre and outwards
```

#### Appendix D. MATLAB code - PD method with RAM Nulling

```
shift = Line_Cent_Freq-YYY(Line_Cent_Index);
YYY = YYY+shift;

% 3.9 Wavelength values for each data channel
YYY_wavelength = 3e8./YYY;

% 3.9 Wavelength values for each data channel
XXX = 3e8./YYY;
sep_FM = [XXX' sep_FM];
%
% figure
% plot(gas)
% title('before shift')

% 5.4.7 Find indices for the theoretical wavelengths that match two ends of
% experimental data
IND1 = find(lambda <= YYY_wavelength(1));
IND1 = IND1(1);
IND2 = find(lambda <= YYY_wavelength(xx));
IND2 = IND2(1);
% 5.4.8 Calculate the wavelengths and amplitudes of the theory data in range
% of experimental data
cut_theory_lambda = linspace(lambda(IND2),lambda(IND1),IND1-IND2+1);
cut_theory_amps = theory_amps(IND2:IND1);
% 5.4.9 Interpolating theory data over length of experimental
% data, making sets of data over equal range and equal length
amps_chopped = interp1(cut_theory_lambda,cut_theory_amps,YYY_wavelength,'linear','extrap');

% 5.4.10 Setting the experimental baseline to theoretical
% baseline
gap = gas(1800) - amps_chopped(1800);

normalised_direct_absorption = gas+abs(gap);

% [error1, RAM_Start_Index] = min(abs(theory_lambda - XXX(1)));
% Vertical_Shift = abs(theory_amps(RAM_Start_Index) - normalised_direct_absorption(1));
%
% if normalised_direct_absorption(1) > theory_amps(RAM_Start_Index)
%     % 10.1.1 If Experiment above Theory shift Experimental values down
%     normalised_direct_absorption = normalised_direct_absorption - Vertical_Shift;
% else
%     % 10.1.2 If Experiment below Theory shift Experimental values up
%     normalised_direct_absorption = normalised_direct_absorption + Vertical_Shift;
% end

% figure
% plot(normalised_direct_absorption);
% title('Plot of calculated RAM');

% 1.5 Read in channel X
X_LIA_axis = AM_whole;
X_LIA_axis = [XXX' X_LIA_axis];

% 1.6 Separate the files into frequencies and amplitudes
X_LIA_axis_amps = X_LIA_axis(:,2)';
```

*Appendix D. MATLAB code - PD method with RAM Nulling*

```

% convert from wavelength to frequency
X_LIA_axis_frequencies = 3e8 ./ (X_LIA_axis(:,1)' * 1e-9)';
sep_FM_amps = sep_FM(:,2)';
sep_FM_amps = sep_FM_amps * -1;
% convert from wavelength to frequency
sep_FM_frequencies = 3e8 ./ (X_LIA_axis(:,1)' * 1e-9)';

%-----
%          Correction Factors
%-----

% 10.2.3 Ask user for current dither size
current_dither_size= inputnumber(6)/2;

% 10.2.5 separate frequencies and amplitudes into different vectors
sep_AM_freqs = YYY * 1e9; %sep_FM_frequencies;
sep_AM_amps = gas;
sep_AM_waves = 1e9*(3e8./sep_AM_freqs);

% 10.2.6 Read in delta_nu/delta_i value,obtained previously from laser
% characterisation procedure
del_nu= inputnumber(9);
del_nu = del_nu * current_dither_size;
del_nu = del_nu * 1e9;
del_nu_cm = del_nu/3e10;

% Assume constant gamma (GHz)
% Probably best going for 2.1-2.2 GHz for 1% CH_4 and 2.4-2.5 GHz for 10%
gamma = 2.2511;
gamma = 1e9*gamma;
gamma_cm = 1e9*gamma/3e10;

% Calculate HWHM magnitude as frequency difference between FWHM_freq and line centre
line_cent_index_1=find(sep_AM_amps==min(sep_AM_amps));
line_cent_freq=sep_AM_freqs(line_cent_index_1(1));
line_cent_freq=line_cent_freq(1);

% Set up correction integral
I_min = min(sep_AM_amps);
sep_AM_amps_corrected(:,1) = normalised_direct_absorption;
multiplier1 = linspace(1,1,length(normalised_direct_absorption));
multiplier2 = linspace(1,1,360);
theta = linspace(0,pi,360);
theta_x = theta';
theta_x = theta_x*multiplier1;

% -----determining m-----
if inputnumber(11) == 1
    %-----start of m code least squares method-----
    % Define arbitrary Lorentzian on which to apply distortions
    m_ref = 0.1;
    ref_peak_depth = 0.997;
    A_2 = -log(ref_peak_depth);

    % Calculate line centre frequency
    line_cent_index_1=find(sep_AM_amps==min(sep_AM_amps));
    line_cent_freq=sep_AM_freqs(line_cent_index_1(1));

```

```

line_cent_freq=line_cent_freq(1);

% Define delta for reference signal
% HWHM_ref = gamma*1e9;
HWHM_ref = del_nu/m_ref;
delta_0_ref = (sep_AM_freqs-line_cent_freq)./HWHM_ref;
delta_ref = delta_0_ref;
delta_ref = delta_ref'*multiplier2;
delta_ref = delta_ref';

% Define a_0
y_0 = 1./(1+((delta_ref+m_ref.*cos(theta_x)).^2));
z_0 = trapz(theta,y_0);
a_0 = (1./pi).*z_0;

% Define a_2
y_2 = cos(2.*theta_x)./(1+((delta_ref+m_ref.*cos(theta_x)).^2));
z_2 = trapz(theta,y_2);
a_2 = (2./pi).*z_2;

% Define simulated first harmonic signal amplitudes
I_ref(:,1) = 1-A_2.*(a_0-(a_2./2));
I_ref_min = min(I_ref);

% Normalising the reference Lorentzian to the signal to be corrected
ratio = (1-I_min)./(1-I_ref_min);
I_ref = (1-I_ref).*ratio;
I_ref = 1-I_ref;

% Define arbitrarily high initial value for 'sum_errors' for implementing a
% while loop
sum_errors = 100;

% Measure the amplitude error between the corrected signal and the
% equivalent simulated Lorentzian, then take the square and sum over many
% points around line-centre.
errors = I_ref-sep_AM_amps_corrected;
errors = errors.^2;
sum_errors(:,2) = sum(errors);

% Open while loop to do additional iterations. By defining an artificially
% high initial value for sum_errors, the loop can be terminated when the
% sum of squared errors reaches a minimum value (i.e. when the corrected
% signal most closely approximates a pure Lorentzian)
i = 2;
while sum_errors(:,i)<sum_errors(:,i-1)
    % 10.3.5 Define incremental m values from previously obtained m and then
    % calculate the equivalent HWHM
    m_ref(:,i) = m_ref(:,i-1)+0.05;
    HWHM_ref = del_nu/m_ref(:,i);
    delta_0_ref = (sep_AM_freqs-line_cent_freq)/HWHM_ref;
    delta_ref = delta_0_ref;
    delta_ref = delta_ref'*multiplier2;
    delta_ref = delta_ref';

    % Define a_0

```

Appendix D. MATLAB code - PD method with RAM Nulling

```

y_0 = 1./(1+((delta_ref+m_ref(:,i)).*cos(theta_x)).^2));
z_0 = trapz(theta,y_0);
a_0 = (1./pi).*z_0;

% Define a_2
y_2 = cos(2.*theta_x)./(1+((delta_ref+m_ref(:,i)).*cos(theta_x)).^2));
z_2 = trapz(theta,y_2);
a_2 = (2./pi).*z_2;

% Define simulated first harmonic signal amplitudes
I_ref(:,i) = 1-A_2.*(a_0-(a_2./2));
I_ref_min(:,i) = min(I_ref(:,i));

% Normalising the reference Lorentzian to the signal to be corrected
ratio(:,i) = (1-I_min)./(1-I_ref_min(:,i));
I_ref(:,i) = (1-I_ref(:,i)).*ratio(:,i);
I_ref(:,i) = 1-I_ref(:,i);

errors = I_ref(:,i)-sep_AM_amps_corrected;
errors = errors.^2;
sum_errors(:,i+1) = sum(errors);

i = i+1;
end

m_ref(:,i-2)
m = m_ref(:,i-2);

% Split reference into wavelengths and amplitudes
point2_waves = theory_lambda;
point2_amps = theory_amps;

point2_min = min(point2_amps);
A = -log(point2_min);

% figure
% plot(m_ref, sum_errors(2:i))
% title('Plot of Summed Squared Errors with m (Simulated Lorentzian at Low Conc)')
% xlabel('m')
% ylabel('Summed Square Errors')
%-----end of m code least squares method-----
else
% -----start of m code ratio method-----
% ref file
% point2 = xlsread('direct_result.xls');

% Split into wavelengths and amplitudes
point2_waves = theory_lambda;
point2_amps = theory_amps;

point2_min = min(point2_amps);
distorted_min = min(sep_AM_amps_corrected(:,1));
% Calculate 'A' factor; A=alphaCl
A = -log(point2_min);
% Calculate ratio
ratio = (1-distorted_min)/A;

```

Appendix D. MATLAB code - PD method with RAM Nulling

```

% Define number of reference points in look-up table
n_increments =1000;

for n = 1:n_increments
    bbb = 2.5/n_increments;
    m(:,n) = 0+(bbb*n);

    y = (sin(theta).^2).*(1-exp(-A./(1+(m(:,n)^2).*(cos(theta).^2))));
    z_corr = trapz(theta,y);
    P_m(:,n) = (2/(pi*A))*z_corr;
end

%    figure
%    plot(m, P_m)

look_up_table = [m' P_m'];
look_up_table = look_up_table';
[zero look_up_index] = min(abs(ratio-look_up_table(2,:)));
m = look_up_table(1,look_up_index)
% -----end of m code ratio method-----
end

% Define HWHM for delta, based on new m
HWHM = del_nu/m;

% 10.3.6 Calculating Correction Factors, start with delta values
delta = (abs(sep_AM_freqs)-line_cent_freq)./HWHM;
delta_i = delta'*multiplier2;
delta_i = delta_i';

%-----correction equation codes-----
if inputnumber(12) == 1 % from excel file
    %-----start of correction equations for high concentrations-----
    % y is the integrand of the correction factor
    y = (1-cos(2*theta_x)).*(1-(exp(-A./(1+((delta_i+(m.*cos(theta_x)).^2))))));

    % Use 'trapz' function to approximate definite integral 'trapz' derived
    % from 'trapz' gives approximation of integral of 'y' with respect to
    % 'theta', which was previously defined between 0 and pi.
    % 'trapz.m' downloaded from: http://www.mathworks.com/matlabcentral/fileexchange
    % Alternatively use 'trapz' as before.
    z_corr = trapz(theta,y);

    % Obtain correction factor
    correction_factor = (1./(pi.*(1-exp(-A./(1+(delta.^2)))))).*z_corr;
    %-----end of correction equation for high concentrations-----
else
    %-- start of correction equations for low concentrations-----
    % y is the integrand of the correction factor
    y = (1-cos(2*theta_x))./(1+(delta_i+(m_ref(:,i-2)*cos(theta_x)).^2));
    z_corr = trapz(theta,y);

    % 10.3.6.2 Obtain correction factor
    correction_factor = ((1+delta.^2)./pi).*z_corr;
    %-----end of correction equation for low concentrations-----
end
end

```

#### Appendix D. MATLAB code - PD method with RAM Nulling

```
correction_factor = 1./correction_factor;

% Apply each new correction factor to original data and record in new column
sep_AM_amps_corrected(:,2) = (1-sep_AM_amps_corrected(:,1)).*correction_factor';
sep_AM_amps_corrected(:,2) = 1-sep_AM_amps_corrected(:,2);

% Find the minimum amplitude in the experimental plot
K_1 = min(theory_amps);
K_Index_1 = find(theory_amps == K_1);
Line_Cent_Wave_1 = theory_lambda(K_Index_1);

K_2 = min(sep_AM_amps_corrected(:,2));
K_Index_2 = find(sep_AM_amps_corrected(:,2) == K_2);
Line_Cent_Wave_2 = sep_AM_waves(K_Index_2);
% The lateral shift at high modulation indices is calculated and corrected
line_centre_shift = Line_Cent_Wave_2 - Line_Cent_Wave_1;
sep_AM_waves = sep_AM_waves - line_centre_shift;

LLL = min(point2_amps) - 0.005;
LL = max(point2_amps) + 0.01;

figure
hold on
plot(point2_waves,point2_amps, '--','LineWidth',2)
plot(sep_AM_waves,sep_AM_amps_corrected(:,1), 'r','LineWidth',2)
plot(sep_AM_waves,sep_AM_amps_corrected(:,2),'g','LineWidth',2)
xlabel('Wavelength (nm)')
ylabel('Transmission')
title(input_text(12,:))
axis([1650.8 1651.1 LLL 1])
legend('Theory','Uncorrected','Corrected','Location','SouthEast')

saveas(gcf,input_text(19,:))

gas = sep_AM_amps_corrected(:,2);
%%%%%%%%%%%%%%%%%%%%%%%%%%%%%%%%%%%%%%%%%%%%%%%%%%%%%%%%%%%%%%%%%%%%%%%%
% 4.0 Reading in of all spectroscopic constants and variables
%%%%%%%%%%%%%%%%%%%%%%%%%%%%%%%%%%%%%%%%%%%%%%%%%%%%%%%%%%%%%%%%%%%%%%%%
% 4.2 Defining temperature
T_0 = 296; % Reference Temperature in Kelvin
T_K = 273.15; %0 degrees celcius in Kelvin
degreeT = inputnumber(15); %input('\n Temperature in Celsius: ');
T = degreeT+T_K; %Converting to Kelvin

% 4.3 Reading in pressure and converting from bar to atm
% pressure = input('\n Initial Pressure: '); %bar
pressure = inputnumber(14)*0.986926; %atm

%4.3.1 Pressure range for fitting loop
coeff = linspace(pressure-0.1,pressure+0.1,50);

%4.3.2 Defining Start Concentrations
actual_methane_concentration=[0,0.5,1];

% 4.4 Frequency Range
```

## Appendix D. MATLAB code - PD method with RAM Nulling

```
vsteps = 2000;
v = linspace(6054,6064,vsteps); %theory frequency range
lambda = 1./v.*1e7;

% 4.5 Calculation of individual line-strengths
Q_T0 = (7.0192e-9*T_0^4)-(3.6651e-6*T_0^3)+(0.0031476*T_0^2)+(1.4428*T_0)-71.184;
Q_T = (7.0192e-9*T^4)-(3.6651e-6*T^3)+(0.0031476*T^2)+(1.4428*T)-71.184;
S1 = 1-exp(-(h*c.*methanelines(:,1))/(k*T));
S2 = 1-exp(-(h*c.*methanelines(:,1))/(k*T_0));
S3 = S1./S2;
S4 = Q_T0./Q_T;
S5 = T_0/T;
S6 = exp((-h*c.*methanelines(:,5)/k)*((1/T)-(1/T_0)));
S7 = S3.*S4.*S5.*S6;
S_T=S7.*methanelines(:,2); %Total linestrength

% 4.6 Calculation of Broadening Parameters

%4.6.1 Gaussian Broadening
gammag = 7.1625e-7.*methanelines(:,1).*(T/16)^0.5;
gammag = gammag';

% 4.6.2 Air broadening parameter
air_broadening_parameter = c_AIR*methanelines(:,3).*(T_0/T).^0.73;

% 4.6.3 Self Broadening parameter
self_broadening_parameter = methanelines(:,4)*(T_0/T)^0.8;

% 4.7 X values for Voigt Profile
for j = 1:z
X(:,j) = 2*sqrt(log(2))*(v-methanelines(j,1)-methanelines(j,7))./gammag(j);
end

% 4.8 A-D values for Voigt Profile
A = [-1.2150 -1.3509 -1.2150 -1.3509];
B = [1.2359 0.3786 -1.2359 -0.3786];
C = [-0.3085 0.5906 -0.3085 0.5906];
D = [0.0210 -1.1858 -0.0210 1.1858];

%%%%%%%%%%%%%%%%%%%%%%%%%%%%%%%%%%%%%%%%%%%%%%%%%%%%%%%%%%%%%%%%%%%%%%%%%%
% 5.0 Pressure Loop and Golden Section Search
%%%%%%%%%%%%%%%%%%%%%%%%%%%%%%%%%%%%%%%%%%%%%%%%%%%%%%%%%%%%%%%%%%%%%%%%%%

for why = 1:50
why
% 5.1 Constants for Golden Section Search
tol=0.001;
Ce = (3-sqrt(5))/2;
R = 1-Ce;

% 5.2 Pressure and Concentration Variables
total_pressure = coeff(why);
x0 = actual_methane_concentration(1);
x3 = actual_methane_concentration(3);

% 5.3 Defining Initial Values for methane concentrations
```

```

if (abs(actual_methane_concentration(3)-actual_methane_concentration(2))
> abs(actual_methane_concentration(2)-actual_methane_concentration(1))),
    x1 = actual_methane_concentration(2);
    x2 = actual_methane_concentration(2) +
        Ce*(actual_methane_concentration(3)-actual_methane_concentration(2));
else
    x2 = actual_methane_concentration(2);
    x1 = actual_methane_concentration(2) -
        Ce*(actual_methane_concentration(2)-actual_methane_concentration(1));
end

% 5.4 GOLDEN SECTION SEARCH
while abs(x3-x0) > tol*(abs(x1)+abs(x2)),

    % 5.4.1 Concentrations
    methane_concentration(1) = x1;
    methane_concentration(2) = x2;
    nitrogen_concentration = 1-methane_concentration;

    % 5.4.2 Lorentzian Broadening
    gammal = 2*total_pressure.*((air_broadening_parameter*nitrogen_concentration)+
    (self_broadening_parameter*methane_concentration));
    gammal = gammal';

    % 5.4.3 Voigt Y values
    Y1 = (gammal(1,:)./gammag)*sqrt(log(2));
    Y2 = (gammal(2,:)./gammag)*sqrt(log(2));

    % 5.4.4 Creating Voigt V Values
    for j = 1:z
        for i = 1:4
            V_top1(i,:) = (C(i)*(Y1(j)-A(i)))+(D(i)*(X(:,j)-B(i)));
            V_bottom1(i,:) = (Y1(j)-A(i))^2+(X(:,j)-B(i)).^2;
            V_top2(i,:) = (C(i)*(Y2(j)-A(i)))+(D(i)*(X(:,j)-B(i)));
            V_bottom2(i,:) = (Y2(j)-A(i))^2+(X(:,j)-B(i)).^2;
        end
        V1 = V_top1./V_bottom1;
        V12(:,j) = (2/gammag(j))*(log(2)/pi)^0.5*methane_concentration(1)
        *(7.339e21/T_0)*S_T(j)*sum(V1);
        V2 = V_top2./V_bottom2;
        V22(:,j) = (2/gammag(j))*(log(2)/pi)^0.5*methane_concentration(2)
        *(7.339e21/T_0)*S_T(j)*sum(V2);
    end

    % 5.4.5 Spectral Absorption Coefficients
    kv1 = total_pressure*sum(V12');
    kv2 = total_pressure*sum(V22');

    % 5.4.6 Fractional Transmission
    T1 = exp(-kv1.*L);
    T2 = exp(-kv2.*L);

    % 5.4.7 Find indices for the theoretical wavelengths that match two ends of
    % experimental data
    IND1 = find(lambda <= YYY_wavelength(1));
    IND1 = IND1(1);

```

*Appendix D. MATLAB code - PD method with RAM Nulling*

```
IND2 = find(lambda <= YYY_wavelength(xx));
IND2 = IND2(1);

% 5.4.8 Calculate the wavelengths and amplitudes of the theory data in range
%       of experimental data
cut_theory_lambda = linspace(lambda(IND2),lambda(IND1),IND1-IND2+1);
cut_theory_amps1 = T1(IND2:IND1);
cut_theory_amps2 = T2(IND2:IND1);

% 5.4.9 Interpolating theory data over length of experimental
%       data, making sets of data over equal range and equal length
amps_chopped1 = interp1(cut_theory_lambda,cut_theory_amps1,YYY_wavelength,
'linear','extrap');
amps_chopped2 = interp1(cut_theory_lambda,cut_theory_amps2,YYY_wavelength,
'linear','extrap');

% 5.4.10 Setting the experimental baseline to theoretical
%       baseline
gap1 = gas(1800) - amps_chopped1(1800);
gap2 = gas(1800) - amps_chopped2(1800);

norm_amps1 = gas-gap1;
norm_amps2 = gas-gap2;

% 5.4.11 Least squares fit of theory and experimental
f1=sum((amps_chopped1(Line_Cent_Index-500:Line_Cent_Index+500)-
norm_amps1(Line_Cent_Index-500:Line_Cent_Index+500)).^2);
f2=sum((amps_chopped2(Line_Cent_Index-500:Line_Cent_Index+500)-
norm_amps2(Line_Cent_Index-500:Line_Cent_Index+500)).^2);

% 5.4.12 New values for the Golden Section Search
if f2 < f1,
    x0 = x1;
    x1 = x2;
    x2 = R*x1 + Ce*x3;
    f1 = f2;
    concentration = methane_concentration(2);
    finalvalue(1,why) = f1;
    finalvalue(2,why) = f2;
    finalvalue(3,why) = concentration;
    finalvalue(4,why) = total_pressure;
else
    x3 = x2;
    x2 = x1;
    x1 = R*x2 + Ce*x0;
    f2 = f1;
    concentration = methane_concentration(2);
    finalvalue(1,why) = f1;
    finalvalue(2,why) = f2;
    finalvalue(3,why) = concentration;
    finalvalue(4,why) = total_pressure;
end
end
end
```

#### Appendix D. MATLAB code - PD method with RAM Nulling

```
%%%%%%%%%%%%%%%%%%%%%%%%%%%%%%%%%%%%%%%%%%%%%%%%%%%%%%%%%%%%%%%%%%%%%%%%%
% 6.0 Finding final concentration
%%%%%%%%%%%%%%%%%%%%%%%%%%%%%%%%%%%%%%%%%%%%%%%%%%%%%%%%%%%%%%%%%%%%%%%%%

% 6.1 Finding data set with minimum lsq fit
min_index = min(finalvalue(1,:));
min_index = find(finalvalue(1,:) == min_index);

% 6.2 Final concentration, error, and pressure
final_methane_conc = finalvalue(3,min_index);
final_press = finalvalue(4,min_index);
error = abs((((final_methane_conc*100)-inputnumber(16))/inputnumber(16))*100);
final_nitrogen_conc = 1-final_methane_conc;

% 6.3 Final Lorentzian Broadening
gammal=2*final_press.*((air_broadening_parameter*final_nitrogen_conc)
+(self_broadening_parameter*final_methane_conc));
gammal=gammal';

% 6.4 Final voigt Y-value
Y = (gammal./gammag)*sqrt(log(2));

% 6.5 final voigt V-value
for j = 1:z
    for i = 1:4
        V_top(i,:) = (C(i)*(Y(j)-A(i)))+(D(i)*(X(:,j)-B(i)));
        V_bottom(i,:) = (Y(j)-A(i))^2+(X(:,j)-B(i)).^2;
    end
    V = V_top./V_bottom;
    Vfinal(:,j) = (2/gammag(j))*(log(2)/pi)^0.5*final_methane_conc*(7.339e21/T_0)*S_T(j)*sum(V);
end

% 6.6 Final spectral absorption coefficient
kv = final_press*sum(Vfinal');

% 6.7 Final fractional transmission
T = exp(-kv.*L);

% 6.8 Changing range of theory data to the range of experimental data
cut_theory_amps = T(IND2:IND1);
amps_chopped = interp1(cut_theory_lambda,cut_theory_amps,YYY_wavelength,'linear','extrap');

% 6.9 Setting the experimental baseline to theoretical
%    baseline
gap = gas(1800)-amps_chopped(1800);
gas = gas-gap;

% 6.10 Calculating theory/experimental residual
residual = amps_chopped-gas';

% 6.11 Stating final concentration
final_methane_conc = (final_methane_conc*100)
final_press = final_press/0.986926
error_press = abs((((final_press)-(pressure/0.986926))/(pressure/0.986926))*100);

%% 6.12 Plots comparisons of the experimental data and the Matlab theory file, and
```

*Appendix D. MATLAB code - PD method with RAM Nulling*

```
% %      also a residual subtraction of the two sets of data
figure
axes('position',[.1 .1 .8 .5])
hold on
plot (YYY_wavelength,gas,'linewidth',1.5)
% plot (YYY_wavelength,gas2,'m','linewidth',1.5)
plot(cut_theory_lambda,cut_theory_amps,'r','linewidth',1.5)
xlabel('Wavelength, nm')
ylabel('Relative Transmission')
title(['Methane Absorption Spectra at ', num2str(degreeT),'^{o}C'];
['Calculated Concentration ',num2str(final_methane_conc),'% (error ',num2str(error),'%')']
;['Calculated Pressure ',num2str(final_press),'bar (error ',num2str(error_press),'%')'])
legend('Experimental Data', 'Theoretical Fit',4)
axes('position',[.1 .75 .8 .2])
plot(YYY_wavelength,residual)
xlabel('Wavelength, nm')
ylabel('Residual')

% theory(:,1) = cut_theory_lambda;
% theory(:,2) = cut_theory_amps;
% waves = YYY_wavelength;

sheetname = input_text(15,:);
sheetname = sheetname(1:6);
result = [YYY_wavelength' gas sep_AM_waves' sep_AM_amps_corrected(:,2)];
xlswrite(input_text(9,:),result,sheetname);

theory = [theory_lambda' theory_amps'];
xlswrite('theory.xls',theory);
figure(3);
```

# Appendix E

## MATLAB code - Amplitude Investigation Part I

```
%-----  
%   Amplitude Investigation Part I  
%   Keith Ruxton  
%-----  
clear all;  
clc;  
close all;  
format long;  
  
pp = 6;  
  
Io = 339; %Intensity at line centre  
A1 = 0.4705*.1013*9.9; %calculate A factor !!REMEMBER TO CHANGE CONCENTRATION!!  
gamma1 = 2.2511; %HWHM GHz  
tuning1 = [0.26444249 0.199530433 0.170103236 0.137969934 0.124208437  
0.119154429]; %GHz/mA  
tuning2 = [0.124208437 0.078585135 0.059472524 0.053255453 0.047953628  
0.047325368 0.047320182];  
kappa1 = 4.8957; %uW/mA  
  
m_plot = [0.2 0.5 1 1.5 2 2.2];  
  
onef_coeff = [0.12706925 0.286197658 0.435928217 0.489068631 0.500000459 0.498893388];  
twof_coeff = [0.018215047 0.098675569 0.241626833 0.316742468 0.340626994 0.342131736];  
  
for d = 1:pp  
    theory_FM(d) = onef_coeff(d) * Io * A1;  
    theory_2f(d) = twof_coeff(d) * Io * A1;  
end  
  
%Generate RAM coeff  
theta = 0:pi/100:pi;  
  
i=1;  
  
for m = 0:0.01:5  
    AA = m / pi;
```

*Appendix E. MATLAB code - Amplitude Investigation Part I*

```

    B = (1 - cos(2.*theta)) ./ (1 + m^2 .* (cos(theta).^2));
    C = trapz(theta,B);
    D(i) = AA * C;
    i = i+1;
end

m_axis = 0:0.01:5;

p1 = polyfit(m_axis,D,10);
f1 = polyval(p1,m_axis);

coeff_RAM1 = [polyval(p1,0.2) polyval(p1,0.5) polyval(p1,1) polyval(p1,1.5)
polyval(p1,2) polyval(p1,2.2)]';
coeff_RAM = coeff_RAM1 .* (A1 * gamma1 * kappa1);

theory_RAM_10kHz = coeff_RAM / tuning1(1);
theory_RAM_30kHz = coeff_RAM / tuning1(2);
theory_RAM_50kHz = coeff_RAM / tuning1(3);
theory_RAM_80kHz = coeff_RAM / tuning1(4);
theory_RAM_100kHz = coeff_RAM / tuning1(5);
theory_RAM_110kHz = coeff_RAM / tuning1(6);

theory_RAM_100kHz = coeff_RAM / tuning2(1);
theory_RAM_250kHz = coeff_RAM / tuning2(2);
theory_RAM_500kHz = coeff_RAM / tuning2(3);
theory_RAM_750kHz = coeff_RAM / tuning2(4);
theory_RAM_1MHz = coeff_RAM / tuning2(5);
theory_RAM_1_1MHz = coeff_RAM / tuning2(6);
theory_RAM_1_2MHz = coeff_RAM / tuning2(7);

theory_RAM = theory_RAM_10kHz;

name = '10kHz';
sheet1 = '10kHz RAM';
sheet2 = '10kHz 1f';
sheet3 = '10kHz 2f';

% reading in all user data
[gas_RAM_data] = xlsread('amp_results2.xls','10kHz RAM', 'a1:l8000');
[gas_FM_data] = xlsread('amp_results2.xls','10kHz 1f', 'a1:l8000');
[SF_1f_data] = xlsread('nogas_amp_1results_check.xls','1f 10kHz', 'a1:f8000');

% reading in all user data
[gas_2f_data] = xlsread('amp_results2.xls','10kHz 2f', 'a1:l8000');
[SF_2f_data] = xlsread('nogas_amp_results_check.xls','2f 10kHz', 'a1:f8000');

for tt = 1:pp
    RAM_max(tt) = (gas_RAM_data(1,(tt*2)) - gas_RAM_data(end,(tt*2)))/2
    + gas_RAM_data(end,(tt*2));
    FM_max(tt) = (max(gas_FM_data(:,(tt*2))) - min(gas_FM_data(:,(tt*2)))) / 2;
    twof_max(tt) = max(gas_2f_data(:,(tt*2)));
end

SF_1f = theory_FM(5) / FM_max(5);
SF_RAM = theory_RAM(6) / RAM_max(6);
SF_2f = theory_2f(6) / twof_max(6);

```

```

FM_max = FM_max .* SF_1f;
RAM_max = RAM_max .* SF_RAM;
twof_max = twof_max .* SF_2f;
m_axis_2 = 0.2:0.01:2.2;
xlswrite('scaled_max_amp.xls',pchip(m_plot,theory_RAM,m_axis_2),sheet1);
xlswrite('scaled_max_amp.xls',pchip(m_plot,theory_FM,m_axis_2),sheet2);
xlswrite('scaled_max_amp.xls',pchip(m_plot,theory_2f,m_axis_2),sheet3);

xlswrite('scaling_factor.xls',SF_RAM,sheet1);
xlswrite('scaling_factor.xls',SF_1f,sheet2);
xlswrite('scaling_factor.xls',SF_2f,sheet3);

figure
hold on
plot(m_axis_2,(pchip(m_plot,theory_RAM,m_axis_2)),'-k','LineWidth',2);
plot(m_axis_2,(pchip(m_plot,RAM_max,m_axis_2)),'-r','LineWidth',2);
plot(m_axis_2,(pchip(m_plot,theory_FM,m_axis_2)),'--k','LineWidth',2);
plot(m_axis_2,(pchip(m_plot,FM_max,m_axis_2)),'-b','LineWidth',2);
plot(m_axis_2,(pchip(m_plot,theory_2f,m_axis_2)),':k','LineWidth',2);
plot(m_axis_2,(pchip(m_plot,twof_max,m_axis_2)),'-c','LineWidth',2);
plot(m_plot,RAM_max,'r^','LineWidth',2);
plot(m_plot,FM_max,'b^','LineWidth',2);
plot(m_plot,twof_max,'c^','LineWidth',2);
xlabel('Modulation Index')
ylabel('Intensity (mW)')
legend('RAM','1f','2f','location','SouthOutside','Orientation','horizontal')
title(['Comparison 1f and RAM amplitudes - 10.13%CH_4:N_2 @ ',name])
legend('Theory - RAM','Results - RAM','Theory - 1f','Results - 1f',
'location','EastOutside','Orientation','vertical')

```

# Appendix F

## MATLAB code - Amplitude Investigation Part II

```
%-----  
%   Amplitude Investigation Part II  
%   Keith Ruxton  
%-----  
close all;  
clc;  
clear all;  
  
m_plot = [0.1 0.25 0.5 0.75 1 1.1 1.2];  
% m_plot = [10 30 50 80 100 110];  
name = 'm=2.2';  
name2 = 'm=2_2';  
iii=6;  
  
RAM1 = xlsread('scaled_max_amp.xls','100kHz RAM');  
RAM2 = xlsread('scaled_max_amp.xls','250kHz RAM');  
RAM3 = xlsread('scaled_max_amp.xls','500kHz RAM');  
RAM4 = xlsread('scaled_max_amp.xls','750kHz RAM');  
RAM5 = xlsread('scaled_max_amp.xls','1MHz RAM');  
RAM6 = xlsread('scaled_max_amp.xls','1_1MHz RAM');  
RAM7 = xlsread('scaled_max_amp.xls','1_2MHz RAM');  
  
FM1 = xlsread('scaled_max_amp.xls','100kHz 1f');  
FM2 = xlsread('scaled_max_amp.xls','250kHz 1f');  
FM3 = xlsread('scaled_max_amp.xls','500kHz 1f');  
FM4 = xlsread('scaled_max_amp.xls','750kHz 1f');  
FM5 = xlsread('scaled_max_amp.xls','1MHz 1f');  
FM6 = xlsread('scaled_max_amp.xls','1_1MHz 1f');  
FM7 = xlsread('scaled_max_amp.xls','1_2MHz 1f');  
  
two1 = xlsread('scaled_max_amp.xls','100kHz 2f');  
two2 = xlsread('scaled_max_amp.xls','250kHz 2f');  
two3 = xlsread('scaled_max_amp.xls','500kHz 2f');  
two4 = xlsread('scaled_max_amp.xls','750kHz 2f');  
two5 = xlsread('scaled_max_amp.xls','1MHz 2f');  
two6 = xlsread('scaled_max_amp.xls','1_1MHz 2f');  
two7 = xlsread('scaled_max_amp.xls','1_2MHz 2f');
```

```

% RAM1 = xlsread('scaled_max_amp.xls','10kHz RAM');
% RAM2 = xlsread('scaled_max_amp.xls','30kHz RAM');
% RAM3 = xlsread('scaled_max_amp.xls','50kHz RAM');
% RAM4 = xlsread('scaled_max_amp.xls','80kHz RAM');
% RAM5 = xlsread('scaled_max_amp.xls','100kHz RAM');
% RAM6 = xlsread('scaled_max_amp.xls','110kHz RAM');
%
% FM1 = xlsread('scaled_max_amp.xls','10kHz 1f');
% FM2 = xlsread('scaled_max_amp.xls','30kHz 1f');
% FM3 = xlsread('scaled_max_amp.xls','50kHz 1f');
% FM4 = xlsread('scaled_max_amp.xls','80kHz 1f');
% FM5 = xlsread('scaled_max_amp.xls','100kHz 1f');
% FM6 = xlsread('scaled_max_amp.xls','110kHz 1f');
%
% two1 = xlsread('scaled_max_amp.xls','10kHz 2f');
% two2 = xlsread('scaled_max_amp.xls','30kHz 2f');
% two3 = xlsread('scaled_max_amp.xls','50kHz 2f');
% two4 = xlsread('scaled_max_amp.xls','80kHz 2f');
% two5 = xlsread('scaled_max_amp.xls','100kHz 2f');
% two6 = xlsread('scaled_max_amp.xls','110kHz 2f');

RAM_max = [RAM1(iii) RAM2(iii) RAM3(iii) RAM4(iii) RAM5(iii) RAM6(iii) RAM7(iii)];
FM_max = [FM1(iii) FM2(iii) FM3(iii) FM4(iii) FM5(iii) FM6(iii) FM7(iii)];
twof_max = [two1(iii) two2(iii) two3(iii) two4(iii) two5(iii) two6(iii) two7(iii)];

% m_axis_2 = 10:0.01:110;
m_axis_2 = 0.1:0.01:1.2;

figure
hold on
plot(m_axis_2,(pchip(m_plot,RAM_max,m_axis_2)),'-k','LineWidth',2);
plot(m_axis_2,(pchip(m_plot,FM_max,m_axis_2)),'--k','LineWidth',2);
plot(m_axis_2,(pchip(m_plot,twof_max,m_axis_2)),':k','LineWidth',2);
xlabel('Frequency (MHz)')
ylabel('Intensity (mW)')
title(['Comparison Experimental 1f, 2f and RAM amplitudes - 1.02%CH_4:N_2 @ ',name])
legend('RAM','1f','2f','location','SouthOutside','Orientation','horizontal')

```